Dynamics Based Vibration Signal Modeling and Fault Detection of Planetary Gearboxes

by

Xihui Liang

A thesis submitted in partial fulfillment of the requirements for the degree of

Doctor of Philosophy

Department of Mechanical Engineering
University of Alberta

Abstract

Vibration analysis has been widely used to detect gear tooth fault inside a planetary gearbox. However, the vibration characteristics of a planetary gearbox are very complicated. Inside a planetary gearbox, there are multiple vibration sources as several sun-planet gear pairs and several ring-planet gear pairs are meshing simultaneously. In addition, due to the rotation of the carrier, distance varies between vibration sources and a transducer installed on gearbox housing. This thesis aims to simulate and understand the vibration signals of a planetary gear set, and then propose a signal processing method to detect gear tooth fault more effectively. First, an analytical method derives the equations of a healthy planetary gear set's time-varying gear mesh stiffness. Then, a gear tooth crack growth model is proposed and equations are derived to quantify the effect of gear tooth crack on the time-varying mesh stiffness. After that, a two-dimensional lumped-mass model is developed to simulate the vibration source signals of a planetary gear set; an analytical model is proposed to represent the effect of transmission path; and the resultant vibration signals of a planetary gear set at a sensor location are generated by considering multiple vibration sources and the effect of transmission path. Finally, a signal decomposition method is proposed to detect a single tooth crack in a single planet gear and experimental validation is performed. The methods proposed in this thesis help us understand the vibration properties of planetary gearboxes and give insights into developing new signal processing methods for gear tooth fault detection.

Preface

The main body of this thesis is composed of four published/submitted journal papers and four refereed conference papers. See below for details.

Chapter 2 of this thesis is mainly based on a published journal paper: X. Liang, M. J. Zuo, and T. H. Patel, "Evaluating Time-varying Mesh Stiffness of a Planetary Gear Set Using Potential Energy Method," *Proc. Inst. Mech. Eng. Part C J. Mech. Eng. Sci.*, vol. 228, no. 3, pp. 535–547, Feb. 2014. Some preliminary results of this journal paper were published in a refereed conference paper: X. Liang, M. J. Zuo, and Y. Guo, "Evaluating the Time-Varying Mesh Stiffness of a Planetary Gear Set Using the Potential Energy Method," in *Proceedings of the 7th World Congress on Engineering Asset Management*, Springer International Publishing, 2015, pp. 365–374. I proposed this topic and was responsible for equations derivation, data analysis and paper writing. Dr. M. J. Zuo is the supervisory author who checked results and revised the manuscript. Dr. T. H. Patel gave comments to improve the journal paper. Dr. Y. Guo gave some comments to improve the conference paper.

Chapter 3 of this thesis is mainly based on a published journal paper: X. Liang, M. J. Zuo, and M. Pandey, "Analytically Evaluating the Influence of Crack on the Mesh Stiffness of a Planetary Gear Set," *Mech. Mach. Theory*, vol. 76, pp. 20–38, Jun. 2014. Some preliminary results of this journal paper were published in a refereed conference paper: X. Liang and M. J. Zuo, "Dynamic Simulation of a Planetary Gear Set and Estimation of Fault Growth on the Sun Gear," in *Proceedings of 2013 International Conference on Quality, Reliability, Risk, Maintenance, and Safety Engineering*, 2013, pp.

1667–1672. I proposed this topic and was responsible for equations derivation, data analysis and paper writing. Dr. M. J. Zuo is the supervisory author who checked results and revised the manuscript. Dr. M. Pandey gave comments to improve the journal paper.

Chapter 4 of this thesis is mainly based on a published journal paper: X. Liang, M. J. Zuo, and M. R. Hoseini, "Vibration Signal Modeling of a Planetary Gear Set for Tooth Crack Detection," *Eng. Fail. Anal.*, vol. 48, pp. 185–200, Feb. 2015. Some preliminary results of this journal paper were published in a refereed conference paper: X. Liang, M. J. Zuo, and M. R. Hoseini, "Understanding Vibration Properties of a Planetary Gear Set for Fault Detection," in *Proceedings of 2014 IEEE Conference on Prognostics and Health Management*, 2014, pp. 1–6. I proposed this topic and was responsible for numerical simulation, data analysis and paper writing. Dr. M. J. Zuo is the supervisory author who checked results and revised the manuscript. Dr. M. R. Hoseini gave comments to improve the journal paper.

Chapter 5 of this thesis is mainly based on a submitted journal paper: X. Liang, M. J. Zuo, and L. Liu, "A Windowing and Mapping Strategy for Gear Tooth Fault Detection of a Planetary Gearbox." *Mech. Syst. Signal Pr.*, Submitted: 06-Jun-2015. Some preliminary results of this journal paper were published in a refereed conference paper: X. Liang and M. J. Zuo, "Investigating Vibration Properties of a Planetary Gear Set with a Cracked Tooth in a Planet Gear," in *Proceedings of 2014 Annual Conference of the Prognostics and Health Management Society*, Fort Worth, Texas, 2014, pp. 1–8. I proposed this topic and was responsible for numerical simulation, data analysis and paper writing. Dr. M. J. Zuo is the supervisory author who checked results and revised the manuscript. Mr. L. Liu gave comments to improve the journal paper.

Acknowledgements

I gratefully thank my supervisor Dr. Ming J. Zuo for his guidance, support, care and encouragement during my Ph.D. study. Under his guidance, I have gained not only valuable academic knowledge but also useful logic and methodology to deal with real-word problems. It is my honor to conduct research under his guidance.

I sincerely thank my Ph.D. examining committee members, Dr. Bob Koch, Dr. Yongsheng Ma, Dr. Walied Moussa, and Dr. Robert G. Parker for their valuable comments on my thesis.

Many thanks to Dr. Zhigang Tian, Dr. Chongqing Ru, Dr. Xiaodong Wang, Dr. Amit Kumar, and Dr. John Doucette for their help in my Ph.D. study.

I am also grateful to all the members in our Reliability Research Lab for their help and support. Working with them is an exciting and beneficial experience.

Finally, I express my gratitude to my family members. Without them, my journey would not have been possible. I would like to dedicate this work to my wife, my daughter, my parents and my parents-in-law. Without their help and encourage, I could not achieve this goal.

Table of Contents

List of Tables

List of Figures

Nomenclature

a	Pressure angle of gear pairs
A_x	Area of tooth section whose distance from the tooth root is x
c	Contact ratio of gear pairs
c_{cx}, c_{cy}	Damping coefficient of carrier bearing in x, y direction
c_{pnx}, c_{pny}	Damping coefficient of the n^{th} planet in x, y direction
c_{rx}, c_{ry}	Damping coefficient of ring gear bearing in x, y direction
c_{rt}	Damping coefficient of ring gear in torsional direction
c_{spn}, c_{rpn}	Mesh damping coefficient of the n^{th} sun-planet, ring-planet
c_{sx}, c_{sy}	Damping coefficient of sun gear bearing in x, y direction
d	Distance from the contact point to gear root
E	Young's modulus
F	Acting force of contact teeth
f_m	Gear mesh frequency
f_{main}	Sizable amplitude frequencies when the gearbox is in perfect condition
f_s, f_p, f_c	Rotational frequency of sun gear, planet gear, carrier
f_{scrack}	Characteristic frequency of cracked sun gear tooth
$h_m(\mathrm{t})$	Hamming function: $h_m(\mathrm{t}) = 0.54 - 0.46\cos(w_c t + \psi_n)$
$h_n(\mathrm{t})$	Hanning function: $h(\mathrm{t}) = 0.5 - 0.5\cos(w_c t + \psi_n)$

I_x	Area moment of inertia of gear tooth section
J_s , J_p , J_r , J_c	Mass moment of inertia of sun gear, planet gear, ring gear, carrier
k_a	Axial compressive stiffness
k_b	Bending stiffness
k_{cx} , k_{cy}	Stiffness of carrier bearing in x, y direction
k_h	Hertzian contact stiffness
k_{pnx} , k_{pny}	Stiffness of the n^{th} planet bearing in x, y direction
k_r	Total effective mesh stiffness
k_{rx} , k_{ry}	Stiffness of ring gear bearing in x, y direction
k_{rt}	Stiffness of ring gear in torsional direction
k_s	Shear stiffness
k_{spn} , k_{rpn}	Mesh stiffness of the n^{th} sun-planet, ring-planet
k_{sx} , k_{sy}	Stiffness of sun gear bearing in x, y direction
L	Width of gear tooth
m_s , m_p , m_r , m_c	Mass of sun gear, planet gear, ring gear, carrier
N	Number of planet gears in a planetary gear set
r_c	Radius of the circle passing through planet gear centers
r_s , r_p , r_r	Base circle radius of sun gear, planet gear, ring gear
R_{b1}	Base circle radius of an external gear
R_{rb}	Base circle radius of an internal gear

R_{rr}	Root circle radius of an internal gear
R_{O2}	Inner radius of an internal gear
T_c	Rotational period of the carrier
T_m	Gear mesh period
T_i, T_o	Input torque on sun gear, output torque on the carrier
Z_s, Z_p, Z_r	Number of tooth of sun gear, planet gear, ring gear
α_0	Pressure angle
α_1	Angle of force component F_b and force F for an external gear
α_2	Half tooth angle on the base circle for an external gear
β_1	Angle of force component F_b and force F for an internal gear
β_2	Half tooth angle on the base circle for an internal gear
γ_{sn}	Relative phase between n^{th} sun-planet pair and 1^{st} sun-planet pair
γ_{rn}	Relative phase between n^{th} ring-planet pair and 1^{st} ring-planet pair
γ_{rs}	Relative phase between n^{th} ring-planet pair and n^{th} sun-planet pair
δ	Deformation of contact teeth due to force F
δ_{spn}, δ_{rpn}	Relative displacement in line of action of the n^{th} sun-planet, ring-planet
θ	Rotation angular displacement of a gear
θ_m	Rotation angular displacement of a planet gear in one mesh period
θ_p	Rotation angular displacement of a planet gear

ϕ	Half tooth angle on the root circle for an internal gear
ψ_n	Circumferential angle of the n^{th} planet
Ω	Rotation speed of the carrier
ν	Poisson's ratio
ω_p	Angular rotation speed of the planet gear

Chapter 1: Introduction

This chapter is divided into three sections. I introduce the background of this thesis topic in Section 1. Section 2 provides a detailed literature review of the research challenges around the dynamics based vibration signal modeling and fault detection of planetary gearboxes. Section 3 provides the research objectives and the organizational structure of this whole thesis.

1.1 Background

Planetary gearboxes are common in industrial applications due to their compactness and high torque-to-weight ratio [1.1]. A planetary gear set normally consists of a centrally pivoted sun gear, a ring gear and several planet gears which rotate around the sun gear and ring gear simultaneously as shown in Fig. 1.1. The sun gear and planet gears are external gears; the ring gear is an internal gear. An external gear has its teeth formed on the outer surface of a cylinder or cone, while an internal gear has its teeth formed on the inner surface of a cylinder or cone [1.2]. Transducers usually rest on the housing of planetary gearboxes or the casing of bearings to collect the vibration signals as shown in Fig. 1.2. In this study, I focus only on modeling and investigating the vibration signals to be collected by the transducers mounted on the housing of planetary gearboxes.

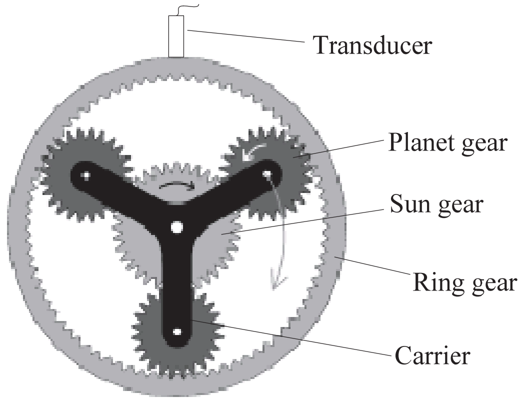

Fig. 1.1: Structure of a planetary gear set [1.3]

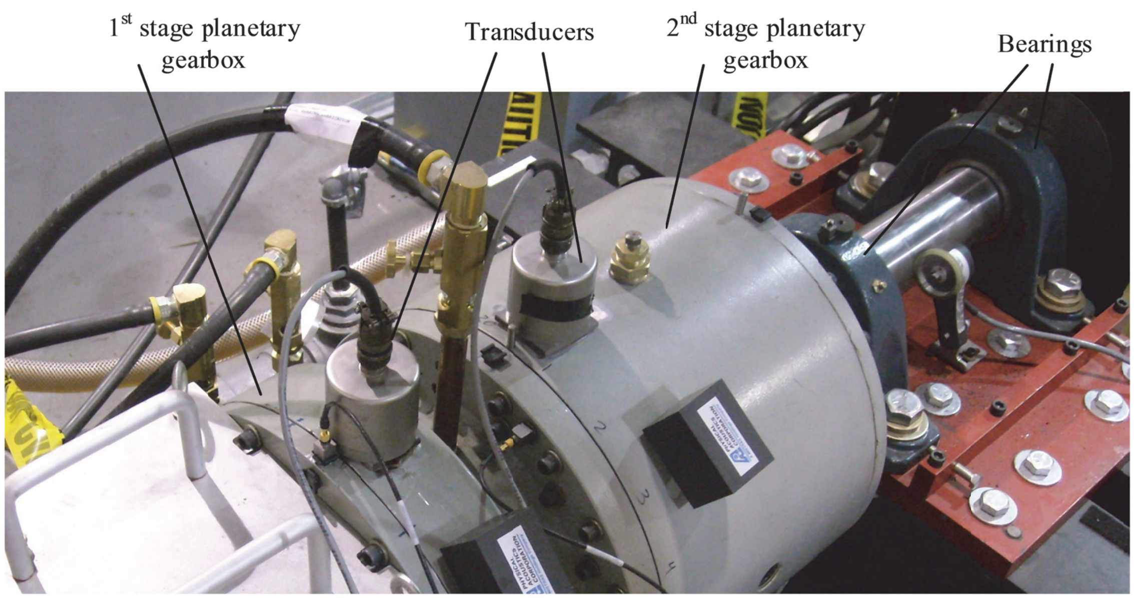

Fig. 1.2: Planetary gearboxes and transducers

Due to high service load, harsh operating conditions or simple fatigue, faults may develop in gears [1.4]. Gear faults are responsible for approximately 60% of gearbox failures [1.5]. Most of these come from damage to the gear teeth such as pitting, cracking, and spalling [1.5]. The ASM handbook [1.6] classifies gear tooth failures into the following five categories: overload, bending fatigue, Hertzian fatigue, wear, and scuffing.

Observation during application of planetary gearboxes at Syncrude Canada Ltd, indicated fatigue crack and pitting are the two commonest failure modes of the planetary gearbox [1.7]. Fatigue crack is a non-lubrication-related failure mode while pitting is a lubrication-related failure mode [1.5]. This study will model gear tooth fatigue crack and investigate its effect on a planetary gearbox's dynamic responses and vibration signals.

If the gear faults cannot be detected early, the health will continue to degrade, perhaps causing large economic loss or catastrophe. In a rotorcraft, the transmission system has a single load path without duplication or redundancy. The gearboxes are the system's main components. If the gears fail during a flight, the rotorcraft may crash. "As a helicopter was flying to Aberdeen from the Miller platform in the North Sea on the afternoon of 1 April 2009 the main rotor came off and the aircraft crashed into the sea. All 14 offshore workers and the two crewmen died. It was the gear that failed as a result of a fatigue crack, causing the failure of the main rotor gearbox." [1.8] According to P.R. Veillette [1.9], "More than half the accidents in U.S. helicopter logging operations in 1983 through 1999 involved failures of engines or transmission systems."

It is important to monitor the health of gearbox systems and detect early faults in advance. Condition monitoring techniques have been developed and widely used to monitor and diagnose the health of gear systems. Vibration analysis, acoustic analysis, oil debris analysis, temperature analysis, and strain analysis are common techniques in the condition monitoring of gearbox systems. Vibration analysis relies on the analysis of vibration signals to detect faults in equipment, most often in rotating equipment such as gearboxes, motors, fans and pumps. Acoustic analysis detects fault in a device through evaluating voice quality using fundamental frequency, perturbation and noise measures.

Oil debris analysis is the analysis of a lubricant's properties, suspended contaminants, and wears debris; mostly is performed during routine predictive analysis to provide meaningful and accurate information on lubricant and machine condition. Temperature analysis measures and analyzes temperature data. Strain analysis determines the stresses and strains in materials and structures subjected to forces and loads for condition monitoring. Among these, commonest condition monitoring technique for a gearbox is vibration analysis [1.10, 1.11].

The vibrations of a planetary gearbox are much more complicated than those of a fixed-shaft gearbox. In a fixed-shaft gearbox, every gear revolves around its own shaft axis and will not revolve around any other gear's. A planetary gear set has multiple external gear pairs and multiple internal gear pairs meshing simultaneously. A sun-planet gear pair contains two meshing external gears. A ring-planet gear pair contains one external gear meshing with one internal gear. Each sun-planet gear pair produces similar but phase shifted vibration signal [1.12]. So does each ring-planet gear pair. This phase shift cancels or neutralizes some of the excitations induced by gear pairs but augments others [1.13]. In addition, the rotation of the carrier varies the transmission path of the vibration signals to a fixed transducer. Multiple vibration sources and the effect of transmission path lead to the complexity of the vibration signals of a planetary gearbox.

Several researchers have used mathematical models to investigate the vibration properties of a planetary gearbox [1.14, 1.15]. However, these models lack connections with physical parameters of a gearbox, like gear mesh stiffness and damping. In addition, they can hardly model the process of the fault growth. A dynamic model is more closely connected with the physical parameters of a planetary gearbox than the mathematical model. It can model fault growth and the corresponding effects. It has further advantages over lab systems or field systems [1.16]: (1) environmental noises can be eliminated so that the changes in vibration signals caused by the faults can be identified easily; (2) with a good dynamic simulation model, it is easy to simulate different types and levels of faults, and observe changes in the vibration signal they cause. In this thesis, a lab system means an experimental setup in a lab for scientific research while a field system means an onsite system where the phenomenon occurs naturally without isolating it from other systems or altering the original conditions of the test.

Dynamic simulation can simulate the vibration signals of each gear inside a planetary gearbox. Multiple vibration signals inside a planetary gearbox go through different transmission paths and are eventually synthesized as a resultant vibration signal at the sensor position. To obtain the vibration signals of the whole planetary gearbox, both multiple vibration sources and the effect of transmission path must be considered.

In the dynamic modeling of a gear system, gear mesh interfaces are usually modeled as a spring-damper system [1.17, 1.18]. The spring stiffness, also called mesh stiffness, is one of the major sources of gear vibration [1.19]. Correctly evaluating the time-varying mesh stiffness is essential to ensure accuracy of the simulated vibration signals through dynamic simulation.

For a planetary gear set, tooth cracking is one of the commonest failure models [1.1]. As the tooth crack grows, gear mesh stiffness will decrease and the gear system' vibration characteristics will change. To simulate the vibration signals of a planetary gear set with various crack severity levels, it is essential to establish the relationship between the crack severity and the mesh stiffness reduction. In addition, tooth crack may occur in the sun gear, the planet gears, or the ring gear. Mesh stiffness shapes are not the same for each different tooth crack location. The differences will result in different fault symptoms in vibration signals, which can help identify the fault location.

Many signal processing methods have been proposed to diagnose the health of gearboxes [1.20, 1.21]. However, most researchers treat the gearbox as a black box ignoring the generation mechanism of the vibration signals. Dynamics based vibration signal modeling is an effective way to model and reveal the vibration properties of a planetary gearbox. If we can "open" the black box, "see" all the sub-signals, understand the generation mechanisms of vibration signals, and consider the effects of vibration transmission path properly, effective tools can be developed to detect gear faults.

Though vibration analysis techniques have been widely used in the fault detection of planetary gearboxes, the vibration characteristics of planetary gearboxes are still not fully understood. This thesis aims to develop a dynamics based method to simulate and analyze the vibration signals of a planetary gear set at various levels of single tooth crack with the effects of transmission path considered. Then a signal decomposition method is proposed to detect a single tooth crack fault in a single planet gear.

1.2 Literature review

This section reviews the available work on gear mesh stiffness evaluation for both fixed-shaft gearboxes and planetary gearboxes; using dynamics based vibration signal modeling, and vibration signal decomposition techniques for planetary gearboxes. This section is organized as follows: Section 1.2.1 reviews the differences between finite element method (FEM) and analytical method (AM) in terms of gear mesh stiffness evaluation. Section 1.2.2 reviews the analytical methods in mesh stiffness evaluation of fixed-shaft gears. Section 1.2.3 reviews the analytical methods in mesh stiffness evaluation of a planet gear set. Section 1.2.4 reviews the gear tooth crack modeling and the crack effect on the gear mesh stiffness. Section 1.2.5 reviews dynamics based vibration signal modeling. Section 1.2.6 reviews vibration signal decomposition techniques for gear tooth fault detection.

1.2.1 Finite element method versus analytical method on mesh stiffness evaluation

Finite element method (FEM) and Analytical method (AM) have both been used to evaluate the mesh stiffness of gear pairs. Wang and Howard [1.22] evaluated the torsional stiffness of a pair of involute spur gears using FEM. FEM is flexible to model any shaped gear, for example, the gears with non-standard tooth geometries [1.23]. FEM can also model faulty gears and evaluate the influence of gear faults on the mesh stiffness. Jia and Howard [1.24] evaluated the mesh stiffness of external spur gears when tooth spalling or tooth crack is present using a 3-D finite element model. Pandya et al. [1.25] used a 2-D finite element model to evaluate the crack effect on the mesh stiffness of an external gear pair. Song et al. [1.26] developed a finite element model for a pair of marine crossed beveloid gear and found that the gear misalignment had a slight effect on the mesh stiffness. However, FEM is sensitive to contact tolerances, mesh density and the types of finite elements selected [1.23]. As the mesh density increases, the numerical accuracy is improved, while the computational cost goes up [1.27].

Parker et al. [1.28] proposed a combined element/contact mechanics model to investigate the non-linear dynamic response of a spur gear pair. Later, this model was extended to investigate the dynamic response of a planetary gear system [1.29]. Ambarisha and Parker [1.30] used this model to calculate the mesh stiffness of a planetary gear set. This model reduces the number of finite elements used and enables the mesh stiffness calculation with practically feasible run time. However, this model relies on the unique commercial finite element-contact analysis software: Calyx [1.31].

AM is easy to use and also effective in evaluating gear mesh stiffness. The contribution of individual component, like bending stiffness, shear stiffness, and Hertzian contact stiffness, can be analyzed separately [1.23]. Chaari et al. [1.32] and Zhou et al. [1.33] both analytically evaluated the mesh stiffness of an external gear pair with tooth crack, and their mesh stiffness results were demonstrated to have a good agreement with the FEM results. AM can also be used to evaluate the mesh stiffness of gears when gear faults are present, like crack [1.25, 1.32], spalling [1.34], and tooth breakage [1.4]. Most researchers analytically model the gear tooth as a nonlinear cantilever beam and the beam theory was used to evaluate the gear mesh stiffness. However, some component deformations and/or component faults are not easy to be modeled analytically, like gear distributed pitting and gear misalignment.

In the analytical method, the gear tooth is modeled as a cantilever beam and a beam theory is used. The two widely used classical beam theories are Euler-Bernoulli and Timoschenko [1.35]. In the Euler-Bernoulli beam theory, shear deformations and rotational inertia are neglected, and during deformation, the cross section of the beam is assumed to remain planar and normal to the deformed axis of the beam. In the Timoshenko beam theory, shear deformations and rotational inertia are both considered, and during deformation, the cross section of the beam will remain planar, but no longer normal to the deformed axis of the beam. Later, refined beam theories were developed to deal with the effects that cannot be solved using either of the two classical beam theories, such as warping, plane deformations, torsional-bending coupling, and localized boundary conditions [1.35]. The Carrera Unified Formulation (CUF) permits one to develop a large number of beam theories with a variable number of displacement unknowns by means of a concise notation and by referring to a few fundamental beam theories. The number of unknown variables is a free parameter of the problem. A 3D stress/strain field can be obtained by an appropriate selection of these variables for any type of beam problem: compact sections, thin-walled sections, bending, torsion, shear, localized loadings, static and dynamic problems [1.35].

The potential energy method is a widely used analytical method to evaluate the mesh stiffness of perfect gears and gears with crack [1.36]. In this method, the gear tooth is considered as a non-uniform cantilever beam and the Timoshenko beam theory is used. This method will be used directly in this study to evaluate the gear mesh stiffness.

1.2.2 Mesh stiffness evaluation of fixed-shaft gears

Many studies have been reported to analytically evaluate the mesh stiffness of fixed-shaft external gear pairs. Yang and Lin [1.17] analytically evaluated the mesh stiffness of a pair of fixed-shaft external spur gears using the potential energy method. They considered Hertzian energy, bending energy and axial compressive energy corresponding to Hertzian contact stiffness, bending stiffness and axial compressive stiffness, respectively. Later, Tian et al. [1.37] added another energy component called the shear energy corresponding to the shear stiffness. Utilizing the properties of involute curve, Tian et al. [1.37] also simplified the expressions of the bending stiffness, shear stiffness and axial compressive stiffness to facilitate the application. Zhou et al. [1.33] added the deformation of the gear body into the model reported in [1.37]. Refs. [1.17, 1.32, 1.36] modeled the gear tooth as a cantilever beam and assumed that the beam started from the gear base circle. Actually, the gear tooth starts from the root circle rather than the base circle as shown in Fig. 1.3. Thus, their models ignored the influence of a part of the gear tooth between the root circle and the base circle. The tooth profile of this part (tooth fillet area) is not an involute curve and it is basically determined by the cutting tool tip trajectory. Using a different cutting tool, the generated curve will be different and there is no uniform function to depict it [1.38]. However, neglecting this part will cause inaccuracy of the estimated mesh stiffness of gear pairs, especially when the distance between the base circle and the root circle is large. Refs. [1.27, 1.39, 1.40] modeled the gear tooth as a cantilever beam which started from gear root circle. However, their equations are not convenient to use. They only gave the stiffness equations for a specific mesh point. In this case, for time-varying stiffness measurement, it is required to manually calculate the gear profile information at every mesh point which is repeated in nature for different gears and this is time consuming. Another shortcoming is that they did not demonstrate how to match the mesh points. For example, one point on one tooth is in meshing, then how to find the corresponding meshing point on the other tooth. For a pair of spur gears whose contact ratio is between 1 and 2, the alternation of one pair and two pairs of teeth in contact is observed. They also did not mention how to determine the single-tooth-pair duration and the double-tooth-pair duration. These shortcomings will be addressed in this thesis. In the Chapter 3 of this thesis, equations of the mesh stiffness of an external gear pair will be derived with the tooth fillet area considered in the external gear tooth model.

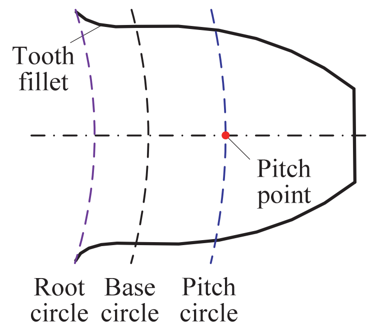

Fig. 1.3: Gear tooth profile of an external gear

In contrast, the investigations on the mesh stiffness evaluation of the internal gears are limited. The most detailed research is done by Pintz et al. [1.41]. They introduced an iterative procedure to evaluate the mesh stiffness of an internal gear pair through digitizing the tooth profile into a large scale of discrete points. In their method, the mesh stiffness was expressed as a function of the transmitted load, gear profile errors, gear tooth deflections, gear hub deformations, location of tooth contact and the number of tooth pairs in contact. The mesh stiffness at each discrete point was evaluated iteratively. However, they only gave the stiffness equations for a specific mesh point. The same as discussed in the previous paragraph, their equations are not convenient to use. To address this shortcoming, in Chapter 2 of this thesis, easy to use equations are derived for the mesh stiffness of an internal gear pair.

1.2.3 Mesh stiffness evaluation of a planetary gear set

In Section 1.2.2, I reviewed the gear mesh stiffness evaluation for a fixed-shaft external gear pair and a fixed-shaft internal gear pair. In a planetary gear set, there are several pairs of sun-planet gears and several pairs of ring-planet gears meshing simultaneously. Actually, the gear mesh stiffness evaluation of a pair of sun-planet gears is the same as that of an external gear pair since both the sun gear and the planet gear are all external gears. The gear mesh stiffness evaluation of a ring-planet gear pair is the same as that of an internal gear pair since the ring gear is an internal gear and the planet gear is an external gear. In this section, I will review how to obtain the mesh stiffness of a planetary gear set when the mesh stiffness of a pair of sun-planet gears and the mesh stiffness of a pair of ring-planet gears are known.

While each of the sun-planet gear pair has the same shape of mesh stiffness variation, they are not necessarily in phase with one another [1.42]. August et al. [1.43] evaluated the mesh stiffness of a planetary gear set with three planet gears. The sun-planet gears were treated as a fixed-shaft external gear pair whose mesh stiffness was evaluated using the method proposed by Kasuba and Evans [1.39]. A ring-planet gear pair was treated as a fixed-shaft internal gear pair whose mesh stiffness was evaluated using the method proposed by Pintz et al. [1.41]. By considering the mesh phasing relationships, they obtained the mesh stiffness of the whole planetary gear set. Two significant shortcomings of their methods are: (a) the methods to evaluate the mesh stiffness of the external gears and the internal gears are not convenient to use as described in the last paragraph of Section 1.2.2, (b) the mesh phasing relationships are not well defined. Parker and Lin [1.42] proposed an analytical method later to calculate mesh phasing relationships.

Some other researchers [1.44, 1.45] used a square waveform to approximate the time-varying mesh stiffness of a planetary gear set as shown in Fig. 1.4. However, no specific guidelines were presented on how to get the magnitudes of the time-varying stiffness. The magnitudes were assumed without confirmation of the physical parameters. Besides, the square waveform ignored the variation of the mesh stiffness caused by the change of the contact point with the gear rotation. In addition, unwanted frequency components may be generated due to the flatness of the stiffness curve. The approach to be used in the Chapter 2 of this thesis aims to overcome these shortcomings. With directly using the mesh phasing relationships reported by Parker and Lin [1.42], equations are derived to get the mesh stiffness of a planetary gear set given the mesh stiffness of a pair of sun-planet gears and the mesh stiffness of a pair of ring-planet gears are known.

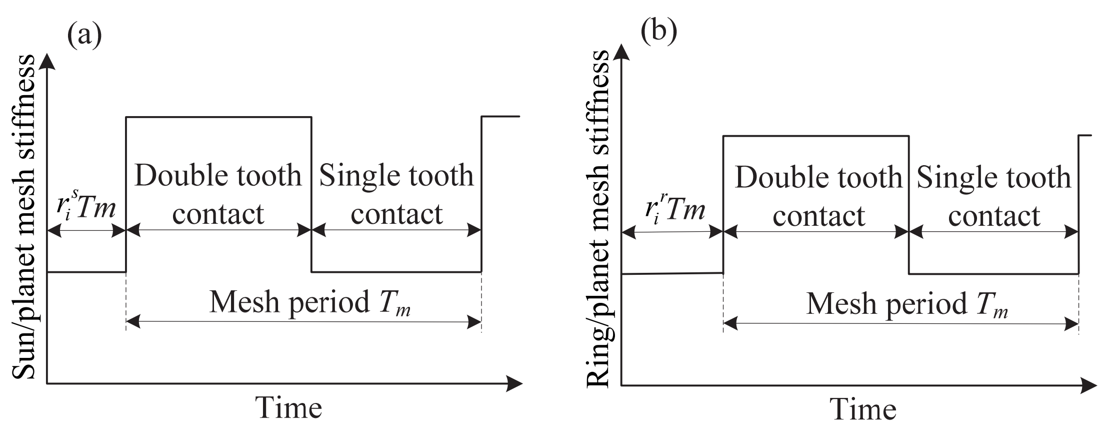

Fig. 1.4: Approximation of the gear mesh stiffness using the square waveform [1.45]: T_m denotes the meshing period, r_i^s denotes the contact ratio between the sun gear and the i^{th} planet gear and r_i^r denotes the contact ratio between the ring gear and the i^{th} planet gear.

1.2.4 Crack effect on the mesh stiffness

In Section 1.2.2 and Section 1.2.3, I reviewed the mesh stiffness evolution of fixed-shaft gear pairs and planetary gears. In those two sections, all the gears are in the healthy condition. In this section, the gear tooth crack effect on a fixed-shaft external gear pair and a planetary gear set will be reviewed.

Many studies have evaluated the crack effect on the mesh stiffness of a fixed-shaft external gear pair. Refs. [1.25, 1.33, 1.37] modeled the gear crack propagation in a linear path shape starting from the point of intersection of the base circle and the involute curve as shown in Fig. 1.5 (a). However, it is pointed out by both Kramberger et al. [1.46] and Belsak and Flasker [1.47] that gear tooth crack mostly initiated at the point of the maximum principal stress in the tensile side of a gear tooth (critical area in Fig. 1.6). Chaari et al. [1.32] presented an analytical method to evaluate the mesh stiffness of an external gear pair and modeled the crack in a straight line shape starting from the tooth root. They mentioned that the gear mesh stiffness could be evaluated by taking into account the tooth thickness reduction. Chen and Shao [1.40] proposed an analytical model to evaluate the mesh stiffness of an external gear pair with tooth root crack propagating along both the tooth width and the crack depth as shown in Fig. 1.5 (b). However, the methods reported in Refs. [1.32, 1.40] are based on single point estimation of the mesh stiffness. As stated in Section 1.2.2, these methods are not convenient to use. To address this shortcoming, an external gear tooth crack model will be proposed in Chapter 3 of this thesis and equations of the mesh stiffness of a fixed-shaft external gear pair with a single gear tooth crack will be derived.

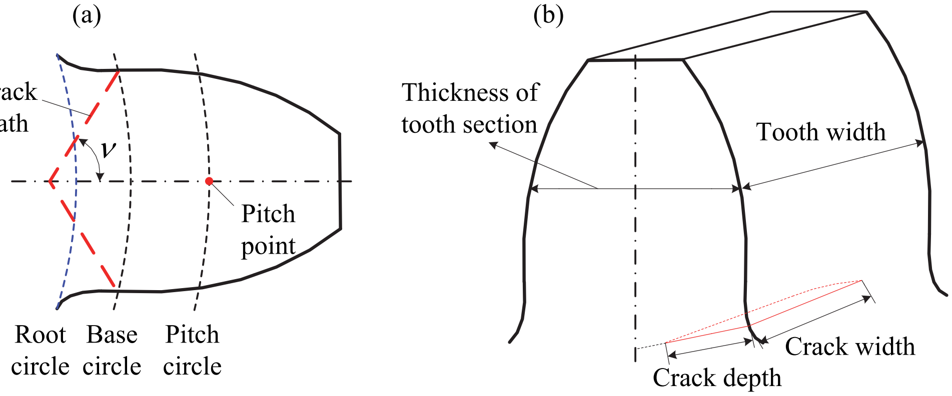

Fig. 1.5: Crack modeling

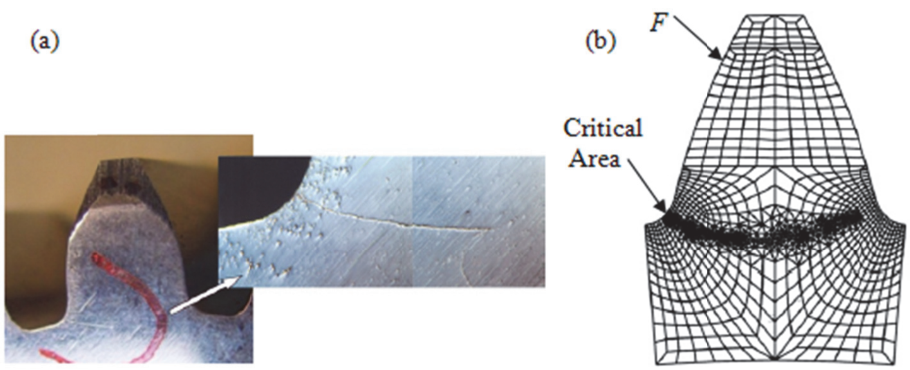

Fig. 1.6: Gear crack propagation path [1.47] (a) experiment and (b) finite element method

In contrast, the studies on the crack effect on the mesh stiffness of a planetary gear set are limited. Chaari et al. [1.1] used a square waveform to approximate the time-varying mesh stiffness of a planetary gear set. They presented that the amplitude modulation can be used to obtain the mesh stiffness of a planetary gear set with crack. Fig. 1.7 [1.1] illustrated the amplitude loss of 50% due to a crack in the sun gear. Physical meaning of this loss was not described, like how much crack propagation will lead to the amplitude loss by 50%. In addition, they only modeled the stiffness reduction in the double tooth contact duration while ignored the stiffness decrease in the single tooth contact duration. Chen and Shao [1.48] investigated the crack effect on the mesh stiffness when a tooth crack occurred in the sun gear or the planet gear. They used the same method for fixed-shaft gears reported in [1.40] to evaluate the mesh stiffness of sun-planet gears and ring-planet gears. The gear mesh stiffness was evaluated based on single point estimation of the mesh stiffness. When a crack is present in a planetary gear set, the crack could be in the sun gear, a planet gear (sun gear side), a planet gear (ring gear side) or the ring gear. The differences of the mesh stiffness when a tooth crack appears in different gears are not extensively investigated. In Chapter 3 of this thesis, crack effect on the mesh stiffness of a planetary gear set is investigated on three situations: crack in the sun gear, crack in a planet gear (sun gear side) and crack in a planet gear (ring gear side). The differences of the mesh stiffness shape in these three situations are studied.

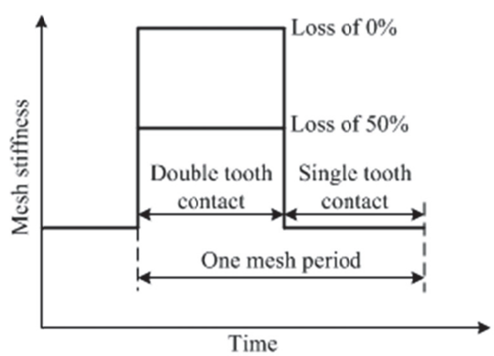

Fig. 1.7: Amplitude loss of 50% due to a crack in the sun gear

1.2.5 Dynamics based vibration signal modeling

In the field applications, vibration sensors are usually mounted on the housing of the gearbox and/or the bearings to collect the vibration signals. The vibration signals generated by each vibration source go through different transmission paths and are eventually synthesized as a resultant vibration at the sensor position. To simulate the resultant vibration signal of a planetary gearbox at the sensor location, both multiple vibration sources and the effect of transmission path must be considered.

Mathematical models have been used by several researchers to investigate the vibration properties of a planetary gearbox. Inalpolat and Kahraman [1.14] proposed a simplified mathematical model to describe the mechanisms leading to modulation sidebands of planetary gear sets. Feng and Zuo [1.15] mathematically modeled the gear faults using the amplitude modulation and the frequency modulation, and then analyzed the spectral structure of the vibration signals of a planetary gear system. The effect of the transmission path was modeled as a Hanning function [1.14, 1.15] with the assumption that, as planet i approaches to the transducer location, its influence increases, reaching its maximum when the planet i is at the transducer location, then, its influence decreases as the planet i goes away from the transducer. Even though mathematical models can exhibit some basic vibration properties of a planetary gearbox, they lack the connection with the physical parameters of a planetary gearbox. In addition, they can hardly model the process of fault growth. This shortcoming will be solved in Chapter 4 of this thesis by using dynamic modeling.

Dynamic simulation is a better choice to investigate the vibration properties of a planetary gearbox. Kahraman [1.49] proposed a nonlinear dynamic model to investigate the load sharing characteristics of a planetary gear set. Three degrees of freedom were modeled for each component: transverse motions in the x-axis direction, y-axis direction, and rotation. The equations were built in a fixed coordinate system. Inalpolat and

Kahraman [1.50] used the same model proposed by Kahraman [1.49] to predict modulation sidebands of a planetary gear set having manufacturing errors. The effect of transmission path was represented by a Hanning function. Lin and Parker [1.18] modified the model proposed by Kahraman [1.49] in two items: (a) used a rotating frame coordinate system in order to consider the gyroscopic effect, (b) the planet deflections were described in the radical and the tangential coordinates. Using this model, they investigated the free vibration properties of a planetary gear set. Cheng et al. [1.51] developed a pure torsional dynamic model to investigate the properties of a planetary gear set when a single pit was present on a tooth of the sun gear. Chaari et al. [1.52] developed a similar model as the one reported by Lin and Parker [1.18] to investigate the manufacturing errors on the dynamic behavior of planetary gears. In addition, they investigated the vibration properties of a planetary gear set with tooth crack or a single pit on the sun gear. In their studies, the gear mesh stiffness was approximated as a square waveform. Chen and Shao [1.48] studied the dynamic features of a planetary gear system with tooth crack under different sizes and inclination angles. The displacement signal of the sun gear and the planet gear was investigated when a crack was present on the sun gear or the planet gear.

To better understand the vibration properties of a planetary gear set with faults, more studies are required to investigate the vibration properties of a planetary gear set. The dynamic model can be further improved by considering more factors, like the centrifugal force generated due to the rotation of the carrier. The effect of the transmission path can be further investigated rather than only use the Hanning function. A dynamic model for a planetary gear set and a modified Hamming function for the modeling of transmission path effect will be proposed in Chapter 4 of this thesis to address these shortcomings.

1.2.6 Vibration signal decomposition for gear tooth fault detection

In Section 1.2.5, I reviewed the research on vibration signal modeling of a planetary gear set. Once vibration signals are generated based on dynamics models considering gear tooth crack effects and the effect of transmission path as reviewed earlier, the last step is to process the simulated vibration signals aiming to reflect health condition. In this section, vibration signal decomposition for gear tooth fault detection will be reviewed.

The fault detection of a planetary gearbox is much complicated compared with that of a fixed-shaft gearbox as the planetary gearbox's properties of multiple vibration sources and the effect of transmission path lead to the complexity of the vibration signals. Signal decomposition techniques were raised by some researchers to emphasize fault symptoms and eliminate the interferences from irrelevant factors. McFadden [1.53] proposed a windowing and mapping strategy to obtain the vibration signal of individual planet gears and of the sun gear in a planetary gearbox. In his method, a window function was applied to sample the vibration signals when a specific planet gear was passing by the transducer and then the samples were mapped to the corresponding meshing teeth of the sun gear or the planet gear to form the vibration signals of the sun gear or the planet gear. Many additional studies attempted to improve the performance of the method reported in [1.53]. Refs. [1.54-1.57] investigated the techniques to index the positions of each planet gear, which were used to find the best location of putting the windows. Refs. [1.50, 1.55, 1.58-1.60] tried to find the best window type and window length for the sampling. The performances of Rectangular window, Hanning window, Turkey window and Cosine window were investigated in Refs. [1.53-1.60]. All these efforts were trying to decompose the vibration signal of a planetary gearbox while focusing on the vibration signal of the sun gear or the planet gear of interest. The decomposed signal can reduce the interference from the vibration of other gears and consequently emphasize the fault symptoms of the gear of interest. This study does not intend to improve the existing signal decomposition methods. But a new signal decomposition method will be proposed in Chapter 5 of this thesis to decompose the vibration signal of a planetary gear set into the gear tooth level of a planet gear. The decomposed vibration signal can reduce the interference from the vibrations of other teeth of the planet gear of interest. Examining the signals of all the teeth of a planet gear, the health differences of the teeth can be measured.

1.3 Objective and outline

Based on the reviews summarized in the previous section, four main issues have been identified that will be addressed in this thesis. This thesis's overall objective is to investigate the vibration properties of a planetary gearbox through the dynamics based vibration signal modeling and then develop an effective method to detect gear tooth fault. This objective is divided into these four research topics:

(1) An analytical method is developed to evaluate the time-varying mesh stiffness of a planetary gear set. Equations of the mesh stiffness of a fixed-shaft external gear pair are derived with the fillet curve area considered in the gear tooth model. Equations of a fixed-shaft internal gear pair are derived. These equations are expressed as a

function of the rotation angle of a gear, which is convenient to use. Then, by incorporating the effect of transmission path, the mesh stiffness of a planetary gear set is evaluated. Examples are illustrated for three structures of a planetary gear set: carrier fixed, sun gear fixed and ring gear fixed.

(2) A tooth crack model is proposed and the tooth crack effect on the time-varying mesh stiffness is evaluated. An external gear tooth crack model is proposed for the purpose of gear mesh stiffness evaluation. Equations of the mesh stiffness of a fixed-shaft external gear pair with tooth crack are derived. Then, the mesh stiffness of a planetary gear set is evaluated by considering the mesh phasing relationships and compared in three situations: tooth crack in the sun gear, tooth crack in a planet gear (sun gear side) and tooth crack in a planet gear (ring gear side).

(3) A two-dimensional lumped mass model is proposed to simulate the vibration signals generated by each gear. Incorporating multiple vibration sources and the effect of transmission path, the vibration signals of the whole planetary gearbox in healthy and sun gear cracked tooth conditions are simulated and investigated. Certain vibration properties present in the simulated signals are confirmed by those in the experimental signals.

(4) A signal decomposition method is proposed to decompose the vibration signals of a planetary gearbox into gear tooth level of a planet gear. This method is tested on both simulated and experimental vibration signals, and is demonstrated to be able to detect a single tooth fault in a planet gear.

This thesis follows the paper format except for Chapter 1. Chapters 2-5 are written in the form of a paper including introduction, literature review, problem definition, methodology, and research contributions. To be specific, here is a description of each chapter:

In Chapter 1, background of this research topic is described followed by a literature review. The objective and the outline of this thesis are defined.

In Chapter 2, potential energy method is applied to evaluate the time-varying mesh stiffness of a planetary gear set. Equations of the time-varying mesh stiffness are derived. The developed equations are applicable to any transmission structure of a planetary gear set. Detailed discussions are given to three widely used transmission structures: fixed carrier, fixed ring gear and fixed sun gear. This chapter is based on a journal paper [1.61] and a refereed conference paper [1.62].

In Chapter 3, a modified cantilever beam model is proposed to represent the external gear tooth and for the time-varying mesh stiffness evaluation. Equations of bending stiffness, shear stiffness and axial compressive stiffness are derived for an external gear pair. A crack propagation model is developed and the mesh stiffness reduction is quantified when a tooth crack occurs in the sun gear or the planet gear. This chapter is based on a journal paper [1.63] and a refereed conference paper [1.64].

In Chapter 4, vibration signals of a planetary gearbox are simulated and investigated. A dynamic model is developed to simulate the vibration source signals. A modified Hamming function is proposed to represent the effect of the transmission path. By incorporating multiple vibration sources and the effect of transmission path, the vibration signals of a whole planetary gearbox at the sensor location are generated. Through analyzing the vibration signals, certain vibration properties of a planetary gearbox are recognized and the fault symptoms of sun gear tooth crack are identified and located. This chapter is based on a journal paper [1.65] and a refereed conference paper [1.66].

In Chapter 5, a windowing and mapping strategy is proposed to decompose the vibration signals of a planetary gearbox into the tooth level of a planet gear. The fault symptoms generated by a single cracked tooth of the planet gear of interest are emphasized. The health condition of the planet gear is assessed by comparing the differences among the signals of all teeth of the planet gear of interest. The proposed windowing and mapping strategy is tested on both simulated and experimental vibration signals. The vibration signals can be successfully decomposed and a single tooth crack on a planet gear can be effectively detected. This chapter is based on a journal paper [1.67] and a refereed conference paper [1.68].

In summary, this thesis provides a dynamics based method to simulate the vibration signals of a planetary gear set in the sensor location and then a fault detection technique is proposed to detect the tooth crack in a planet gear. The gear mesh stiffness evaluation method developed in Chapter 2 and Chapter 3 can effectively evaluate the time-varying mesh stiffness of a planetary gear set in healthy and cracked tooth conditions. Accurate gear mesh stiffness is indispensable in obtaining the correct dynamic response in the dynamic simulation. The dynamics based vibration signal modeling method proposed in Chapter 4 can simulate the vibration signals of a planetary gear set in the sensor location. Based on the understanding of the vibration properties of a planetary gear set, a signal decomposition method is proposed in Chapter 5. This signal decomposition method can effectively detect a single tooth crack when it appears in a single planet gear. The techniques developed in this thesis help us better understand the vibration characteristics of a planetary gear set and give insights into developing new signal processing methods for gear tooth fault detection.

References

[1.1] F. Chaari, T. Fakhfakh, and M. Haddar, “Dynamic Analysis of a Planetary Gear Failure Caused by Tooth Pitting and Cracking,” *J. Fail. Anal. Prev.*, vol. 6, no. 2, pp. 73–78, Apr. 2006.

[1.2] “Gear,” *Wikipedia, the free encyclopedia*. Accessed on 13-May-2015.

[1.3] S. Vorkoetter, “Demystifying Gearing and Gearboxes,” *Sailplane & Electric Modeler Magazine*, 01-Mar-2000.

[1.4] F. Chaari, W. Baccar, M. S. Abbes, and M. Haddar, “Effect of Spalling or Tooth Breakage on Gearmesh Stiffness and Dynamic Response of a One-stage Spur Gear Transmission,” *Eur. J. Mech. - ASolids*, vol. 27, no. 4, pp. 691–705, Jul. 2008.

[1.5] L. Gelman, R. Zimroz, J. Birkel, H. Leigh-Firbank, D. Simms, B. Waterland, and G. Whitehurst, “Adaptive Vibration Condition Monitoring Technology for Local Tooth Damage in Gearboxes,” *Insight - Non-Destr. Test. Cond. Monit.*, vol. 47, no. 8, pp. 461–464, Aug. 2005.

[1.6] A. I. H. Committee, *Friction, Lubrication, and Wear Technology*. ASM International Handbook, 1992.

[1.7] M. R. Hoseini and M. J. Zuo, “Literature Review for Creating and Quantifying Faults in Planetary Gearboxes,” Reliability Research Lab, Mechanical Department, University of Alberta, Technical Report, May 2009.

[1.8] P. Association, “North Sea Helicopter Crash Report Says Gearbox Failed after Maintenance Error,” *The Guardian*, 24-Nov-2011.

[1.9] P. R. Veillette, “Engine, Transmission Failures Lead Causes of Accidents in U.S. Helicopter Logging Operations,” *Helicopter Safety*, vol. 26, no. 3, pp. 1–12, 2000.

[1.10] J. Liu, W. Wang, and F. Golnaraghi, “An Extended Wavelet Spectrum for Bearing Fault Diagnostics,” *IEEE Trans. Instrum. Meas.*, vol. 57, no. 12, pp. 2801–2812, Dec. 2008.

[1.11] A. K.S. Jardine, D. Lin, and D. Banjevic, “A Review on Machinery Diagnostics and Prognostics Implementing Condition-based Maintenance,” *Mech. Syst. Signal Process.*, vol. 20, no. 7, pp. 1483–1510, Oct. 2006.

[1.12] D. M. Blunt and J. A. Keller, “Detection of a Fatigue Crack in a UH-60A Planet Gear Carrier Using Vibration Analysis,” *Mech. Syst. Signal Process.*, vol. 20, no. 8, pp. 2095–2111, Nov. 2006.

[1.13] Y. Lei, D. Kong, J. Lin, and M. J. Zuo, “Fault Detection of Planetary Gearboxes Using New Diagnostic Parameters,” *Meas. Sci. Technol.*, vol. 23, no. 5, p. 055605, May 2012.

[1.14] M. Inalpolat and A. Kahraman, “A Theoretical and Experimental Investigation of Modulation Sidebands of Planetary Gear Sets,” *J. Sound Vib.*, vol. 323, no. 3–5, pp. 677–696, Jun. 2009.

[1.15] Z. Feng and M. J. Zuo, “Vibration Signal Models for Fault Diagnosis of Planetary Gearboxes,” *J. Sound Vib.*, vol. 331, no. 22, pp. 4919–4939, Oct. 2012.

[1.16] Z. Tian, M. J. Zuo, and S. Wu, “Crack Propagation Assessment for Spur Gears Using Model-based Analysis and Simulation,” *J. Intell. Manuf.*, vol. 23, no. 2, pp. 239–253, Apr. 2012.

[1.17] D. C. H. Yang and J. Y. Lin, “Hertzian Damping, Tooth Friction and Bending Elasticity in Gear Impact Dynamics,” *J. Mech. Des.*, vol. 109, no. 2, pp. 189–196, Jun. 1987.

[1.18] J. Lin and R. G. Parker, “Analytical Characterization of the Unique Properties of Planetary Gear Free Vibration,” *J. Vib. Acoust.*, vol. 121, no. 3, pp. 316–321, Jul. 1999.

[1.19] J. Lin and R. G. Parker, “Mesh Stiffness Variation Instabilities in Two-Stage Gear Systems,” *J. Vib. Acoust.*, vol. 124, no. 1, pp. 68–76, Sep. 2001.

[1.20] P. D. Samuel and D. J. Pines, “A Review of Vibration-based Techniques for Helicopter Transmission Diagnostics,” *J. Sound Vib.*, vol. 282, no. 1–2, pp. 475–508, Apr. 2005.

[1.21] Y. Lei, J. Lin, M. J. Zuo, and Z. He, “Condition Monitoring and Fault Diagnosis of Planetary Gearboxes: A review,” *Measurement*, vol. 48, pp. 292–305, Feb. 2014.

[1.22] J. Wang and I. Howard, “The Torsional Stiffness of Involute Spur Gears,” *Proc. Inst. Mech. Eng. Part C J. Mech. Eng. Sci.*, vol. 218, no. 1, pp. 131–142, Jan. 2004.

[1.23] J. Meagher, X. Wu, D. Kong, and C. H. Lee, “A Comparison of Gear Mesh Stiffness Modeling Strategies,” in *Structural Dynamics, Volume 3*, T. Proulx, Ed. Springer New York, 2011, pp. 255–263.

[1.24] S. Jia and I. Howard, “Comparison of Localised Spalling and Crack Damage from Dynamic Modelling of Spur Gear Vibrations,” *Mech. Syst. Signal Process.*, vol. 20, no. 2, pp. 332–349, Feb. 2006.

[1.25] Y. Pandya and A. Parey, “Failure Path Based Modified Gear Mesh Stiffness for Spur Gear Pair with Tooth Root Crack,” *Eng. Fail. Anal.*, vol. 27, pp. 286–296, Jan. 2013.

[1.26] C. Song, C. Zhu, and L. Liu, “Mesh Characteristics for Marine Beveloid Gears with Crossed Axes,” *J. Xian Tiaotong Univ.*, vol. 46, pp. 64–69, 2012.

[1.27] R. Tuo, C. J. Wu, and D. Yu, “Surrogate Modeling of Computer Experiments with Different Mesh Densities,” *Technometrics*, vol. 56, no. 3, pp. 372–380, 2014.

[1.28] R. G. Parker, S. M. Vijayakar, and T. Imajo, “Non-Linear Dynamic Response of a Spur Gear Pair: Modelling and Experimental Comparisons,” *J. Sound Vib.*, vol. 237, no. 3, pp. 435–455, Oct. 2000.

[1.29] R. G. Parker, V. Agashe, and S. M. Vijayakar, “Dynamic Response of a Planetary Gear System Using a Finite Element/Contact Mechanics Model,” *J. Mech. Des.*, vol. 122, no. 3, pp. 304–310, May 1999.

[1.30] V. K. Ambarisha and R. G. Parker, “Nonlinear Dynamics of Planetary Gears Using Analytical and Finite Element Models,” *J. Sound Vib.*, vol. 302, no. 3, pp. 577–595, May 2007.

[1.31] S. M. Vijayakar, “Calyx Users Manual,” 2005, *http://ansol.us*.

[1.32] F. Chaari, T. Fakhfakh, and M. Haddar, “Analytical Modelling of Spur Gear Tooth Crack and Influence on Gearmesh Stiffness,” *Eur. J. Mech. - ASolids*, vol. 28, no. 3, pp. 461–468, May 2009.

[133] X. Zhou, Y. Shao, Y. Lei, and M. Zuo, “Time-varying Meshing Stiffness Calculation and Vibration Analysis for a 16DOF Dynamic Model with Linear Crack Growth in a Pinion,” *J. Vib. Acoust.*, vol. 134, no. 1, p. 011011, 2012.

[1.34] Z. Cheng, N. Hu, F. Gu, and G. Qin, “Pitting Damage Levels Estimation for Planetary Gear Sets based on Model Simulation and Grey Relational Analysis,” *Trans. Can. Soc. Mech. Eng.*, vol. 35, no. 3, pp. 403–417, 2011.

[1.35] E. Carrera, G. Giunta, and M. Petrolo, *Beam Structures: Classical and Advanced Theories*. John Wiley & Sons, 2011.

[1.36] H. Ma, J. Zeng, R. Feng, X. Pang, Q. Wang, and B. Wen, “Review on Dynamics of Cracked Gear Systems,” *Eng. Fail. Anal.*, vol. 55, pp. 224–245, Sep. 2015.

[1.37] X. Tian, M. J. Zuo, and K. R. Fyfe, “Analysis of the Vibration Response of a Gearbox with Gear Tooth Faults,” presented at the 2004 ASME International Mechanical Engineering Congress and Exposition, Anaheim, California USA, 2004, pp. 785–793.

[1.38] A. Kapelevich and Y. Shekhtman, “Tooth Fillet Profile Optimization for Gears with Symmetric and Asymmetric Teeth,” *Gear Technol.*, pp. 73–79, 2009.

[1.39] R. Kasuba and J. W. Evans, “An Extended Model for Determining Dynamic Loads in Spur Gearing,” *J. Mech. Des.*, vol. 103, no. 2, pp. 398–409, Apr. 1981.

[1.40] Z. Chen and Y. Shao, "Dynamic Simulation of Spur Gear with Tooth Root Crack Propagating along Tooth Width and Crack Depth," *Eng. Fail. Anal.*, vol. 18, no. 8, pp. 2149–2164, Dec. 2011.

[1.41] A. Pintz, R. Kasuba, J. L. Frater, and R. August, "Dynamic Effects of Internal Spur Gear Drives," National Aeronautics and Space Administration, Scientific and Technical Information Branch, NASA Technical Report No. 3692, 1983.

[1.42] R. G. Parker and J. Lin, "Mesh Phasing Relationships in Planetary and Epicyclic Gears," *J. Mech. Des.*, vol. 126, no. 2, pp. 365–370, May 2004.

[1.43] R. August, R. Kasuba, J. L. Frater, and A. Pintz, "Dynamics of Planetary Gear Trains," National Aeronautics and Space Administration, Scientific and Technical Information Branch, NASA Technical Report No. 3793, 1984.

[1.44] A. Al-shyyab and A. Kahraman, "A Non-linear Dynamic Model for Planetary Gear Sets," *Proc. Inst. Mech. Eng. Part K J. Multi-Body Dyn.*, vol. 221, no. 4, pp. 567–576, Jan. 2007.

[1.45] W. Kim, J. Y. Lee, and J. Chung, "Dynamic Analysis for a Planetary Gear with Time-varying Pressure Angles and Contact Ratios," *J. Sound Vib.*, vol. 331, no. 4, pp. 883–901, Feb. 2012.

[1.46] J. Kramberger, M. Šraml, S. Glodež, J. Flašker, and I. Potrč, "Computational Model for the Analysis of Bending Fatigue in Gears," *Comput. Struct.*, vol. 82, no. 23–26, pp. 2261–2269, Sep. 2004.

[1.47] A. Belsak and J. Flasker, "Detecting Cracks in the Tooth Root of Gears," *Eng. Fail. Anal.*, vol. 14, no. 8, pp. 1466–1475, Dec. 2007.

[1.48] Z. Chen and Y. Shao, "Dynamic Features of a Planetary Gear System with Tooth Crack under Different Sizes and Inclination Angles," *J. Vib. Acoust.*, vol. 135, no. 3, pp. 1–12, Mar. 2013.

[1.49] A. Kahraman, "Load Sharing Characteristics of Planetary Transmissions," *Mech. Mach. Theory*, vol. 29, no. 8, pp. 1151–1165, Nov. 1994.

[1.50] M. Inalpolat and A. Kahraman, “A Dynamic Model to Predict Modulation Sidebands of a Planetary Gear Set Having Manufacturing Errors,” *J. Sound Vib.*, vol. 329, no. 4, pp. 371–393, Feb. 2010.

[1.51] Z. Cheng, N. Hu, F. Gu, and G. Qin, “Pitting Damage Levels Estimation for Planetary Gear Sets Base on Model Simulation and Grey Relational Analysis,” *Trans. Can. Soc. Mech. Eng.*, vol. 35, no. 3, pp. 403–417, 2011.

[1.52] F. Chaari, T. Fakhfakh, R. Hbaieb, J. Louati, and M. Haddar, “Influence of Manufacturing Errors on the Dynamic Behavior of Planetary Gears,” *Int. J. Adv. Manuf. Technol.*, vol. 27, no. 7–8, pp. 738–746, Jan. 2006.

[1.53] P. D. McFadden, “A Technique for Calculating the Time Domain Averages of the Vibration of the Individual Planet Gears and the Sun Gear in an Epicyclic Gearbox,” *J. Sound Vib.*, vol. 144, no. 1, pp. 163–172, Jan. 1991.

[1.54] G. D’Elia, E. Mucchi, and G. Dalpiaz, “On the Time Synchronous Average in Planetary Gearboxes,” presented at the International Conference: Surveillance 7, Institute of Technology of Chartres, France, 2013, pp. 1–11.

[1.55] D. G. Lewicki, K. E. LaBerge, R. T. Ehinger, and J. Fetty, “Planetary Gearbox Fault Detection Using Vibration Separation Techniques,” National Aeronautics and Space Administration, Glenn Research Center, Technical Report NASA/TM—2011-217127, 2011.

[1.56] J. M. Ha, J. Park, B. D. Youn, and Y. H. Jung, “Fault Diagnostics of Planet Gears in Wind Turbine Using Auto-correlation-based Time Synchronous Averaging (ATSA),” presented at the Second European Conference of the Prognostics and Health Management Society 2014, Nantes, France, July 8 - 10, pp. 1–8.

[1.57] F. Combet and L. Gelman, “An Automated Methodology for Performing Time Synchronous Averaging of a Gearbox Signal without Speed Sensor,” *Mech. Syst. Signal Process.*, vol. 21, no. 6, pp. 2590–2606, Aug. 2007.

[1.58] P. D. McFadden, “Window Functions for the Calculation of the Time Domain Averages of the Vibration of the Individual Planet Gears and Sun Gear in an Epicyclic Gearbox,” *J. Vib. Acoust.*, vol. 116, no. 2, pp. 179–187, Apr. 1994.

[1.59] B. D. Forrester, “Method for the Separation of Epicyclic Planet Gear Vibration Signatures,” Patent: US6298725B1, Oct-2001.

[1.60] P. D. Samuel, J. K. Conroy, and D. J. Pines, “Planetary Transmission Diagnostics,” NASA Technical Report, NASA technical report NASA/CR—2004-213068, 2004.

[1.61] X. Liang, M. J. Zuo, and T. H. Patel, “Evaluating the Time-varying Mesh Stiffness of a Planetary Gear Set Using the Potential Energy Method,” *Proc. Inst. Mech. Eng. Part C J. Mech. Eng. Sci.*, vol. 228, no. 3, pp. 535–547, Feb. 2014.

[1.62] X. Liang, M. J. Zuo, and Y. Guo, “Evaluating the Time-Varying Mesh Stiffness of a Planetary Gear Set Using the Potential Energy Method,” in *Proceedings of the 7th World Congress on Engineering Asset Management (WCEAM 2012)*, Springer International Publishing, 2015, pp. 365–374.

[1.63] X. Liang, M. J. Zuo, and M. Pandey, “Analytically Evaluating the Influence of Crack on the Mesh Stiffness of a Planetary Gear Set,” *Mech. Mach. Theory*, vol. 76, pp. 20–38, Jun. 2014.

[1.64] X. Liang and M. J. Zuo, “Dynamic Simulation of a Planetary Gear Set and Estimation of Fault Growth on the Sun Gear,” in *Proceedings of 2013 International Conference on Quality, Reliability, Risk, Maintenance, and Safety Engineering (QR2MSE)*, 2013, pp. 1667–1672.

[1.65] X. Liang, M. J. Zuo, and M. R. Hoseini, “Vibration Signal Modeling of a Planetary Gear Set for Tooth Crack Detection,” *Eng. Fail. Anal.*, vol. 48, pp. 185–200, Feb. 2015.

[1.66] X. Liang, M. J. Zuo, and M. R. Hoseini, “Understanding Vibration Properties of a Planetary Gear Set for Fault Detection,” in *Proceedings of 2014 IEEE Conference on Prognostics and Health Management (PHM)*, 2014, pp. 1–6.

[1.67] X. Liang, M. J. Zuo, and L. Liu, “A Windowing and Mapping Strategy for the Gear Fault Detection of a Planetary Gearbox.” *Mech. Syst. Signal Pr.*, 06-Jun-2015.

[1.68] X. Liang and M. J. Zuo, "Investigating Vibration Properties of a Planetary Gear Set with a Cracked Tooth in a Planet Gear," in *Proceedings of 2014 Annual Conference of the Prognostics and Health Management Society*, Fort Worth, Texas, 2014, pp. 1–8.

Chapter 2: Evaluating Time-Varying Mesh Stiffness of a Planetary Gear Set Using Potential Energy Method

Time-varying mesh stiffness is one of the main excitations of vibration of a gear transmission system. An efficient and effective way to evaluate it is essential to comprehensive understanding of the dynamic properties of a planetary gear set. This chapter is devoted to evaluating the time-varying mesh stiffness of a healthy planetary gear set using the potential energy method. The method developed in this chapter will be extended in Chapter 3 to evaluate the crack effect on the time-varying mesh stiffness of a planetary gear. The obtained time-varying mesh stiffness will also be used in Chapter 4 to generate the vibration signals of a planetary gear set using dynamic simulation. This chapter is organized as follows. In Section 2.1, background of this research topic is described and a literature review is given on time-varying gear mesh stiffness evaluation of gears. In Section 2.2, equations are derived for the mesh stiffness evaluation of an internal gear pair. In Section 2.3, the procedures of obtaining the time-varying mesh stiffness of a planetary gear set are described; the gear mesh stiffness evaluation of three transmission structures (fixed carrier, fixed ring gear and fixed sun gear) are discussed. A summary is provided in Section 2.4. This chapter is based on a journal paper [2.1] and a refereed conference paper [2.2].

2.1 Introduction

Planetary gears are common in aeronautic and industrial applications due to their compactness and high torque-to-weight ratios [2.3]. According to Lin and Parker [2.4], mesh stiffness variation is one of the major sources of gear vibration. Finite element method (FEM) and analytical method (AM) have been used by many researchers to evaluate the mesh stiffness of gears. Wang and Howard [2.5] evaluated the torsional stiffness of a pair of involute spur gears using FEM. FEM can also model complicated shaped gears, for example, the gears with non-standard tooth geometries [2.6]. FEM can also model the faulty gears and evaluate the influence of gear faults on the mesh stiffness. Jia et al. [2.7] evaluated the mesh stiffness of an external spur gear pair when tooth spalling and crack are present using a 3-D finite element model. Pandya and Parey [2.8] used a 2-D finite element model to evaluate the crack effect on the mesh stiffness of an external gear pair. Song et al. developed a finite element model for a pair of marine crossed beveloid gears and found gear misalignment had a slight effect on the mesh stiffness [2.9]. However, FEM is sensitive to tolerances, mesh density and mesh element. And, it is more time-consuming in computation than AM [2.6].

AM is simple and also effective in evaluating gear mesh stiffness. It can separately analyze relative contribution of individual component, like bending stiffness, shear stiffness, and Hertzian contact stiffness [2.6]. Chaari et al. [2.10] and Zhou et al. [2.11] both used it to evaluate the mesh stiffness of an external gear pair and their results matched FEM results well. AM can also evaluate the mesh stiffness of gears with faults, like crack [2.8, 2.10], spalling, and broken teeth [2.12]. Most researchers who used AM treated the gear tooth as a nonlinear cantilever beam and used the beam theory to evaluate gear mesh stiffness. However, some component deformation and faults like gear distributed pitting and gear misalignment defy easy application of AM.

Many researchers have analytically evaluated the mesh stiffness of an external gear pair. Kasuba and Evans [2.13] introduced an iterative procedure of digitizing the tooth profile into a large scale of discrete points. They expressed the mesh stiffness as a function of transmitted load, gear profile errors, gear tooth deflections, gear hub deformations, position of tooth contact and the number of tooth pairs in contact. Pintz et al. [2.14] used the similar technique as Ref. [2.13] to evaluate the mesh stiffness of an internal gear pair. The method used in Refs. [2.13, 2.14] can investigate the mesh stiffness variation when gear profile errors are present. Yang and Sun [2.15] analytically derived the Hertzian contact stiffness of an external gear pair and considered the Hertzian contact stiffness as the gear mesh stiffness. Chaari et al. [2.10] considered the bending deflection, fillet-foundation deflection and contact deflection in the evaluation of the mesh stiffness of an external gear pair. Yang and Lin [2.16] proposed the potential energy method to evaluate the mesh stiffness of an external spur gear pair. They considered Hertzian energy, bending energy, and axial compressive energy corresponding to Hertzian contact stiffness, bending stiffness, and axial compressive stiffness. They gave the mesh stiffness equations for a single gear tooth. As shown in Fig. 2.1, if force F is acting at the point p, the stiffness value at the point p in the direction of force F can be analytically evaluated using the equations in [2.16]. However, when a pair of gears is in meshing, the contact position changes with the rotation of the gears. There is also the phenomenon of the alternation from one pair to two pairs of teeth in contact. As shown in Fig. 2.2, there are two pairs of teeth in meshing simultaneously. The four points (A and C on one gear, and B and D on the other gear) also change with the rotations of the two gears. If we know point A is in meshing, how can we know the position of points B, C, and D? This knowledge is not provided in Ref. [2.16] but it is needed in the mesh stiffness evaluation. Later, Tian et al. [2.17] added another energy component called the shear energy corresponding to the shear stiffness. In addition, they added the relationships between the four points (A, B, C and D as shown in Fig. 2.2) in the mesh stiffness equations. Finally, they expressed the mesh stiffness of an external gear pair as a function of gear rotation angle (given gear geometry and material information). Users can use these equations directly to evaluate gear mesh stiffness even though they are not familiar with beam and/or gear meshing theories. Recently, Zhou et al. [2.11] and Chen et al. [2.18] added the deformation of the gear body to Tian's model [2.17]. All of the above references focused on the mesh stiffness evaluation of an external gear pair. The research on the mesh stiffness evaluation of an internal gear pair is very limited. Only a method reported in [2.14] evaluated the mesh stiffness of an internal gear pair. But only the equations for a single gear tooth are given and the relationships between the four points (A, B, C and D) are not incorporated in their model. Users would still need to calculate these relationships by themselves. In this chapter, I will solve this problem. The potential energy method reported in Ref. [2.16, 2.17] will be extended to evaluate the mesh stiffness of an internal gear pair. Meanwhile, I will derive the relationships between the four points (A, B, C and D as shown in Fig. 2.2) for an internal gear pair and incorporate the relationships in the derivation of mesh stiffness equations. Finally, I will get the mesh stiffness of an internal gear pair as a function of gear rotation angle. Users will be able to use these equations directly to evaluate gear mesh stiffness of an internal gear pair even though they are not familiar with beam and/or gear meshing theories.

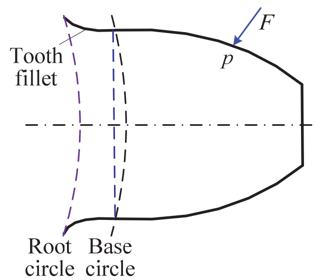

Fig. 2.1: Tooth modeled as a cantilever beam

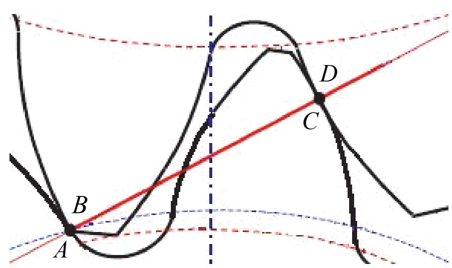

Fig. 2.2: Double tooth pairs in meshing

A planetary gear set has the sun-planet gear meshing (external gear pairs) and the ring-planet gear meshing (internal gear pairs) simultaneously. Due to the lack of an effective way to evaluate the time-varying mesh stiffness of an internal gear pair, a square waveform was used by several researchers [2.19, 2.20] to approximate the time-varying mesh stiffness of a planetary gear set. However, no specific guidelines were presented in [2.19, 2.20] on how to get the magnitudes of the time-varying stiffness. The magnitudes were assumed without confirmation of the physical situation. Furthermore, the square waveform ignored the variation of mesh stiffness caused by the change of the tooth contact point. The flatness of the stiffness curve will generate unwanted frequency components. The approach to be used in this study aims to overcome these shortcomings.

Overall, this chapter derives equations of the time-varying mesh stiffness of a healthy planetary gear set. First, formulas are derived to evaluate the time-varying mesh stiffness of an internal gear pair using the potential energy method. The total potential energy of meshing gears is the summation of Hertzian energy, bending energy, shear energy, and axial compressive energy. Despite the complexity in gear geometry, mesh stiffness equations are derived for involute spur gears. The obtained time-varying mesh stiffness reflects the stiffness variation caused not only by the change of the number of contact tooth pairs but also the change of the contact positions of the gear teeth. Later, by incorporating the mesh stiffness equations reported in [2.17] for an external gear pair and the mesh phasing relationships reported in [2.21], the mesh stiffness of a planetary gear set is evaluated. Case studies are given for three structures of a planetary gear set: carrier fixed, sun gear fixed and ring gear fixed.

2.2 Mesh stiffness of a fixed-shaft internal gear pair

In this section, the mesh stiffness equations for a fixed-shaft internal gear pair will be derived analytically. These equations will be used later in the mesh stiffness evaluation of ring-planet gears of a planetary gear set. In [2.17], the mesh stiffness of a fixed-shaft external gear pair is evaluated. In their research, all the gears are assumed to be involute spur gears and the deflection of the gear body is ignored. More details of this work can be found in [2.22]. The same assumptions will be applied in this study. Hertzian stiffness, bending stiffness, axial compressive stiffness and shear stiffness will be considered.

2.2.1 Hertzian stiffness

According to the Hertzian law, the elastic compression of two isotropic elastic bodies can be approximated by two paraboloidal bodies in the vicinity of the contact point [2.15]. For the planet-ring contact, I approximate the planet gear as a cylinder with radius r_1, and the ring gear as a circular groove with radius r_2, as shown in Fig. 2.3.

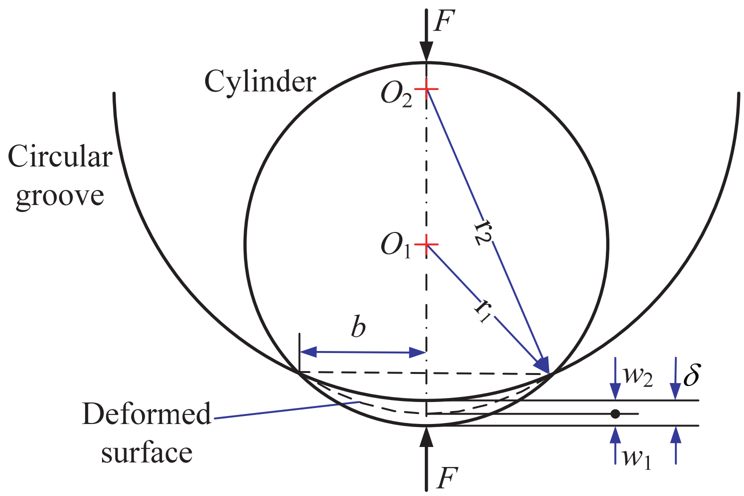

Fig. 2.3: Approximation of the ring-planet contact

The half width of the contact region can be expressed as [2.23]:

$$b = \sqrt{\frac{8(1-\nu^2)F}{\pi EL} \cdot \frac{r_1 r_2}{r_2 - r_1}}, \tag{2.2.1}$$

where E, L, ν represent Yong's modulus, tooth width and Poisson's ratio, respectively, and F is the acting force.

The deformation of the contact teeth due to the force F can be calculated as:

$$\delta = r_1 - r_2 + O_1O_2 = r_1 - r_2 + r_2\sqrt{1-\left(\frac{b}{r_2}\right)^2} - r_1\sqrt{1-\left(\frac{b}{r_1}\right)^2} . \qquad (2.2.2)$$

The square-root terms in Eq. (2.2.2) can be approximated by the first two terms of the binomial expansion (See Eq. (2.2.3)). The error of this approximation is on the order of $(b/r)^4$, and will be less than 0.5 percent for steel gears [2.15].

$$\sqrt{1-\left(\frac{b}{r}\right)^2} \approx 1 - \frac{b^2}{2r^2} . \qquad (2.2.3)$$

Substituting Eq. (2.2.3) into Eq. (2.2.2) gives:

$$\delta = r_1 - r_2 + r_2\left(1-\frac{b^2}{2r_2^{\ 2}}\right) - r_1\left(1-\frac{b^2}{2r_1^{\ 2}}\right) = \frac{1}{2}\left(\frac{1}{r_1}-\frac{1}{r_2}\right)b^2 . \qquad (2.2.4)$$

Combining Eq. (2.2.1) and Eq. (2.2.4), the Hertzian stiffness k_h is expressed as:

$$k_h = \frac{F}{\delta} = \frac{\pi EL}{4(1-\nu^2)} , \qquad (2.2.5)$$

where k_h is a constant for an internal gear pair. This expression of the Hertzian stiffness for an internal gear pair is the same as that for an external gear pair which was derived in [2.15].

2.2.2 Bending, shear and axial compressive stiffness

In this section, the potential energy method is used to evaluate the bending, shear and axial compressive stiffness for an external gear and an internal gear, respectively. The gear tooth is treated as a non-uniform cantilever beam.

2.2.2.1 External gear

For the external gear, the expressions of the bending stiffness k_b, shear stiffness k_s and axial compressive stiffness k_a are derived in [2.17] as follows:

$$\frac{1}{k_b}=\int_{-\alpha_1}^{\alpha_2}\frac{3\left\{1+\cos\alpha_1\left[(\alpha_2-\alpha)\sin\alpha-\cos\alpha\right]\right\}^2(\alpha_2-\alpha)\cos\alpha}{2EL[\sin\alpha+(\alpha_2-\alpha)\cos\alpha]^3}d\alpha\,, \tag{2.2.6}$$

$$\frac{1}{k_s}=\int_{-\alpha_1}^{\alpha_2}\frac{1.2(1+\nu)(\alpha_2-\alpha)\cos\alpha\cos^2\alpha_1}{EL[\sin\alpha+(\alpha_2-\alpha)\cos\alpha]}d\alpha\,, \tag{2.2.7}$$

$$\frac{1}{k_a}=\int_{-\alpha_1}^{\alpha_2}\frac{(\alpha_2-\alpha)\cos\alpha\sin^2\alpha_1}{2EL[\sin\alpha+(\alpha_2-\alpha)\cos\alpha]}d\alpha\,, \tag{2.2.8}$$

where α_2 is the half tooth angle on the base circle of the external gear, α_1 is the angle between the force component F_b and the acting force F which can be decomposed into two orthogonal component forces: F_a and F_b (see Fig. 2.4).

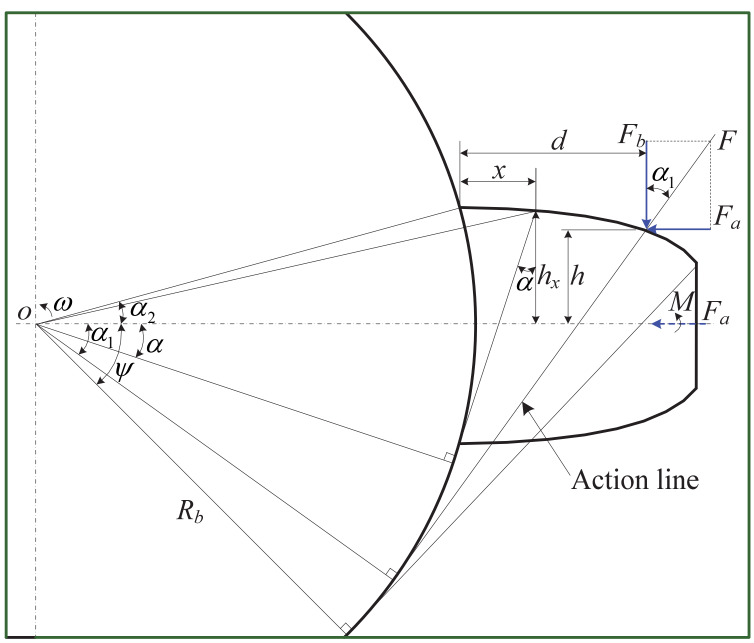

Fig. 2.4: Elastic force on the external gear tooth [2.17]

Eqs. (2.2.6) to (2.2.8) can be used to evaluate the mesh stiffness of the external gear of an internal gear pair. However, due to the configuration differences between an external gear pair and an internal gear pair, the expression for α_1 changes. The angle α_1 is the only variable in Eqs. (2.2.6) to (2.2.8), which reflects the change of contact position of the meshing gears. It is significant to derive the expression of α_1 which is not mentioned in [2.17] for an internal gear pair.

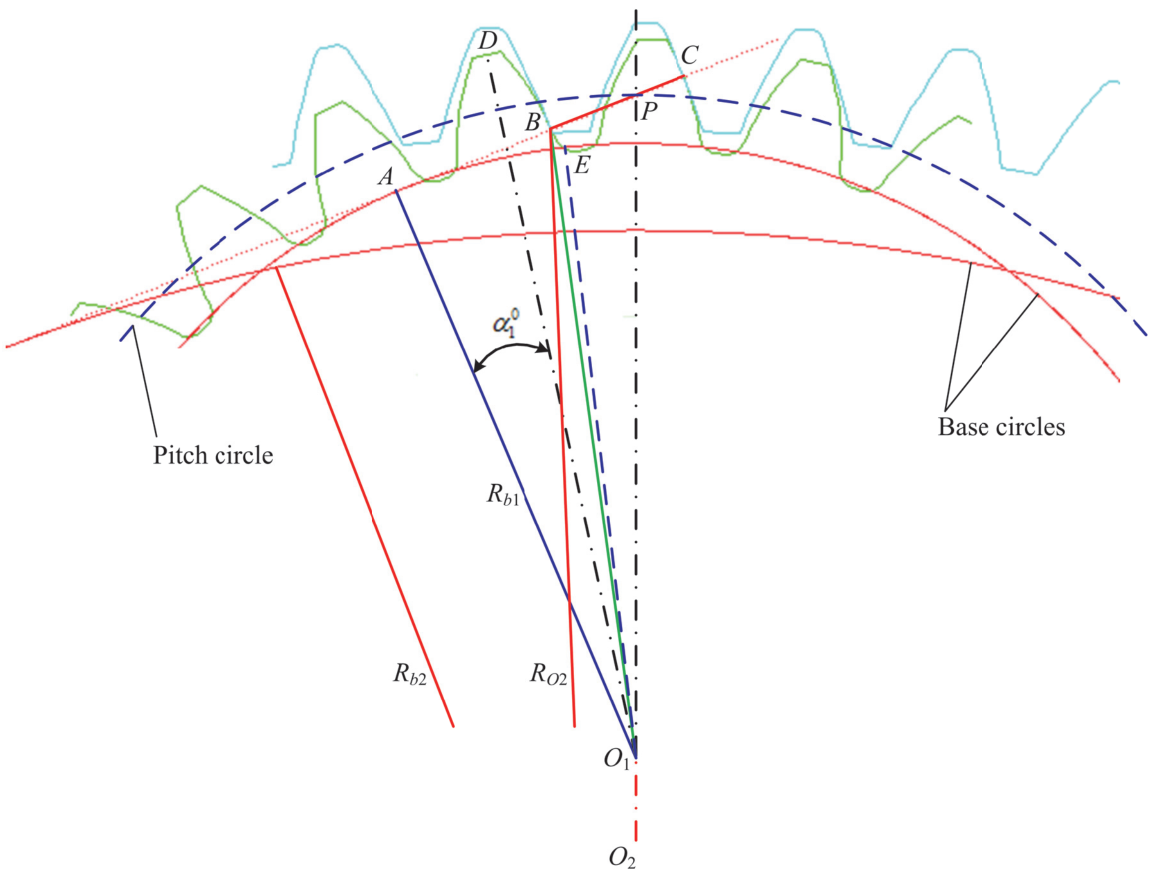

Fig. 2.5: Gear meshing sketch of an internal gear pair

In Fig. 2.5, consider point B as the reference point, which corresponds to the initial meshing point of the first pair of meshing teeth. At this point, the angular displacement of the external gear (θ_1) and the internal gear (θ_2), are assumed to be zero. The corresponding angle α_1^0 can be expressed as (see Fig. 2.5):

$$\alpha_1^0 = \angle AO_1D = \angle AO_1B - \angle BO_1D. \quad (2.2.9)$$

From the properties of the involute curve, the gear meshing action line BC is tangent to the base circles. Therefore, the line AO_1 is perpendicular to the line AC. The angle $\angle AO_1B$ can be expressed as:

$$\angle AO_1B = \arccos\frac{R_{b1}}{\overline{O_1B}}. \quad (2.2.10)$$

The line segment $\overline{O_1B}$ can be obtained in the triangle BO_1O_2 as:

$$\overline{O_1B} = \sqrt{R_{O2}^2 + \overline{O_1O_2} - 2R_{O2}\overline{O_1O_2}\cos\angle O_1O_2B}, \quad (2.2.11)$$

where R_{b1} is the base circle radius of the external gear, R_{O2} is the inner radius of the internal gear and $\overline{O_1O_2}$ is the center distance of the two gears.

We can express $\angle BO_1D$ as:

$$\angle BO_1D = \angle DO_1E - \angle BO_1E = \alpha_2 - \angle BO_1E, \quad (2.2.12)$$

where $\alpha_2 = \frac{\pi}{2N_1} + \tan\alpha_0 - \alpha_0$, $\angle BO_1E = \tan\angle AO_1B - \angle AO_1B$ [2.22].

Substituting Eqs. (2.2.10) - (2.2.12) into Eq. (2.2.9), the angle α_1^0 can be expressed finally as:

$$\alpha_1^0 = -\alpha_2 + \tan\angle AO_1B = -\frac{\pi}{2N_1} - \tan\alpha_0 + \alpha_0 + \quad (2.2.13)$$

$$\tan\left[\arccos\frac{N_1\cos\alpha_0}{\sqrt{(N_2-2)^2+(N_2-N_1)^2-2(N_2-2)(N_2-N_1)\cos(\alpha_0-\arccos\frac{N_2\cos\alpha_0}{N_2-2})}}\right],$$

where N_1 and N_2 represent the number of teeth of the external gear and the internal gear, respectively, and α_0 is the pressure angle.

Eq. (2.2.13) gives the formula of the angle α_1 when the angular displacement of the external gear is zero. When the angular displacement of the external gear is θ, the angle α_1 will be:

$$\alpha_1 = \theta+\alpha_1^0 = \theta-\frac{\pi}{2N_1}-\tan\alpha_0+\alpha_0+ \tag{2.2.14}$$

$$\tan\left[\arccos\frac{N_1\cos\alpha_0}{\sqrt{(N_2-2)^2+(N_2-N_1)^2-2(N_2-2)(N_2-N_1)\cos(\alpha_0-\arccos\frac{N_2\cos\alpha_0}{N_2-2})}}\right].$$

2.2.2.2 Internal gear

According to the properties of the involute curve, the acting force is always along the action line which is normal to the tooth profile and tangent to the gear base circle. The acting force F can be divided into two orthogonal forces F_a and F_b as shown in Fig. 2.6.

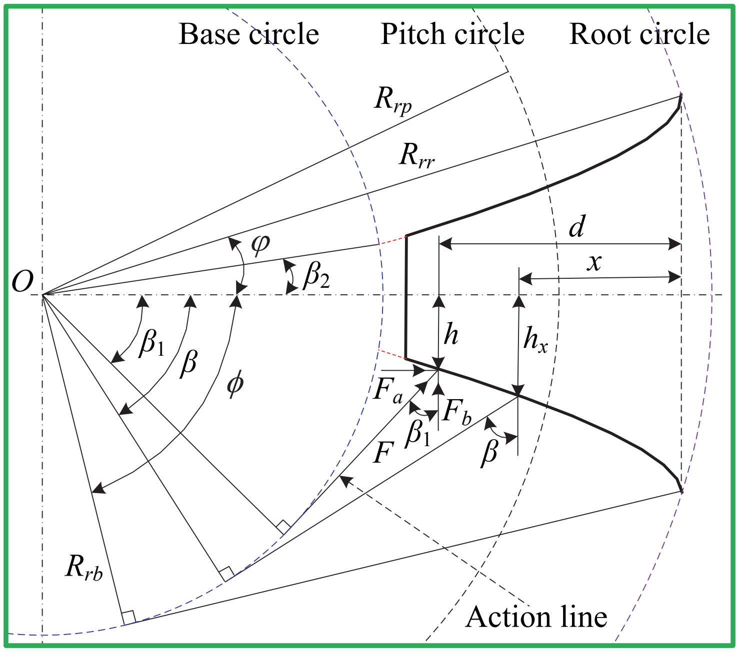

Fig. 2.6: Elastic force on an internal gear tooth

$$F_a = F\sin\beta_1. \tag{2.2.15}$$

$$F_b = F\cos\beta_1. \tag{2.2.16}$$

Based on the beam theory, the bending, shear and axial compressive energies stored in a tooth can be calculated as follows [2.16, 2.17]:

$$U_b = \frac{F^2}{2k_b} = \int_0^d \frac{[F_b(d-x)-F_a h]}{2EI_x}dx\,, \tag{2.2.17}$$

$$U_s = \frac{F^2}{2k_s} = \int_0^d \frac{1.2F_b^{\,2}}{2GA_x}dx\,, \tag{2.2.18}$$

$$U_a = \frac{F^2}{2k_a} = \int_0^d \frac{F_a^{\,2}}{2EA_x}dx\,, \tag{2.2.19}$$

where k_b, k_s and k_a represent the bending, the shear and the axial compressive stiffness, respectively, E and G denote Young's modulus and shear modulus, respectively, h is the distance between the gear contact point and the central line, d is the distance from the contact point to the gear root, and A_x and I_x indicate the area and the area moment of inertia of the tooth section where the distance to the tooth root is x (see Fig. 2.6).

According to the properties of involute curve, h, h_x, d, I_x and A_x can be expressed as follows:

$$h = R_{rb}(\sin\beta_1 - (\beta_1 - \beta_2)\cos\beta_1), \tag{2.2.20}$$

$$h_x = R_{rb}(\sin\beta - (\beta - \beta_2)\cos\beta), \tag{2.2.21}$$

$$d = R_{rr}\cos\varphi - \frac{R_{rb}}{\cos\beta_1} + h\tan\beta_1, \tag{2.2.22}$$

$$I_x = \frac{1}{12}(2h_x)^3 L = \frac{2}{3}h_x{}^3 L, \tag{2.2.23}$$

$$A_x = 2h_x L, \tag{2.2.24}$$

where R_{rb}, R_{rr} and L represent the base circle radius, the root circle radius and the width of the tooth of the internal gear, respectively, β_2 and φ denote the half tooth angle on the base circle and the root circle, respectively, and h_x is the height of the section where the distance to the tooth root is x (see Fig. 2.6).

Substituting Eqs. (2.2.15), (2.2.16) and (2.2.20) - (2.2.23) into Eq. (2.2.17), the bending stiffness of the internal gear is obtained as:

$$\frac{1}{k_b} = \int_{\phi}^{\beta_1} \frac{3\left\{1 + \cos\beta_1\left[(\beta_2 - \beta)\sin\beta - \cos\beta\right]\right\}^2 (\beta_2 - \beta)\cos\beta}{2EL[\sin\beta + (\beta_2 - \beta)\cos\beta]^3} d\beta, \tag{2.2.25}$$

where $\beta_2 = \frac{\pi}{2N_2} - \tan\alpha_0 + \alpha_0$ and $\phi = \beta_2 + \tan(\arccos\frac{R_{rb}}{R_{rr}})$ (see Fig. 2.6).

Substituting Eq. (2.2.16) and Eq. (2.2.24) into Eq. (2.2.18), the shear stiffness can be expressed as:

$$\frac{1}{k_s}=\int_{\phi}^{\beta_1}\frac{1.2(1+\nu)(\beta_2-\beta)\cos\beta\cos^2\beta_1}{EL[\sin\beta+(\beta_2-\beta)\cos\beta]}d\beta\,. \tag{2.2.26}$$

Substituting Eq. (2.2.15) and Eq. (2.2.24) into Eq. (2.2.19), the axial compressive stiffness is obtained as:

$$\frac{1}{k_a}=\int_{\phi}^{\beta_1}\frac{(\beta_2-\beta)\cos\beta\sin^2\beta_1}{2EL[\sin\beta+(\beta_2-\beta)\cos\beta]}d\beta\,. \tag{2.2.27}$$

Similar to the external gear, it is significant to derive the expression of the angle β_1 for the internal gear. Firstly, I derive the expression of angle β_1^0 which is the angle of β_1 when the gears mesh at the reference point (point B at Fig. 2.7).

$$\beta_1^0=\angle FO_2G=\angle FO_2B+\angle BO_2G$$

$$=\angle FO_2B+\angle BO_2K+\angle KO_2G=\angle FO_2B+\angle BO_2K+\beta_2\,, \tag{2.2.28}$$

where the point K is the intersection of the internal gear base circle and the extension of the involute curve.

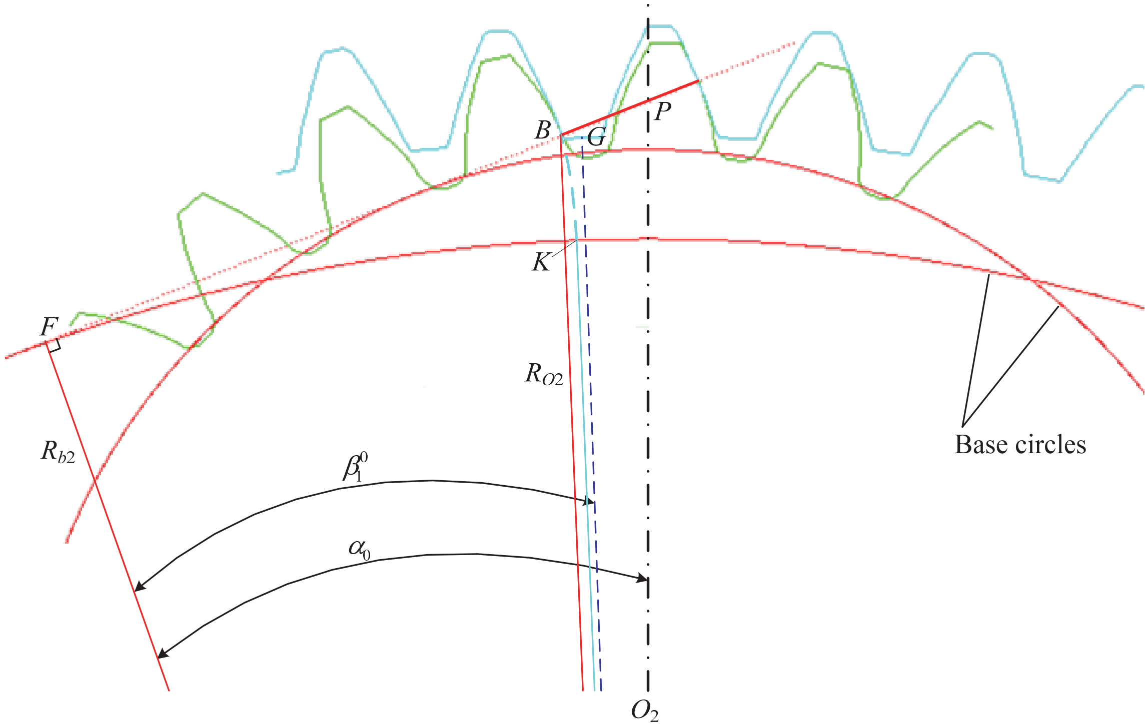

Fig. 2.7: Meshing of an internal gear pair

Using the properties of the involute curve, the angle $\angle BO_2K$ can be expressed as [2.22]:

$$\angle BO_2K = \angle FO_2K - \angle FO_2B = \tan\angle FO_2B - \angle FO_2B\,. \tag{2.2.29}$$

Substituting Eq. (2.2.29) into Eq. (2.2.28), the expression of β_1^0 can be rewritten as:

$$\beta_1^0 = \tan\angle FO_2B + \beta_2 = \tan(\arccos\frac{R_{b2}}{R_{O2}}) + \frac{\pi}{2N_2} - \tan\alpha_0 + \alpha_0$$

$$= \tan(\arccos\frac{N_2\cos\alpha_0}{N_2 - 2}) + \frac{\pi}{2N_2} - \tan\alpha_0 + \alpha_0\,. \tag{2.2.30}$$

When the angular displacement of the internal gear is η, the angle β_1 will be:

$$\beta_1 = \eta + \beta_1^0 = \frac{N_1}{N_2}\theta + \tan(\arccos\frac{N_2\cos\alpha_0}{N_2 - 2}) + \frac{\pi}{2N_2} - \tan\alpha_0 + \alpha_0\,, \qquad (2.2.31)$$

where θ is the angular displacement of the external gear with respect to the reference point B.

In this section, the bending stiffness, the shear stiffness and the axial compressive stiffness of an internal gear are derived first time in the literature. These equations are convenient to use. Given geometry and material parameters of an internal gear, the bending stiffness, the shear stiffness and the axial compressive stiffness are expressed as a function of the rotation angle of the gear.

2.2.3 Overall mesh stiffness of an internal gear pair

For a pair of standard spur gears whose contact ratio is always between 1 and 2, the alternation of one pair and two pairs of teeth in contact is observed. The single-tooth-pair duration and the double-tooth-pair duration of an internal gear pair are derived as the rotation angular displacement of the external gear as follows [2.17]:

Single-tooth-pair duration: $\theta \in \left[(n-1)\frac{2\pi}{N_1} + \theta_d,\ n\frac{2\pi}{N_1}\right]\quad (n = 1, 2,\ \cdots)$,

Double-tooth-pair duration: $\theta \in \left[(n-1)\frac{2\pi}{N_1},\ \theta_d + (n-1)\frac{2\pi}{N_1}\right]\quad (n = 1, 2,\ \cdots)$,

where θ and N_1 denote the angular displacement and the number of teeth of the external gear, respectively, $\theta_d = (c-1)\frac{2\pi}{N_1}$, and c is the contact ratio.

For the single-tooth-pair meshing duration, the total effective mesh stiffness can be calculated as [2.17]:

$$k_r(\theta) = \frac{1}{\dfrac{1}{k_h} + \dfrac{1}{k_{b1}} + \dfrac{1}{k_{s1}} + \dfrac{1}{k_{a1}} + \dfrac{1}{k_{b2}} + \dfrac{1}{k_{s2}} + \dfrac{1}{k_{a2}}}, \qquad (2.2.32)$$

where k_r is the total effective mesh stiffness which is expressed as a function of the angular displacement of the external gear. Subscripts 1 and 2 represent the external gear and the internal gear, respectively.

For the double-tooth-pair meshing duration, there are two pairs of gears meshing at the same time. The total effective mesh stiffness can be obtained as [2.17]:

$$k_r(\theta) = k_{r1}(\theta) + k_{r2}(\theta) = \sum_{i=1}^{2} \frac{1}{\dfrac{1}{k_{h,i}} + \dfrac{1}{k_{b1,i}} + \dfrac{1}{k_{s1,i}} + \dfrac{1}{k_{a1,i}} + \dfrac{1}{k_{b2.i}} + \dfrac{1}{k_{s2,i}} + \dfrac{1}{k_{a2,i}}}, \qquad (2.2.33)$$

where $i = 1$ for the first pair of meshing teeth and $i = 2$ for the second pair.

The equations to evaluate the mesh stiffness of an internal gear pair will be used later to evaluate the mesh stiffness of a ring-planet gear pair since it is an internal gear pair.

2.3 Mesh stiffness of a planetary gear set

A planetary gear set consists of a centrally pivoted sun gear, a ring gear and several planet gears which rotate between the sun gear and ring gear. The mesh stiffness evaluation of a planetary gear set (one sun gear, one ring gear and four equally spaced planet gears) will be illustrated in this section. The number of teeth for the sun gear, the planet gear and the ring gear are 19, 31, and 81, respectively. The other properties of this planetary gear set are the same for the sun gear, planet gear and the ring gear as shown in Table 2.1.

Table 2.1: Physical parameters of the gears

Module	Pressure angle	Face width	Young's modulus	Poisson's ratio
3.2 mm	20^{o}	0.0381 m	2.068×10^{11} Pa	0.3

2.3.1 Mesh stiffness when the carrier is fixed

For a planetary gear set, if the carrier is fixed, each planet gear will rotate only around its own fixed-shaft center; the sun gear and the ring gear will both rotate around the sun gear shaft center. The sun-planet gear pair is equivalent to a fixed-shaft external gear pair while the ring-planet gear pair is equivalent to a fixed-shaft internal gear pair. No matter a sun-planer gear pair or a ring-planet gear pair, the overall mesh stiffness can be expressed as a function of the rotation angular displacement of the planet gear θ_p:

$$k_{sp1} = k_s(\theta_p)\,, \tag{2.3.1}$$

$$k_{rp1} = k_r(\theta_p)\,, \tag{2.3.2}$$

where k_{sp1} and k_{rp1} represent the mesh stiffness of the first pair of sun-planet gears and the first pair of the ring-planet gears, respectively, k_s and k_r denote the mesh stiffness formulas for a fixed-shaft external gear pair (derived in [2.17]) and a fixed-shaft internal gear pair (derived in Section 2.2 of this chapter), respectively.

Using Eq. (2.3.1) and Eq. (2.3.2), the mesh stiffness of the first pair of sun-planet gears and the first pair of ring-planet gears are plotted in Fig. 2.8 and Fig. 2.9, respectively. Because the planet gear has 31 teeth, the sun-planet pair and the ring-planet pair will experience tooth meshing 15.5 times in half revolution of the planet gear. The point B' showed in Fig. 2.8 is the reference point, which corresponds to the initial meshing point of a pair of sun-planet teeth. Point P' is the pitch point where two teeth mesh at the pitch circle. Similarly, point B and point P are the reference point and the pitch point of a pair of ring-planet teeth, respectively. The angle ϕ_{sp} indicates the rotation angular displacement of the planet gear meshing with the sun gear rotation from point B' to point P'. The angle ϕ_{rp} represents the rotation angular displacement of the planet gear meshing with the ring gear rotation from point B to point P. The expressions for ϕ_{sp} and ϕ_{rp} will be described later.

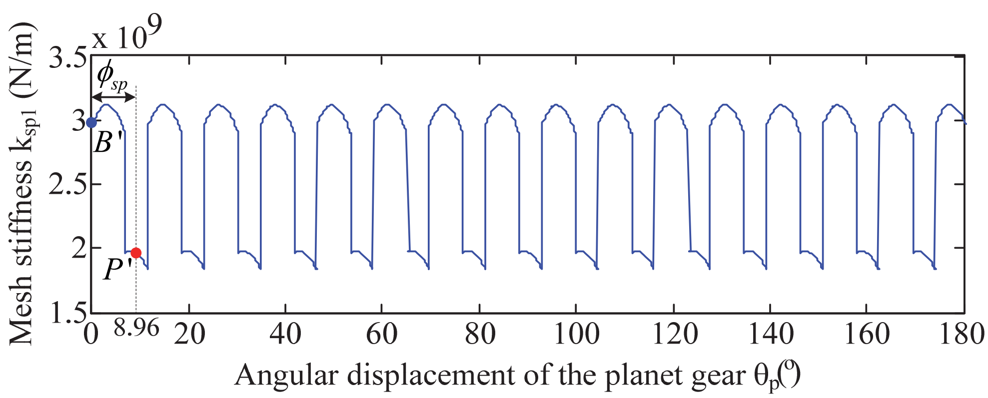

Fig. 2.8: Mesh stiffness of the first pair of sun-planet gears when the carrier is fixed

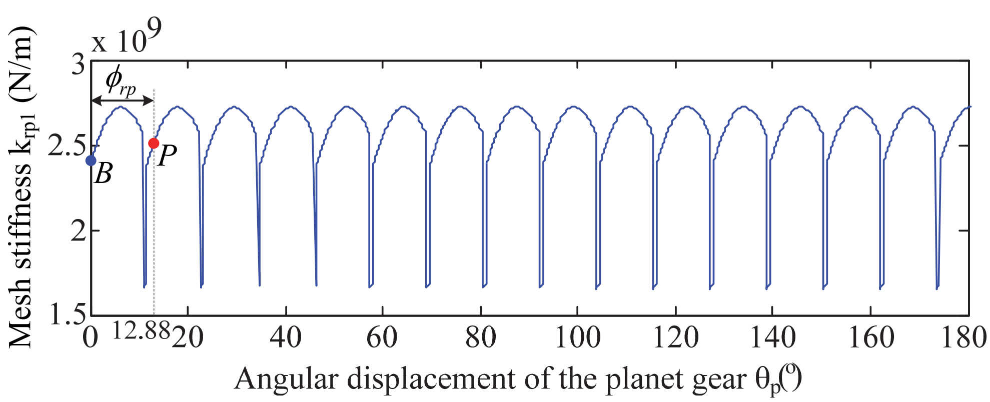

Fig. 2.9: Mesh stiffness of the first pair of ring-planet gears when the carrier is fixed

In a planetary gear set, there are several pairs of sun-planet gears and several pairs of ring-planet gears meshing simultaneously. While each of the sun-planet meshes has the same shape of mesh stiffness variation, they are not necessarily in phase with each other [2.21]. Similar comments apply to the ring-planet meshes. The mesh phasing relationships given in [2.21] will be applied in this study to get the mesh stiffness of the n^{th} sun-planet pair (k_{spn}) and the n^{th} ring-planet pair (k_{rpn}), where n may go up to the total number of planet gears which are equally spaced.

The stiffness of the n^{th} sun-planet pair (k_{spn}) with respect to the 1st sun-planet pair (k_{sp1}) and the stiffness of the n^{th} ring-planet pair (k_{rpn}) with respect to the 1st ring-planet pair (k_{rp1}) are given as follows [2.21]:

$$k_{spn} = k_{sp1}(t - \gamma_{sn} T_m), \qquad (2.3.3)$$

$$k_{rpn} = \kappa_{rp1}(t - \gamma_{rn} T_m - \gamma_{rs} T_m), \qquad (2.3.4)$$

where γ_{sn} is the relative phase between the n^{th} sun-planet pair with respect to the 1st sun-planet pair, γ_{rn} is the relative phase between the n^{th} ring-planet pair with respect to the 1st ring-planet pair, γ_{rs} is the relative phase between the n^{th} ring-planet mesh with respect to the n^{th} sun-planet mesh, κ_{rp1} is the time-varying mesh stiffness of the 1st ring-planet pair with t = 0 meshing at the pitch point, and T_m is the mesh period which is the same for both the sun-planet meshing and the ring-planet meshing. Without loss of generality, the 1st sun-planet pair is assumed to mesh at the pitch point at t = 0.

Ref. [2.21] provided an analytical way to calculate the relative phase between the n^{th} sun-planet pitch point meshing and the n^{th} ring-planet pitch point meshing. However, Ref. [2.21] did not mention how to obtain the position of the pitch point meshing in one mesh period of two gears. In this chapter, the position of the pitch point is defined as the angular difference between the pitch point meshing and the reference point meshing. The angle ϕ_{sp} (see Fig. 2.8) and ϕ_{rp} (see Fig. 2.9) define the pitch point meshing position in one mesh period for a fixed-shaft external gear pair and a fixed-shaft internal gear pair, respectively. A derivation is given below to get the value of angle ϕ_{rp} and ϕ_{sp}.

Using the properties of the involute curve, the angle ϕ_{rp} can be expressed as (see Fig. 2.5):

$$\phi_{rp} = \frac{\overline{BP}}{R_{b1}} = \frac{\overline{AP} - \overline{AB}}{R_{b1}} = \tan\alpha_0 - \tan\left[\arccos\frac{N_1\cos\alpha_0}{\sqrt{(N_2-2)^2+(N_2-N_1)^2-2(N_2-2)(N_2-N_1)\cos(\alpha_0-\arccos\frac{N_2\cos\alpha_0}{N_2-2})}}\right]. \quad (2.3.5)$$

Similarly, the angle ϕ_{sp} can be calculated by:

$$\phi_{sp} = \tan\alpha_0' - \tan\left[\arccos\frac{N_1'\cos\alpha_0'}{\sqrt{(N_2'+2)^2+(N_1'+N_2')^2-2(N_2'+2)(N_1'+N_2')\cos(\arccos\frac{N_2'\cos\alpha_0'}{N_2'+2}-\alpha_0')}}\right], \quad (2.3.6)$$

where N_1' and N_2' are the number of teeth of a fixed-shaft external gear pair, α_0' is the pressure angle.

Applying the methods proposed in [2.21] and the parameters listed in Table 2.1, the relative phases of this planetary gear set are shown in Table 2.2. The zero value of γ_{rs}

means the sun-planet gear pair and the ring-planet gear pair mesh at the pitch point simultaneously.

Table 2.2: Relative phases of the planetary gear set

γ_{s1}	γ_{s2}	γ_{s3}	γ_{s4}	γ_{r1}	γ_{r2}	γ_{r3}	γ_{r4}	γ_{rs}
0	0.75	0.5	0.25	0	-0.25	-0.5	-0.75	0

When the carrier is fixed, the time-varying mesh stiffness of this planetary gear set is shown in Fig. 2.10. The curves k_{sp1}, k_{sp2}, k_{sp3} and k_{sp4} represent the 1st, the 2nd, the 3rd and the 4th pairs of the sun-planet mesh stiffness, respectively. Similarly, the curves k_{rp1} k_{rp2}, k_{rp3} and k_{rp4} denote the 1st, the 2nd, the 3rd and the 4th pairs of the ring-planet mesh stiffness, respectively. The mesh stiffness is expressed as a function of rotation angular displacement of the planet gear. If the phase difference of the sun-planet gear pairs is $\gamma_{sn}T_m$ in time, the corresponding phase difference in terms of the rotation angle of the planet gear is $\theta_{sn} = \gamma_{sn}T_m\omega_p = \gamma_{sn}\theta_m$. The symbol ω_p represents the angular rotation speed of the planet gear and the symbol θ_m is the rotation angular displacement of the planet gear in one mesh period, $\theta_m = \dfrac{2\pi}{Z_p}$. Similarly, the phase difference of the ring-planet gear pairs can be expressed as $\theta_{rn} = \gamma_{rn}T_m\omega_p = \gamma_{rn}\theta_m$. The point p' and p show that both the sun-planet gear pair and the ring-planet gear pair mesh at the pitch point at t = 0.

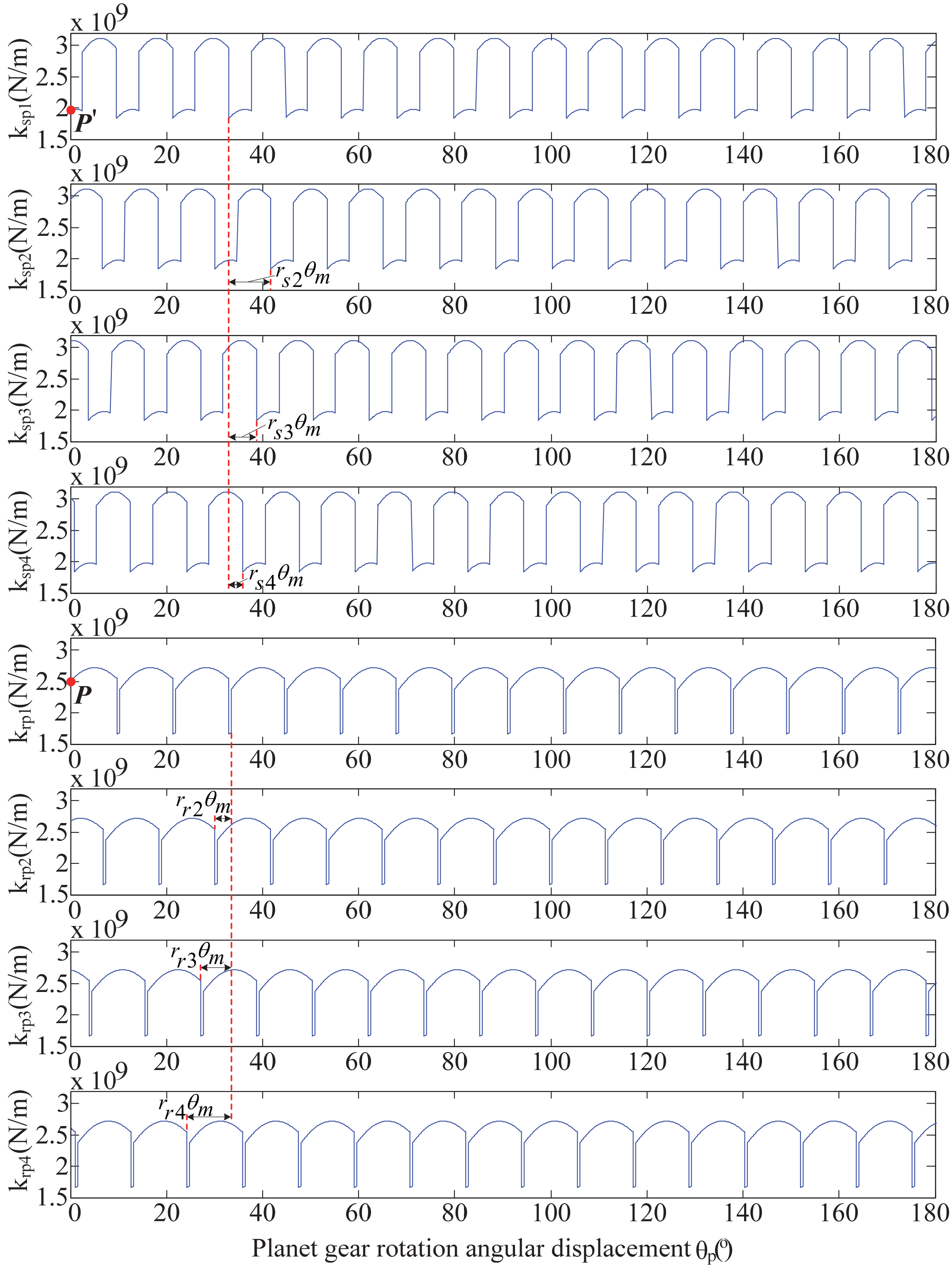

Fig. 2.10: Time-varying mesh stiffness of a planetary gear set when the carrier is fixed

2.3.2 Mesh stiffness when the carrier is rotating

When the carrier is rotating, each planet gear not only revolves on its own axis but also revolves around the sun gear shaft axis. In this situation, the sun gear or the ring gear can be fixed, but not both, since the gearbox will not work if both the sun gear and the ring gear are fixed. In the structure of differential planet gears, all the gears are rotating including the carrier.

Whether the carrier is fixed or rotating, the meshing areas of the two gears are always the same, which means the mesh stiffness shapes of the two cases are the same. The only difference is the mesh period. If the gear mesh frequency ratio between the cases of rotating carrier and fixed carrier is λ, the mesh stiffness of the rotating case can be obtained through an expansion of the mesh stiffness shape of the fixed case by $1/\lambda$ times. Based on Eq. (2.3.1) and Eq. (2.3.2), when the carrier is not fixed, the formulas for the first pair of sun-planet gears and the first pair of the ring-planet gears can be expressed respectively as:

$$k_{sp1} = k_s(\lambda\theta_p), \qquad (2.3.7)$$

$$k_{rp1} = k_r(\lambda\theta_p), \qquad (2.3.8)$$

where the symbol λ is the mesh frequency ratio between the rotating case and the fixed case.

In the followings, the mesh stiffness evaluation of two other commonly used planetary gear transmission structures will be described, namely fixed sun gear structure and fixed ring gear structure. If the ring gear is fixed, the planetary gear set can earn the maximum transmission ratio. On the other hand, if the sun gear is fixed, the planetary gear set will attain the minimum transmission ratio.

2.3.2.1 The ring gear is fixed

According to Kahraman [2.24], the gear mesh frequency ω_m is determined from kinematic relationships as a function of the rotational speeds of the sun (Ω_s) and the ring gears (Ω_r):

$$\omega_m = \begin{cases} Z_s Z_r \Omega_s / (Z_s + Z_r), & \text{fixed ring gear} \\ Z_s Z_r \Omega_r / (Z_s + Z_r), & \text{fixed sun gear} \\ Z_s \Omega_s (\text{or } Z_r \Omega_r), & \text{fixed carrier} \end{cases} \tag{2.3.9}$$

where Z_s and Z_r are the numbers of teeth of the sun gear and the ring gear, respectively.

The gear mesh frequency ω_m when the ring gear is fixed is smaller than the situation when the carrier is fixed. This is because in the first case the planet gear is revolving around the sun gear in addition to meshing with the sun gear. The mesh frequency ratio between the ring gear fixed case and the carrier fixed case can be calculated from Eq. (2.3.9) as:

$$\lambda_r = \frac{Z_s Z_r \Omega_s / (Z_s + Z_r)}{Z_s \Omega_s} = \frac{Z_r}{Z_s + Z_r}. \tag{2.3.10}$$

Therefore, the mesh stiffness when the ring gear is fixed can be obtained through an expansion of the shape of the mesh stiffness when the carrier is fixed by $1/\lambda_r$ times as shown in Fig. 2.11. In half a revolution of the planet gear, 12.56 times ($\lambda_r Z_p / 2$) of gear meshing are experienced.

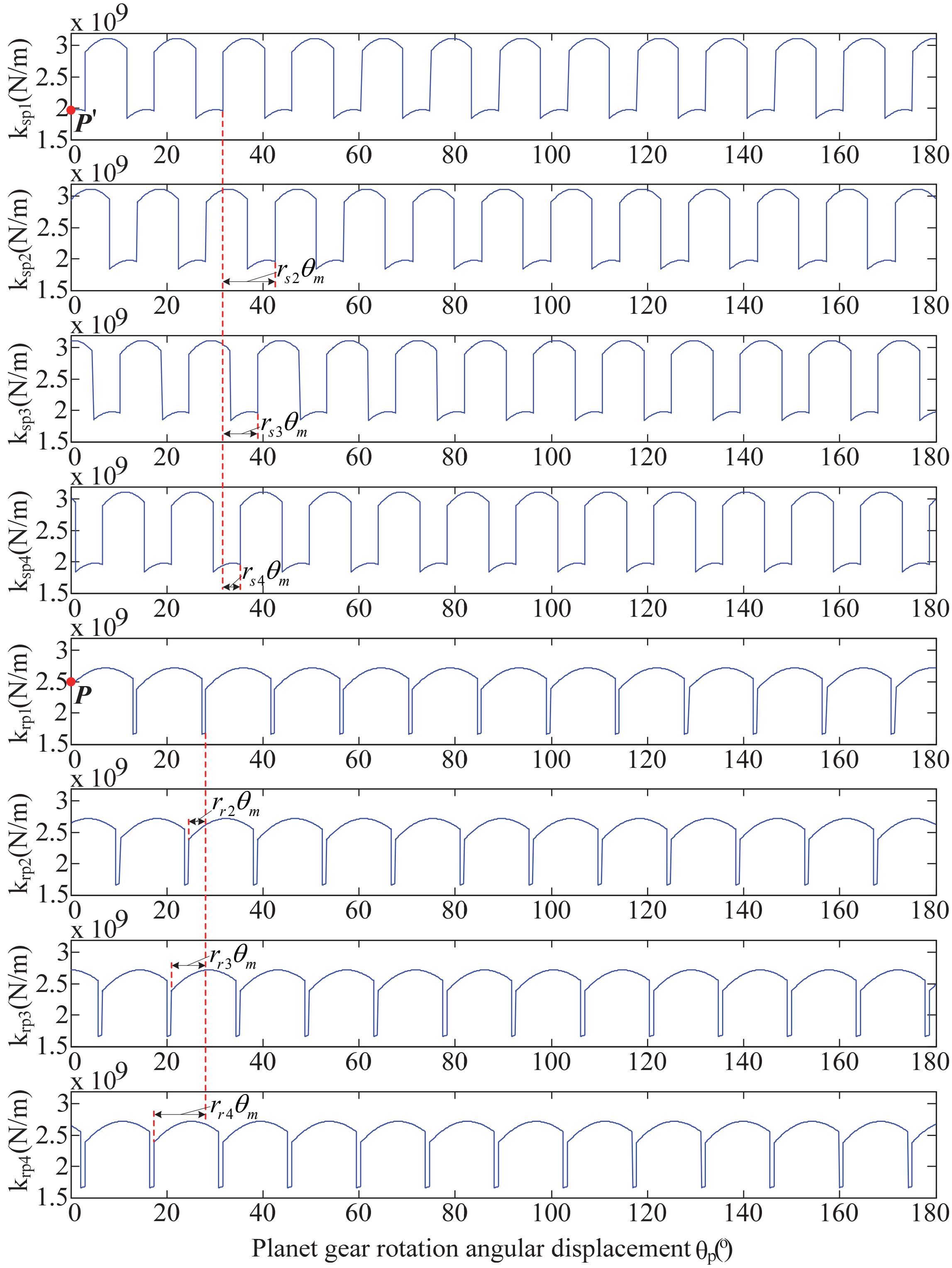

Fig. 2.11: Time-varying mesh stiffness of a planetary gear set when ring gear is fixed

2.3.2.2 The sun gear is fixed

In this case, the mesh frequency ratio between the sun gear fixed case and the carrier fixed case can be obtained based on Eq. (2.3.9) as:

$$\lambda_s = \frac{Z_s Z_r \Omega_r / (Z_s + Z_r)}{Z_r \Omega_r} = \frac{Z_s}{Z_s + Z_r}. \tag{2.3.11}$$

Then, the mesh stiffness when the sun gear is fixed can be obtained through an expansion of the shape of the mesh stiffness when the carrier is fixed by $1/\lambda_s$ times. The number of gear meshing in half a revolution of the planet gear is $\lambda_s Z_p / 2$.

We now provide a summary of the gear mesh stiffness equations either reported in the literature or derived in the earlier sections of this chapter. For the external gear, the equations of bending stiffness, shear stiffness and axial compressive stiffness were derived in [2.17] and are listed in Eq. (2.2.6) - Eq. (2.2.8) of this thesis. For the internal gear, the equations of bending stiffness, shear stiffness and axial compressive stiffness are derived in this research and are presented in Eq. (2.2.25) - Eq. (2.2.27). The bending, shear and axial compressive stiffness equations of the external gear and the internal gear have the same integrand because the tooth profile of both external gear teeth and internal gear teeth is the involute curve. However, the limits of the integral reflect the differences between the external gear tooth and the internal gear tooth. The expression of the Hertzian contact stiffness derived in Section 2.2.1 of this chapter for an internal gear pair (shown in Eq. (2.2.5)) is the same as that for an external gear pair reported in Ref. [2.15]. A summary of these equations is given in Table 2.3.

Table 2.3: A summary of gear mesh stiffness equations

	Integrand		Limits of integral	
	External gear	Internal gear	External gear	Internal gear
Bending stiffness	$\frac{3\left\{1+\cos\alpha_1\left[(\alpha_2-\alpha)\sin\alpha-\cos\alpha\right]\right\}^2(\alpha_2-\alpha)\cos\alpha}{2EL[\sin\alpha+(\alpha_2-\alpha)\cos\alpha]^3}$		$[-\alpha_1,\ \alpha_2]$	$[\phi,\beta_1]$
Shear stiffness	$\frac{1.2(1+\nu)(\alpha_2-\alpha)\cos\alpha\cos^2\alpha_1}{EL[\sin\alpha+(\alpha_2-\alpha)\cos\alpha]}$		$[-\alpha_1,\ \alpha_2]$	$[\phi,\beta_1]$
Axial compressive stiffness	$\frac{(\alpha_2-\alpha)\cos\alpha\sin^2\alpha_1}{2EL[\sin\alpha+(\alpha_2-\alpha)\cos\alpha]}$		$[-\alpha_1,\ \alpha_2]$	$[\phi,\beta_1]$
Hertzian stiffness	Constant: $\frac{\pi EL}{4(1-\nu^2)}$			

2.4 Conclusions

The analytical method evaluates the time-varying mesh stiffness of a planetary gear set using the potential energy method. Mesh stiffness equations for a fixed-shaft *internal* gear pair are derived in this chapter. Hertzian stiffness, bending stiffness, shear stiffness and axial compressive stiffness are analytically derived for the internal involute gear tooth. Different transmission structures may exist for a planetary gear set. If the carrier is fixed, a sun-planet gear pair is regarded as a fixed-shaft external gear pair while a ring-planet gear pair is regarded as a fixed-shaft internal gear pair. Combining the relative mesh phases of gear pairs, the mesh stiffness of a planetary gear set when the carrier is fixed is obtained. If the carrier is not fixed, the mesh stiffness is obtained through an expansion of the mesh stiffness shape when the carrier is fixed. The obtained mesh stiffness considers both the variation of the mesh position and the number of contact tooth pairs. The results reported in this chapter will be further extended in Chapter 3 of this thesis for stiffness evaluation of a planetary gear set when gear tooth crack is present. The gear mesh stiffness equations derived in this chapter will be used in the dynamic model of a planetary gear set to be desribed in Chapter 4 of this thesis.

References

[2.1] X. Liang, M. J. Zuo, and T. H. Patel, "Evaluating the Time-varying Mesh Stiffness of a Planetary Gear Set Using the Potential Energy Method," *Proc. Inst. Mech. Eng. Part C J. Mech. Eng. Sci.*, vol. 228, no. 3, pp. 535–547, Feb. 2014.

[2.2] X. Liang, M. J. Zuo, and Y. Guo, "Evaluating the Time-Varying Mesh Stiffness of a Planetary Gear Set Using the Potential Energy Method," in *Proceedings of the 7th World Congress on Engineering Asset Management (WCEAM 2012)*, Springer International Publishing, 2015, pp. 365–374.

[2.3] F. Chaari, T. Fakhfakh, and M. Haddar, "Dynamic Analysis of a Planetary Gear Failure Caused by Tooth Pitting and Cracking," *J. Fail. Anal. Prev.*, vol. 6, no. 2, pp. 73–78, Apr. 2006.

[2.4] J. Lin and R. G. Parker, "Mesh Stiffness Variation Instabilities in Two-Stage Gear Systems," *J. Vib. Acoust.*, vol. 124, no. 1, pp. 68–76, Sep. 2001.

[2.5] J. Wang and I. Howard, "The Torsional Stiffness of Involute Spur Gears," *Proc. Inst. Mech. Eng. Part C J. Mech. Eng. Sci.*, vol. 218, no. 1, pp. 131–142, Jan. 2004.

[2.6] J. Meagher, X. Wu, D. Kong, and C. H. Lee, "A Comparison of Gear Mesh Stiffness Modeling Strategies," in *Structural Dynamics, Volume 3*, T. Proulx, Ed. Springer New York, 2011, pp. 255–263.

[2.7] S. Jia and I. Howard, "Comparison of Localised Spalling and Crack Damage from Dynamic Modelling of Spur Gear Vibrations," *Mech. Syst. Signal Process.*, vol. 20, no. 2, pp. 332–349, Feb. 2006.

[2.8] Y. Pandya and A. Parey, “Failure Path Based Modified Gear Mesh Stiffness for Spur Gear Pair with Tooth Root Crack,” *Eng. Fail. Anal.*, vol. 27, pp. 286–296, Jan. 2013.

[2.9] C. Song, C. zhu, and L. Liu, “Mesh Characteristics for Marine Beveloid Gears with Crossed Axes,” *J. Xian Tiaotong Univ.*, vol. 46, pp. 64–69, 2012.

[2.10] F. Chaari, T. Fakhfakh, and M. Haddar, “Analytical Modelling of Spur Gear Tooth Crack and Influence on Gearmesh Stiffness,” *Eur. J. Mech. - ASolids*, vol. 28, no. 3, pp. 461–468, May 2009.

[2.11] X. Zhou, Y. Shao, Y. Lei, and M. Zuo, “Time-varying Meshing Stiffness Calculation and Vibration Analysis for a 16DOF Dynamic Model with Linear Crack Growth in a Pinion,” *J. Vib. Acoust.*, vol. 134, no. 1, p. 011011, 2012.

[2.12] F. Chaari, W. Baccar, M. S. Abbes, and M. Haddar, “Effect of Spalling or Tooth Breakage on Gearmesh Stiffness and Dynamic Response of a One-stage Spur Gear Transmission,” *Eur. J. Mech. - ASolids*, vol. 27, no. 4, pp. 691–705, Jul. 2008.

[2.13] R. Kasuba and J. W. Evans, “An Extended Model for Determining Dynamic Loads in Spur Gearing,” *J. Mech. Des.*, vol. 103, no. 2, pp. 398–409, Apr. 1981.

[2.14] A. Pintz, R. Kasuba, J. L. Frater, and R. August, “Dynamic Effects of Internal Spur Gear Drives,” National Aeronautics and Space Administration, Scientific and Technical Information Branch, NASA Technical Report No. 3692, 1983.

[2.15] D. C. H. Yang and Z. S. Sun, “A Rotary Model for Spur Gear Dynamics,” *J. Mech. Transm. Autom. Des.*, vol. 107, no. 4, pp. 529–535, Dec. 1985.

[2.16] D. C. H. Yang and J. Y. Lin, “Hertzian Damping, Tooth Friction and Bending Elasticity in Gear Impact Dynamics,” *J. Mech. Des.*, vol. 109, no. 2, pp. 189–196, Jun. 1987.

[2.17] X. Tian, M. J. Zuo, and K. R. Fyfe, “Analysis of the Vibration Response of a Gearbox with Gear Tooth Faults,” in *2004 ASME International Mechanical Engineering Congress and Exposition*, Anaheim, California USA, 2004, pp. 785–793.

[2.18] Z. Chen and Y. Shao, "Dynamic Simulation of Spur Gear with Tooth Root Crack Propagating along Tooth Width and Crack Depth," *Eng. Fail. Anal.*, vol. 18, no. 8, pp. 2149–2164, Dec. 2011.

[2.19] A. Al-shyyab and A. Kahraman, "A Non-linear Dynamic Model for Planetary Gear Sets," *Proc. Inst. Mech. Eng. Part K J. Multi-Body Dyn.*, vol. 221, no. 4, pp. 567–576, Jan. 2007.

[2.20] W. Kim, J. Y. Lee, and J. Chung, "Dynamic Analysis for a Planetary Gear with Time-varying Pressure Angles and Contact Ratios," *J. Sound Vib.*, vol. 331, no. 4, pp. 883–901, Feb. 2012.

[2.21] R. G. Parker and J. Lin, "Mesh Phasing Relationships in Planetary and Epicyclic Gears," *J. Mech. Des.*, vol. 126, no. 2, pp. 365–370, May 2004.

[2.22] X. Tian, "Dynamic Simulation for System Response of Gearbox Including Localized Gear Faults," Master Thesis, University of Alberta, Canada, 2004.

[2.23] B. Xu, Y. Huang, X. Liu, and X. Sun, *Elasticity and Application*. Beijing: China Machine Press, 1983.

[2.24] A. Kahraman, "Load Sharing Characteristics of Planetary Transmissions," *Mech. Mach. Theory*, vol. 29, no. 8, pp. 1151–1165, Nov. 1994.

Chapter 3: Gear Tooth Crack Influence on the Mesh Stiffness of a Planetary Gear Set

In Chapter 2, the time-varying mesh stiffness of a healthy planetary gear set is evaluated using the potential energy method. However, tooth faults like crack and pitting may occur on gears. The gear mesh stiffness shape will change if a tooth fault appears and consequently the vibration properties of the gear system will change. In this chapter, the potential energy method used in Chapter 2 is improved and extended to evaluate the gear tooth crack effect on the time-varying mesh stiffness of a planetary gear set. The obtained time-varying stiffness in this chapter will be used in Chapter 4 to simulate the vibration signals of a planetary gearbox in the faulty condition. The fault symptoms found in Chapter 4 will be further processed in Chapter 5 to develop a fault detection method. This chapter is organized as follows. In Section 3.1, background of this research topic is described and a literature review is given on gear mesh stiffness evaluation, gear tooth crack modeling, and gear tooth crack effect on the gear mesh stiffness. In Section 3.2, an improved cantilever beam model is proposed for an external gear tooth and equations are derived for the mesh stiffness evaluation of an external gear pair. In Section 3.3, procedures of obtaining the time-varying mesh stiffness of an internal gear pair are described. In Section 3.4, procedures of obtaining the time-varying mesh stiffness of a planetary gear set are described. In Section 3.5, a tooth crack model is proposed and equations are derived to evaluate the time-varying mesh stiffness of a planet gear set with a tooth crack. In Section 3.6, the crack effect on the time-varying mesh stiffness of a planetary gear set is analyzed; three fault conditions are considered: crack in the sun gear, crack in a planet gear (sun gear side) and crack in a planet gear (ring gear side). In Section 3.7, conclusions are given. This chapter is based on a journal paper [3.1] and a refereed conference paper [3.2].

3.1 Introduction

When a pair of spur gear meshes, the tooth contact number and the tooth mesh position change during meshing. This leads to a periodic variation in the gear mesh stiffness. The mesh stiffness variation is one of the main sources of vibration in a gear transmission system [3.3]. Cracks may occur in gears due to excessive service load, inappropriate operating conditions or simply fatigue [3.4]. When a crack occurs, the gear mesh stiffness will be reduced resulting in changed vibration characteristics of a gear system. If the stiffness reduction can be quantified for different crack levels, the corresponding vibration signal can be obtained through dynamic simulation. The vibration signal can be processed further for crack diagnostics and prognostics. Both the finite element method (FEM) and the analytical method (AM) have been used to evaluate the gear mesh stiffness [3.4-3.6]. But, FEM is complicated and time consuming. While AM can offer a simple and also effective way to evaluate the time-varying mesh stiffness.

Many researchers have applied the analytical method to evaluate the mesh stiffness of a fixed-shaft external gear pair. Yang and Lin [3.7] proposed the potential energy method to evaluate the mesh stiffness of an external spur gear pair by considering Hertzian contact stiffness, bending stiffness and axial compressive stiffness. Later, Tian et al. [3.8] added another component called shear stiffness in the potential energy method. Recently, Zhou et al. [3.9] took the deformation of the gear body into consideration. The gear tooth was modeled as a cantilever beam which started from the base circle [3.7-3.9]. Also, Tian et al. [3.8], Zhou et al. [3.9], Pandya and Parey [3.10] and Wu et al. [3.11] considered that the gear crack follows a linear path starting from the point of intersection of the base circle and the involute curve as shown in Fig. 3.1. Actually, the gear tooth starts from the root circle rather than the base circle as given in Fig. 3.1. Thus, their models ignored the gear tooth part between the root circle and the base circle. The tooth profile of this part (tooth fillet area) is not an involute curve and it is basically determined by cutting tool tip trajectory. A different cutting tool tip trajectory will generate a different curve and there is not a uniform function to depict it [3.12]. However, the ignorance of this part will change the stiffness of the meshing gears, especially when the distance between the base circle and root circle is large. Chaari et al. [3.13] presented an analytical method to evaluate the mesh stiffness of an external gear pair and modeled the crack as a straight line starting from the root circle. They mentioned that the gear mesh stiffness can be evaluated by taking into account tooth thickness reduction. However, they did not provide the equations of the mesh stiffness for a crack gear. Chen and Shao [3.14] proposed an analytical mesh stiffness model with tooth root crack propagating along both the tooth width and the crack depth. Further, they [3.15] investigated the effect of tooth profile modification on the mesh stiffness. Their model is more realistic than other models.

To sum up, Refs. [3.13, 3.14] modeled the gear tooth crack starting from the tooth root, but they only gave the equations of the mesh stiffness for a gear tooth. In other words, they did not incorporate the gear meshing theory in their model. Ref. [3.8-3.11] incorporated the gear meshing theory in their model, but they modeled the gear tooth crack starting from the gear base circle. In this chapter, I will model the gear tooth crack starting from the tooth root and also incorporate the gear meshing theory in our equations. Finally, the mesh stiffness equations will be expressed as a function of gear rotation angle given gear geometry, material and tooth crack information (crack angle, crack length and crack position). Users can use these equations directly to evaluate gear mesh stiffness of gears with tooth crack even though they are not familiar with beam and gear meshing theories.

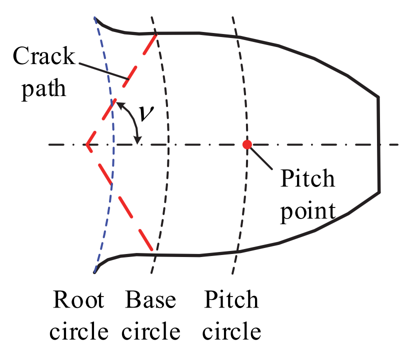

Fig. 3.1: Crack modeling from Refs. [3.8-3.11]

For a planetary gear set, there are pairs of sun-planet gears (external gear pairs) and pairs of ring-planet gears (internal gear pairs) meshing simultaneously. Chaari et al. [3.16] and Walha et al. [3.17] used a square waveform to approximate the time-varying mesh stiffness of a planetary gear set. In their method, the amplitudes of the sun-planet mesh stiffness and the ring-planet mesh stiffness were assumed without a specific qualification method. Besides, the square waveform reflects only the effect of the change in tooth contact number, but ignores the effect of the change in tooth contact position. Liang et al. [3.18] evaluated the mesh stiffness of a perfect planetary gear set using the potential energy method. They also treated the sun gear and the planet gear as a cantilever beam starting from the base circle. It is mentioned in [3.16] that the amplitude modulation can be used to obtain the mesh stiffness of a planetary gear set with crack. Fig. 3.2 illustrated the amplitude loss of 50% due to a crack in the sun gear. But, they modeled the stiffness reduction only in the double tooth contact duration while ignored the stiffness decrease in the single tooth contact duration. Also, physical meaning of this loss was not described, like how much crack propagation will lead to the amplitude loss by 50%. In this study, I propose an approach to overcome these shortcomings.

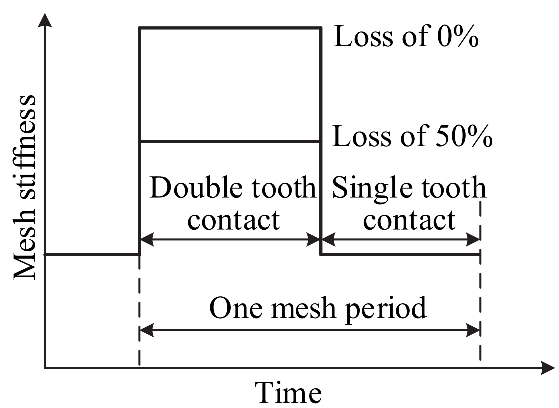

Fig. 3.2: Crack modeling in the sun gear [3.16]

In this chapter, the potential energy method is used to evaluate the crack effect on the time-varying mesh stiffness of a planetary gear set. To model an external gear, i.e. the sun gear and the planet gear, a modified beam model is proposed by considering the gear tooth starting from the root circle. Further, a crack propagation model is developed and the mesh stiffness equations are derived when a crack takes place in the sun gear or a planet gear. Examples are given to show the crack effect for three fault locations: crack in the sun gear, crack in a planet gear (sun side) and crack in a planet gear (ring side).

3.2 Mesh stiffness of a fixed-shaft external gear pair

In Chapter 2, I derived equations of the mesh stiffness of a perfect internal gear tooth. These equations are expressed as a function of gear angular displacement. For a perfect external gear tooth, I used the equations reported in [3.7-3.9] directly. In [3.7-3.9], they derived the equations of a perfect external gear tooth by considering the gear tooth starting from the base circle instead of the root circle.

In this section, I will derive equations of a perfect external gear tooth by considering the gear tooth starting from the *root* circle using the potential energy method. These equations will be expressed as a function of gear angular displacement. These equations are the improved versions of those reported in [3.7-3.9] as crack usually starts from the root circle rather than the base circle [3.19]. The differences of these two modeling methods on the mesh stiffness will be illustrated.

In the potential energy, Hertzian energy, bending energy, shear energy and axial compressive energy are considered. The new equations for the bending stiffness, shear stiffness and axial compressive stiffness will be derived. Hertzian stiffness equation remains the same. The overall mesh stiffness is represented as a function of the rotation angular displacement of the driven gear. In Refs. [3.9-3.11], the gear system is assumed to be perfect without friction and transmission error and the gear body is treated as solid. The same assumptions will be used in this chapter.

3.2.1 Bending, shear and axial compressive stiffness

For an external gear, the gear root circle may be bigger or smaller than the base circle according to the geometry of gears. If a gear is a standard spur gear with the pressure angle of 20 degrees, the root circle is bigger if the tooth number is more than 41. It is smaller if the tooth number is less than 41. In the industrial applications, both types of gears are commonly used. In this chapter, these two cases will be discussed separately.

Case 1: The gear root circle is smaller than the base circle

If the root circle is smaller than the base circle, the beam model of the gear tooth is shown in Fig. 3.3. Gear tooth profile follows involute curve up to the base circle (curves IN' and JD'). The tooth profile between the base circle and the root circle is not an involute curve and hard to describe analytically [3.12]. Therefore, straight lines NN' and DD' are used to simplify the curve.

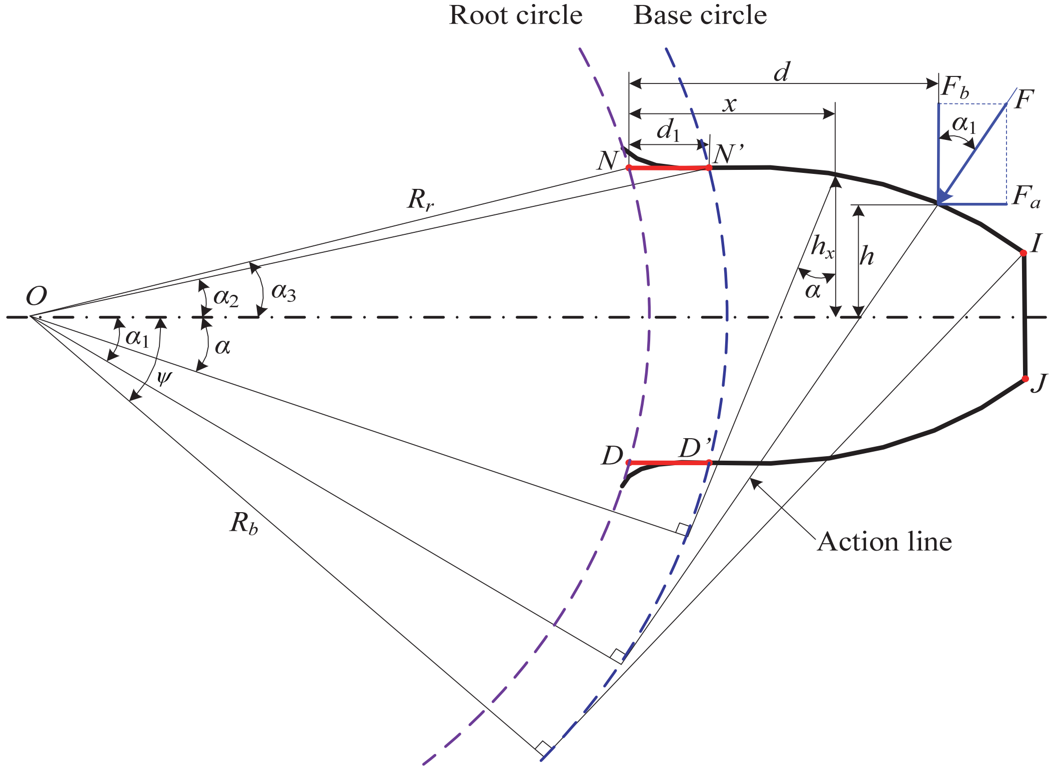

Fig. 3.3: Beam model of an external gear tooth with root circle smaller than base circle

According to the properties of involute curve, the action line of two meshing gears is always tangent to the gear base circle and normal to the tooth involute profile. The action force F which is along the action line, can be decomposed into two orthogonal forces F_a and F_b, as shown in Fig. 3.3.

$$F_a = F \sin \alpha_1 . \tag{3.2.1}$$

$$F_b = F \cos \alpha_1 . \tag{3.2.2}$$

Applying the beam theory, the bending, shear and axial compressive energies stored in a tooth can be expressed as follows [3.7, 3.8]:

$$U_b = \frac{F^2}{2k_b} = \int_0^d \frac{[F_b(d-x) - F_a h]^2}{2EI_x} dx , \tag{3.2.3}$$

$$U_s = \frac{F^2}{2k_s} = \int_0^d \frac{1.2F_b^{\ 2}}{2GA_x} dx, \tag{3.2.4}$$

$$U_a = \frac{F^2}{2k_a} = \int_0^d \frac{F_a^{\ 2}}{2EA_x} dx, \tag{3.2.5}$$

where k_b, k_s and k_a denote bending, shear and axial compressive stiffness, respectively, E and G represent Young's modulus and shear modulus, respectively, h shows the distance between the gear contact point and the tooth central line, d is the distance from the contact point to the gear root, A_x and I_x indicate the area and the area moment of inertia of the section where the distance to the tooth root is x (see Fig. 3.3).

According to the characteristics of involute curve, h, h_x, d, I_x and A_x can be expressed as follows:

$$h = R_b\left[\left(\alpha_1 + \alpha_2\right)\cos\alpha_1 - \sin\alpha_1\right], \tag{3.2.6}$$

$$h_x = \begin{cases} R_b \sin\alpha_2, & \text{if } 0 \le x \le d_1 \\ R_b\left[\left(\alpha + \alpha_2\right)\cos\alpha - \sin\alpha\right], & \text{if } d_1 < x \le d \end{cases}, \tag{3.2.7}$$

$$d = R_b\left[\left(\alpha_1 + \alpha_2\right)\sin\alpha_1 + \cos\alpha_1\right] - R_r \cos\alpha_3, \tag{3.2.8}$$

$$I_x = \frac{1}{12}(2h_x)^3 L = \frac{2}{3} h_x^{\ 3} L, \tag{3.2.9}$$

$$A_x = 2h_x L, \tag{3.2.10}$$

where R_b, R_r and L denote base circle radius, root circle radius and tooth width of the external gear, respectively, h_x is the height of the section where the distance to the tooth root is x, α_2 represents the half tooth angle on the base circle [3.19] while α_3 describes the approximated half tooth angle on the root circle (see Fig. 3.3).

$$\alpha_2 = \frac{\pi}{2N} + \tan\alpha_0 - \alpha_0 , \tag{3.2.11}$$

$$\alpha_3 = \arcsin(\frac{R_b \sin\alpha_2}{R_r}) , \tag{3.2.12}$$

where N is the tooth number of the external gear and α_0 is the pressure angle.

Substituting Eqs (3.2.1), (3.2.2) and (3.2.6) to (3.2.9) into Eq. (3.2.3), the bending stiffness of an external gear can be expressed as:

$$\begin{aligned} \frac{1}{k_b} = & \frac{\left[1 - \frac{(N-2.5)\cos\alpha_1 \cos\alpha_3}{N\cos\alpha_0}\right]^3 - (1-\cos\alpha_1 \cos\alpha_2)^3}{2EL\cos\alpha_1 \sin^3\alpha_2} \\ & + \int_{-\alpha_1}^{\alpha_2} \frac{3\left\{1 + \cos\alpha_1\left[(\alpha_2 - \alpha)\sin\alpha - \cos\alpha\right]\right\}^2 (\alpha_2 - \alpha)\cos\alpha}{2EL[\sin\alpha + (\alpha_2 - \alpha)\cos\alpha]^3} d\alpha \end{aligned} . \tag{3.2.13}$$

Substituting Eqs. (3.2.2), (3.2.7) and (3.2.10) into Eq. (3.2.5), the shear stiffness of an external gear is given as:

$$\begin{aligned} \frac{1}{k_s} = & \frac{1.2(1+\nu)\cos^2\alpha_1 \left(\cos\alpha_2 - \frac{N-2.5}{N\cos\alpha_0}\cos\alpha_3\right)}{EL\sin\alpha_2} \\ & + \int_{-\alpha_1}^{\alpha_2} \frac{1.2(1+\nu)(\alpha_2 - \alpha)\cos\alpha \cos^2\alpha_1}{EL[\sin\alpha + (\alpha_2 - \alpha)\cos\alpha]} d\alpha \end{aligned} . \tag{3.2.14}$$

Substituting Eqs. (3.2.1), (3.2.7) and (3.2.10) into Eq. (3.2.4), the axial compressive stiffness of an external gear can be obtained:

$$\begin{aligned} \frac{1}{k_a} = & \frac{\sin^2\alpha_1 \left(\cos\alpha_2 - \frac{N-2.5}{N\cos\alpha_0}\cos\alpha_3\right)}{2EL\sin\alpha_2} \\ & + \int_{-\alpha_1}^{\alpha_2} \frac{(\alpha_2 - \alpha)\cos\alpha \sin^2\alpha_1}{2EL[\sin\alpha + (\alpha_2 - \alpha)\cos\alpha]} d\alpha \end{aligned} . \tag{3.2.15}$$

Case 2: The gear root circle is bigger than the base circle

If the root circle is bigger than the base circle, the beam model of the gear tooth is considered starting from the root circle as shown in Fig. 3.4. The whole gear tooth profile (curves IN and JD) follows the involute curve. As compared to Case 1 when the root circle is smaller than the base circle, the expressions for the tooth effective length d and tooth section width h_x changes as follows:

$$d=R_b\left[\left(\alpha_1+\alpha_2\right)\sin\alpha_1+\cos\alpha_1\right]-R_r\cos\alpha_4\,, \tag{3.2.16}$$

$$h_x=R_b\left[\left(\alpha+\alpha_2\right)\cos\alpha-\sin\alpha\right], \tag{3.2.17}$$

where α_4 is the half tooth angle on the root circle of Case 2.

Applying the similar derivation procedures as Case 1, the bending, shear and axial compressive stiffness of Case 2 can be expressed as followings:

$$\frac{1}{k_b}=\int_{-\alpha_1}^{\alpha_5}\frac{3\left\{1+\cos\alpha_1\left[(\alpha_2-\alpha)\sin\alpha-\cos\alpha\right]\right\}^2(\alpha_2-\alpha)\cos\alpha}{2EL[\sin\alpha+(\alpha_2-\alpha)\cos\alpha]^3}d\alpha\,, \tag{3.2.18}$$

$$\frac{1}{k_s}=\int_{-\alpha_1}^{\alpha_5}\frac{1.2(1+\nu)(\alpha_2-\alpha)\cos\alpha\cos^2\alpha_1}{EL[\sin\alpha+(\alpha_2-\alpha)\cos\alpha]}d\alpha\,, \tag{3.2.19}$$

$$\frac{1}{k_a}=\int_{-\alpha_1}^{\alpha_5}\frac{(\alpha_2-\alpha)\cos\alpha\sin^2\alpha_1}{2EL[\sin\alpha+(\alpha_2-\alpha)\cos\alpha]}d\alpha\,. \tag{3.2.20}$$

The symbol α_5 represents the angle between the action force F and the decomposed force F_b when the distance between the meshing point and the root circle is 0. The value of α_5 can be obtained through the following equation set.

$$\begin{cases} R_r\sin\alpha_4=R_b\left[(\alpha_2-\alpha_5)\cos\alpha_5-\sin\alpha_5\right] \\ R_r\cos\alpha_4-R_b\cos\alpha_2=R_b\left[\cos\alpha_5-(\alpha_2-\alpha_5)\sin\alpha_5-\cos\alpha_5\right] \end{cases}. \tag{3.2.21}$$

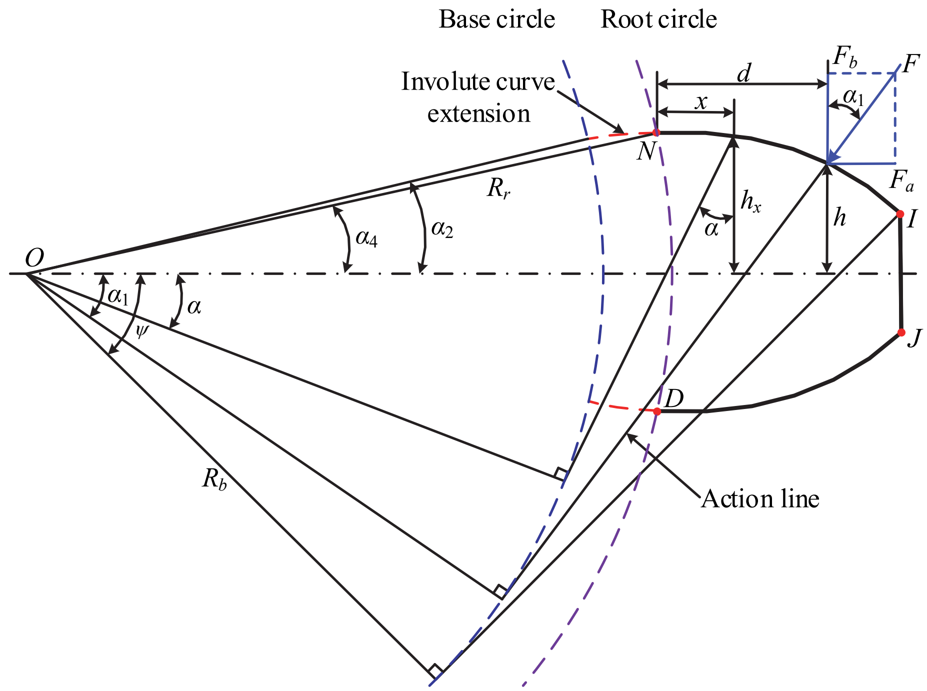

Fig. 3.4: Beam model for an external gear tooth with root circle bigger than base circle

3.2.2 Hertzian contact stiffness

From the result derived by Yang and Sun [3.20], the Hertzian contact stiffness k_h, for an external gear pair, is linearized to a constant along the entire line of action independent of both the position of contact and the depth of interpenetration.

$$k_h = \frac{\pi E L}{4(1-\nu^2)}, \tag{3.2.22}$$

where E, L, ν denote Yong's modulus, tooth width and Poisson's ratio, respectively.

3.2.3 Overall mesh stiffness of an external gear pair

For a pair of spur gears with contact ratio between 1 and 2, one pair and two pairs of tooth contact take place alternatively. For the single-tooth-pair meshing duration, the total effective mesh stiffness can be calculated as [3.8]:

$$k_t = \frac{1}{\frac{1}{k_h} + \frac{1}{k_{b1}} + \frac{1}{k_{s1}} + \frac{1}{k_{a1}} + \frac{1}{k_{b2}} + \frac{1}{k_{s2}} + \frac{1}{k_{a2}}}, \tag{3.2.23}$$

where subscripts 1 and 2 represent the driving gear and the driven gear, respectively.

For the double-tooth-pair meshing duration, there are two pairs of gears meshing at the same time. The total effective mesh stiffness can be obtained as [3.8]:

$$k_t = k_{t1} + k_{t2} = \sum_{i=1}^{2} \frac{1}{\frac{1}{k_{h,i}} + \frac{1}{k_{b1,i}} + \frac{1}{k_{s1,i}} + \frac{1}{k_{a1,i}} + \frac{1}{k_{b2.i}} + \frac{1}{k_{s2,i}} + \frac{1}{k_{a2,i}}}, \tag{3.2.24}$$

where $i = 1$ for the first pair and $i = 2$ for the second pair of meshing teeth.

Table 3.1 gives the parameters of a planetary gear set [3.18]. Suppose the parameters of the driving gear and the driven gear of an external gear pair are the same to the sun gear and the planet gear (see Table 3.1), respectively. The mesh stiffness of this external gear pair can be evaluated using the method developed in this chapter. The proposed model is compared with the model given in [3.8]. The results are shown in Fig. 3.5.

Table 3.1: Physical parameters of the planetary gear set for mesh stiffness evaluation

Parameters	Sun gear	Planet gear	Ring gear
Number of teeth	19	31	81
Module (mm)	3.2	3.2	3.2
Pressure angle	20^o	20^o	20^o
Face width (m)	0.0381	0.0381	0.0381
Young's modulus (Pa)	2.068×10^{11}	2.068×10^{11}	2.068×10^{11}
Poisson's ratio	0.3	0.3	0.3
Base circle radius	28.3	46.2	120.8
Root circle radius	26.2	45.2	132.6

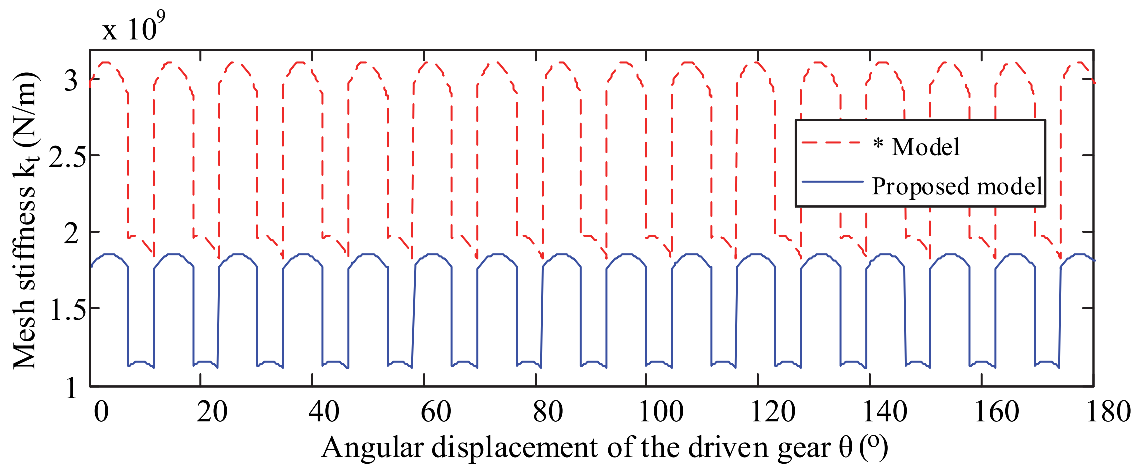

Fig. 3.5: Mesh stiffness of a fixed-shaft external gear pair
* Model from Tian et al. [3.8]

Fig. 3.5 illustrates the mesh stiffness (15.5 mesh periods) in half revolution of the driven gear. In [3.8], the gear tooth is considered starting from the base circle, while in this chapter it is modeled starting from the root circle. The difference in the radius of the base circle and the root circle is 2.1 mm (7.4% of the base circle radius) for the sun gear and 1 mm (2.2% of the base circle radius) for the planet gear as given in Table 3.1. It is found that the mesh stiffness decreases about 40%, if the gear tooth is considered starting from the root circle. This demonstrates that substantial difference in the mesh stiffness of an external gear pair is likely when the origin of the gear tooth is changed from the base circle to the root circle, especially when the difference between the base circle and the root circle is large. It is important to consider this difference because the dynamic response of the gear system will be affected due to the stiffness change.

3.3 Mesh stiffness of a fixed-shaft internal gear pair

In this section, the procedures to obtain the mesh stiffness of a fixed-shaft internal gear pair are presented. These procedures will be used later in the mesh stiffness evaluation of ring-planet gears of a planetary gear set. An internal gear pair includes two types of gears, namely an external gear and an internal gear. For an external gear, the root circle may be bigger or smaller than the base circle. However, for an internal gear, the root circle is always bigger than the base circle. Liang et al. [3.18] derived equations of the mesh stiffness for an internal gear pair. But, they modeled the external gear tooth starting from the base circle. In this study, I will improve the results of Liang et al. [3.18] by modeling the gear tooth starting from the tooth root circle. The stiffness equations of the external gear are derived in Section 3.2. For the internal gear, the equations of bending, shear, and axial compressive stiffness reported in [3.18] will be used directly here. Thus, the difference of the mesh stiffness for an internal gear pair between our model and the model from [3.18] comes from the difference in the modeling of the external gear teeth.

I evaluate the mesh stiffness of a fixed-shaft internal gear pair of which the external gear and the internal gear have the same parameters as the planet gear and the ring gear (listed in Table 3.1), respectively. The overall mesh stiffness is shown in Fig. 3.6. The comparison with Liang et al. [3.18] is also presented in Fig. 3.6.

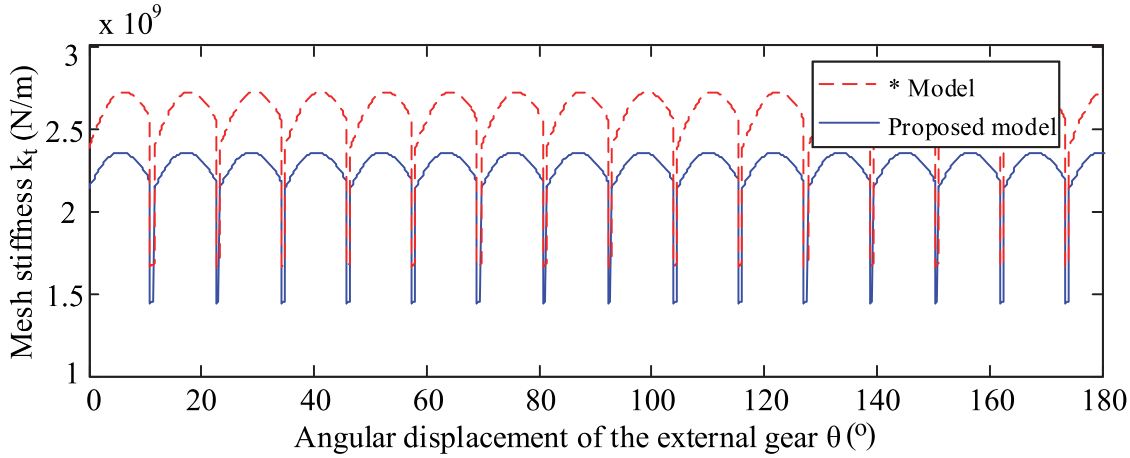

Fig. 3.6: Mesh stiffness of a fixed-shaft internal gear pair
* Model from Liang et al. [3.18]

It can be seen that even the radius difference of the base circle and the root circle is only 1 mm for the planet gear; the mesh stiffness decreased about 17% in the double-tooth-pair meshing duration and about 23% in the single-tooth-pair meshing duration. This percentage change is smaller than that of an external gear pair because the same stiffness equations are used for the internal gear in these two models. Though relatively small, this result indicates the importance of modeling the gear tooth of the external gear starting from the root circle as it is more realistic.

3.4 Mesh stiffness of a planetary gear set

Fig. 3.7 shows the structure of a planetary gear set which will be considered in this study. It is comprised of a sun gear (*s*), a ring gear (*r*) and four equally-spaced planets (*p*) which are held by a common carrier (*c*). In this structure, the ring gear is fixed. The parameters of this planetary gear set are listed in Table 3.1.

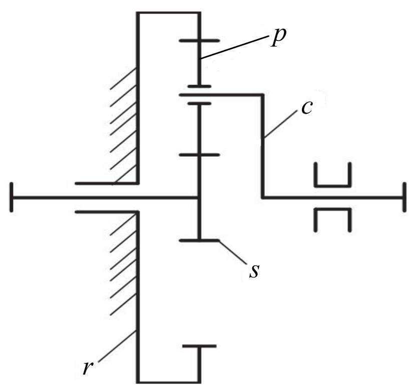

Fig. 3.7: Structure of a planetary gear set with the ring gear fixed

A planetary gear set comprises several pairs of sun-planet gears (external gear pairs) and ring-planet gears (internal gear pairs) meshing simultaneously. While each of the sun-planet meshes (or ring-planet meshes) has the same shape of mesh stiffness variation, they are not in phase with each other [3.21]. The phasing relationships of multiple meshing gears must be considered. The mesh phasing of the planetary gear set were calculated in [3.18] and shown in Table 2.2 of Chapter 2. The value of γ_{sn} (n = 1, 2, 3, 4) is the relative phase between the n^{th} sun-planet pair with respect to the 1^{st} sun-planet pair. The value of γ_{rn} is the relative phase between the n^{th} ring-planet pair with respect to the 1^{st} ring-planet pair. The value of γ_{rs} is the relative phase between the n^{th} ring-planet mesh with respect to the n^{th} sun-planet mesh. The $\gamma_{rs} = 0$ shows that the sun-planet gears and the ring-planet gears mesh at the pitch point simultaneously [3.18].

Once the mesh stiffness equations for a fixed-shaft external gear pair and a fixed-shaft internal gear pair are derived, the mesh stiffness of a planetary gear set can be obtained using the approach reported in [3.18]. The time-varying mesh stiffness of the planetary gear set is plotted in Fig. 3.8.

There are 12.56 times of gear meshing in half revolution of the planet gear. The point P' and P denote the pitch points of one sun-planet gear pair and one ring-planet gear pair, respectively. It can be seen from Fig. 3.8 that both the sun-planet pair and the ring-planet pair mesh at the pitch point at t = 0. The curves k_{sp1} , k_{sp2} , k_{sp3} and k_{sp4} represent the 1st, 2nd, 3rd and 4th pairs of the sun-planet mesh stiffness, respectively. Similarly, the curves k_{rp1} k_{rp2} , k_{rp3} and k_{rp4} denote the 1st, 2nd, 3rd and 4th pairs of the ring-planet mesh stiffness, respectively. The symbol θ_m is the rotation angular displacement of the planet gear in one mesh period, $\theta_m = 2\pi Z_r / Z_p / (Z_s + Z_r)$ [3.18]. Z_s, Z_p, and Z_r are the tooth number of the sun gear, planet gear and ring gear, respectively.

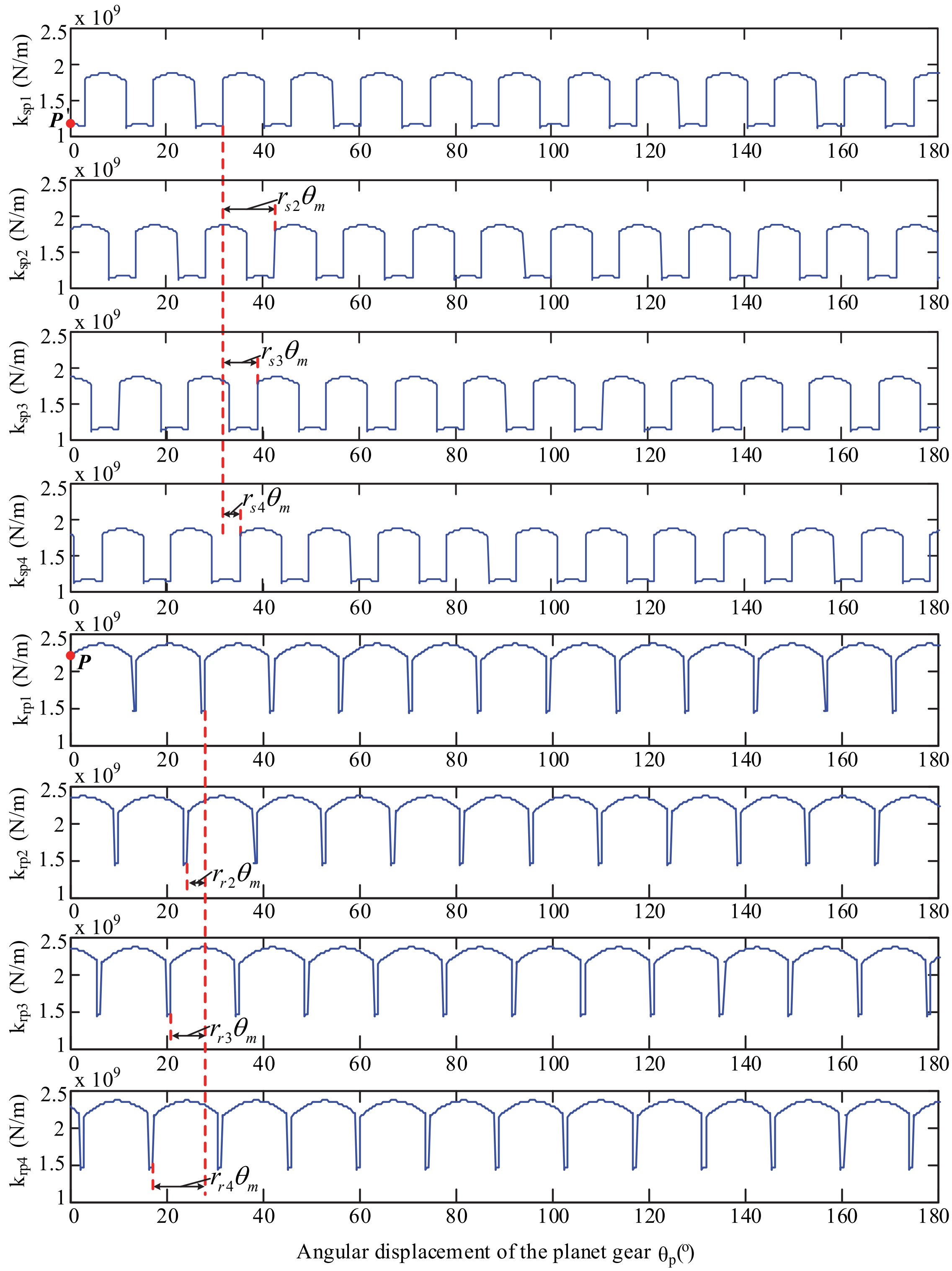

Fig. 3.8: Improved mesh stiffness of a planetary gear set when the ring gear is fixed

3.5 Crack modeling of the external gear

Lewichi [3.22] found that several factors such as rim and web thicknesses, initial crack location and backup ratio (rim thickness divided by tooth height) decided the gear crack propagation. Belsak and Flasker [3.23] investigated the propagation path of the crack both experimentally and computationally. The results (see Fig. 3.9) indicated that the crack propagation paths were smooth, continuous, and in most cases, rather straight with only a slight curvature; similar to the findings in [3.22]. It is pointed out by both Kramberger et al. [3.24] and Belsak and Flasker [3.23] that the crack mostly initiated at the point of the maximum principal stress in the tensile side of a gear tooth (critical area in Fig. 3.9).

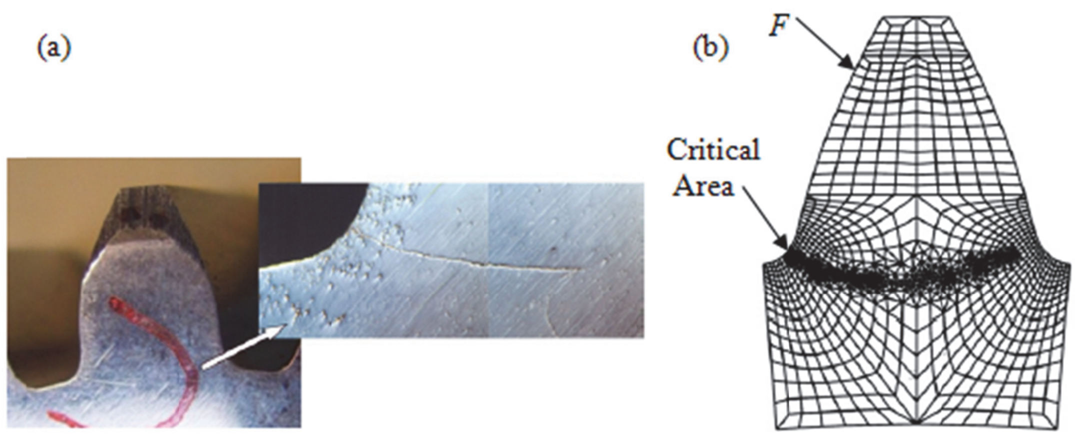

Fig. 3.9: Gear crack propagation path [3.23] (a) experiment and (b) finite element method

In the analytical modeling of gear tooth crack, straight lines were used to approximate the tooth crack curve in [3.8, 3.11, 3.15]. In this section, the same idea is used. The tooth crack is modeled as a straight line starting from the critical area of the tooth and two cases will be analyzed. The first case is when the gear root circle is smaller than the base circle and the second case is when the root circle is bigger than the base circle. When the crack happens, the gear mesh stiffness reduction is modeled by taking into account the thickness reduction of the tooth section and the effective length changing of the beam model.

Case 1: The gear root circle is smaller than the base circle

The point M (see Fig. 3.10), located within the critical area of the tooth, is considered as the starting point of the crack. The crack is modeled as a straight line which passes through point N which is the intersection of the straight line NN' and the root circle. The crack propagates along the straight line until reaching the tooth central line at point B. Then, it changes the propagation direction towards point D where the tooth breaks. The line segment MN can be interpreted as an initial notch which stimulates higher stress concentration which then leads to fully developed crack. It is similar to what Lewicki et al. [3.25] described as an initial notch in his crack experiment. This notch will not be considered in the mesh stiffness derivation in this chapter. The fillet curve is difficult to express analytically [3.12], therefore, in the proposed beam model, I simplify it and represent it using a straight line NN' as shown in Fig. 3.10. The angle between the crack line and the tooth central line is defined as υ. Though I have modeled that the crack gradually grows until it reaches the breaking point D, sometimes, sudden tooth breakage may also take place especially when the crack goes over the central line.

Similar to the perfect situation, the overall mesh stiffness is considered as the summation of Hertzian stiffness, bending stiffness, shear stiffness and axial compressive stiffness. The Hertzian stiffness and the axial compressive stiffness will not be affected by the crack propagation [3.8, 3.11]. Only the bending stiffness and the shear stifness will be affected due to the change in the tooth length and the tooth height caused by the crack. In order to derive the bending and shear stiffness with the propagation of the crack, we need to consider four conditions. Condition 1 and condition 2 may happen when the crack is below the tooth central line. Condition 3 and condition 4 may happen when the crack goes over the tooth central line.

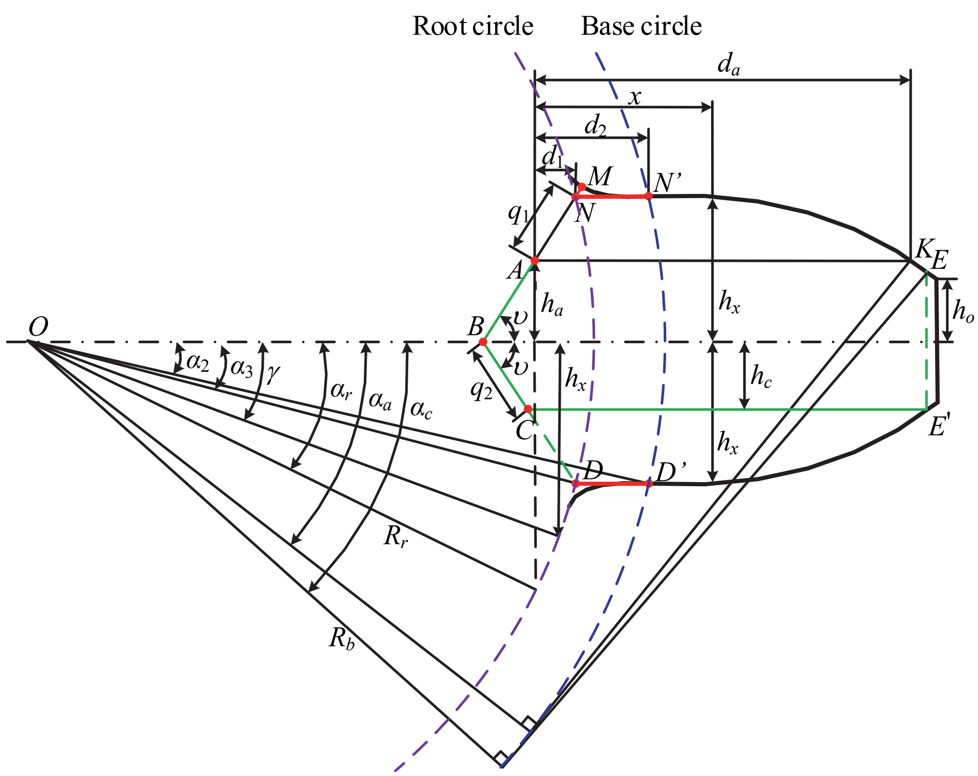

Fig. 3.10: Cracked tooth model when root circle is smaller than base circle

Condition 1: *When* $h_a \geq h_o$ & $\alpha_1 > \alpha_a$

The symbol h_a represents the distance from the crack end point A to the tooth central line when the crack has not reached the tooth central line. Half of the roof chordal tooth thickness is denoted by h_o. The angle α_a corresponds to the force action point K (see Fig. 3.10). For a tooth with crack, the tooth section area and the area moment of inertia can be expressed as follows:

$$A_x = \begin{cases} (h_a + h_x)L & \text{if } x \le d_a \\ 2h_x L & \text{if } x > d_a \end{cases}, \tag{3.5.1}$$

$$I_x = \begin{cases} \frac{1}{12}(h_a + h_x)^3 L & \text{if } x \le d_a \\ \frac{1}{12}(2h_x)^3 L & \text{if } x > d_a \end{cases}, \tag{3.5.2}$$

where h_a and h_x have the following expressions:

$$h_a = R_b \sin\alpha_2 - q_1 \sin\upsilon, \tag{3.5.3}$$

$$h_x = \begin{cases} R_r \sin\gamma, & \text{if } 0 \le x \le d_1 \\ R_b \sin\alpha_2, & \text{if } \mathrm{d}_1 \le x \le d_2 \\ R_b\left[(\alpha + \alpha_2)\cos\alpha - \sin\alpha\right], & \text{if } d_2 < x \le d \end{cases}. \tag{3.5.4}$$

Substituting Eq. (3.5.2) into Eq. (3.2.3) and substituting Eq. (3.5.1) into Eq. (3.2.4), the bending and the shear stiffness of a cracked tooth can be obtained respectively:

$$\frac{1}{k_b} = \int_{\alpha_3}^{\alpha_r} \frac{12\sin\alpha\left[\frac{N\cos\alpha_0}{N-2.5} - \left(\cos\alpha + \cos\alpha_3 - \cos\alpha_r - \frac{q_1}{R_r}\cos\upsilon\right)\cos\alpha_1\right]}{EL\left(\sin\alpha_3 + \sin\alpha - \frac{q_1}{R_r}\sin\upsilon\right)^3} d\alpha$$

$$+\frac{4\left[1-\frac{(N-2.5)\cos\alpha_1\cos\alpha_3}{N\cos\alpha_0}\right]^3-4(1-\cos\alpha_1\cos\alpha_2)^3}{EL\cos\alpha_1\left(2\sin\alpha_2-\frac{q_1}{R_b}\sin\upsilon\right)^3}$$

$$+\int_{-\alpha_g}^{\alpha_2}\frac{12\left\{1+\cos\alpha_1\left[(\alpha_2-\alpha)\sin\alpha-\cos\alpha\right]\right\}^2(\alpha_2-\alpha)\cos\alpha}{EL\left[\sin\alpha_2-\frac{q_1}{R_b}\sin\upsilon+\sin\alpha+(\alpha_2-\alpha)\cos\alpha\right]^3}d\alpha\,, \tag{3.5.5}$$

$$+\int_{-\alpha_1}^{-\alpha_g}\frac{3\left\{1+\cos\alpha_1\left[(\alpha_2-\alpha)\sin\alpha-\cos\alpha\right]\right\}^2(\alpha_2-\alpha)\cos\alpha}{2EL[\sin\alpha+(\alpha_2-\alpha)\cos\alpha]^3}d\alpha$$

$$\frac{1}{k_s}=\int_{\alpha_3}^{\alpha_r}\frac{2.4(1+\nu)\cos^2\alpha_1\sin\alpha}{EL\left(\sin\alpha_3-\frac{q_1}{R_r}\sin\upsilon+\sin\alpha\right)^3}d\alpha+\frac{2.4(1+\nu)\cos^2\alpha_1(\cos\alpha_2-\frac{N-2.5}{N\cos\alpha_0}\cos\alpha_3)}{EL(2\sin\alpha_2-\frac{q_1}{R_b}\sin\upsilon)}$$

$$+\int_{-\alpha_g}^{\alpha_2}\frac{2.4(1+\nu)(\alpha_2-\alpha)\cos\alpha\cos^2\alpha_1}{EL\left[\sin\alpha_2-\frac{q_1}{R_b}\sin\upsilon+\sin\alpha+(\alpha_2-\alpha)\cos\alpha\right]}d\alpha\,, \tag{3.5.6}$$

$$+\int_{-\alpha_1}^{-\alpha_g}\frac{1.2(1+\nu)(\alpha_2-\alpha)\cos\alpha\cos^2\alpha_1}{EL[\sin\alpha+(\alpha_2-\alpha)\cos\alpha]}d\alpha$$

Condition 2: *When* $h_a < h_o$ *or when* $h_a \geq h_o$ & $\alpha_1 \leq \alpha_a$

In this condition, the expressions of the tooth section area and the area moment of inertia are as follows:

$$I_x=\frac{1}{12}(h_a+h_x)^3L\,, \tag{3.5.7}$$

$$A_x=(h_a+h_x)L\,. \tag{3.5.8}$$

Similar to Condition 1, the bending and the shear stiffness of the cracked tooth are obtained:

$$\frac{1}{k_b}=\int_{\alpha_3}^{\alpha_r}\frac{12\sin\alpha\left[\frac{N\cos\alpha_0}{N-2.5}-\left(\cos\alpha+\cos\alpha_3-\cos\alpha_r-\frac{q_1}{R_r}\cos\upsilon\right)\cos\alpha_1\right]}{EL\left(\sin\alpha_3+\sin\alpha-\frac{q_1}{R_r}\sin\upsilon\right)^3}d\alpha$$

$$+\frac{4\left[1-\frac{(N-2.5)\cos\alpha_1\cos\alpha_3}{N\cos\alpha_0}\right]^3-4(1-\cos\alpha_1\cos\alpha_2)^3}{EL\cos\alpha_1\left(2\sin\alpha_2-\frac{q_1}{R_b}\sin\upsilon\right)^3}$$

$$+\int_{-\alpha_1}^{\alpha_2}\frac{12\left\{1+\cos\alpha_1\left[(\alpha_2-\alpha)\sin\alpha-\cos\alpha\right]\right\}^2(\alpha_2-\alpha)\cos\alpha}{EL\left[\sin\alpha_2-\frac{q_1}{R_b}\sin\upsilon+\sin\alpha+(\alpha_2-\alpha)\cos\alpha\right]^3}d\alpha, \tag{3.5.9}$$

$$\frac{1}{k_s}=\int_{\alpha_3}^{\alpha_r}\frac{2.4(1+\nu)\cos^2\alpha_1\sin\alpha}{EL\left(\sin\alpha_3-\frac{q_1}{R_r}\sin\upsilon+\sin\alpha\right)^3}d\alpha+\frac{2.4(1+\nu)\cos^2\alpha_1(\cos\alpha_2-\frac{N-2.5}{N\cos\alpha_0}\cos\alpha_3)}{EL(2\sin\alpha_2-\frac{q_1}{R_b}\sin\upsilon)}$$

$$+\int_{-\alpha_1}^{\alpha_2}\frac{2.4(1+\nu)(\alpha_2-\alpha)\cos\alpha\cos^2\alpha_1}{EL\left[\sin\alpha_2-\frac{q_1}{R_b}\sin\upsilon+\sin\alpha+(\alpha_2-\alpha)\cos\alpha\right]}d\alpha. \tag{3.5.10}$$

Condition 3: *When* $h_c<h_o$ *or when* $h_c\ge h_o$ & $\alpha_1\le\alpha_c$

The angle α_c corresponds to the force action point E which is the mirror of the point E'. The point E' is relative to the crack point C in the Fig. 3.10. The tooth section area and the area moment of inertia are given by:

$$I_x=\frac{1}{12}(h_x-h_c)^3L, \tag{3.5.11}$$

$$A_x=(h_x-h_c)L, \tag{3.5.12}$$

where $h_c=q_2\sin\upsilon$.

The bending and the shear stiffness of the cracked tooth are derived as:

$$\frac{1}{k_b}=\int_{\alpha_3}^{\alpha_r}\frac{12\sin\alpha\left[\frac{N\cos\alpha_0}{N-2.5}-\left(\cos\alpha+\cos\alpha_3-\cos\alpha_r-\left(\frac{\sin\alpha_3}{\sin\upsilon}-\frac{q_2}{R_r}\right)\cos\upsilon\right)\cos\alpha_1\right]}{EL\left(\sin\alpha-\frac{q_2}{R_r}\sin\upsilon\right)^3}d\alpha$$

$$+\frac{4\left[1-\frac{(N-2.5)\cos\alpha_1\cos\alpha_3}{N\cos\alpha_0}\right]^3-4(1-\cos\alpha_1\cos\alpha_2)^3}{EL\cos\alpha_1\left(\sin\alpha_2-\frac{q_2}{R_b}\sin\upsilon\right)^3}, \tag{3.5.13}$$

$$+\int_{-\alpha_1}^{\alpha_2}\frac{12\left\{1+\cos\alpha_1\left[(\alpha_2-\alpha)\sin\alpha-\cos\alpha\right]\right\}^2(\alpha_2-\alpha)\cos\alpha}{EL\left[\sin\alpha+(\alpha_2-\alpha)\cos\alpha-\frac{q_2}{R_b}\sin\upsilon\right]^3}d\alpha$$

$$\frac{1}{k_s}=\int_{\alpha_3}^{\alpha_r}\frac{2.4(1+\nu)\cos^2\alpha_1\sin\alpha}{EL\left(\sin\alpha-\frac{q_2}{R_r}\sin\upsilon\right)^3}d\alpha+\frac{2.4(1+\nu)\cos^2\alpha_1(\cos\alpha_2-\frac{N-2.5}{N\cos\alpha_0}\cos\alpha_3)}{EL(\sin\alpha_2-\frac{q_2}{R_b}\sin\upsilon)}$$

$$+\int_{-\alpha_1}^{\alpha_2}\frac{2.4(1+\nu)(\alpha_2-\alpha)\cos\alpha\cos^2\alpha_1}{EL\left[\sin\alpha+(\alpha_2-\alpha)\cos\alpha-\frac{q_2}{R_b}\sin\upsilon\right]}d\alpha\,. \tag{3.5.14}$$

Condition 4: *When* $h_c \geq h_o$ & $\alpha_1 > \alpha_c$

In this condition, the tooth is considered as the constitution of the tooth sections whose height h_x are bigger than h_c [3.11]. If the section height h_x is smaller than h_c, the corresponding tooth part can be ignored. If the section height h_x is bigger than h_c, the expressions of the tooth section area and the area moment of inertia are the same in Eq.

(3.5.11) and Eq. (3.5.12). The bending and the shear stiffness of the cracked tooth are expressed as follows:

$$\frac{1}{k_b}=\int_{\alpha_3}^{\alpha_r}\frac{12\sin\alpha\left[\frac{N\cos\alpha_0}{N-2.5}-\left(\cos\alpha+\cos\alpha_3-\cos\alpha_r-\left(\frac{\sin\alpha_3}{\sin\upsilon}-\frac{q_2}{R_r}\right)\cos\upsilon\right)\cos\alpha_1\right]}{EL\left(\sin\alpha-\frac{q_2}{R_r}\sin\upsilon\right)^3}d\alpha$$

$$+\frac{4\left[1-\frac{(N-2.5)\cos\alpha_1\cos\alpha_3}{N\cos\alpha_0}\right]^3-4(1-\cos\alpha_1\cos\alpha_2)^3}{EL\cos\alpha_1\left(\sin\alpha_2-\frac{q_2}{R_b}\sin\upsilon\right)^3}$$

$$+\int_{-\alpha_c}^{\alpha_2}\frac{12\left\{1+\cos\alpha_1\left[(\alpha_2-\alpha)\sin\alpha-\cos\alpha\right]\right\}^2(\alpha_2-\alpha)\cos\alpha}{EL\left[\sin\alpha+(\alpha_2-\alpha)\cos\alpha-\frac{q_2}{R_b}\sin\upsilon\right]^3}d\alpha\,, \tag{3.5.15}$$

$$\frac{1}{k_s}=\int_{\alpha_3}^{\alpha_r}\frac{2.4(1+\nu)\cos^2\alpha_1\sin\alpha}{EL\left(\sin\alpha-\frac{q_2}{R_r}\sin\upsilon\right)^3}da+\frac{2.4(1+\nu)\cos^2\alpha_1(\cos\alpha_2-\frac{N-2.5}{N\cos\alpha_0}\cos\alpha_3)}{EL(\sin\alpha_2-\frac{q_2}{R_b}\sin\upsilon)}$$

$$+\int_{-\alpha_c}^{\alpha_2}\frac{2.4(1+\nu)(\alpha_2-\alpha)\cos\alpha\cos^2\alpha_1}{EL\left[\sin\alpha+(\alpha_2-\alpha)\cos\alpha-\frac{q_2}{R_b}\sin\upsilon\right]}d\alpha\,. \tag{3.5.16}$$

Case 2: The gear root circle is bigger than the base circle

Fig. 3.11 shows the tooth crack model when the root circle is bigger than the base circle. The crack is modeled as a straight line starting from the intersection (point M) of the involute curve and the root circle. The point M is within the critical area of the gear tooth.

Similar to Case 1, four conditions are considered in the derivation of bending and shear stiffness. In each condition, the expressions of the tooth section area and the area moment of inertia are the same as derived for the condition when the root circle is smallar than the base circle. But, the expression of the tooth height, h_x, changes as:

$$h_x = \begin{cases} R_r \sin\gamma, & \text{if } 0 \le x \le d_1 \\ R_b\left[\left(\alpha+\alpha_2\right)\cos\alpha - \sin\alpha\right], & \text{if } d_1 < x \le d \end{cases}. \tag{3.5.17}$$

Applying the same procedure as stated in Case 1, the bending stiffness k_b, and the shear stiffness k_s for the four cinditioins are derived and listed as follows:

Condition 1: *When* $h_a \ge h_o$ & $\alpha_1 > \alpha_a$

$$\begin{aligned} \frac{1}{k_b} = & \int_{\alpha_3}^{\alpha_r} \frac{12\sin\alpha\left[\dfrac{N\cos\alpha_0}{N-2.5} - \left(\cos\alpha + \cos\alpha_4 - \cos\alpha_r - \dfrac{q_1}{R_r}\cos\upsilon\right)\cos\alpha_1\right]}{EL\left(\sin\alpha_4 + \sin\alpha - \dfrac{q_1}{R_r}\sin\upsilon\right)^3} d\alpha \\ & + \int_{-\alpha_g}^{\alpha_5} \frac{12\left\{1+\cos\alpha_1\left[(\alpha_2-\alpha)\sin\alpha - \cos\alpha\right]\right\}^2(\alpha_2-\alpha)\cos\alpha}{EL\left[\sin\alpha_2 - \dfrac{q_1}{R_b}\sin\upsilon + \sin\alpha + (\alpha_2-\alpha)\cos\alpha\right]^3} d\alpha \\ & + \int_{-\alpha_1}^{-\alpha_g} \frac{3\left\{1+\cos\alpha_1\left[(\alpha_2-\alpha)\sin\alpha - \cos\alpha\right]\right\}^2(\alpha_2-\alpha)\cos\alpha}{2EL[\sin\alpha + (\alpha_2-\alpha)\cos\alpha]^3} d\alpha \end{aligned}, \tag{3.5.18}$$

$$\begin{aligned} \frac{1}{k_s} = & \int_{\alpha_3}^{\alpha_r} \frac{2.4(1+\nu)\cos^2\alpha_1\sin\alpha}{EL\left(\sin\alpha_4 + \sin\alpha - \dfrac{q_1}{R_r}\sin\upsilon\right)^3} d\alpha + \int_{-\alpha_1}^{-\alpha_g} \frac{1.2(1+\nu)(\alpha_2-\alpha)\cos\alpha\cos^2\alpha_1}{EL[\sin\alpha + (\alpha_2-\alpha)\cos\alpha]} d\alpha \\ & + \int_{-\alpha_g}^{\alpha_5} \frac{2.4(1+\nu)(\alpha_2-\alpha)\cos\alpha\cos^2\alpha_1}{EL\left[\sin\alpha_2 - \dfrac{q_1}{R_b}\sin\upsilon + \sin\alpha + (\alpha_2-\alpha)\cos\alpha\right]} d\alpha . \end{aligned} \tag{3.5.19}$$

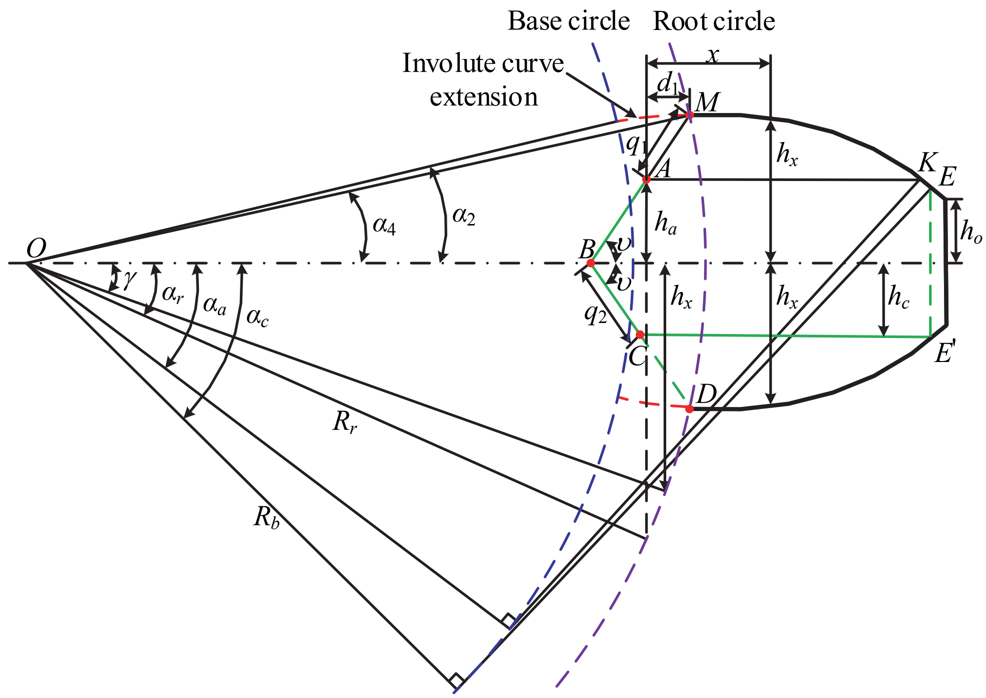

Fig. 3.11: Cracked tooth model when root circle is bigger than base circle

Condition 2: *When* $h_a < h_o$ *or when* $h_a \geq h_o$ & $\alpha_1 \leq \alpha_a$

$$\frac{1}{k_b} = \int_{\alpha_3}^{\alpha_r} \frac{12\sin\alpha\left[\dfrac{N\cos\alpha_0}{N-2.5} - \left(\cos\alpha + \cos\alpha_4 - \cos\alpha_r - \dfrac{q_1}{R_r}\cos\upsilon\right)\cos\alpha_1\right]}{EL\left(\sin\alpha_4 + \sin\alpha - \dfrac{q_1}{R_r}\sin\upsilon\right)^3} d\alpha$$

$$+\int_{-\alpha_1}^{\alpha_5} \frac{12\left\{1+\cos\alpha_1\left[(\alpha_2-\alpha)\sin\alpha - \cos\alpha\right]\right\}^2(\alpha_2-\alpha)\cos\alpha}{EL\left[\sin\alpha_2 - \dfrac{q_1}{R_b}\sin\upsilon + \sin\alpha + (\alpha_2-\alpha)\cos\alpha\right]^3} d\alpha\,. \qquad (3.5.20)$$

$$\frac{1}{k_s}=\int_{\alpha_3}^{\alpha_r}\frac{2.4(1+\nu)\cos^2\alpha_1\sin\alpha}{EL\left(\sin\alpha_4+\sin\alpha-\frac{q_1}{R_r}\sin\upsilon\right)^3}d\alpha + \int_{-\alpha_1}^{\alpha_5}\frac{2.4(1+\nu)(\alpha_2-\alpha)\cos\alpha\cos^2\alpha_1}{EL\left[\sin\alpha_2-\frac{q_1}{R_b}\sin\upsilon+\sin\alpha+(\alpha_2-\alpha)\cos\alpha\right]}d\alpha \quad (3.5.21)$$

Condition 3: *When* $h_c < h_o$ *or when* $h_c \geq h_o$ & $\alpha_1 \leq \alpha_c$

$$\frac{1}{k_b}=\int_{\alpha_3}^{\alpha_r}\frac{12\sin\alpha\left[\frac{N\cos\alpha_0}{N-2.5}-\left(\cos\alpha+\cos\alpha_4-\cos\alpha_r-\left(\frac{\sin\alpha_4}{\sin\upsilon}-\frac{q_2}{R_r}\right)\cos\upsilon\right)\cos\alpha_1\right]}{EL\left(\sin\alpha-\frac{q_2}{R_r}\sin\upsilon\right)^3}d\alpha$$

$$+\int_{-\alpha_1}^{\alpha_5}\frac{12\left\{1+\cos\alpha_1\left[(\alpha_2-\alpha)\sin\alpha-\cos\alpha\right]\right\}^2(\alpha_2-\alpha)\cos\alpha}{EL\left[\sin\alpha+(\alpha_2-\alpha)\cos\alpha-\frac{q_2}{R_b}\sin\upsilon\right]^3}d\alpha\,. \quad (3.5.22)$$

$$\frac{1}{k_s}=\int_{\alpha_3}^{\alpha_r}\frac{2.4(1+\nu)\cos^2\alpha_1\sin\alpha}{EL\left(\sin\alpha-\frac{q_2}{R_r}\sin\upsilon\right)^3}d\alpha + \int_{-\alpha_1}^{\alpha_5}\frac{2.4(1+\nu)(\alpha_2-\alpha)\cos\alpha\cos^2\alpha_1}{EL\left[\sin\alpha+(\alpha_2-\alpha)\cos\alpha-\frac{q_2}{R_b}\sin\upsilon\right]}d\alpha \quad (3.5.23)$$

Condition 4: *When* $h_c \geq h_o$ & $\alpha_1 > \alpha_c$

$$\frac{1}{k_b}=\int_{\alpha_3}^{\alpha_r}\frac{12\sin\alpha\left[\frac{N\cos\alpha_0}{N-2.5}-\left(\cos\alpha+\cos\alpha_4-\cos\alpha_r-\left(\frac{\sin\alpha_4}{\sin\upsilon}-\frac{q_2}{R_r}\right)\cos\upsilon\right)\cos\alpha_1\right]}{EL\left(\sin\alpha-\frac{q_2}{R_r}\sin\upsilon\right)^3}d\alpha$$

$$+\int_{-\alpha_c}^{\alpha_5} \frac{12\left\{1+\cos\alpha_1\left[(\alpha_2-\alpha)\sin\alpha-\cos\alpha\right]\right\}^2(\alpha_2-\alpha)\cos\alpha}{EL\left[\sin\alpha+(\alpha_2-\alpha)\cos\alpha-\frac{q_2}{R_b}\sin\upsilon\right]^3}d\alpha\,. \tag{3.5.24}$$

$$\frac{1}{k_s}=\int_{\alpha_3}^{\alpha_r}\frac{2.4(1+\nu)\cos^2\alpha_1\sin\alpha}{EL\left(\sin\alpha-\frac{q_2}{R_r}\sin\upsilon\right)^3}d\alpha + \int_{-\alpha_c}^{\alpha_5}\frac{2.4(1+\nu)(\alpha_2-\alpha)\cos\alpha\cos^2\alpha_1}{EL\left[\sin\alpha+(\alpha_2-\alpha)\cos\alpha-\frac{q_2}{R_b}\sin\upsilon\right]}d\alpha\,. \tag{3.5.25}$$

3.6 Crack effect on the mesh stiffness of a planetary gear set

In this section, the crack effect on the mesh stiffness of a planetary gear set (see Fig. 3.7) is investigated when a crack takes place in the sun gear or a planet gear. Two cases exist when a crack occurs in a planet gear (sun gear side or ring gear side). If it is the sun gear side, the ring-planet mesh stiffness is assumed not to be affected as the cracked tooth can still bear the compressive stiffness as if no crack exists. Similarly, if it is the ring gear side, the sun-planet mesh stiffness will not be affeced. Overall, three cases are considered in this study; crack in the sun gear, crack in a planet gear (sun side) and crack in a planet gear (ring side). For each case, the mesh stiffness at four crack levels will be evaluated. These levels are 25%, 50%, 75% and 100% crack (tooth missing). Fifty percent (50%) crack occurs when the crack line q_1 reaches the tooth central line (see Fig. 3.10). Twenty five percent (25%) crack means the crack length is half of 50% crack length. One hundred percent (100%) crack indicates the crack line q_2 reaches the tooth root circle when the tooth breaks. Seventy five percent (75%) crack happens when the crack line q_2

has the same length of q_1 with 25% crack. The angle, υ, between the crack line and the tooth central line is assumed to be a constant in the calculation and set as 45°.

Case 1: Crack in the sun gear

Table 3.2 shows four crack levels in the sun gear and the corresponding crack length. According to the parameters of the planetary gear set (parameters are listed in Table 3.1), the root circle of the sun gear is smaller than the base circle. Applying the equations derived in the Section 3.2 and the Section 3.5, the mesh stiffness of a pair of sun-planet gears (k_{sp1}) are shown in Fig. 3.12 for four crack levels. The mesh stifness is represented as a function of the angular displacement of the planet gear. As the size of the crack grows, the mesh stiffness reduces correspondingly. Correct stiffness measurement is important for fault diagnosis of the gears. For each crack level,corresponding vibration signal can be obtained through dynamic simulation. By analysing these vibration signals, fault severity indicators can be generated, which can be then used to detect the fauly severity of the gear system.

Table 3.2: Crack levels and the corresponding crack length in the sun gear

Crack levels	Crack length
25%	q_1 = 1.95 mm
50%	q_1 = 3.90 mm
75%	q_1 = 3.90 mm, q_2 = 1.95 mm
100%	q_1 = 3.90 mm, q_2 = 3.90 mm

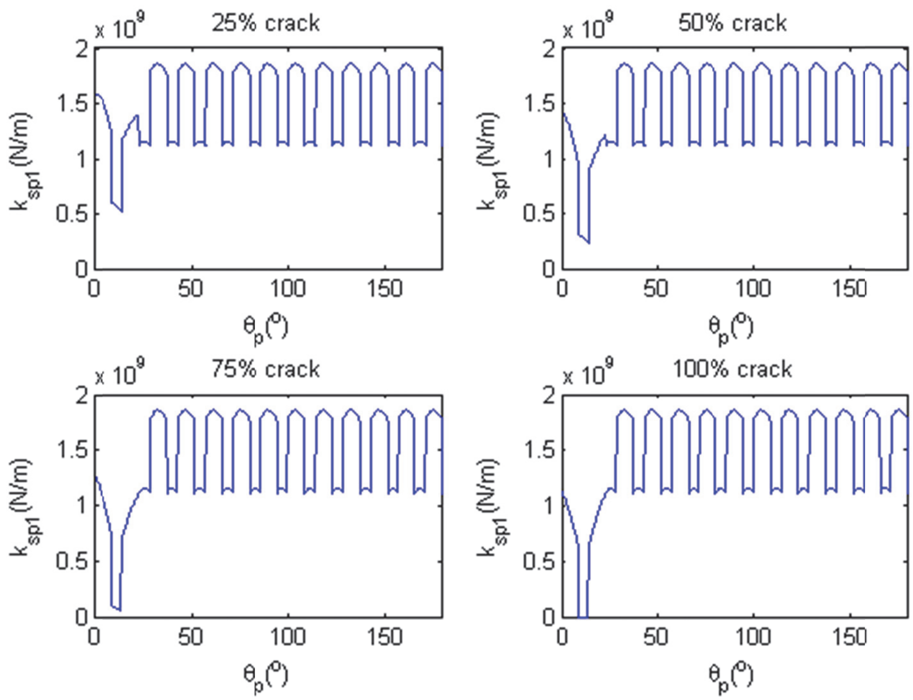

Fig. 3.12: Mesh stiffness of a sun-planet pair of four crack levels in sun gear

If the sun gear has a crack, the crack tooth will mesh with each of the planet gears successively. Therefore, the mesh stiffness of all sun-planet pairs will be affected. Fig. 3.13 shows one crack mesh cycle of the sun-planet mesh stiffness, which is 19 times of gear meshes corresponding to a 272.4 degree revolution of the planet gear. The symbol θ_m represents the angular displacement of the planet gear in one mesh period; the expression was given in Section 3.4. The point P' is the pitch point. The mesh stiffness of the ring-planet gears are not affected by the crack just like what is shown in Fig. 3.8.

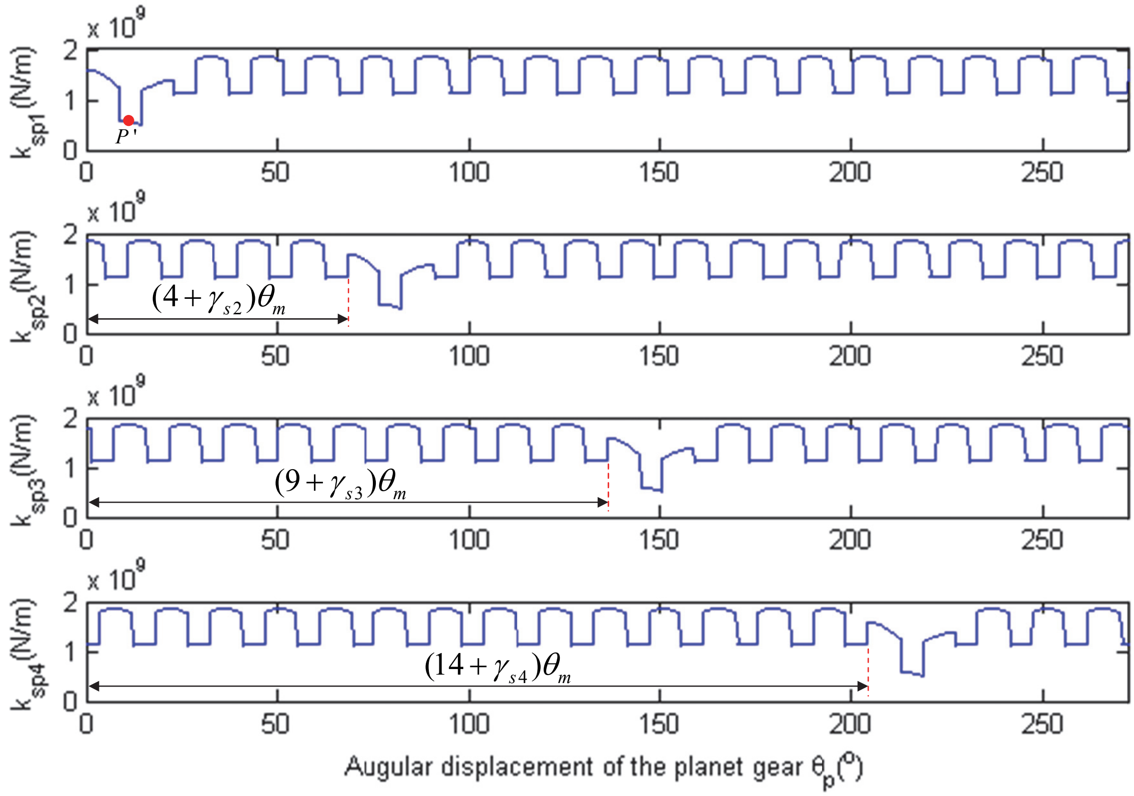

Fig. 3.13: Mesh stiffness of sun-planet gear pairs with 25% crack in sun gear

Case 2: Crack in a planet gear (sun gear side)

Table 3.3 gives the information about the four crack levels in a planet gear. For the planet gear given in Table 3.1, the root circle is also smaller than the base circle. The mesh stiffness will decrease gradually along with the crack growth as shown in Fig. 3.14. In this case, one crack mesh cycle includes 31 times of the gear meshing corresponding to a 444.4 degree revolution of the planet gear. The ring-planet gear pairs are treated as the perfect condition (seen Fig. 3.15 for the mesh stiffness of the perfect case). One big difference from Case 1 is that the mesh stiffness of only one pair of sun-planet gears will be affected by the crack (see Fig. 3.15). This difference in the mesh stiffness will cause the corresponding difference in the vibration signal which can be obtained through dynamic simulation. Signal processing methods can be applied to distinguish the crack location in the sun gear or the planet gear.

Table 3.3: Crack levels and the corresponding crack length in the planet gear

Crack levels	Crack length
25%	$q_1 = 2.15$ mm
50%	$q_1 = 4.30$ mm
75%	$q_1 = 4.30$ mm, $q_2 = 2.15$ mm
100%	$q_1 = 4.30$ mm, $q_2 = 4.30$ mm

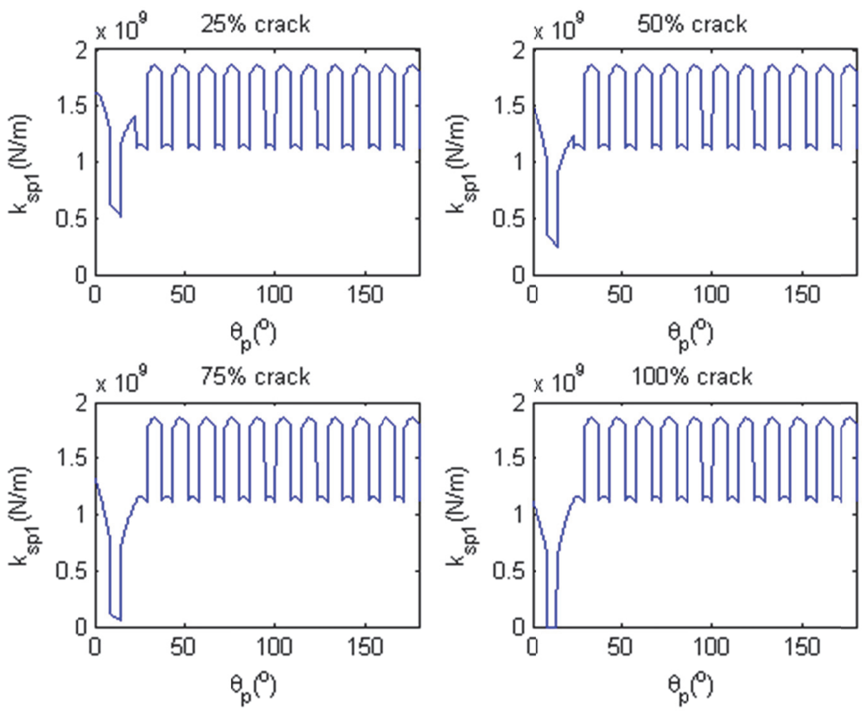

Fig. 3.14: Mesh stiffness of a sun-planet pair of four crack levels in planet gear

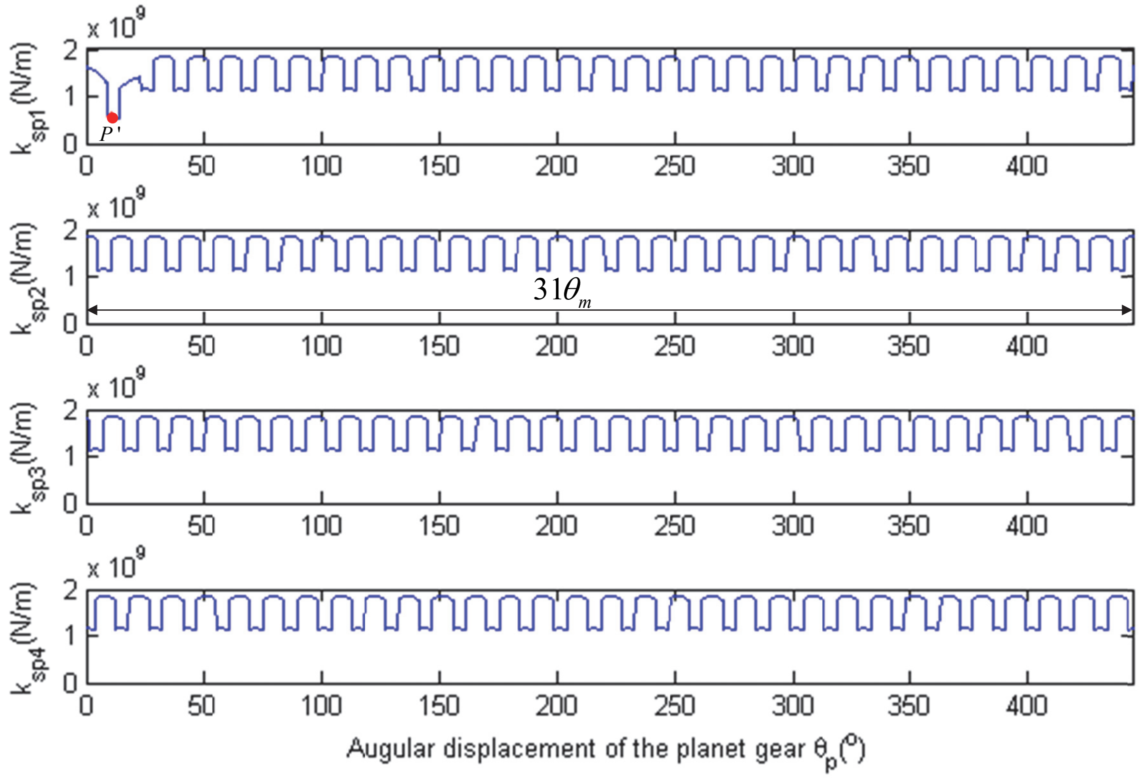

Fig. 3.15: Mesh stiffness of a sun-planet pair with 25% crack in planet gear

Case 3: Crack in a planet gear (ring gear side)

In this case, the crack lengths of the four crack levels are the same as the Case 2 (see Table 3.3). Fig. 3.16 illustrates the mesh stiffness reduction trend for a pair of ring-planet gears at four crack levels. For each crack level, the mesh stiffness reduction is quantified. This information is essential to obtain the dynamic response of a planetary gear set when crack is present. Fig. 3.17 presents the mesh stiffness of a pair of ring-planet gears when the planet gear has the crack level of 25%. Gear mesh takes place 31 times during one crack mesh cycle which corresponds to a 444.4 degree revolution of the planet gear. The point P corresponds to the pitch point. The sun-planet gear pairs are regarded as the perfect condition (seen Fig. 3.15 for the mesh stiffness of the perfect case). In the Case 1 and the Case 2, when the crack happens, the sun-planet mesh stiffness decreases and the ring-planet mesh stiffness keeps the same as the perfect situation. This difference in the mesh stiffness can be used in the dynamic simulation to observe the vibration response when crack happens in different positions. By analyzing these vibration signals, fault position indicators can be generated to track the crack position of a planetary gear set.

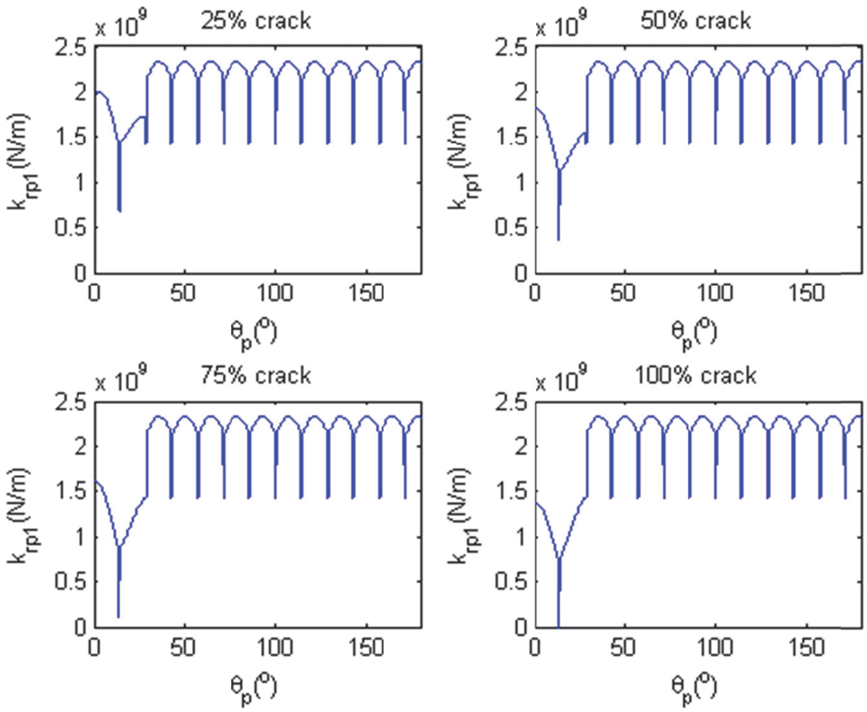

Fig. 3.16: Mesh stiffness of a ring-planet pair of four crack levels in planet gear

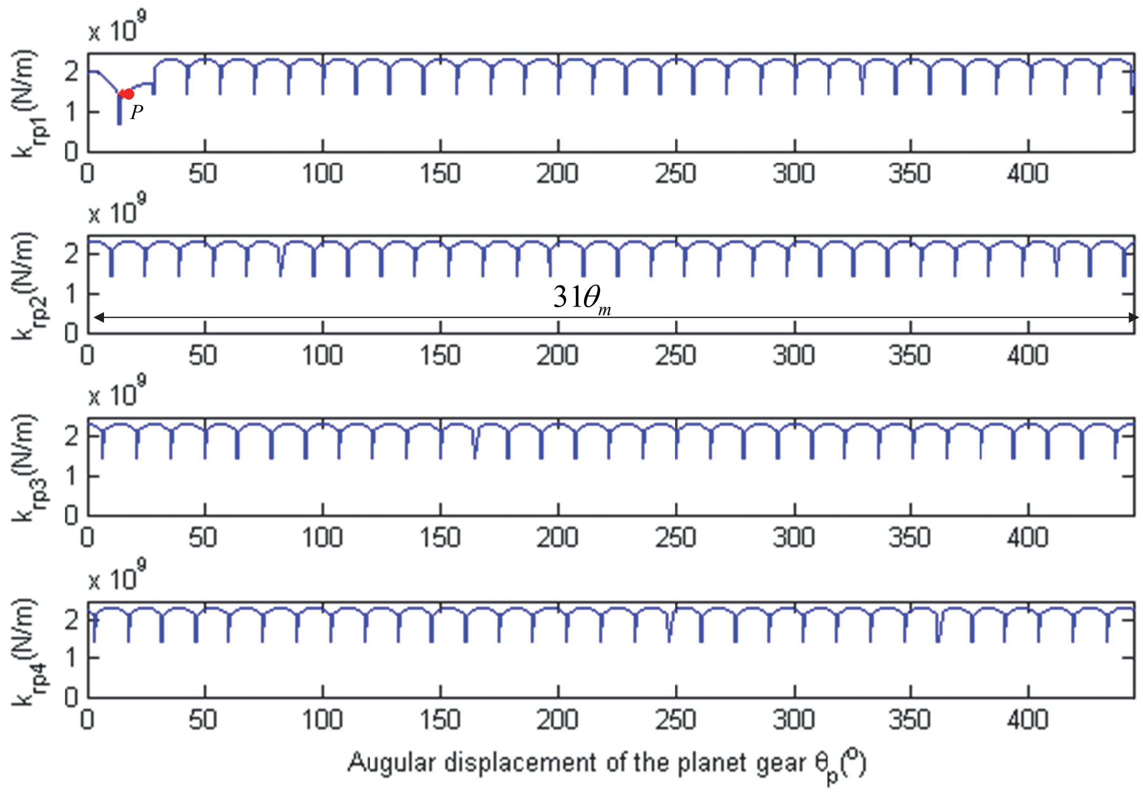

Fig. 3.17: Mesh stiffness of ring-planet pairs with 25% crack in planet gear

3.7 Validation

In [3.26], a two-dimensional (2-D) finite element model (see Fig. 3.18) was developed to evaluate the torsional mesh stiffness of a pair of external gears with 1:1 transmission ratio. The gears were modeled using quadratic 2-D plane strain elements and the contact effect was modeled using 2-D line-to-line general contact elements which included elastic Coulomb frictional effects. The torsional mesh stiffness is the ratio between the torque and the angular deflection of gear body. The mesh stiffness calculated in this study (see Eq. (3.2.23) and Eq. (3.2.24)) is the linear mesh stiffness which is the ratio of contact force to the linear displacement along the line of action. The relationship between linear and torsional mesh stiffness can be expressed as follows [3.26]:

$$k_{tb} = k_t \times R_b^2 \qquad (3.7.1)$$

where k_{tb} and k_t represent the torsional mesh stiffness and linear mesh stiffness, respectively, and R_b is the radius of the gear base circle.

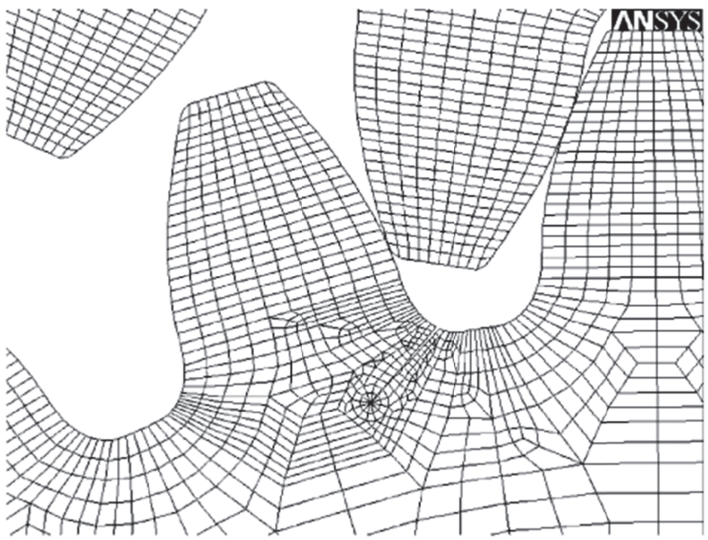

Fig. 3.18: Two-dimensional finite element model [3.26]

The key parameters of the gear pair used in [3.26] are listed in Table 3.4. I first calculated the gear mesh stiffness (linear mesh stiffness) using the proposed method for the same gear pair with parameters listed in Table 3.4. Then, I converted the linear mesh stiffness to torsional mesh stiffness using Eq. (3.7.1). A comparison between the torsional mesh stiffness results from [3.26] and that obtained in this study is given in Table 3.5 and Fig. 3.19. Two health conditions are analyzed: healthy condition with no crack and crack condition with a 4.7 mm crack at the root of one gear tooth. The biggest relative difference in the mesh stiffness between the FEM result in [3.26] and the analytical result from this thesis is within 7%.

Table 3.4: Major parameters of the spur gears used for validation [3.26]

Gear type	Standard involute, full-depth teeth
Material	Aluminium
Modulus of easticity	69 Gpa
Poisson's ratio	0.33
Face width	0.015 m
Module	6 mm
Number of teeth	23
Pressure angle	20^0
Theoretical contact ratio	1.59
Theoretical angle of meshing cycle	24.912^0
Addendum	1.00 m
Dedendum	1.25 m

Table 3.5: Mesh stiffness comparision

Gear tooth condition	Maximum difference (%)	
	Single mesh period	Double mesh periods
Perfect	5.9	6.3
4.7 mm crack	6.7	2.9

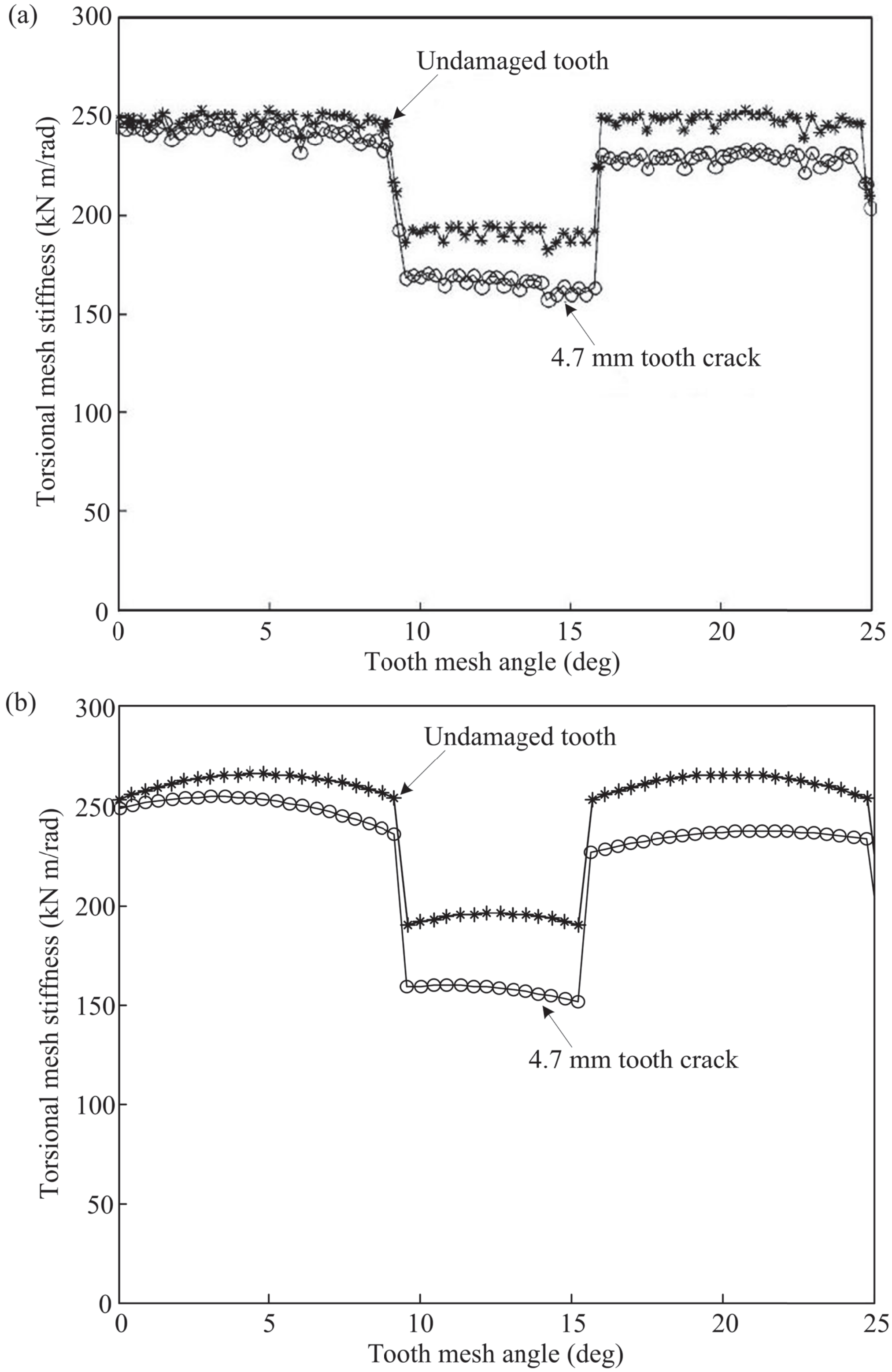

Fig. 3.19: Time-varying mesh stiffness validation

(a) FEM result from [3.26] and (b) obtained from the method developed in this study

3.8 Conclusions

In this chapter, equations are derived to evaluate the time-varying mesh stiffness of a planetary gear set with tooth crack based on the potential energy method and the gear mesh theory. The time-varying mesh stiffness is represented as a function of the angular displacement of the gears. To use these equations, users only need to provide gear geometry, material and tooth crack information (crack angle, crack length and crack location).

A modified cantilever beam model is proposed for an external gear tooth in mesh stiffness evaluation. Comparison results show that modeling gear tooth starting from the *root* circle rather than from the base circle may cause a stiffness variation of up to 40%. This shows that it is important to model the gear tooth starting from the root circle.

The mesh stiffness reduction due to crack is quantified when the crack appears in the sun gear, in a planet gear (sun gear side), or in a planet gear (ring gear side). The stiffness obtained in this chapter will be used in Chapter 4 to simulate the vibration signals of a planetary gear set in the faulty condition.

In this chapter, the gear body is assumed to be rigid, and tooth profile and lead modifications are not considered. These factors will be further investigated in the future.

References

[3.1] X. Liang, M. J. Zuo, and M. Pandey, “Analytically Evaluating the Influence of Crack on the Mesh Stiffness of a Planetary Gear Set,” *Mech. Mach. Theory*, vol. 76, pp. 20–38, Jun. 2014.

[3.2] X. Liang and M. J. Zuo, “Dynamic Simulation of a Planetary Gear Set and Estimation of Fault Growth on the Sun Gear,” in *Proceedings of 2013 International Conference on Quality, Reliability, Risk, Maintenance, and Safety Engineering (QR2MSE)*, 2013, pp. 1667–1672.

[3.3] T. Eritenel and R. G. Parker, “An Investigation of Tooth Mesh Nonlinearity and Partial Contact Loss in Gear Pairs Using a Lumped-parameter Model,” *Mech. Mach. Theory*, vol. 56, pp. 28–51, Oct. 2012.

[3.4] F. Chaari, W. Baccar, M. S. Abbes, and M. Haddar, “Effect of Spalling or Tooth Breakage on Gearmesh Stiffness and Dynamic Response of a One-stage Spur Gear Transmission,” *Eur. J. Mech. - ASolids*, vol. 27, no. 4, pp. 691–705, Jul. 2008.

[3.5] A. Fernandez del Rincon, F. Viadero, M. Iglesias, P. García, A. de-Juan, and R. Sancibrian, “A Model for the Study of Meshing Stiffness in Spur Gear Transmissions,” *Mech. Mach. Theory*, vol. 61, pp. 30–58, Mar. 2013.

[3.6] V. K. Ambarisha and R. G. Parker, “Nonlinear Dynamics of Planetary Gears Using Analytical and Finite Element Models,” *J. Sound Vib.*, vol. 302, no. 3, pp. 577–595, May 2007.

[3.7] D. C. H. Yang and J. Y. Lin, “Hertzian Damping, Tooth Friction and Bending Elasticity in Gear Impact Dynamics,” *J. Mech. Des.*, vol. 109, no. 2, pp. 189–196, Jun. 1987.

[3.8] X. Tian, M. J. Zuo, and K. R. Fyfe, “Analysis of the Vibration Response of a Gearbox with Gear Tooth Faults,” in *2004 ASME International Mechanical Engineering Congress and Exposition*, Anaheim, California USA, 2004, pp. 785–793.

[3.9] X. Zhou, Y. Shao, Y. Lei, and M. Zuo, “Time-varying Meshing Stiffness Calculation and Vibration Analysis for a 16DOF Dynamic Model with Linear Crack Growth in a Pinion,” *J. Vib. Acoust.*, vol. 134, no. 1, p. 011011, 2012.

[3.10] Y. Pandya and A. Parey, “Failure Path Based Modified Gear Mesh Stiffness for Spur Gear Pair with Tooth Root Crack,” *Eng. Fail. Anal.*, vol. 27, pp. 286–296, Jan. 2013.

[3.11] S. Wu, M. J. Zuo, and A. Parey, “Simulation of Spur Gear Dynamics and Estimation of Fault Growth,” *J. Sound Vib.*, vol. 317, no. 3–5, pp. 608–624, Nov. 2008.

[3.12] A. Kapelevich and Y. Shekhtman, “Tooth Fillet Profile Optimization for Gears with Symmetric and Asymmetric Teeth,” *Gear Technol.*, pp. 73–79, 2009.

[3.13] F. Chaari, T. Fakhfakh, and M. Haddar, “Analytical Modelling of Spur Gear Tooth Crack and Influence on Gearmesh Stiffness,” *Eur. J. Mech. - ASolids*, vol. 28, no. 3, pp. 461–468, May 2009.

[3.14] Z. Chen and Y. Shao, “Dynamic Simulation of Spur Gear with Tooth Root Crack Propagating along Tooth Width and Crack Depth,” *Eng. Fail. Anal.*, vol. 18, no. 8, pp. 2149–2164, Dec. 2011.

[3.15] Z. Chen and Y. Shao, “Mesh Stiffness Calculation of a Spur Gear Pair with Tooth Profile Modification and Tooth Root Crack,” *Mech. Mach. Theory*, vol. 62, pp. 63–74, Apr. 2013.

[3.16] F. Chaari, T. Fakhfakh, and M. Haddar, “Dynamic Analysis of a Planetary Gear Failure Caused by Tooth Pitting and Cracking,” *J. Fail. Anal. Prev.*, vol. 6, no. 2, pp. 73–78, Apr. 2006.

[3.17] L. Walha, T. Fakhfakh, and M. Haddar, “Nonlinear Dynamics of a Two-stage Gear System with Mesh Stiffness Fluctuation, Bearing Flexibility and Backlash,” *Mech. Mach. Theory*, vol. 44, no. 5, pp. 1058–1069, May 2009.

[3.18] X. Liang, M. J. Zuo, and T. H. Patel, “Evaluating the Time-varying Mesh Stiffness of a Planetary Gear Set Using the Potential Energy Method,” *Proc. Inst. Mech. Eng. Part C J. Mech. Eng. Sci.*, vol. 228, no. 3, pp. 535–547, Feb. 2014.

[3.19] F. L. Litvin and A. Fuentes, *Gear Geometry and Applied Theory*, 2 edition. New York: Cambridge University Press, 2004.

[3.20] D. C. H. Yang and Z. S. Sun, “A Rotary Model for Spur Gear Dynamics,” *J. Mech. Transm. Autom. Des.*, vol. 107, no. 4, pp. 529–535, Dec. 1985.

[3.21] R. G. Parker and J. Lin, “Mesh Phasing Relationships in Planetary and Epicyclic Gears,” *J. Mech. Des.*, vol. 126, no. 2, pp. 365–370, May 2004.

[3.22] D. G. Lewicki, “Gear Crack Propagation Path Studies-Guidelines for Ultra-Safe Design,” *J. Am. Helicopter Soc.*, vol. 47, no. 1, pp. 64–72, 2002.

[3.23] A. Belsak and J. Flasker, “Detecting Cracks in the Tooth Root of Gears,” *Eng. Fail. Anal.*, vol. 14, no. 8, pp. 1466–1475, Dec. 2007.

[3.24] J. Kramberger, M. Šraml, S. Glodež, J. Flašker, and I. Potrč, “Computational Model for the Analysis of Bending Fatigue in Gears,” *Comput. Struct.*, vol. 82, no. 23–26, pp. 2261–2269, Sep. 2004.

[3.25] D. G. Lewicki, K. E. LaBerge, R. T. Ehinger, and J. Fetty, “Planetary Gearbox Fault Detection Using Vibration Separation Techniques,” National Aeronautics and Space Administration, Glenn Research Center, Technical Report NASA/TM—2011-217127, 2011.

[3.26] I. Howard, S. Jia, J. Wang, “The dynamic modeling of a spur gear in mesh including friction and a crack,” *Mech. Syst. Signal Pr.*, vol. 15, pp. 831-853, 2001.

Chapter 4: Vibration Signal Modeling of a Planetary Gear Set for Tooth Fault Detection

In Chapter 2 and Chapter 3, the time-varying mesh stiffness is analytically evaluated using the potential energy method for a planetary gear set in healthy and cracked tooth conditions. The time-varying mesh stiffness obtained in the previous two chapters will be used in this chapter to simulate the vibration signals of a planetary gear set. In this chapter, a dynamics based vibration signal modeling method is proposed to simulate the vibration signals of a planetary gearbox at the sensor location. The vibration properties found in this chapter for a planetary gearbox in healthy and faulty conditions enlighten the development of a fault detection method to be proposed in Chapter 5. This chapter is organized as follows. In Section 4.1, background of this research topic is described and a literature review is given on vibration signal modeling and vibration analysis of a planetary gear set. In Section 4.2, a lumped parameter model is proposed to simulate the vibration source signals of a planetary gear set. In Section 4.3, a mathematical model is proposed to represent the effect of transmission path. In Section 4.4, properties of the resultant vibration signals are analyzed in time and frequency domains. In Section 4.5, the proposed vibration properties of a planetary gear set are compared with experimental signals. In Section 4.6, conclusions of this research topic are given. This chapter is based on a journal paper [4.1] and a refereed conference paper [4.2].

4.1 Introduction

The vibration signals of a planetary gearbox are more complicated than those of a fixed-shaft gearbox. For a planetary gear set, several sun-planet gear pairs and several ring-planet gear pairs mesh simultaneously. The vibration signals generated by each sun-planet gear pair are similar but with different phases [4.3]. So does each ring-planet gear pair. This phase shift cancels or neutralizes some of the excitations induced by gear pairs but augments others [4.4]. In general, vibration transducers, mounted on the housing of a gearbox or the housing of a bearing acquire vibration signals. In addition, the rotation of the carrier varies the transmission paths of the vibration signals to a fixed transducer. Multiple vibration sources and the effect of the transmission path make fault symptoms hard to distinguish.

Even though many signal processing methods have been proposed to detect gear faults [4.3-4.6], such methods still need improvements. The transducer signal is comprised of many sub signals, such as the vibrations of the sun gear, planet gear, ring gear, bearings and shafts. Unfortunately, no mature signal processing methods can effectively denoise and separate these signals [4.7-4.8]. If we can "open" the black box, "see" all the sub-signals, and understand the generation mechanisms of vibration signals, we can develop effective tools to detect gear faults.

Several researchers investigated the vibration properties of a planetary gearbox using mathematical models [4.9-4.10]. However, these models lack connections with physical parameters of a gearbox, like gear mesh stiffness and damping. In addition, they can hardly model the process of the fault growth. A dynamic model can model fault growth and the corresponding effects. It has further advantages over lab systems or field systems [4.11]: (1) we can eliminate environmental noises to identify changes in vibration signals caused by the faults; (2) with a good dynamic simulation model, we can easily simulate different types and levels of faults, and observe changes in the vibration signal they cause.

A large range of dynamic models have been developed to simulate the behavior of planetary gears. Kahraman [4.12] proposed a nonlinear dynamic model to investigate the load sharing characteristics of a planetary gear set. Inalpolat and Kahraman [4.13] used the same model as Ref. [4.12] to predict modulation sidebands of a planetary gear set having manufacturing errors. Lin and Parker [4.14] modified the model of Ref. [4.12] and investigated the free vibration properties of a planetary gear set. Cheng et al. [4.15] developed a pure torsional dynamic model to investigate the properties of a planetary gear set when a single pit was present on one tooth of the sun gear. Chaari et al. [4.16] used a similar model as Ref. [4.14] to investigate manufacturing errors' effect on the dynamic behavior of planetary gears. This study did not consider tooth profile modification or manufacturing errors. Studies on the effect of manufacturing error are given in Refs. [4.13, 4.16] while studies on the effect of tooth profile modification are given in Refs. [4.17-4.20].

However, the investigation of the vibration properties of a planetary gearbox with cracked teeth is limited. Barszcz and Randall [4.21] applied spectra kurtosis to detect a ring gear tooth crack in the planetary gear of a wind turbine. Lewicki et al. [4.22] used vibration separation techniques to detect the tooth damage in the sun gear, planet gear and ring gear, respectively. Chen and Shao [4.23] investigated the vibration properties of a planetary gear set when there was a tooth root crack in the ring gear. Chaari et al. [4.24] applied the dynamic model developed in [4.16] to investigate the vibration properties of the sun gear and the carrier of a planetary gear set with tooth crack or a single pit on the sun gear. In their studies, the gear mesh stiffness was approximated as a square waveform which would generate unwanted frequency components in the dynamic response [4.25]. Chen and Shao [4.26] studied the dynamic features of a planetary gear set when a tooth crack was under different sizes and inclination angles. The displacement signals of the sun gear and the planet gear were investigated when a crack was present on the sun gear or the planet gear. But, Refs [4.23, 4.24, 4.26] did not consider the effect of transmission path in their studies. In this study, I do consider the effect of transmission path while focusing on a tooth crack in the sun gear.

The dynamic models described above can be divided into two categories: fixed coordinate model and rotating coordinate model. A rotating coordinate model is more convenient to consider inertial force effect caused by the rotation of the carrier. The inertial force contains gyroscopic force and centrifugal force. The centrifugal force is a fictitious force generated from the rotation of a planet gear around the axis of the sun gear. Cooley and Parker [4.27] mentioned the centrifugal force in the investigation of eigenvalues of a planetary gear set. They concluded that the constant centrifugal force (it is not constant if the rotation speed of a planet gear around the axis of the sun gear is varying) could be ignored without affecting the eigenvalues. Gu and Velex [4.28] investigated the influence of planet position errors on the quasi-static and dynamic load sharing among planets. In Gu and Velex's model, both gyroscopic and centrifugal forces were considered. In this thesis, both the gyroscopic force and the centrifugal force are also considered as Gu and Velex [4.28] did. But our focus is not to investigate the effect of the gyroscopic and centrifugal forces. Instead, our focus is to find the fault symptoms in the vibration signals of a planetary gear set with tooth crack when the gyroscopic and centrifugal forces are present.

A few studies considered the effect of the transmission path in the vibration signal modeling. Inalpolat and Kahraman [4.9] expressed the resultant acceleration signal of a planetary gear set as follows:

$$a(t) = \sum_{n=1}^{N} C w_n(t) F_{rpn}(t) , \tag{4.1.1}$$

where C is a constant; N represents the number of planet gears; $w_n(t)$ denotes the effect of transmission path for the n^{th} planet gear which is a weighting Hanning function [4.9] with a time duration of T_c / N; and $F_{rpn}(t)$ is the dynamic force of the n^{th} ring-planet mesh.

Later, Inalpolat and Kahraman [4.13] improved the modeling considering the dynamic forces of both sun-planet meshes and ring-planet meshes. They used the same Hanning function as Ref. [4.9] to cover the effect of the transmission path.

$$a(t) = \sum_{n=1}^{N} (C_s w_n(t) F_{spn}(t) + C_r w_n(t) F_{rpn}(t)) , \tag{4.1.2}$$

where C_s and C_r are constants facilitated to establish the relation between the gear mesh forces; and $F_{spn}(t)$ and $F_{rpn}(t)$ represent the dynamic force of the n^{th} sun-planet mesh and the n^{th} ring-planet mesh, respectively.

However, the correctness of Eq. (4.1.2) is worth discussing. The line of force $F_{spn}(t)$ is the internal common tangent of the base circles of the sun gear and the n^{th} planet gear. While the line of force $F_{rpn}(t)$ is the internal common tangent of the base circles of the ring gear and the n^{th} planet gear. Since dynamic forces $F_{spn}(t)$ and $F_{rpn}(t)$ are not in the same direction, it is not proper to add weighted $F_{spn}(t)$ and weighted $F_{rpn}(t)$ together as two scalars.

Feng and Zuo [4.10] investigated possible transmission paths of vibration signals in a planetary gearbox. In Fig. 4.1, three transmission paths are illustrated from its origin to the transducer. According to their studies, the transducer perceived signal arriving along path 2 and 3 will have negligible amplitude. Therefore, only the first transmission path was considered in their studies, and the transmission path was modeled by a Hanning function with a time duration of T_c.

All the previous studies modeled the effect of transmission path using a Hanning function [4.9, 4.10, 4.13]. They all assumed that as planet *n* approached the transducer location, its influence would increase, reaching its maximum when planet *n* was the closest to the transducer location, then, its influence would decrease to zero as the planet went away from the transducer. However, even if the planet *n* is in the farthest location from the transducer, its influence may not be zero. In this study, I propose an approach to overcome this shortcoming.

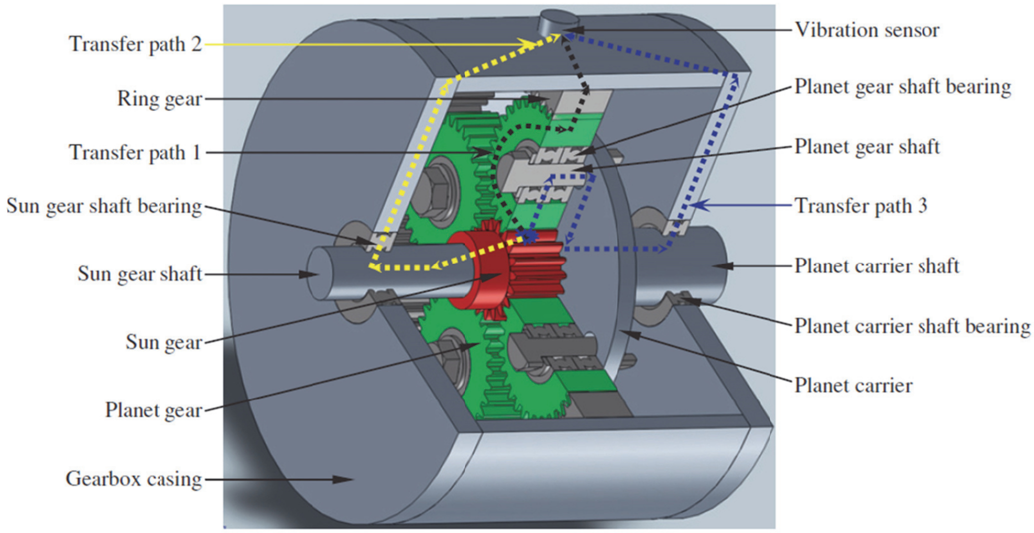

Fig. 4.1: Transmission paths of a planetary gearbox [4.10]

In this chapter, a planetary gear dynamic model is developed to simulate the vibration signals of each gear, including the sun gear, the planet gears, and the ring gear. In this dynamic model, both gyroscopic force and centrifugal force are considered, and more accurate physical parameters are adopted. The vibration signals are simulated in the perfect condition of a planetary gearbox and in the fault condition when there is a cracked tooth in the sun gear. A mathematical model is proposed to represent the effect of transmission path which can fit different planetary gearboxes by choosing proper model parameters. Incorporating the effect of transmission path, the resultant signals of a planetary gearbox at a transducer location are generated. The vibration signals are investigated both in time and frequency domains, and fault symptoms are found which can be used to detect the severity of tooth crack. Finally, the simulated vibration signals are compared with experimental signals.

4.2 Dynamic simulation

In this section, a lumped-parameter model is developed to simulate the vibration signals of each gear of a planetary gear set. This model is similar to that used by Lin and Parker [4.14] with three distinctions: (1) the planet deflections are described in the horizontal and vertical coordinates, (2) both the gyroscopic force and the centrifugal force (inertial force) are incorporated, and (3) more accurate physical parameters are adopted. Whether gear deflections are described in the horizontal and vertical coordinate system, or in the radial and tangential coordinate system, the gear dynamic behaviors will not be affected. However, if the planet deflections are described in the horizontal and vertical coordinates, we can get the motions of all planet gears in the same direction. It has two benefits: (a) we can easily compare the motion of different planet gears, and (b) we can easily do algebraic operations on these vibration signals. For example, in Section 4.3, we need to add the vibrations of planet gears together to generate sensor perceived vibration signal. The inertial forces may play a more important role in the dynamic behavior of a gearbox in high speed applications than that at low speed applications.

Time-varying mesh stiffness is one of the main sources of vibration in a gear transmission system [4.29]. In [4.14], the gear mesh stiffness was approximated by a square waveform. The square waveform reflects only the effect of the change in the tooth contact number, but ignores the effect of the change in the tooth contact position [4.30]. In addition, the physical damping was ignored in their model. In this study, more accurate physical parameters (mesh stiffness and physical damping) will be adopted in the simulation of vibration signals.

4.2.1 Modeling of a planetary gear set

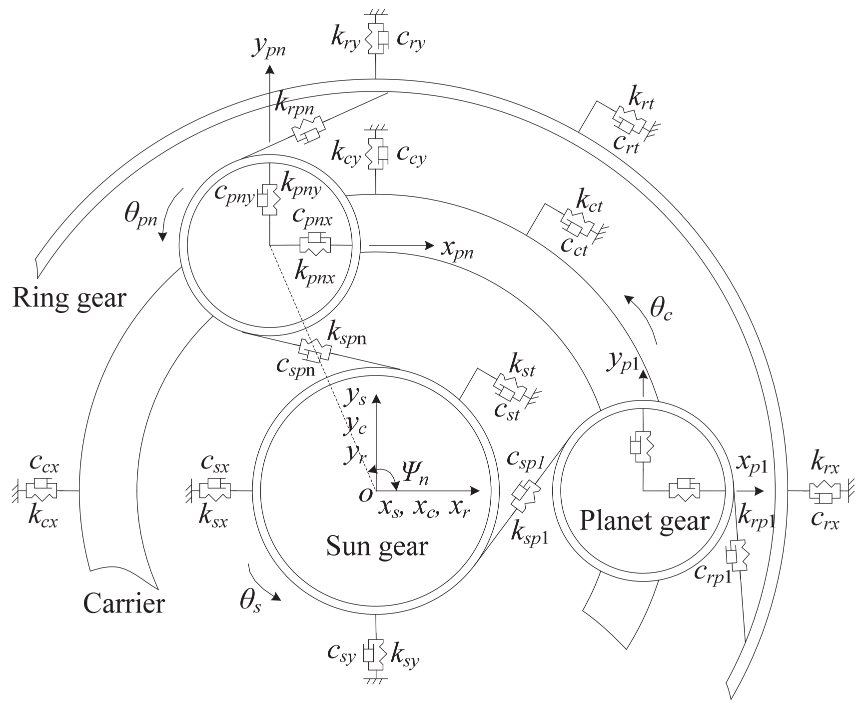

Fig. 4.2: Dynamic modeling of a planetary gear set

Fig. 4.2 shows a two-dimensional lumped-parameter model which is used in this study to simulate the vibration signals of a planetary gear set, which consists of one sun gear (*s*), one ring gear (*r*), one carrier (*c*) and *N* planet gears (*p*). Each component has three degrees of freedom: transverse motions in x-axis and y-axis, and rotation. The rotation coordinates θ_i , $i = s, r, c, p_1,..., p_N$ are the angular displacement. The sun gear, ring gear and carrier translations x_j , y_j , $j = s, r, c$ and planet translations x_{pn} , y_{pn} , $n = 1,..., N$, are measured with respect to a rotating frame of reference fixed to the carrier with the origin o. The gear mesh interface is modeled as a spring-damper system. The directions of all the coordinates at the initial time (time zero) are shown in Fig. 4.2. Since I am focusing on the effects of a growing crack on the vibration response of the meshing gears, I have ignored the effects of transmission errors in the gears, the frictions between the gear teeth, and other practical phenomena such as backlash. The equations of motion of a planetary gear set are expressed as follows:

Equations of motion for the sun gear:

$$m_s\ddot{x}_s + c_{sx}\dot{x}_s + k_{sx}x_s + \sum F_{spn}\cos\psi_{sn} = m_s x_s\Omega^2 + 2m_s\dot{y}_s\Omega + m_s y_s\dot{\Omega},$$

$$m_s\ddot{y}_s + c_{sy}\dot{y}_s + k_{sy}y_s + \sum F_{spn}\sin\psi_{sn} = m_s y_s\Omega^2 - 2m_s\dot{x}_s\Omega - m_s x_s\dot{\Omega},$$

$$(J_s / r_s)\ \ddot{\theta}_s + \sum F_{spn} = T_i / r_s\ , \tag{4.2.1}$$

where F_{spn} represents the dynamic force of the n^{th} sun-planet gear mesh:

$$F_{spn} = k_{spn}\delta_{spn} + c_{spn}\dot{\delta}_{spn},$$

$$\delta_{spn} = (x_s - x_{pn})\cos\psi_{sn} + (y_s - y_{pn})\sin\psi_{sn} + r_s\theta_s + r_{pn}\theta_{pn} - r_c\theta_c\cos a,$$

$$\psi_{sn} = \pi/2 - a + \psi_n,$$

$$\psi_n = 2(n-1)\pi/n; \quad i = 1,2,...,N.$$

Equations of motion for the ring gear:

$$m_r\ddot{x}_r + c_{rx}\dot{x}_r + k_{rx}x_r + \sum F_{rpn}\cos\psi_{rn} = m_r x_r\Omega^2 + 2m_r\dot{y}_r\Omega + m_r y_r\dot{\Omega},$$

$$m_r\ddot{y}_r + c_{ry}\dot{y}_r + k_{ry}y_r + \sum F_{rpn}\sin\psi_{rn} = m_r y_r\Omega^2 - 2m_r\dot{x}_r\Omega - m_r x_r\dot{\Omega},$$

$$(J_r / r_r)\ \ddot{\theta}_r + (c_{rt} / r_r)\ \dot{\theta}_r + (k_{rt} / r_r)\ \theta_r + \sum F_{rpn} = 0, \tag{4.2.2}$$

where F_{rpn} represents the dynamic force of the n^{th} ring-planet gear mesh:

$$F_{rpn} = k_{rpn}\delta_{rpn} + c_{rpn}\dot{\delta}_{rpn},$$

$$\delta_{rpn} = (x_r - x_{pn})\cos\psi_{rn} + (y_r - y_{pn})\sin\psi_{rn} + r_r\theta_r - r_{pn}\theta_{pn} - r_c\theta_c\cos a,$$

$$\psi_{rn} = \pi/2 + a + \psi_n.$$

Equations of motion for the planet gears:

$$m_{pn}\ddot{x}_{pn} + F_{cpnx} - F_{spn}\cos\psi_{sn} - F_{rpn}\cos\psi_{rn} = m_{pn}x_{pn}\Omega^2 + 2m_{pn}\dot{y}_{pn}\Omega + m_{pn}y_{pn}\dot{\Omega} + m_{pn}r_c\Omega^2\cos\psi_n,$$

$$m_{pn}\ddot{y}_{pn} + F_{cpny} - F_{spn}\sin\psi_{sn} - F_{rpn}\sin\psi_{rn} = m_{pn}y_{pn}\Omega^2 - 2m_{pn}\dot{x}_{pn}\Omega - m_{pn}x_{pn}\dot{\Omega} + m_{pn}r_c\Omega^2\sin\psi_n,$$

$$(J_{pn}/r_p)\ \ddot{\theta}_{pn} + F_{spn} - F_{rpn} = 0, \qquad (4.2.3)$$

where F_{cpnx} and F_{cpny} describe the bearing forces between the carrier and the n^{th} planet in the x and y directions:

$$F_{cpnx} = k_{pnx}(x_{pn} - x_c) + c_{pnx}(\dot{x}_{pn} - \dot{x}_c),$$

$$F_{cpny} = k_{pny}(y_{pn} - y_c) + c_{pny}(\dot{y}_{pn} - \dot{y}_c).$$

Equations of motion for the carrier:

$$m_c\ddot{x}_c + c_{cx}\dot{x}_c + k_{cx}x_c - \sum F_{cpnx} = m_c x_c\Omega^2 + 2m_c\dot{y}_c\Omega + m_c y_c\dot{\Omega},$$

$$m_c\ddot{y}_c + c_{cy}\dot{y}_c + k_{cy}y_c - \sum F_{cpny} = m_c y_c\Omega^2 - 2m_c\dot{x}_c\Omega - m_c x_c\dot{\Omega},$$

$$(J_c/r_c)\ \ddot{\theta}_c + \sum F_{cpnx}\sin\psi_n - \sum F_{cpny}\cos\psi_n = T_o/r_c. \qquad (4.2.4)$$

As a planet gear rotates around the center of the sun gear, the inertial force will be generated. The inertial force contains two items $m_{pn}x_{pn}\Omega^2$ (gyroscopic force) and $m_{pn}r_c\Omega^2$ (centrifugal force) which can be observed from the equations of transverse motions of planet gears in Eq. (4.2.3). x_{pn}, which is the x-direction displacement of the n^{th} planet gear, is much smaller than r_c which is the distance between centers of sun gear and planet gear. If $\cos\psi_n$ takes a value near 1, the item $m_{pn}r_c\Omega^2\cos\psi_n$ will dominate the inertial force when the rotation speed of the carrier is large. On the other hand, if $\cos\psi_n$ takes a small value near 0, the item $m_{pn}r_c\Omega^2\sin\psi_n$ will dominate the inertial force when the rotation speed of the carrier is large, but it is in the y-direction motion. Some previous studies [4.16, 4.26] considered the gyroscopic force, but ignored the gyroscopic force. In this study, both these two items are considered.

4.2.2 Crack modeling and mesh stiffness evaluation

Gear tooth crack is one common failure mode in a gear transmission system. It may occur due to excessive service load, inappropriate operating conditions or simply fatigue [4.31]. In the dynamic model described in Section 2.1, the gear mesh interface is modeled as a spring-damper system. When a pair of spur gear meshes, the tooth contact number and the tooth mesh position change during meshing. It leads to a periodic variation in the gear mesh stiffness. When a crack happens in one gear tooth, the mesh stiffness will decrease and consequently the vibration properties of the gear system will change. In order to comprehensively understand the vibration properties of a planetary gear set, it is essential to evaluate the mesh stiffness effectively.

According to the research by Belsak and Flasker [4.32], crack mostly initiates at the critical area of a gear tooth (area of the maximum principal stress), and the propagation paths are smooth, continuous, and in most cases, rather straight with only a slight curvature as shown in Fig. 4.3. Liang et al. [4.30] simplified the crack growth path as a straight line (the red line) starting from the critical area of the tooth root. The same model as Ref. [4.30] will be used in this study.

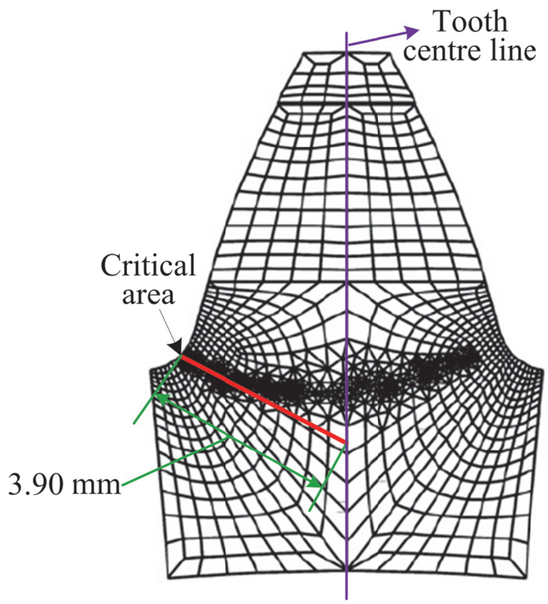

Fig. 4.3: Tooth crack propagation path of an external gear tooth [4.32]

The method reported in [4.30] will be used directly to evaluate the mesh stiffness of a planetary gear set in the perfect and the cracked tooth condition. Potential energy method [4.30, 4.33, 4.34] will be applied to evaluate the mesh stiffness of a pair of sun-planet gear and a pair of ring-planet gear, respectively. The total potential energy of a pair of meshing gears is considered to be the summation of Hertzian energy, bending energy, shear energy, and axial compressive energy. The total effective mesh stiffness can be evaluated based on Hertzian, bending, shear stiffness, and axial compressive mesh stiffness. If there is a tooth crack, the bending stiffness and the shear stifness will reduce due to the change in tooth length and tooth height induced by the crack [4.30], which leads to the decrease of the total mesh stiffness. While each of the sun-planet meshes (or ring-planet meshes) has the same shape of mesh stiffness variation, they are not in phase with each other [4.35]. Incorporating the mesh phasing relationships, the mesh stiffness of all sun-planet gear pairs and all ring-planet gear pairs can be evaluated, thus, the mesh stiffness of a planetary gear set is obtained.

In a planetary gearbox, sun gear teeth easily suffer damage because their multiplicity of meshes with the planet gears increases the potential for damage on the sun gear [4.4]. Fig. 4.4 shows the mesh stiffness of a pair of sun-planet gears with different crack levels (perfect, 0.78 mm crack, 2.34 mm crack and 3.90 mm crack) on a sun gear tooth. The physical parameters of this planetary gear set (one sun gear, one fixed ring gear and four equally spaced planet gears) are listed in Table 4.1. As the growth of tooth crack, the mesh stiffness reduces gradually, which will cause the gearbox vibrating abnormally.

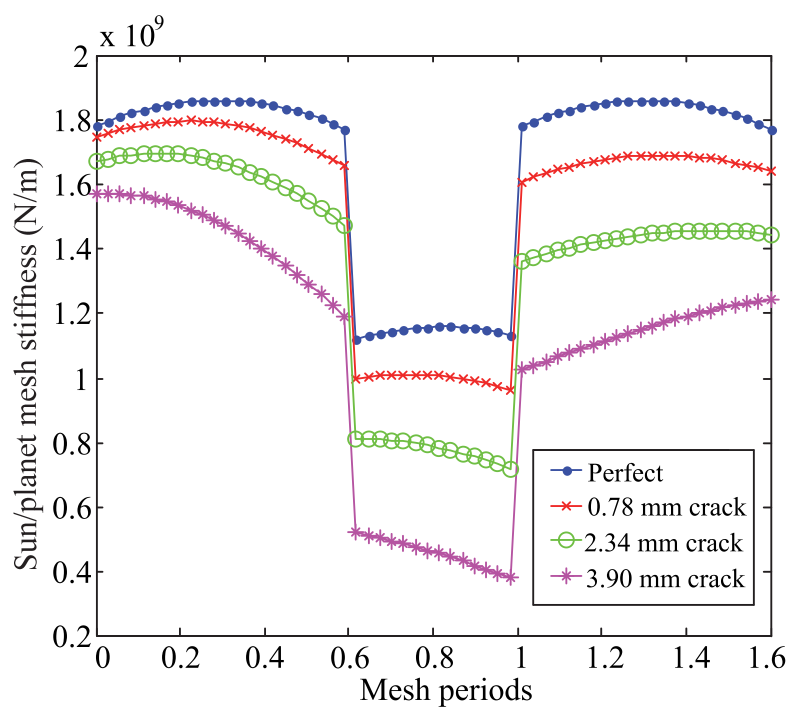

Fig. 4.4: Mesh stiffness reduction of different crack levels on a sun gear tooth [4.30]

Table 4.1: Physical parameters of the planetary gear set for dynamic modelling

Parameters	Sun gear	Planet gear	Ring gear
Number of teeth	19	31	81
Module (mm)	3.2	3.2	3.2
Pressure angle	20^o	20^o	20^o
Mass (kg)	0.700	1.822	5.982
Face width (m)	0.0381	0.0381	0.0381
Young's modulus (Pa)	2.068×10^{11}	2.068×10^{11}	2.068×10^{11}
Poisson's ratio	0.3	0.3	0.3
Base circle radius	28.3	46.2	120.8
Root circle radius	26.2	45.2	132.6
Reduction ratio	5.263		
Bearing Stiffness	$k_{sx} = k_{sy} = k_{rx} = k_{ry} = k_{cx} = k_{cy} = k_{pnx} = k_{pny} = 1.0\times10^8$ *N/m*		
Bearing damping	$c_{sx} = c_{sy} = c_{rx} = c_{ry} = c_{cx} = c_{cy} = c_{pnx} = c_{pny} = 1.5\times10^3$ *kg/s*		

Fig. 4.5 describes the mesh stiffness of four sun-planet gear pairs with the consideration of mesh phasing relationships of multiple gear pairs. The curves k_{sp1}, k_{sp2}, k_{sp3} and k_{sp4} represent the mesh stiffness of the 1st, the 2nd, the 3rd and the 4th pair of the sun-planet gears, respectively. The mesh stiffness of ring-planet gears are assumed not to be affected by the tooth crack on the sun gear and the stiffness equations of the ring-planet gears were derived in [4.30]. The cracked tooth on the sun gear meshes with the four planet gears in turn, therefore, the mesh stiffness of the four pairs of sun-planet gears are all affected. The time intervals of the cracked tooth in meshing are labeled in Fig. 4.5. The symbol γ_{sn} (n = 1, 2, 3, 4) is the relative phase between the n^{th} sun-planet pair with respect to the 1st sun-planet pair. The value of γ_{s1}, γ_{s2}, γ_{s3} and γ_{s4} are 1, 0.75, 0.5 and 0.25, respectively [4.25]. The symbol θ_m denotes the mesh period.

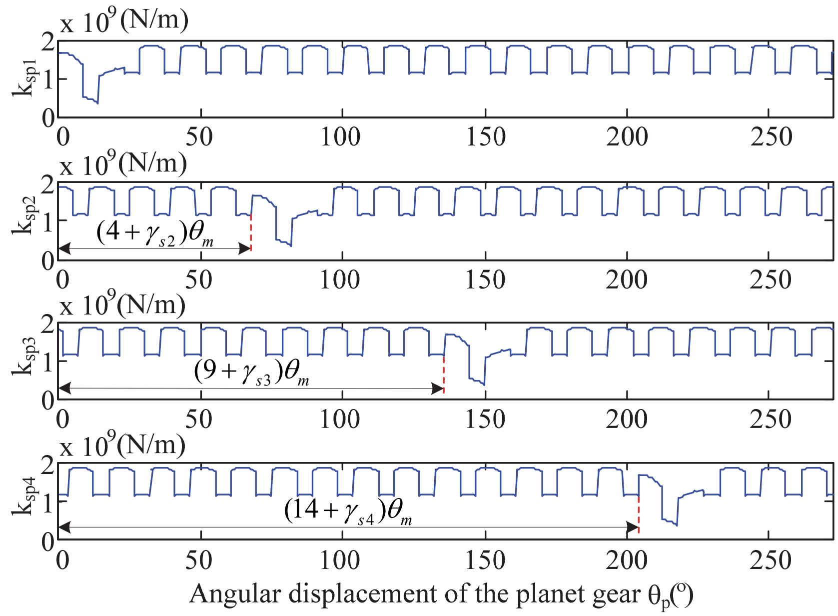

Fig. 4.5: Mesh stiffness of sun-planet gears with 3.90 mm crack in a sun gear tooth [4.30]

4.2.3 Numerical simulation of vibration signals

In this section, vibration signals of each gear of a planetary gear set are numerically simulated using MATLAB ode15s solver. Physical parameters of the planetary gear set are mainly listed in Table 4.1. In addition, the mass of the carrier is 10 kg. A constant torque of 450 *N·m* is applied to the sun gear. The rotation speed of the carrier is 8.87 RPM. The gear mesh damping coefficient *c* is calculated by the following equation [4.36]:

$$c = 2\zeta\sqrt{k\frac{m_1 m_2}{m_1 + m_2}}, \tag{4.2.5}$$

where k denotes the time-varying mesh stiffness of a pair of gears; m_1 and m_2 represent the mass of the pinion and the gear of a pair of gears, respectively; ζ is a constant damping ratio which is set to be 0.07 in this study. Through this simulation, displacement, velocity, and acceleration signals of the sun gear, the planet gears, the ring gear and the carrier are all obtained.

Fig. 4.6 shows displacement signals of the sun gear in three health conditions: perfect, 0.78 mm crack and 3.90 mm crack in one sun gear tooth. The sun gear has 19 teeth and Fig. 4.6 illustrates the signals in 19 mesh periods (T_m). Within 19 meshes, the cracked tooth will mesh with the four planets in turn. The time duration of the cracked tooth in meshing can be calculated analytically [4.30]. For the planetary gear set used in this chapter, the time duration is 4.75 (19/4) T_m which is labeled in Fig. 4.6. When the cracked tooth is in meshing, the sun gear generates a bigger displacement (fault symptom). With the growth of the crack, the fault symptoms enlarge. However, the fault symptom may appear in the x-direction displacement or in the y-direction displacement, even we can see 4 uniformly spaced fault symptoms in the absolute displacement of the sun gear. In the 3.90 mm crack condition, we can observe clearly fault symptoms. However, when the crack length is 0.78 mm, the fault symptom (indicated by the red arrows) is very week. That's why it is hard to detect the fault symptom in the early stage of crack growth.

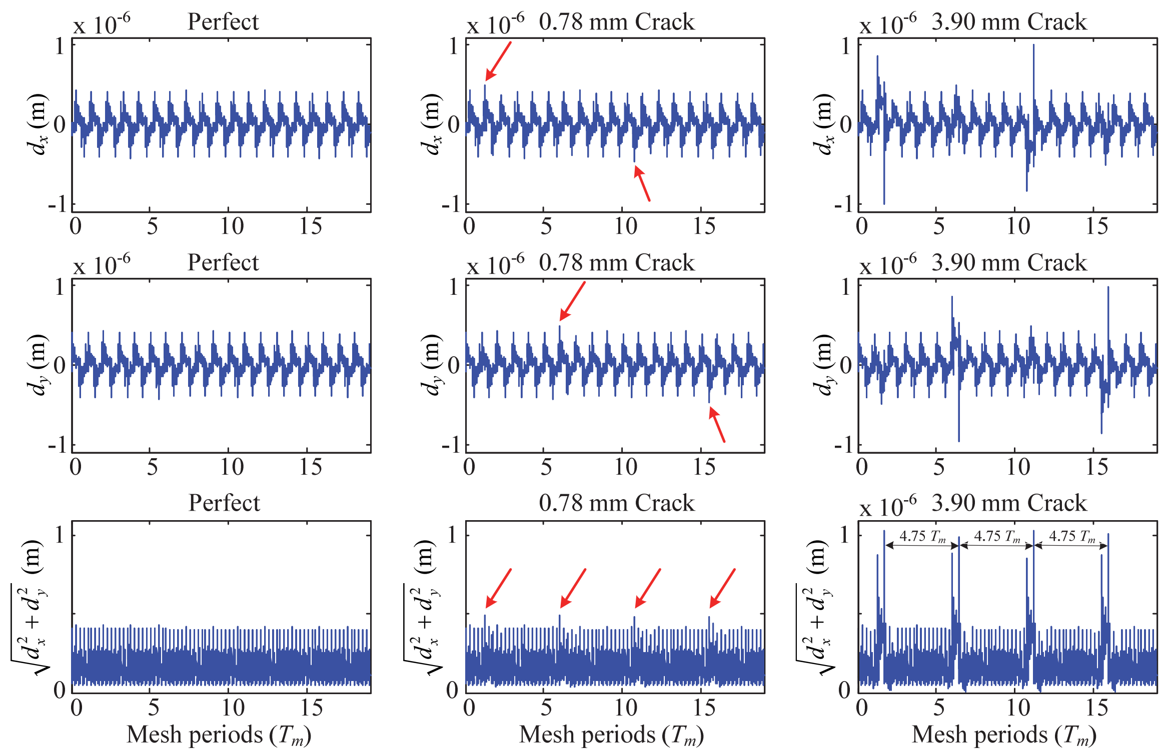

Fig. 4.6: Displacements of the sun gear at different crack levels
d_x: displacement in the x-direction; d_y: displacement in the y-direction

Fig. 4.7 depicts the center locus of the sun gear in one revolution of the carrier in three health conditions: perfect, 0.78 mm crack and 3.90 mm crack in one tooth of the sun gear. For this sun gear, the crack length is 3.90 mm when the crack propagates to the tooth centre line as indicated in Fig. 4.3. To demonstrate the fault symptom when there is a small crack, the vibration signals of 0.78 mm (3.90/5 mm) crack are simulated. According to Table 4.1, the ring gear has 81 teeth, thus in one revolution of the carrier, 81 gear meshes will occur. From Fig. 4.7, we can see 81 spikes in the perfect condition which correspond to the 81 gear meshes. When there is a crack, some even bigger spikes (fault symptom) can be observed from Fig. 4.7. In 81 gear meshes, the cracked tooth is involved in meshing in 17 or 18 times (81/4.75). 17 bigger spikes are illustrated in the crack condition of Fig. 4.7. However, when the crack length is 0.78 mm, the fault symptom is weak.

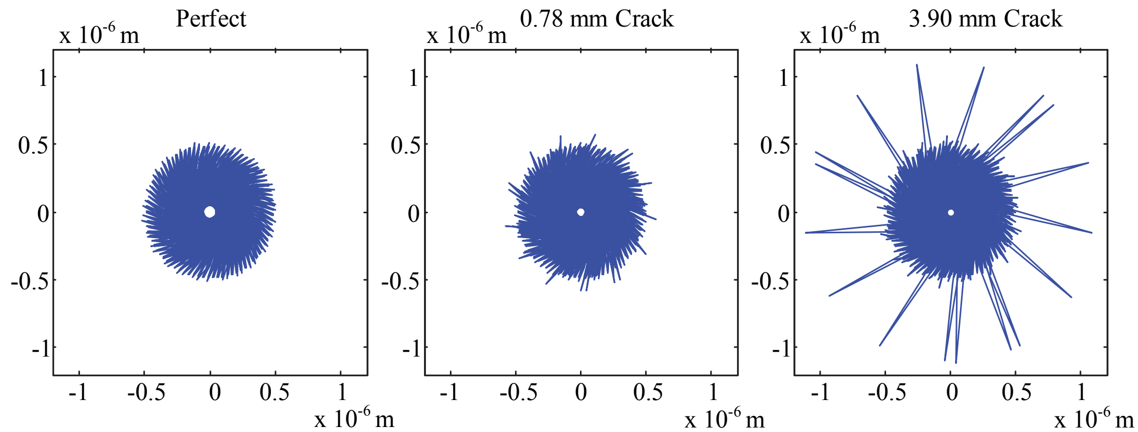

Fig. 4.7: Centre locus of the sun gear

From the displacement signals of the sun gear from Fig. 4.6 and Fig. 4.7, we can see clear fault symptoms when there is a crack in a sun gear tooth. However, in real applications, it is very hard to acquire the vibration signals of the sun gear. Inside a planetary gearbox, there are multiple vibration sources, because several pairs of sun-planet gears and several pairs of ring-planet gears mesh simultaneously. The vibration signals from these vibration sources will interfere with each other. In addition, due to the rotation of the carrier, the transmission paths of the vibration signals, from the vibration sources to a transducer, change. The effect of the multiple vibration sources and the effect of transmission path will lead to the complexity of the resultant vibration signals acquired by a transducer.

To demonstrate the effects of inertial force (including the gyroscopic force and the centrifugal force), I compared the dynamic responses of a planetary gearbox in two cases: considering the inertial force and ignoring the inertial force. Fig. 4.8 shows the y-direction displacement of the sun gear when the carrier is running at 8.87 RPM (correspondingly, the sun gear is running at 46.68 RPM) and 950 RPM (the sun gear is running at 5,000 RPM), respectively. For all the signals shown in Fig. 4.8, there is a 2.34 mm tooth crack in the sun gear. The time duration of the x-axis is one revolution of the sun gear (19 gear meshes). When the carrier is running at 8.87 RPM, there is no visible difference between the two signals with the inertial force considered and ignored (see Fig. 4.8). However, the inertial force effect is obvious when the carrier rotation speed is 5,000 RPM. As shown in Fig. 4.8, in the 5,000 RPM case, if the inertial force is incorporated in the dynamic model, the amplitude of gear vibration signal becomes small and the signal oscillation becomes slow. In addition, the fault symptom becomes weak when the inertial force is considered. Thus, it is essential to incorporate the inertial force in high speed applications in order to precisely reflect the real application. However, in the low speed applications, the inertial force is negligible.

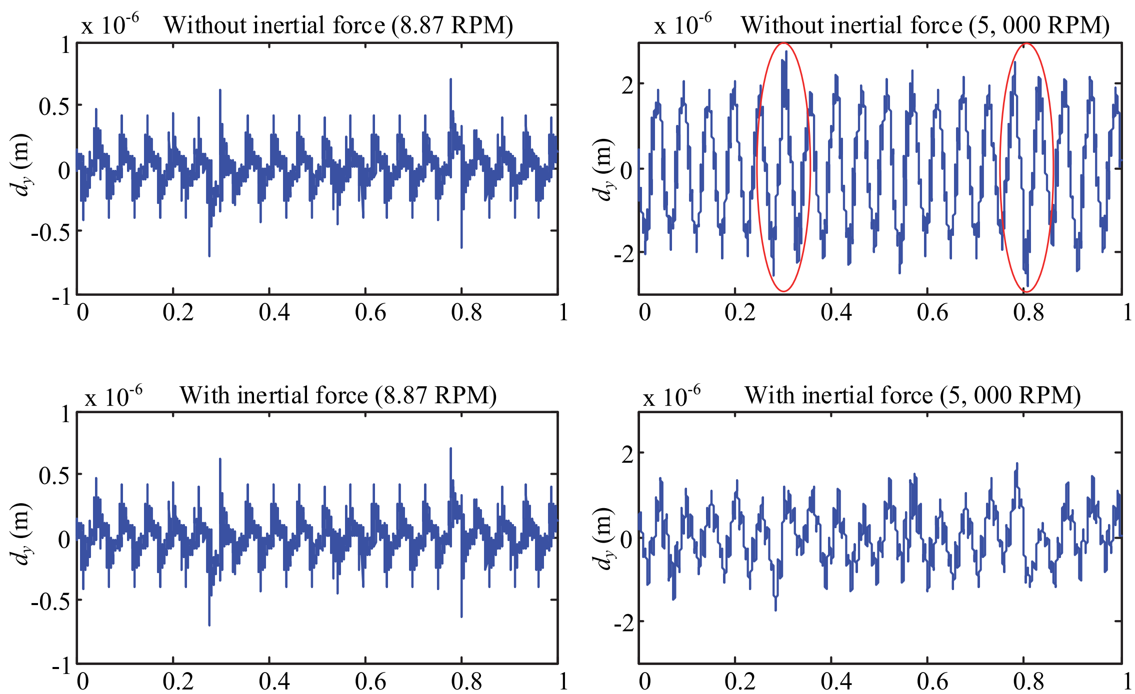

Fig. 4.8: Y-direction displacement of sun gear with a 2.34 mm crack on a sun gear tooth

4.2.4 Numerical validation

A numerical study is performed in this section to validate the correctness of the proposed dynamic model. The work of Lin and Parker [4.14] is the most relevant to our work. They developed an analytical model of a planetary gear set and used it to investigate the natural frequencies and vibration modes.

In this section, I will use their dynamic model to find the natural frequencies and then use our dynamic model to find the natural frequencies. A comparison of these obtained frequencies is used to validate our dynamic model.

Table 4.2 lists the physical parameters of the planetary gear set used in [4.14]. It can be seen that the mesh stiffness is considered constant, i.e. the system is time invariant. For the number of planets *N* from 3 to 5, they provided the obtained the eigen frequencies (natural frequencies) for each case in [4.14]. Using our dynamic model with the parameters specified in Table 4.2, we calculated the natural frequencies, and tabulated our results in Table 4.3. Our results match those of Ref. [4.14] (see Table 2 of Ref. [4.14]) very well. The largest difference in the obtained corresponding natural frequies is 0.4 Hz or 0.04% of the value reported in [4.14]. This means that our dynamic model is validated.

Table 4.2: Parameters of the example system used in [4.14]

Parameters	Sun	Ring	Carrier	Planet
Mass (kg)	0.40	2.35	5.43	0.66
I/r^2 (kg)	0.39	3.00	6.29	0.61
Base diameter (mm)	77.4	275.0	176.8	100.3
Mesh stiffness	$k_{sp} = k_{rp} = 5\times10^8$			
Torsional stiffness	$k_{rt} = 10^9$ $k_{spt} = k_{ct} = 0$			
Pressure angle	24.6°			

Table 4.3: Natural frequencies generated by our own Matlab codes

Multiplicity (m)	Number of planets (N)		
	N = 3	N = 4	N = 5
m = 1 (Rotational modes)	0	0	0
	1475.7	1536.5	1567.4
	1930.3	1970.6	2006.1
	2658.3	2625.6	2614.8
	7462.8	7773.6	8065.4
	11775.3	13071.1	14253.1
m = 2 (Translational modes)	743.2	727.0	710.0
	1102.4	1091.0	1072.4
	1896.0	1892.8	1888.1
	2276.4	2342.5	2425.3
	6986.3	7189.9	7382.3
	9647.9	10437.6	11172.3
m = N - 3 (Planet modes; exists for N>3)	---	1808.2	1808.2
	---	5963.8	5963.8
	---	6981.7	6981.7

4.3 Modeling the effect of transmission path

In this study, the resultant vibration signal is considered to be the summation of weighted vibration of each planet gear as shown in Eq. (4.3.1). The planet gear meshes with the sun gear and the ring gear simultaneously. Therefore, the vibration of the planet gear contains both the information of sun-planet mesh and ring-planet mesh. The effect of the transmission path is modeled as a modified Hamming function. The exponent expression in Eq. (4.3.1) can be used to increase or decrease the bandwidth of the Hamming function by choosing different α values. The value of α is determined by the properties of a gearbox, like its size, bearing characteristics, ring gear-housing interface and ring gear flexibility. A proper accounting of these effects would require a deformable-body dynamic model that can represent the transfer path between a given gear mesh and the point of measurement accurately [4.9]. Fig. 4.9 illustrates the differences of Hanning function, Hamming function and modified Hamming function corresponding to different α values. The bandwidth is increased when α is positive, and decreased when α is negative. However, we need to see that α cannot take a very large positive value. If α is very large, the effect of vibration from the farthest planet (distance to the transducer) is amplified, even overweight the effect of vibration from the nearest planet.

$$a(t) = \sum_{n=1}^{N} e^{\alpha(\mathrm{mod}(w_c t+\psi_n, 2\pi)-\pi)^2} H_n(t) a_n(\mathrm{t}), \tag{4.3.1}$$

where $H_n(t)$ represents Hamming function for the n^{th} planet gear and $a_n(\mathrm{t})$ is the acceleration signal of the n^{th} planet gear.

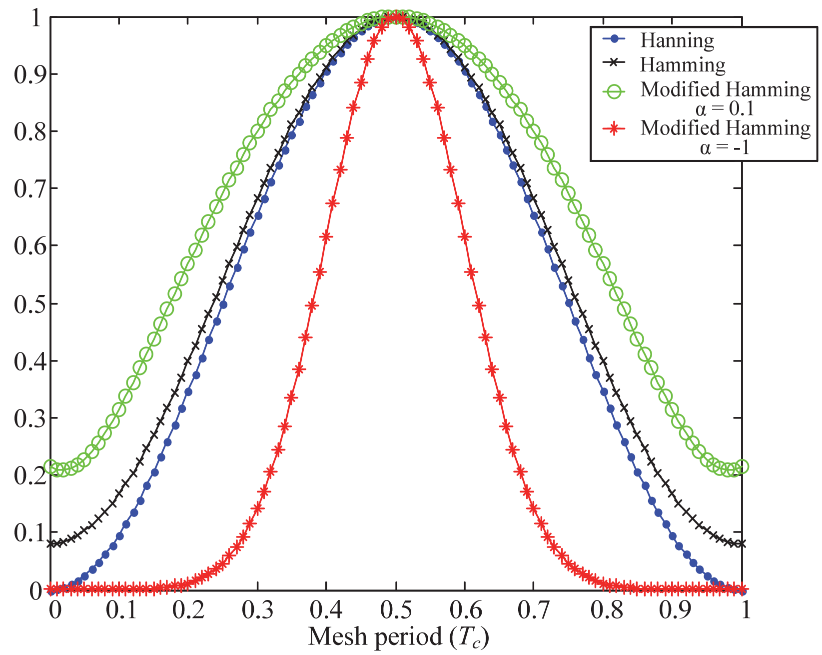

Fig. 4.9: Modelling of transmission path effect

4.4 Properties of resultant vibration signals

In this section, resultant vibration signals of a planetary gearbox are obtained and the vibration properties are investigated. Solving the dynamic equations in Section 4.2.1, we can get acceleration signals of each planet gear in the rotating carrier coordinate system. Applying the theory of acceleration in the rotating coordinate system [4.37], the absolute acceleration of each planet gear in the coordinate system fixed on the housing of a gearbox can be attained. In this study, only the vertical direction (y-direction) of the resultant acceleration signals is considered. The resultant acceleration signals of a planetary gearbox in the y-direction are expressed as the weighted summation of the y-direction acceleration signal of each planet gear.

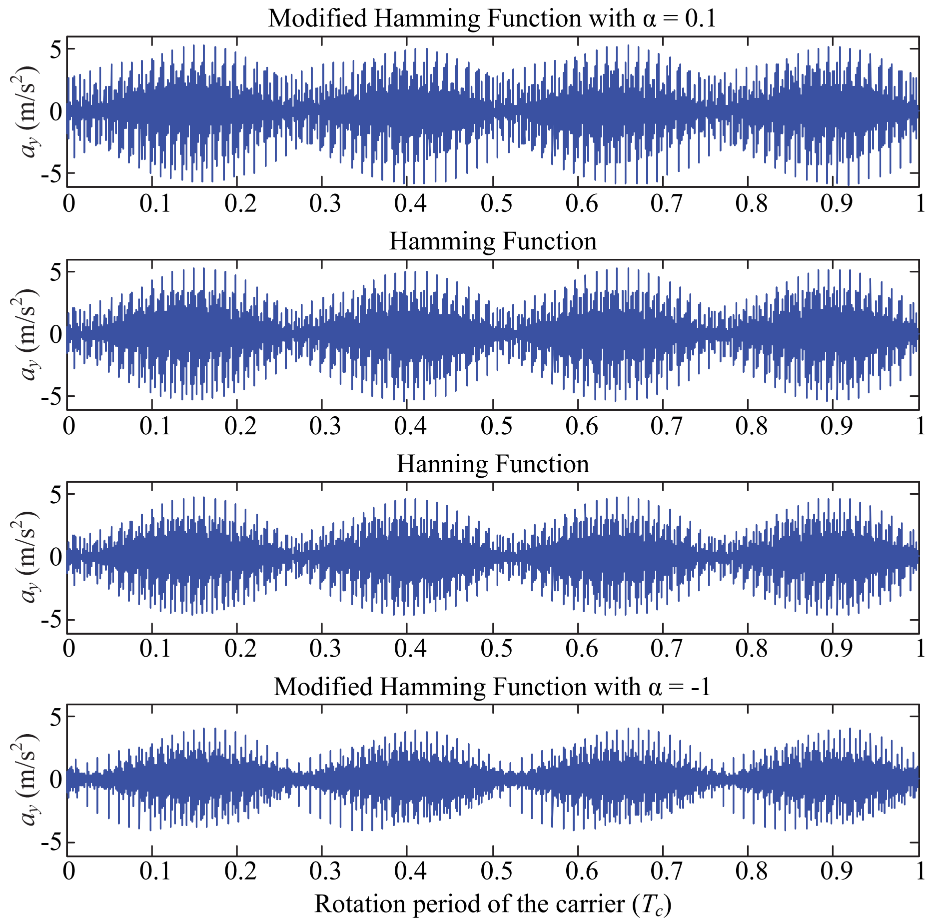

Fig. 4.10: Simulated resultant vibration signals for different transmission path effects

Fig. 4.10 shows the y-direction acceleration signals of a planetary gearbox at four different cases (the effect of transmission path is represented by a modified Hamming function with α = 0.1, Hamming function, Hanning function and modified Hamming function with α = -1). We can see amplitude modulation in all the cases; however, the degree of the amplitude modulation is different. The amplitude modulation is strongest when the effect of the transmission path is represented by a modified Hamming function with α = -1. The second strongest one is in the case of Hanning function. The weakest one is in the case of modified Hamming function with α = 0.1. In addition, we can observe that amplitudes of the vibration signals in the four cases are different. The signal amplitude is largest when the effect of the transmission path is represented by a modified Hamming function with $\alpha = 0.1$, while the signal amplitude is smallest when the effect of the transmission path is represented by a modified Hamming function with $\alpha = -1$. The advantage of the modified Hamming function is capable of representing the effect of different transmission paths while the Hanning function can represent only one specific transmission path.

However, this study does not intend to propose a method to find the optimum value of α for a given planetary gearbox. The selection of α will be investigated in our future work. I have simply tried a few values of α which are 0.1, 0 and -1.0. Correspondingly the modified Hamming function has the values of 0.21, 0.08 and 0.03 when the planet gear is in the farthest location from the transducer. The simulated resultant vibration signals for these α values are presented in Fig. 4.10. Visually comparing the simulated vibration signals shown in Fig. 4.10 with the experimental vibration signal in the perfect condition of the gearbox shown in Fig. 4.17, I believe that the simulated vibration signals match the experimental signals the best when α takes the value of 0.1. Therefore, I have selected α to be 0.1 in the case study. When α takes the value of 0.1, it means that 21% of the vibration amplitude of the planet gear which is at the farthest location from the transducer can be sensed by the transducer. In the following discussions, Hamming function (α=0.1) is used to reflect the effect of the transmission path.

Vibration properties of the resultant vibration signals are studied when the planetary gearbox is in three health conditions: perfect, 0.78 mm crack in a sun gear tooth, and 3.90 mm crack in a sun gear tooth. Fig. 4.11 shows resultant vibration signals of a planetary gearbox (parameters are listed in Table 4.1). The symbol α_y represents vertical direction acceleration of the gearbox. Amplitude modulation can be observed both in the perfect condition and in the crack condition. Signal envelope fluctuates four times in one revolution of the carrier as four planets pass through the transducer location sequentially. In the meshing period of the cracked tooth, a bigger spike should be generated. As we know, in one revolution of the carrier, the cracked tooth will mesh 17 or 18 times. When the crack length is 0.78 mm, the fault symptom is very weak. Only three bigger spikes (the locations are indicated by the arrows) can be visually observable. In the 3.90 mm crack condition, 17 bigger spikes are observed. However, some spikes are attenuated strongly (the circled area) due to the effect of the transmission path.

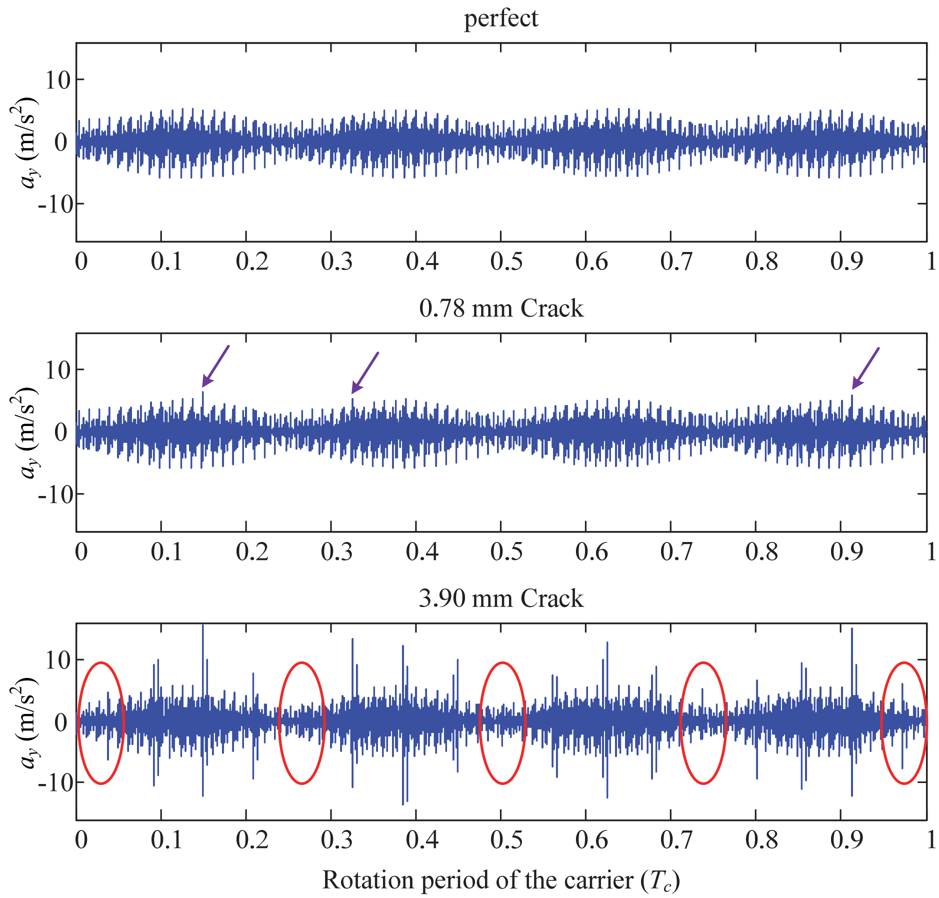

Fig. 4.11: Simulated resultant vibration signals in the y-direction

Fig. 4.12 illustrates the frequency spectrum of the resultant vibration signal in different health conditions. In the perfect condition, there are nearly zero amplitude at the gear mesh frequency f_m and its harmonics. Sizable amplitudes show in the following locations: nf_m if n is an integer and a multiple of 4, $nf_m \pm f_c$ if n is an odd integer, $nf_m \pm 2f_c$ if n is an even integer but not a multiple of 4. The symbol f_c denotes rotation frequency of the carrier. In this study, I represent the above mentioned sizable amplitude frequencies by the symbol f_{main}. This finding confirms the results reported in [4.9] that sizable amplitudes appear at carrier order $H = nN$ in the vicinity of gear mesh frequency and its harmonics (n: integer, N: Number of planet gears). For example, the largest amplitude frequency $59f_m+f_c$ locates in the vicinity of 59th harmonic of gear mesh frequency. While, $59f_m+f_c$ equals to 4780 f_c (f_m = 81 f_c) which is the location of 4780 carrier order. The number 4780 is a multiple of 4 which is the number of planet gears. We also can observe from Fig. 4.12 that if there is crack on a sun gear tooth, the amplitude of frequencies f_{main} are rarely affected. However, a lot of sidebands appear in the vicinity of f_{main}.

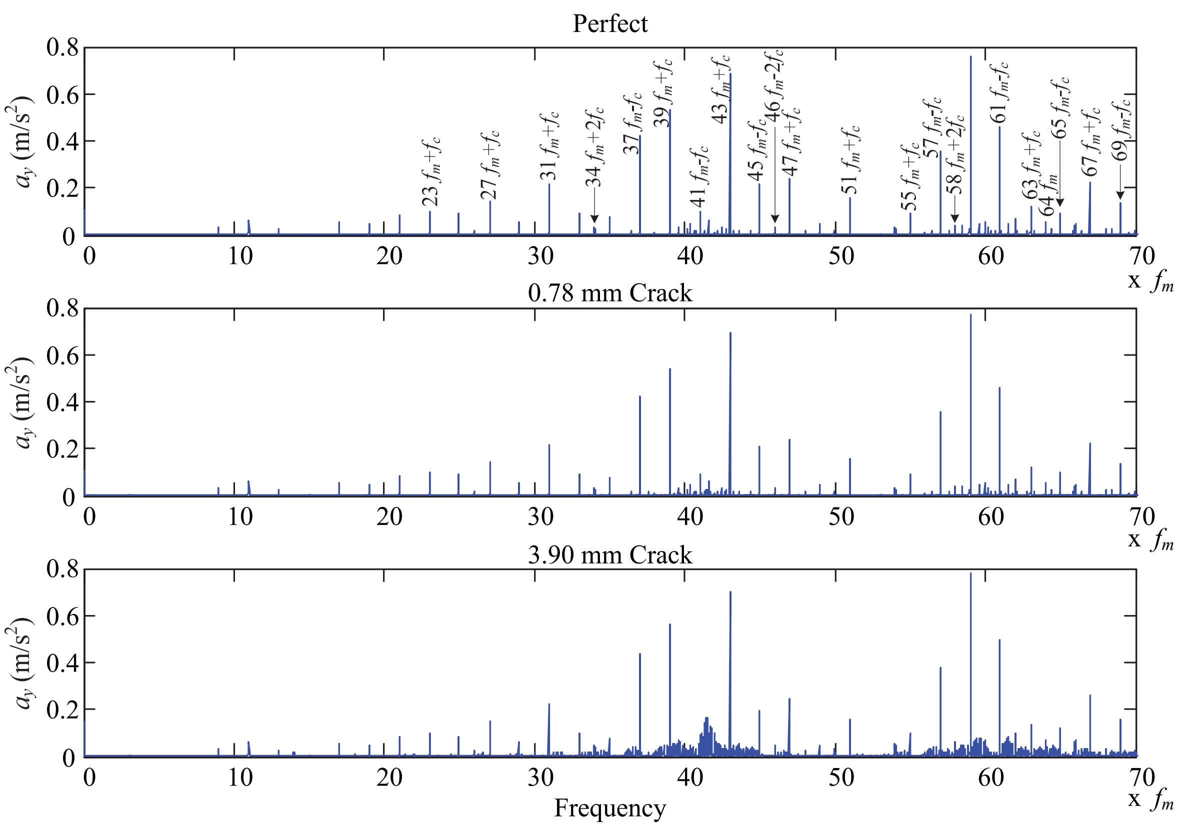

Fig. 4.12: Frequency spectrum of simulated resultant vibration signals

Fig. 4.13 presents the zoomed-in plot of the frequency region from $42f_m$ to $44f_m$. We can see a large amount of sidebands appear but they are not symmetric. Sizable sidebands appear in the following locations: $f_{main} \pm kf_{scrack} \pm mf_s \pm nf_p \pm f_c$ (k, m, and n are integers). For the planetary gear set used in this study, k, m, and n can take the following values: k = 0, 1, 2, 3, 4; m = 0, 1, 2; n = 0, 1, 2, 3, 4. f_s and f_p denotes the rotation frequency of the sun gear and the planet gear, respectively, while f_{scrack} represents the characteristic frequency of the cracked sun gear, which can be calculated as follows [4.10]:

$$f_{scrack} = f_m \times N / Z_{sun}, \tag{4.4.1}$$

where N represents the number of planet gears and Z_{sun} denotes the teeth number of sun gear.

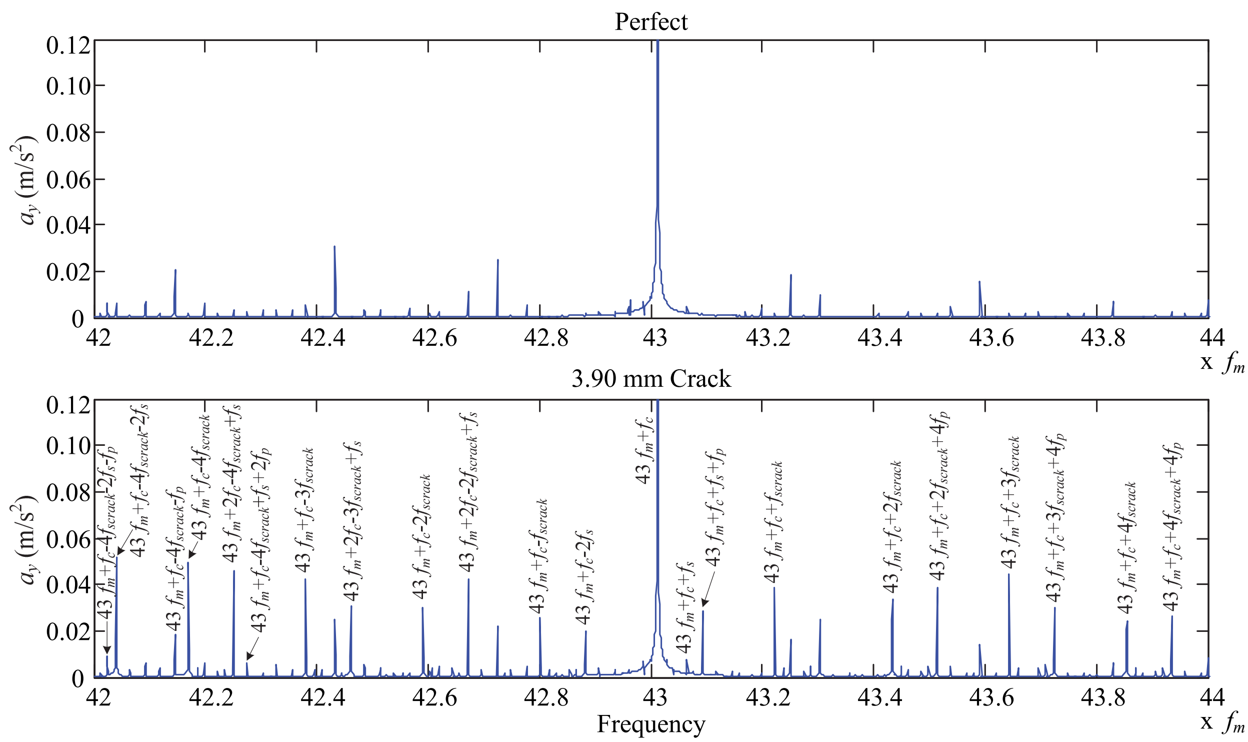

Fig. 4.13: Zoomed-in frequency spectrum of simulated resultant vibration signals

4.5 Comparisons with experimental signals

Experimental signals acquired from a gearbox test rig as reported in [4.39] are used in this study to validate the fault symptoms found in this study. The configuration of the test rig is shown in Fig. 4.14 and the parameters of the gears are listed in Table 4.4. This test rig has a 20 HP drive motor, a one stage bevel gearbox, two stages of planetary gearboxes, two stages of speed-up gearboxes, and a 40 HP load motor. The drive motor is on the first platform, the bevel gearbox and the planetary gearboxes are on the second platform, and the two speed-up gearboxes and the load motor are on the third platform. An acceleration sensor is installed in the vertical direction of the casing of the second stage planetary gearbox to acquire the vibration signals. All the gears in the planetary gearboxes are standard spur gears without tooth profile modification.

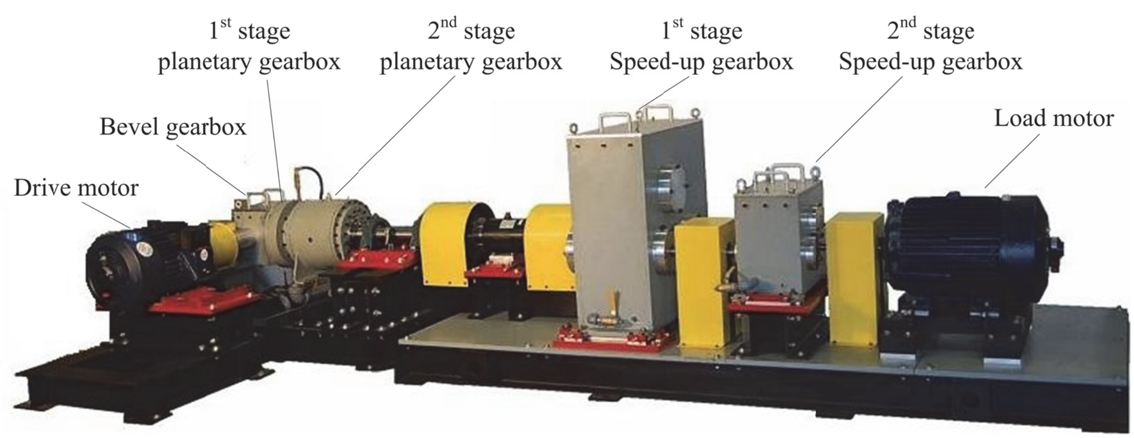

Fig. 4.14: An experimental test rig

Fig. 4.15 shows a diagram of the structure of the two stage planetary gearbox [4.38]. As stated in [4.38]: "The 1st stage sun gear is mounted on the right side of shaft #1 with the driven bevel gear mounted on the left side. The 1st stage planet gears are located on the 1st stage carrier which is connected to shaft #2. The 2nd stage sun gear is mounted on the other side of shaft #2. The 2nd stage planet gears are mounted on the 2nd stage carrier located on output shaft #3. The ring gears of the 1st and 2nd stages are mounted on the housing od the corresponding stage." The detailed experimental procedures and data collection are documented in [4.39, 4.40].

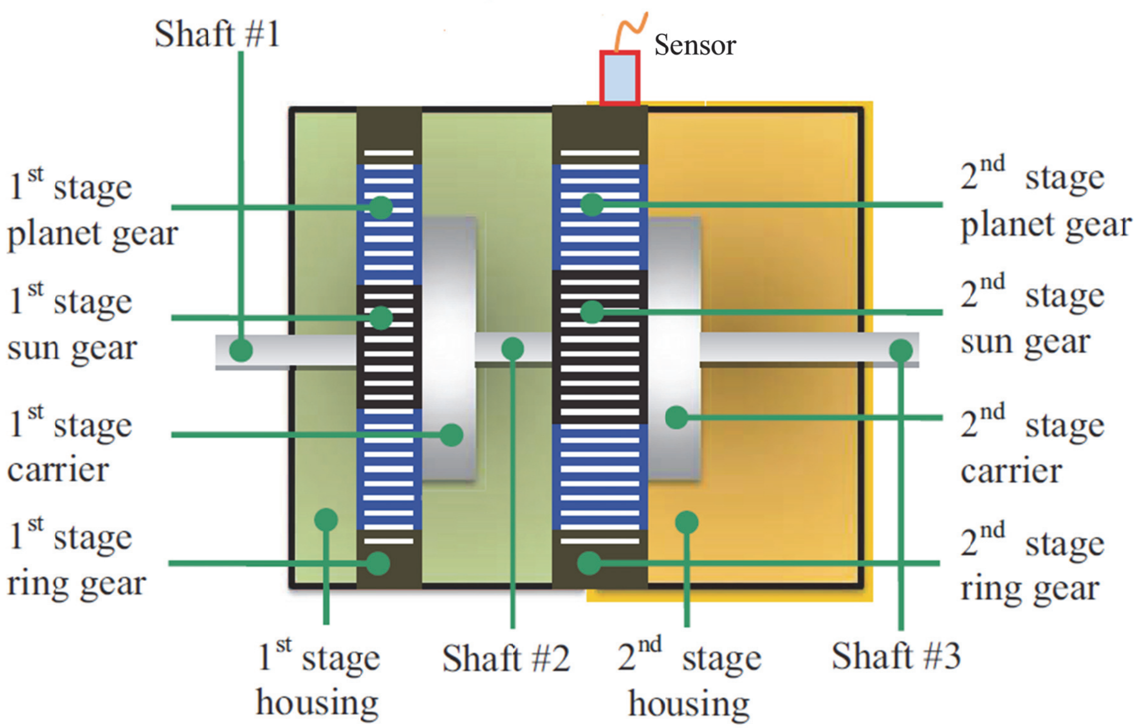

Fig. 4.15: Diagram of two-stage planetary gearboxes [4.38]

The vibration data was acquired when the rotation frequency of the motor was 1200 RPM. Thus, the rotation speed of the sun gear of the second stage planetary gearbox is 46.66 RPM which is the same as the simulated sun gear speed in the Section 4.2.3. To simulate the crack effect on the vibration signals, tooth crack was manually created in the sun gear tooth using the electro discharge machining. When the crack length is small, fault symptoms may submerge in the noise and hard to distinguish. To amplify the fault symptoms, 3.9 mm tooth crack was created in the sun gear tooth. The crack goes through the whole tooth width as shown in Fig. 4.16. The simulated planetary gear set has the same configuration and gear parameters as the second stage planetary gear set.

Table 4.4: Physical parameters of the experimental test rig

Gearbox	Bevel stage		First stage planetary gearbox			Second stage planetary gearbox		
Gear	Input	Output	Sun	Planet	Ring	Sun	Planet	Ring
No. of teeth	18	72	28	62 (4)	152	19	31 (4)	81
Transmission ratio	4		6.429			5.263		

Note: The number of planet gears is indicated in the parenthesis.

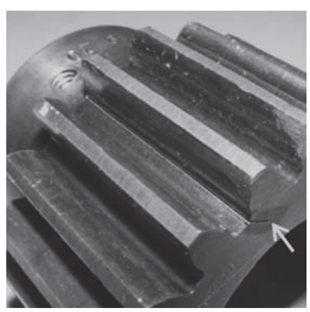

Fig. 4.16: 3.9 mm manually made tooth crack in the sun gear

Fig. 4.17 shows the experimental acceleration signals of the second stage planetary gearbox in the perfect condition. The symbol α_y denotes the vertical direction acceleration of the gearbox. Amplitude modulation presents in the perfect condition of the gearbox and signal envelope fluctuates four times in one revolution of the carrier. Fig.

4.18 describes the experimental acceleration signals of the second stage planetary gearbox both in the perfect condition and in the cracked tooth condition. In the cracked tooth condition, some even bigger spikes show up. In addition, the amplitude modulation is not very obvious, as amplitude modulation and fault signatures together lead to the complexity of the vibration signals.

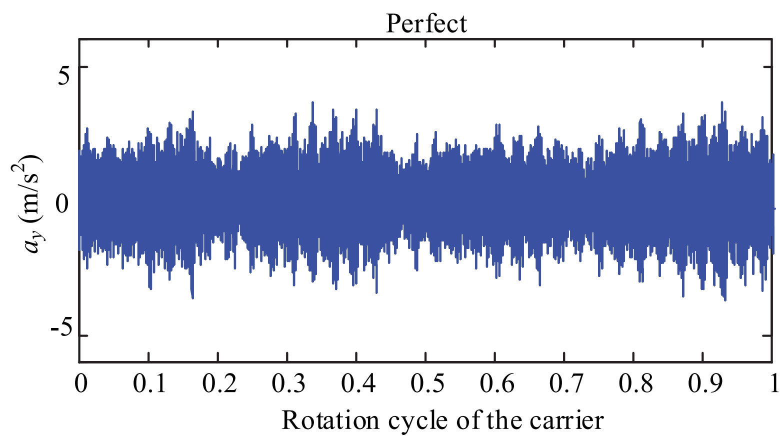

Fig. 4.17: Experimental resultant vibration signal in perfect condition

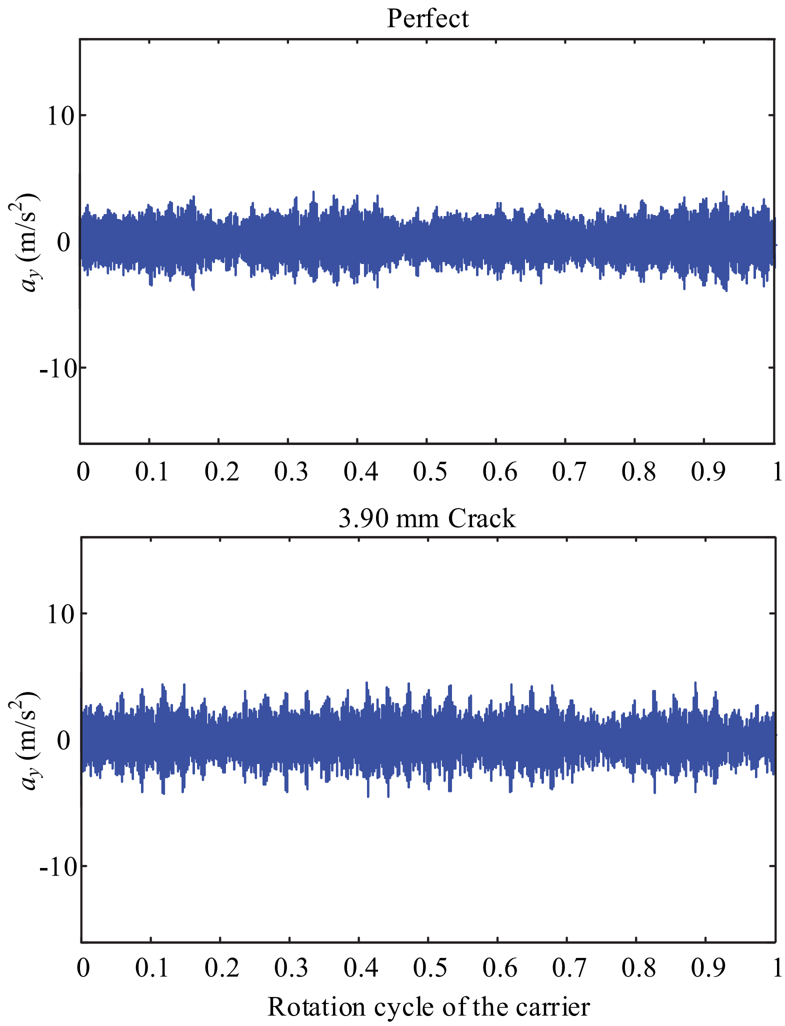

Fig. 4.18: Experimental resultant vibration signals in perfect and cracked tooth conditions

Fig. 4.19 illustrates the frequency spectrum of the experimental signals. In the perfect condition, sizable amplitudes show in the following locations (f_{main}): nf_m if n is an integer and a multiple of 4, $nf_m \pm f_c$ if n is an odd integer, $nf_m \pm 2f_c$ if n is an even integer but not a multiple of 4. When crack is in the sun gear tooth, many sidebands show in the vicinity of f_{main} which is most obvious in the region of $40f_m$ to $50f_m$.

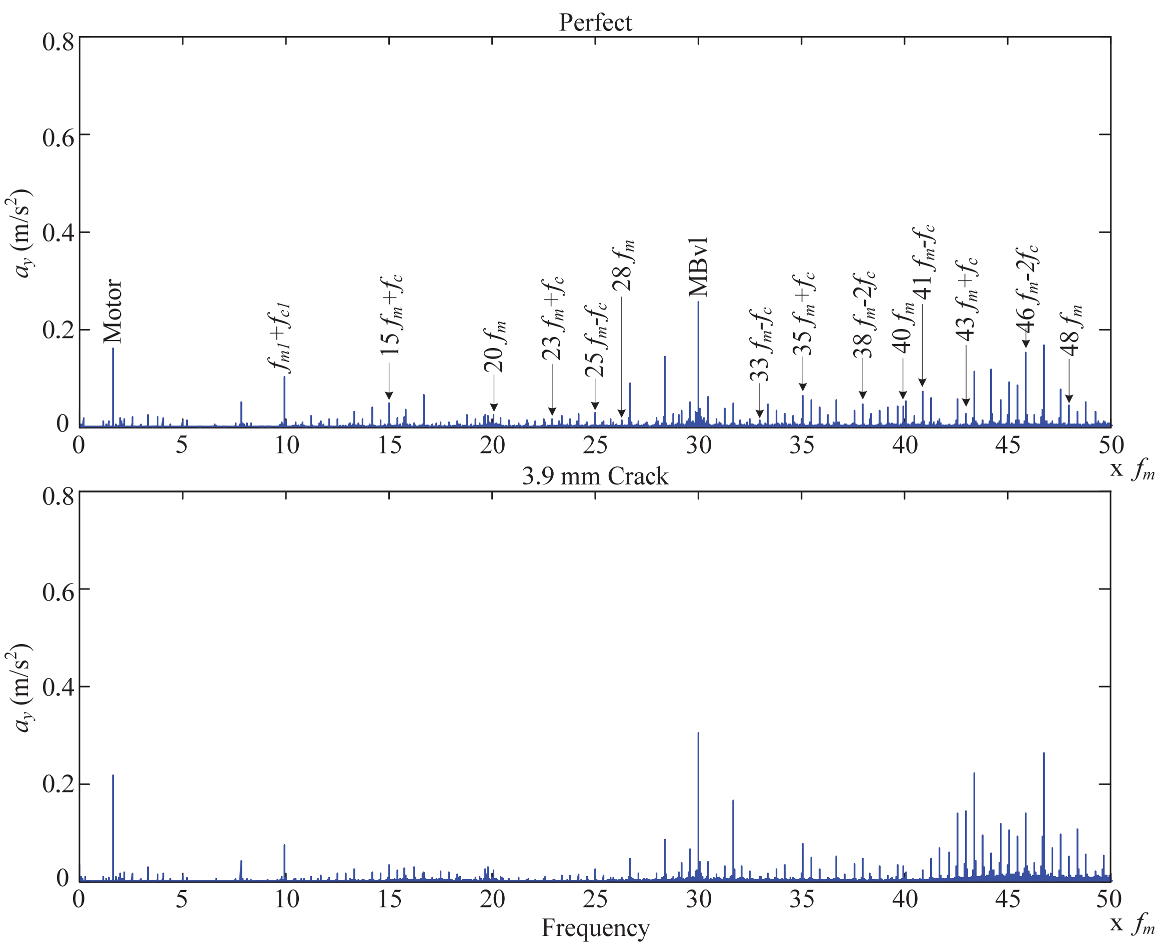

Fig. 4.19: Frequency spectrum of experimental vibration signals

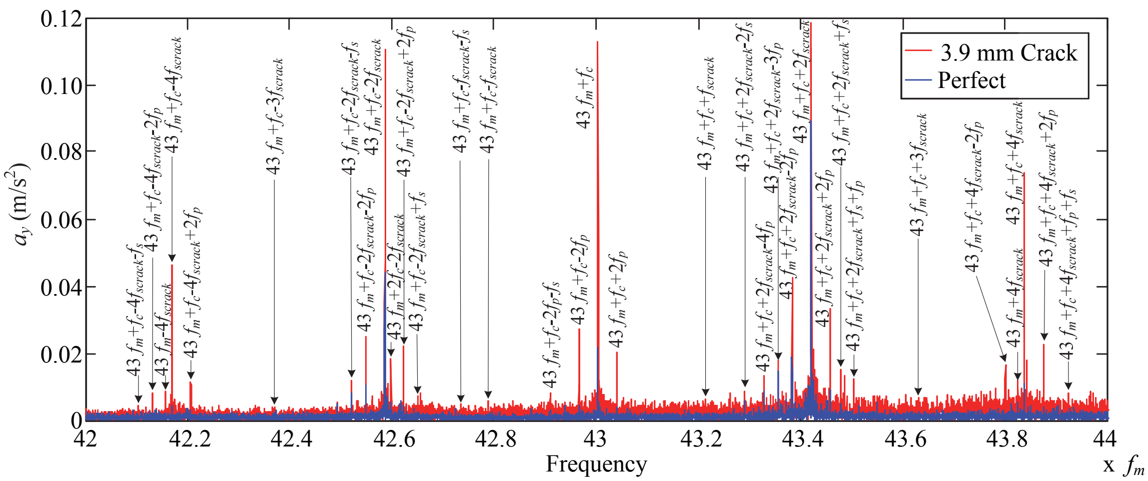

Fig. 4.20: Zoomed-in frequency spectrum of experimental vibration signals

Fig. 4.20 presents the zoomed-in frequency spectrum of the experimental signals from $42f_m$ to $44f_m$. The sidebands are asymmetric and sizable sidebands appear in the following locations: $f_{main} \pm kf_{scrack} \pm mf_s \pm nf_p \pm f_c$. The integers of k, m, and n take the following values: k = 0, 1, 2, 3, 4; m = 0, 1, 2; n = 0, 1, 2, 3, 4. These results confirm the proposed results in Section 4.

In this paragraph, the amplitudes of the simulated vibration signals and experimental signals are compared. In the time domain, the maximum amplitude of the simulated signal is about 5 m/s^2 when the gearbox is perfect as shown in Fig. 4.11. By contrast, the maximum amplitude of the experimental signal is about 4 m/s^2 when the gearbox is perfect as shown in Fig. 4.18. In the condition of 3.90 mm crack, some bigger spikes (fault symptom) are generated in the simulated signal. The amplitude of the bigger spikes reaches to about 10 m/s^2. In the experimental signal of 3.90 mm crack, we can see some bigger spikes present. But the amplitude of these spikes is only about 5 m/s^2. In the frequency domain of a healthy gearbox, the amplitude of sizable frequency components reaches up to 0.8 m/s^2. However, the amplitude of experimental signals reaches to only 0.2 m/s^2. When there is 3.90 mm crack in a sun gear tooth, there is no big change of the amplitude of sizable frequency components both in the simulated signals and in the experimental signals. Some sidebands appear both in the simulated signals and experimental signals. The amplitude difference of sidebands of simulated signals and experimental signals is small. The amplitude of most of the sidebands is below 0.05 m/s^2 both in the simulated signals and experimental signals. Only three sidebands are over 0.05 m/s^2 in the experimental signals, namely $43f_m + f_c - 2f_{scrack}$, $43f_m + f_c + 2f_{scrack}$, and $43f_m + f_c + 2f_{scrack}$. There are three possible reasons to explain the amplitude differences between the numerical and experimental results. Firstly, the numerical model only simulated one stage of planetary gearbox. While the experimental test rig is quite complicated. It includes one stage of bevel gear, two stages of planetary gearboxes and two stages of fixed-shaft gearboxes. Secondly, the shaft mass is not considered in the simulated model, while in the test rig, a very heavy shaft going through the whole system. The big mass of the shaft will damp the amplitude of the vibration. Thirdly, the dynamic model did not consider the damping effect of the connection between gearbox housing and the ground. The gearbox test rig is fixed on the ground by several screws. The damping effect of the screw will also damp the amplitude of the vibration. All these damping effect will limit the amplitude of big spikes. The proposed model finds some properties of a stage of planetary gearbox; however, efforts are still needed to improve the numerical model, like reducing the amplitude difference between the numerical signals and experimental signals.

In summary, the comparisons between simulated signals and experimental signals summarized above are not very conclusive. Some vibration properties present in the simulated signals are confirmed by those in the experimental signals. These properties may be useful for gearbox fault detection. However, there are still many vibration features present in the experimental vibration signals are not present in the simulated signals. This means that either further improvement is required for the proposed vibration signal modeling method or better designed experiments need to be conducted for a more fair comparison.

4.6 Conclusions

In this chapter, a theoretical model is proposed to simulate the resultant vibration signals of a planetary gearbox in healthy and cracked tooth conditions. A lumped-parameter model is developed to simulate the vibration signals of each gear, including the sun gear, the planet gears and the ring gear. A mathematical model is proposed to reflect the effect of the transmission path. Incorporating multiple vibration sources and the effect of transmission path, the resultant vibration signals at the sensor location are simulated. The fault symptoms are found obvious in the time domain vibration signals of an individual gear, like the sun gear. However, the fault symptoms attenuate in the resultant vibration signal at the sensor location. Besides, obvious amplitude modulation is observed in the resultant vibration signal due to the rotation of the carrier. In the frequency domain, a large number of sidebands appear when there is a crack in the sun gear tooth. These sidebands are investigated and located in the simulated signals, which can be used to detect the crack fault. Some of the vibration properties found by the proposed signal modeling method also appear in the experimental signals. These properties found in the time domain will be used in Chapter 5 for the development of a fault detection method. However, future work is needed for further experimental validation of the resultant signal model.

References

[4.1] X. Liang, M. J. Zuo, and M. R. Hoseini, "Vibration Signal Modeling of a Planetary Gear Set for Tooth Crack Detection," *Eng. Fail. Anal.*, vol. 48, pp. 185–200, Feb. 2015.

[4.2] X. Liang, M. J. Zuo, and M. R. Hoseini, "Understanding Vibration Properties of a Planetary Gear Set for Fault Detection," in *Proceedings of 2014 IEEE Conference on Prognostics and Health Management (PHM)*, 2014, pp. 1–6.

[4.3] D. M. Blunt and J. A. Keller, "Detection of a Fatigue Crack in a UH-60A Planet Gear Carrier Using Vibration Analysis," *Mech. Syst. Signal Process.*, vol. 20, no. 8, pp. 2095–2111, Nov. 2006.

[4.4] Y. Lei, D. Kong, J. Lin, and M. J. Zuo, "Fault Detection of Planetary Gearboxes Using New Diagnostic Parameters," *Meas. Sci. Technol.*, vol. 23, no. 5, p. 055605, May 2012.

[4.5] J. Liu, W. Wang, and F. Golnaraghi, "An Extended Wavelet Spectrum for Bearing Fault Diagnostics," *IEEE Trans. Instrum. Meas.*, vol. 57, no. 12, pp. 2801–2812, Dec. 2008.

[4.6] A. K.S. Jardine, D. Lin, and D. Banjevic, "A Review on Machinery Diagnostics and Prognostics Implementing Condition-based Maintenance," *Mech. Syst. Signal Process.*, vol. 20, no. 7, pp. 1483–1510, Oct. 2006.

[4.7] J. Antoni, "Blind Separation of Vibration Components: Principles and Demonstrations," *Mech. Syst. Signal Process.*, vol. 19, no. 6, pp. 1166–1180, Nov. 2005.

[4.8] B. Zhang, T. Khawaja, R. Patrick, G. Vachtsevanos, M. Orchard, and A. Saxena, "A Novel Blind Deconvolution De-noising Scheme in Failure Prognosis," *Trans. Inst. Meas. Control*, vol. 32, no. 1, pp. 3–30, Feb. 2010.

[4.9] M. Inalpolat and A. Kahraman, "A Theoretical and Experimental Investigation of Modulation Sidebands of Planetary Gear Sets," *J. Sound Vib.*, vol. 323, no. 3–5, pp. 677–696, Jun. 2009.

[4.10] Z. Feng and M. J. Zuo, "Vibration Signal Models for Fault Diagnosis of Planetary Gearboxes," *J. Sound Vib.*, vol. 331, no. 22, pp. 4919–4939, Oct. 2012.

[4.11] Z. Tian, M. J. Zuo, and S. Wu, "Crack Propagation Assessment for Spur Gears Using Model-based Analysis and Simulation," *J. Intell. Manuf.*, vol. 23, no. 2, pp. 239–253, Apr. 2012.

[4.12] A. Kahraman, "Load Sharing Characteristics of Planetary Transmissions," *Mech. Mach. Theory*, vol. 29, no. 8, pp. 1151–1165, Nov. 1994.

[4.13] M. Inalpolat and A. Kahraman, "A Dynamic Model to Predict Modulation Sidebands of a Planetary Gear Set Having Manufacturing Errors," *J. Sound Vib.*, vol. 329, no. 4, pp. 371–393, Feb. 2010.

[4.14] J. Lin and R. G. Parker, "Analytical Characterization of the Unique Properties of Planetary Gear Free Vibration," *J. Vib. Acoust.*, vol. 121, no. 3, pp. 316–321, Jul. 1999.

[4.15] Z. Cheng, N. Hu, F. Gu, and G. Qin, "Pitting Damage Levels Estimation for Planetary Gear Sets Base on Model Simulation and Grey Relational Analysis," *Trans. Can. Soc. Mech. Eng.*, vol. 35, no. 3, pp. 403–417, 2011.

[4.16] F. Chaari, T. Fakhfakh, R. Hbaieb, J. Louati, and M. Haddar, "Influence of Manufacturing Errors on the Dynamic Behavior of Planetary Gears," *Int. J. Adv. Manuf. Technol.*, vol. 27, no. 7–8, pp. 738–746, Jan. 2006.

[4.17] T. Eritenel and R. G. Parker, "Nonlinear Vibration of Gears With Tooth Surface Modifications," *J. Vib. Acoust.*, vol. 135, no. 5, pp. 051005–051005, Jun. 2013.

[4.18] C.-J. Bahk and R. G. Parker, "Analytical Investigation of Tooth Profile Modification Effects on Planetary Gear Dynamics," *Mech. Mach. Theory*, vol. 70, pp. 298–319, Dec. 2013.

[4.19] Z. Chen and Y. Shao, "Mesh Stiffness Calculation of a Spur Gear Pair with Tooth Profile Modification and Tooth Root Crack," *Mech. Mach. Theory*, vol. 62, pp. 63–74, Apr. 2013.

[4.20] Y. Shao and Z. Chen, "Dynamic Features of Planetary Gear Set with Tooth Plastic Inclination Deformation Due to Tooth Root Crack," *Nonlinear Dyn.*, vol. 74, no. 4, pp. 1253–1266, Dec. 2013.

[4.21] T. Barszcz and R. B. Randall, "Application of Spectral Kurtosis for Detection of a Tooth Crack in the Planetary Gear of a Wind Turbine," *Mech. Syst. Signal Process.*, vol. 23, no. 4, pp. 1352–1365, May 2009.

[4.22] D. G. Lewicki, K. E. LaBerge, R. T. Ehinger, and J. Fetty, "Planetary Gearbox Fault Detection Using Vibration Separation Techniques," National Aeronautics and Space Administration, Glenn Research Center, Technical Report NASA/TM—2011-217127, 2011.

[4.23] Z. Chen and Y. Shao, "Dynamic Simulation of Planetary Gear with Tooth Root Crack in Ring Gear," *Eng. Fail. Anal.*, vol. 31, pp. 8–18, Jul. 2013.

[4.24] F. Chaari, T. Fakhfakh, and M. Haddar, "Dynamic Analysis of a Planetary Gear Failure Caused by Tooth Pitting and Cracking," *J. Fail. Anal. Prev.*, vol. 6, no. 2, pp. 73–78, Apr. 2006.

[4.25] X. Liang, M. J. Zuo, and T. H. Patel, "Evaluating the Time-varying Mesh Stiffness of a Planetary Gear Set Using the Potential Energy Method," *Proc. Inst. Mech. Eng. Part C J. Mech. Eng. Sci.*, vol. 228, no. 3, pp. 535–547, Feb. 2014.

[4.26] Z. Chen and Y. Shao, "Dynamic Features of a Planetary Gear System with Tooth Crack under Different Sizes and Inclination Angles," *J. Vib. Acoust.*, vol. 135, no. 3, pp. 1–12, Mar. 2013.

[4.27] C. G. Cooley and R. G. Parker, "Unusual Gyroscopic System Eigenvalue Behavior in High-Speed Planetary Gears," *J. Sound Vib.*, vol. 332, no. 7, pp. 1820–1828, Apr. 2013.

[4.28] X. Gu and P. Velex, "A Dynamic Model to Study the Influence of Planet Position Errors in Planetary Gears," *J. Sound Vib.*, vol. 331, no. 20, pp. 4554–4574, Sep. 2012.

[4.29] T. Eritenel and R. G. Parker, "An Investigation of Tooth Mesh Nonlinearity and Partial Contact Loss in Gear Pairs Using a Lumped-parameter Model," *Mech. Mach. Theory*, vol. 56, pp. 28–51, Oct. 2012.

[4.30] X. Liang, M. J. Zuo, and M. Pandey, "Analytically Evaluating the Influence of Crack on the Mesh Stiffness of a Planetary Gear Set," *Mech. Mach. Theory*, vol. 76, pp. 20–38, Jun. 2014.

[4.31] F. Chaari, W. Baccar, M. S. Abbes, and M. Haddar, "Effect of Spalling or Tooth Breakage on Gearmesh Stiffness and Dynamic Response of a One-stage Spur Gear Transmission," *Eur. J. Mech. - ASolids*, vol. 27, no. 4, pp. 691–705, Jul. 2008.

[4.32] A. Belsak and J. Flasker, "Detecting Cracks in the Tooth Root of Gears," *Eng. Fail. Anal.*, vol. 14, no. 8, pp. 1466–1475, Dec. 2007.

[4.33] D. C. H. Yang and J. Y. Lin, "Hertzian Damping, Tooth Friction and Bending Elasticity in Gear Impact Dynamics," *J. Mech. Des.*, vol. 109, no. 2, pp. 189–196, Jun. 1987.

[4.34] S. Wu, M. J. Zuo, and A. Parey, "Simulation of Spur Gear Dynamics and Estimation of Fault Growth," *J. Sound Vib.*, vol. 317, no. 3–5, pp. 608–624, Nov. 2008.

[4.35] R. G. Parker and J. Lin, "Mesh Phasing Relationships in Planetary and Epicyclic Gears," *J. Mech. Des.*, vol. 126, no. 2, pp. 365–370, May 2004.

[4.36] D. J. Inman, *Engineering Vibration*. Prentice Hall, 2001.

[4.37] R. C. Hibbeler, *Engineering Mechanics: Dynamics*. Pearson/Prentice Hall, 2004.

[4.38] J. Qu, "Support-Vector-Machine-Based Diagnostics and Prognostics for Rotating Systems," PhD Thesis, University of Alberta, 2011.

[4.39] M. Pandey, T. Patel, X. Liang, T. Tian, and M. Zuo, "Descriptions of Pitting Experiments, Run-to-failure Experiments, Various Load and Speed Experiments, and Crack Experiments Carried Out on the Planetary Gearbox Test Rig," Reliability Research Lab, Mechanical Department, University of Alberta, Technical Report, 2011.

[4.40] Z. Feng and M. J. Zuo, “Fault diagnosis of planetary gearboxes via torsional vibration signal analysis,” *Mech. Syst. Signal Process.*, vol. 36, no. 2, pp. 401–421, Apr. 2013.

Chapter 5: A Windowing and Mapping Strategy for Gear Tooth Fault Detection of a Planetary Gearbox

In Chapter 4, the resultant vibration signals of a planetary gear set at a sensor location are simulated and the vibration properties are investigated. The fault symptom found in Chapter 4 enlightens the development of a tooth fault detection method in this chapter. This chapter aims to develop a windowing and mapping strategy to decompose the vibration signal of a planetary gearbox into the tooth level of a planet gear to amplify the fault symptom. The proposed approach can effectively detect a single tooth fault on a planet gear. This chapter is organized as follows. In Section 5.1, background of this research topic is described and a literature review is performed in terms of vibration based gear fault detection of planetary gearboxes. In Section 5.2, the vibration properties of a planetary gearbox are examined. In Section 5.3, a windowing and mapping strategy is proposed to generate the vibration signal of each tooth. In Section 5.4, the proposed method is assessed numerically and experimentally for detection of a tooth crack in a planet gear. In Section 5.5, conclusions of this study are given. This chapter is based on a journal paper [5.1] and a refereed conference paper [5.2]

5.1 Introduction

A planetary gear set typically consists of a sun gear, a ring gear and several planet gears as shown in Fig. 1.1 of Chapter 1. Several sun-planet gear pairs and several ring-planet gear pairs mesh simultaneously. Therefore, there are multiple vibration sources inside a planetary gearbox. In addition, with the rotation of the carrier, the distance between a planet gear and a transducer fixed on the top of the housing varies all the time. The time-varying distance will induce the effect of transmission path which attenuates the vibration signals generated from the vibration source far from the transducer. Multiple vibration sources and the effect of transmission path lead to the complexity of fault detection of a planetary gearbox [5.3].

To understand the vibration properties of a planetary gearbox, model based methods have been widely used to simulate the vibration signals of a planetary gearbox. Several studies [5.4-5.7] have simulated and investigated the vibration signals of the sun gear or a planet gear of a planetary gear set. However, transducers were generally installed on the housing of a gearbox or the housing of a bearing to acquire the vibration signals of the whole gearbox rather than the signals of a specific gear. Therefore, it is more helpful for fault detection to model and investigate the vibration signals of a planetary gear set rather than a single gear. Refs. [5.2, 5.3, 5.8-5.10] modeled the vibration signals of a planetary gear set by incorporating the effect of transmission path with the assumption that as planet n approached the transducer location, its influence would increase, reaching its maximum when planet n was the closest to the transducer location, then, its influence would decrease gradually as the planet went away from the transducer. In this chapter, the method reported in [5.3] will be used directly to model the vibration signals of a planetary gear set in healthy and faulty conditions. The simulated signals will help test the effectiveness of the proposed fault detection method.

Many vibration analysis techniques have been developed to detect the gear fault of a planetary gearbox [5.11-5.14]. McFadden [5.15] proposed a windowing and mapping strategy to obtain the vibration of individual planet gears and of the sun gear in a planetary gearbox. He applied a window function to sample the vibration signals when a specific planet gear is passing by the transducer and then mapped the samples to the corresponding meshing teeth of the sun gear or the planet gear to form their vibration signals. Many additional studies attempted to improve the performance of the method reported in [5.15]. Refs. [5.16-5.19] investigated the techniques to index the positions of each planet gear, which were used to find the best location of putting the windows. Refs. [5.17, 5.18, 5.20-5.22] tried to find the best window type and window length for the sampling. Refs. [5.16-5.23] investigated the performances of Rectangular window, Hanning window, Turkey window and Cosine window. All these reported studies tried to decompose the vibration signal of a planetary gearbox while focusing on the vibration of the sun gear or the planet gear of interest. The decomposed signal can reduce the interference from the vibration of other gears and consequently emphasize the fault symptoms of the gear of interest.

In this chapter, a new windowing and mapping strategy is proposed to generate the vibration signal of each tooth of a planet gear. The decomposed vibration signal can reduce the interference from the vibrations of other teeth of the planet gear of interest. Examining the signals of all the teeth of a planet gear, the health differences of the teeth can be measured. To apply the proposed windowing and mapping strategy, an important issue to be addressed is to determine where to apply the windows. A numerical optimization algorithm is developed to find the optimal positions of windows given a vibrations signal of a planetary gearbox with a single tooth fault in a planet gear. The proposed method as numerically and experimentally demonstrated, can detect a cracked tooth in a planet gear.

5.2 Vibration properties of a planetary gear set

It is essential to understand the vibration properties of a planetary gearbox before the development of an effective technique for tooth fault detection. In this section, the method proposed in Chapter 4 will be used directly to simulate the vibration signals of a planetary gear set and illustrate the vibration properties. In the dynamic model, each component is modeled with three degrees of freedom: transverse motions in the x-axis and y-axis, and the rotation motion as shown in Fig. 4.2. A rotating frame of reference fixed to the carrier is applied to all coordinates. The resultant vibration signal of a planetary gear set is modeled as the summation of the weighted vibrations of all planet gears by modeling the effect of transmission path as a modified Hamming function. The planetary gear set investigated in Chapter 4 is used again in this chapter to simulate the vibration signals. The parameters of this planetary gear set are illustrated in Table 4.1 of Chapter 4. The planetary gearbox contains one sun gear, four equally spaced planet gears and one fixed ring gear. Detailed equilibrium equations of this dynamic model are given in Section 4.2 of Chapter 4.

A planet gear tooth has two meshing sides. One side meshes with the sun gear (sun side) and the other side meshes with the ring gear (ring side). Consequently, the tooth fault may appear in the sun side or in the ring side of a planet gear tooth. This windowing and mapping strategy is expected to be effective in the fault detection of either the sun side or the ring side tooth crack of a planet gear as the vibration properties of the two cases share the same properties: the cracked tooth will repeat the mesh every revolution of the planet gear [5.2, 5.23]. In this study, I put our focus on the detection of the ring side tooth crack of a planet gear.

Tooth crack mostly initiates at the critical area of a gear tooth and the propagation paths are smooth and continuous with only a slight curvature [5.24]. Liang et al. [5.23] simplified the crack growth path as a straight line (see Fig. 5.1) starting from the critical area of the tooth root. The potential energy method reported in Refs. [5.23, 5.25, 5.26] can be used to evaluate the time-varying mesh stiffness of a planetary gear set in the perfect and the cracked tooth condition. The crack model and the potential energy method described in [5.23] will be used in this section to evaluate the time-varying mesh stiffness of a planetary gear set. It was assumed in [5.23] that the sun-planet mesh stiffness was not affected if the crack was in the ring side, as the crack part could still bear the compressive stiffness as if no crack existed. The same assumption will be used in this study.

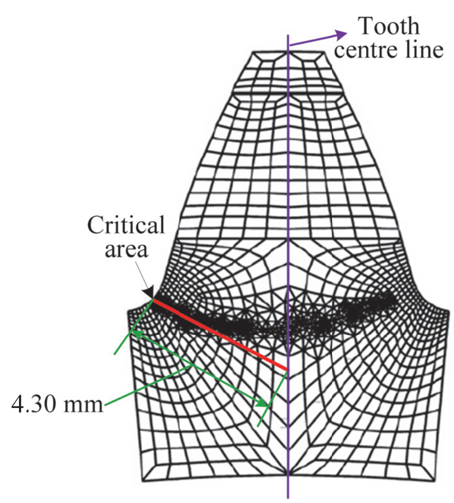

Fig. 5.1: Tooth crack propagation path for a planet gear [5.24]

Fig. 5.2 shows the simulated acceleration signals of a planetary gearbox (parameters are given in Table 4.1 of Chapter 4) in the perfect condition and in the faulty condition with a 4.3mm tooth crack in a single planet gear as shown in Fig. 5.1. A constant torque of 429 $N{\cdot}m$ is applied to the sun gear and the rotation speed of the carrier is set to be 8.87 RPM. The signal sampling frequency is 5, 000 Hz. The simulated vibration signals mimic the vibration signals sensed by a transducer installed vertically on the top of the gearbox. In one revolution of the carrier, 324 (81×4) meshes take place as the ring gear has 81 teeth and there are four planet gears, and signal envelop fluctuates four times caused by the effect of transmission path as the four planet gears approach the transducer sequentially. Since each planet gear has 31 teeth, the single cracked tooth will be in meshing every 31 mesh periods [5.26] and a large spike is generated by the meshing of a cracked tooth. Therefore, in the time interval of 81 mesh periods the single cracked tooth will mesh two or three times. Fig. 5.2 shows the case of three meshes in the time interval of 81 mesh periods and we can observe three large spikes. However, the amplitude of the three large spikes is quite different for two reasons. Firstly, the mesh position of the cracked tooth with the ring gear is changing due to the rotation of the carrier. If the planet gear is far from the transducer, less vibration energy will be sensed by the transducer. Secondly, the rotation of the carrier causes the direction of the mesh force changing which leads to the variance of energy distribution in the vertical direction of the acceleration signal. Another phenomenon we can observe is that the time duration of the large spikes is very short. Most of the time, the healthy teeth are in meshing and we cannot detect the gear fault from the vibration signals especially for example in very noisy environment where the fault symptoms may be submerged.

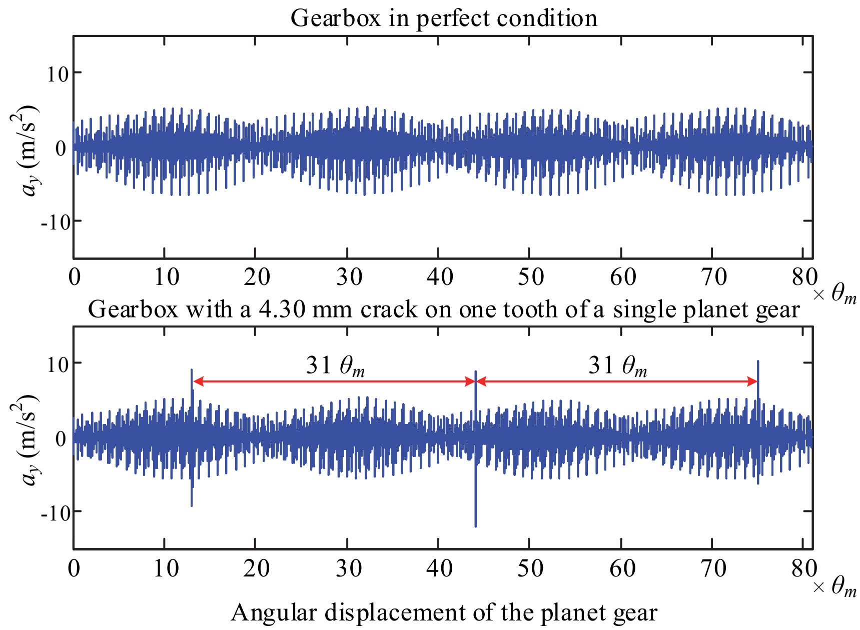

Fig. 5.2: Simulated acceleration signals of the whole gearbox in perfect and faulty conditions

When the cracked tooth is in meshing, an impulse is expected to be generated in the vibration signals. It appears in a very short time and only when the cracked tooth is in messing. If there is only one cracked tooth, such an impulse would appear at a fixed frequency. If we can pick out these weak fault symptoms and assemble them together, the fault symptom will be magnified and become easier to be detected.

5.3 Windowing and mapping

In this section, a windowing and mapping strategy is proposed to generate the vibration signal of each tooth of a planet gear. Fig. 5.3 illustrates the input and the output of the windowing and mapping strategy. The input is the vibration signal of a planetary gearbox and the output is the vibration signal of each tooth of the planet gear of interest. If a planet gear has Z_p teeth, the output will be Z_p signals. Each signal corresponds to a planet gear tooth meshing with all the teeth of the ring gear sequentially. All ring gear teeth are assumed to be identical and healthy and the same assumption applies to the sun gear teeth.

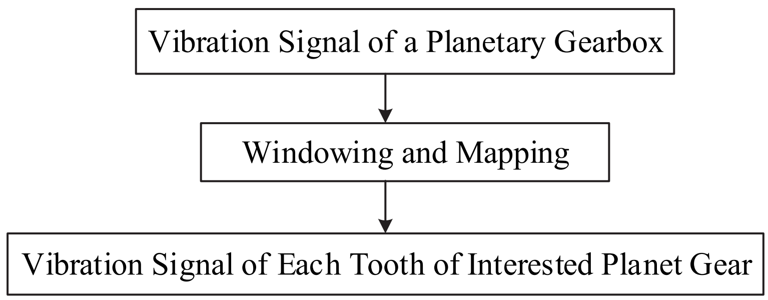

Fig. 5.3: Input and outputs of the windowing and mapping strategy

Fig. 5.4 describes the signal decomposition procedures to obtain one tooth signal of a planet gear. Before applying the windowing and mapping strategy, signal pre-processing is required. The time domain vibration signal needs to be resampled to the angular domain with the same angular step by the help of an order tracking technique [5.27] if the shaft has a large speed variation. As in real applications, the rotation speed of a gearbox is hard to keep constant causing the vibration signal to be non-stationary. While in the angular domain, the vibration signal is sampled at constant angular increments, and the effect of speed variation will be removed. In addition, if we know in advance some frequencies are interferences; these frequency components should be removed to facilitate fault detection. I call these signals with some frequency components removed as residual signals. Next step is to determine the window positions. Once the angular position of applying the first window is determined, other windows can be applied sequentially. Because a window function is applied sequentially to sample the angular domain signal in every angular interval of θ_p, where θ_p is the rotation angle of the planet gear of going through Z_p mesh periods and Z_p represents the number of teeth of the planet gear. The determination of the angular position of applying the first window will be comprehensively discussed later in Section 5.3.2. Right now, I assume that the angular position of applying the first window is known. Without loss of generality, I will illustrate how to obtain the vibration signal of tooth *S* of the planet gear, as the same procedures can be applied to get the vibration signals of other teeth. Assume tooth *S* is meshing with tooth 1 of the ring gear when we apply the first window. After one revolution of the planet gear, the same tooth *S* is meshing with the tooth (Z_p+1) of the ring gear and at this moment we apply the same window the second time. The same n^{th} window is applied when the same tooth *S* is meshing with the tooth *mod* ((n-1) Z_p+1, Z_r) of the ring gear, where n is the number of sequence of the applied windows; Z_r represents the number of teeth of the ring gear; and *mod* () is a function to find the remainder of the division of the two arguments. An exception is that when tooth *S* is meshing with tooth Z_r of the ring gear, the result of the *mod* () is zero. Consequently, after applying Z_r windows, we get Z_r windowed signals. As stated above, the tooth *mod* ((n-1) Z_p+1, Z_r) of the ring gear is enmeshing when the n^{th} window is applied, then the n^{th} windowed signal can be mapped to the tooth *mod* ((n-1) Z_p+1, Z_r) of the ring gear. Assuming that the window angular length is θ_m, assembling these Z_r signal segments will generate an ensemble of vibration signals for tooth *S*, where θ_m represents the rotation angle of a planet gear in one tooth mesh period.

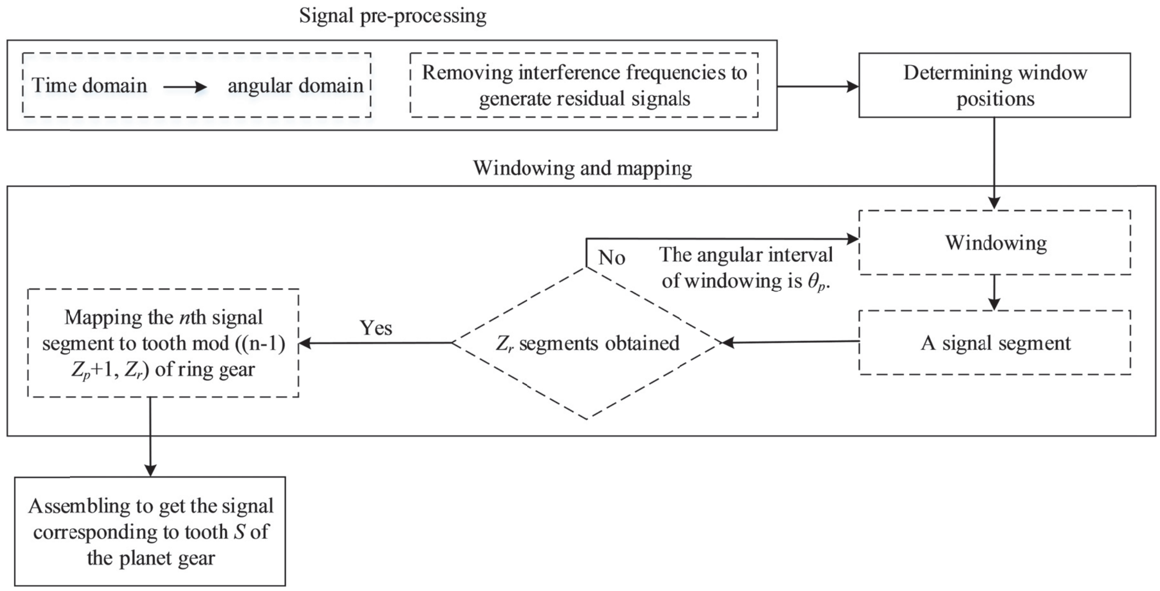

Fig. 5.4: Signal decomposition to get one tooth signal of a planet gear

Fig. 5.5 illustrates an example of implementing the windowing and mapping strategy. In this example, tooth number of the planet gear and the ring gear is 31 and 81, respectively. Fig. 5.5 (*a*) shows the residual vibration signal of a planetary gearbox in the time domain. Fig. 5.5 (*b*) describes the residual vibration signal in the angular domain, where θ denotes the rotation angle of the planet gear of interest referring to its own axis. Fig. 5.5 (*c, d*) shows that 81 windows are applied to get 81 signal segments. Then the n^{th} windowed signal are mapped to the tooth *mod* ((n-1) 31+1, 81) of the ring gear. Assembling these 81 signal segments, we get one tooth signal.

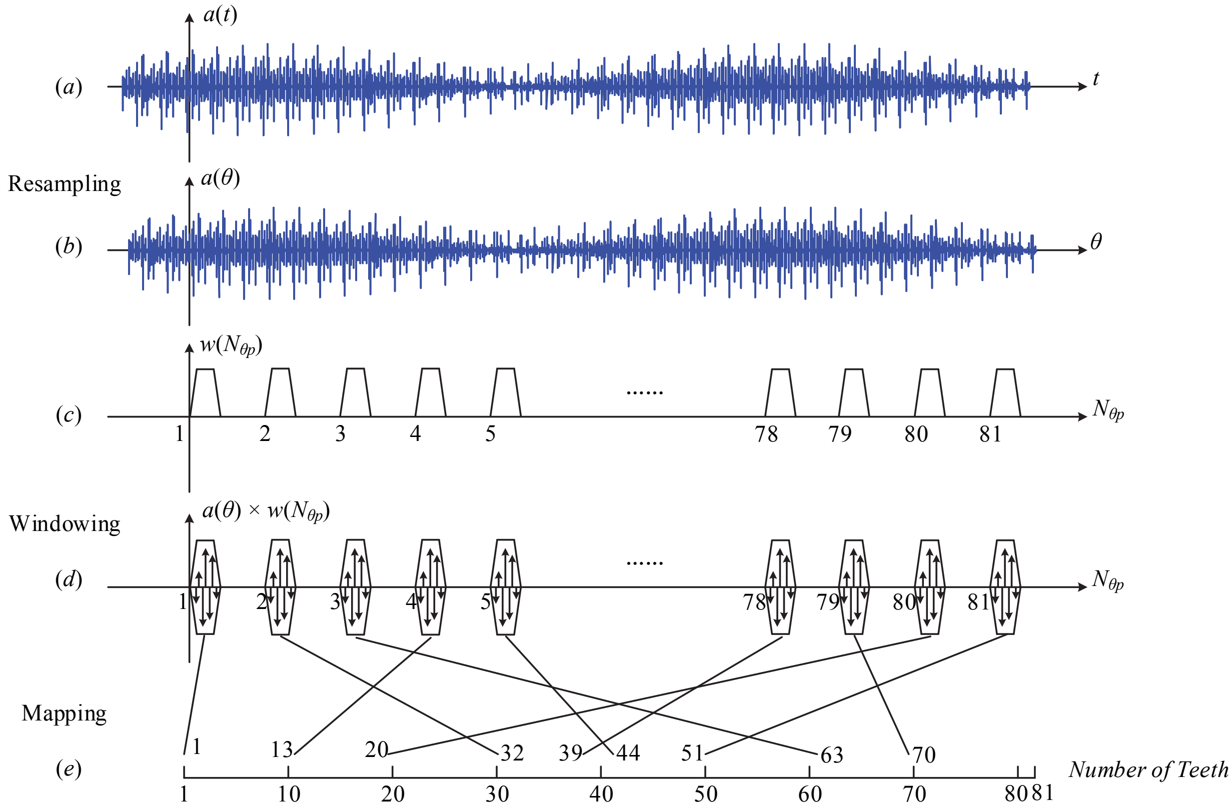

Fig. 5.5: Windowing and mapping strategy (Z_p = 31, Z_r = 81)

The same procedures described in the previous two paragraphs can be applied to obtain the vibration signal of any other tooth of the planet gear of interest. The only thing to change is the angular point of applying the first window. At the point of applying the first window for tooth *S*, tooth *S* is enmeshing with tooth 1 of the ring gear as stated in the above paragraph, and the rotation angle of the planet gear at that moment can be denoted by θ_0. After a rotation angle of θ_m, tooth *S*+1 will be is enmeshing with tooth 1 of the ring gear. To get the vibration signal of tooth *S*+1, the same first window as tooth *S* should be applied in the rotation angle of the planet gear at $\theta_0 + \theta_m$. Sequentially, the time moment of applying the first window for other teeth can be obtained. For example, the time moment should be in the rotation angle of $\theta_0 + N\theta_m$ for tooth *S*+*N*.

Applying the above procedures, total Z_p signals can be generated corresponding to the Z_p teeth of a planet gear. Comparing the differences of these Z_p signals can help detect the faulty tooth of the planet gear of interest.

The windowing process can extract the signal generated by each tooth while the mapping process can assemble them in the right order corresponding to the tooth number of the ring gear. For a cracked planet gear tooth, this strategy collects the weak fault symptoms spreading all over the vibration signals of a planetary gearbox to facilitate fault detection. In addition, the transmission path does not contribute to the differences between the tooth signals. Applying the windowing and mapping strategy, Z_p tooth signals can be decomposed from a planetary gearbox vibration signal segment with the length of Z_p x Z_r mesh periods, These Z_p tooth signals correspond to the Z_p teeth of the planet gear. Each vibration signal has a length of Z_r mesh periods and corresponds to a planet tooth meshing with the ring gear by one cycle. As each tooth of the planet gear meshes with the same teeth of the ring gear and in the same order, the windowing and mapping strategy can make sure that all the tooth signals have the same transmission path. Consequently, the tooth signal differences come from only the diversity of the health condition of the teeth of the planet gear.

5.3.1 Window type and length

Samuel et al. [5.22] proposed the use of a Tukey window in signal windowing. Since the Turkey window has a flat-top as shown in Fig. 5.6, the tooth mesh waveform of interest will be less distorted comparing with the use of other windows, for example a triangular window or a Hanning window. The rectangular window also has the top flat; however, small discontinuities will be generated where the windows meet [5.22]. Thus, the Tukey window will be used in this chapter. An N points Tukey window function is given as follows:

$$w(n)=\begin{cases}\frac{1}{2}\left[1+\cos(\pi(\frac{2n}{\alpha(N-1)}-1))\right] & 0\le n\le\frac{\alpha(N-1)}{2}\\ 1 & \frac{\alpha(N-1)}{2}\le n\le(N-1)(1-\frac{\alpha}{2})\\ \frac{1}{2}\left[1+\cos(\pi(\frac{2n}{\alpha(N-1)}-\frac{2}{\alpha}+1))\right] & (N-1)(1-\frac{\alpha}{2})\le n\le(N-1)\end{cases}. \quad (5.2.1)$$

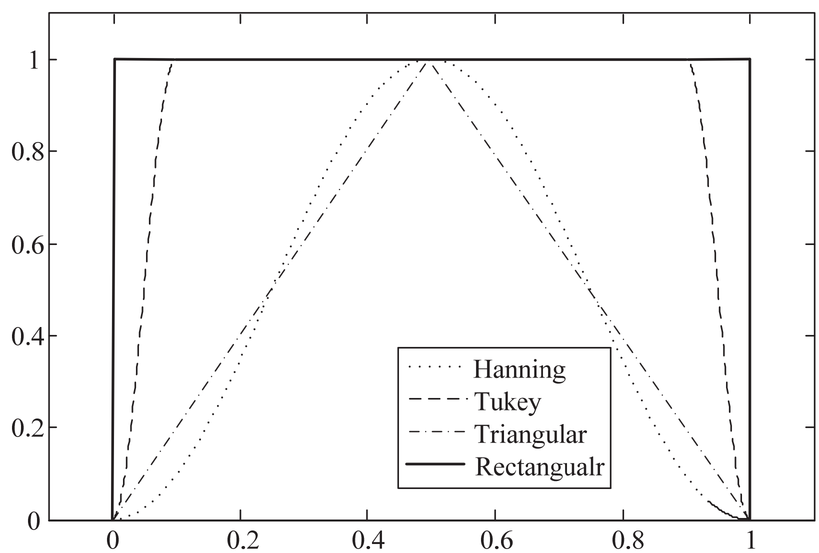

Fig. 5.6: Comparison of window functions

To make sure that there is no unwanted overlapping or gap between windows when we assemble them, the window length must be Mθ_m, where M is an integer. For a pair of standard spur gears, the contact ratio is between 1 and 2. For example, the contact ratio is 1.9 for the planet-ring gear pair, which means that a tooth will be in meshing in a time period of 1.9 θ_m. If the window length is chosen to be θ_m, the window can only cover part of the vibration signal generated by a tooth. If the window length is $2\theta_m$ or longer, the window will totally cover the vibration signal generated by a tooth but with the drawback of covering some vibration signals generated by the neighboring teeth. The longer the window, the more vibration signals generated by other teeth will be covered. Referring to the simulated vibration signal shown in Fig. 5.2, the spikes caused by a single tooth crack appear in a time duration of less than one mesh period even though the contact ratio is 1.9. Therefore, the window length is chosen to be θ_m in this study.

5.3.2 Location optimization of the first window

As described in the beginning of Section 5.3, once the position of applying the first window is determined, other windows can be applied sequentially. Ref. [5.17] proposed assembly and test procedures to experimentally measure the time when the sun, the planet, and the ring gear teeth were in meshing. If it is known when a planet tooth starts to mesh, the position of the first window can be determined. Therefore, the same assembly and test procedures reported in [5.17] can be used to find the position of applying the first window. However, to do this, special indexing and a specific transmission assembly procedure is required. In some circumstances, it is not convenient to implement such assembly and the measurements. Under such scenario, a numerical method is a good choice. In this chapter, a numerical method is proposed to find the position of applying the first window when there is a single tooth crack in a planet gear.

Referring to Fig. 5.2, when the cracked tooth is in meshing, the vibration signal amplitude increases and correspondingly the signal energy generated by the cracked tooth is larger than that of other healthy teeth. Given a vibration signal of a planetary gearbox,

Z_p vibration signals can be generated for the Z_p teeth of a single planet gear assuming it is known where to apply the first window. Among the Z_p signals, the one with the largest energy should correspond to the cracked tooth.

This paragraph proposes a numerical method to find the optimal position of applying the first window. Based on gear mesh theory, there must be a planet tooth initiating its meshing at an angular point during an angular interval of θ_m. The first window can be applied when a planet tooth initiates the meshing. Arbitrarily select a planetary gearbox vibration signal with the angular length of θ_m and count the number of data point in the selected signal segment. I use symbol P to denote the number of data point. These P points are the whole candidates of positions of applying the first window. Pick one point among the P points and apply the first window there. Implementing the proposed windowing and mapping strategy, Z_p signals can be generated. Calculate the energy (like RMS energy: root mean square) of the Z_p signals, and pick the one with the largest energy which possibly corresponds to the cracked tooth. Similar procedures can be applied to other points. For each point, the largest signal energy will be recorded and a total of P energies will be obtained. Comparing these P energies, the largest one corresponds to the optimal position to apply the first window.

The proposed windowing and mapping strategy requires accurate locations for windowing. The proposed numerical algorithm may be ineffective for heavily noisy signals. Therefore, for heavily noisy signal, denoising needs to be performed in advance in order to use the proposed numerical algorithm.

5.4 Fault detection of a single tooth crack of a planet gear

In this section, the proposed windowing and mapping strategy is tested numerically and experimentally, respectively. In Section 5.4.1, the vibration signals are generated numerically using a dynamics based model. In Section 5.4.2, the vibration signals are collected from an experimental test rig located in the Reliability Research Lab in Mechanical Department of the University of Alberta.

5.4.1 Numerical simulation

The windowing and mapping strategy is applied to the simulated vibration signal of a planetary gear set to generate the vibration signal of each tooth of a planet gear. The physical parameters of this planetary gear set are listed in Table 4.1 of Chapter 4. The same boundary conditions listed in Section 5.2 are used to simulate the vibration signals. Because the simulated signals do not have interference frequencies as the experimental signals, the step of removing interference frequencies to generate residual signals as illustrated in Fig. 5.4 is omitted. Fig. 5.7 (a) presents the simulated vibration signal of this planetary gear set with a 4.3 mm tooth crack in a planet gear and illustrates the optimized window positions to generate the vibration signal of the cracked tooth using the algorithm proposed in Section 5.3.2. These windows perfectly cover the fault symptoms generated by the cracked tooth as observable in Fig. 5.7 (a). As stated in Section 5.3.1, the window length is chosen to be θ_m even though the contact ratio of ring-planet gears is 1.9, as the fault symptom lasts less than one mesh period as shown in Fig. 5.7 (a). The angular position of the first window is obtained using the method stated in Section 5.3.2.

Arbitrarily select a signal segment with the angular length of θ_m. There are 418 (33,822/81) data points in the angular length of one mesh period since 33, 822 data points were collected in one revolution of the carrier (81 mesh periods). The angular position of the first window is chosen to be the one with the largest RMS energy. In every Z_p (31) mesh period, a window is applied to extract the signals of interest. For the purpose of comparison, Fig. 5.7 (b) and Fig. 5.7 (c) present the generated vibration signal of a perfect tooth and the cracked tooth, respectively. After the windowing and mapping strategy, gear fault symptoms concentrate on the vibration signal of the cracked tooth. However the signal amplitude corresponds to different teeth of the ring gear varies largely for the cracked tooth signal as shown in Fig. 5.7 (c). This phenomenon is caused by the effect of transmission path and the direction change of the mesh force. However, we can see that the proposed windowing and mapping strategy can highlight the fault symptoms of a gearbox.

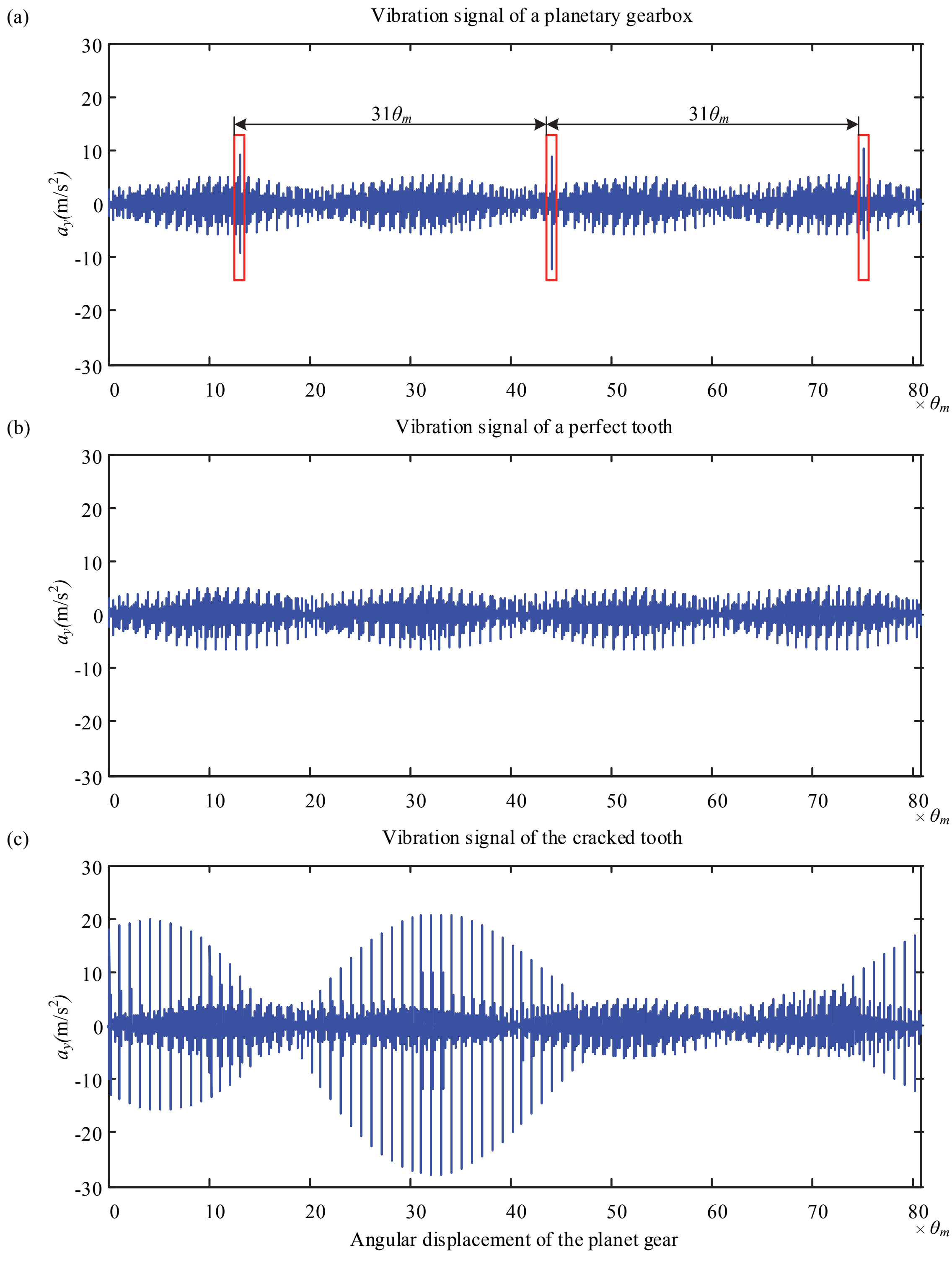

Fig. 5.7: Vibration signal decomposition of a planetary gearbox

To quantify the difference in vibration signals, statistical indicators are widely used. There are many statistical indicators available in the literature. Wu et al. [5.28] simulated the vibration signals of one stage of fixed-shaft gearbox and concluded that root mean square (RMS) and kurtosis factor were two effective indicators to reflect the crack severity. Lewichi et al. [5.17] tested nine statistical indicators to detect the man-made faults in a planetary gearbox and the results showed that the indicator M8A performed the best. Chen and Shao [5.5] simulated the vibration signals of a planetary gear set and demonstrated that the crest factor was sensitive to the crack growth. Lei et al. [5.29] proposed two new statistical indicators: root mean square of the filtered signal (FRMS) and normalized summation of the positive amplitudes of the difference spectrum between the unknown signal and the healthy signal (NSDS), and demonstrated that these two indicators were effective in detecting planetary gearbox faults. Zhao et al. [5.30] summarized 63 statistical indicators for gearbox fault detection. All these statistical indicators have the potential to be used together with the proposed windowing and mapping strategy to detect gearbox tooth crack fault, but the effective of these statistical indicators should be tested. For the illustration purpose, in this study, I only tested one statistical indicator: RMS [11], to quantify the difference of the tooth vibration signals of a planet gear. The effectiveness of other statistical indicators is not tested in this study. They will be tested in our future work. As shown in Fig. 5.7, the signal amplitude of the perfect tooth is quite different from that of the cracked tooth. Correspondingly, the signal energy of the signals will vary largely. RMS is a measurement of a signal's overall energy and is used to reflect the signal difference. The expression of RMS is given by:

$$\mathrm{RMS} = \sqrt{\frac{1}{N}\left[\sum_{i=1}^{N}(x_i)^2\right]}\,, \tag{5.4.1}$$

where N is the number of samples of a signal and x_i is the sample amplitude.

The windowing and mapping strategy is applied to the simulated vibration signals of a planetary gearbox. Five health conditions are considered respectively: healthy condition, 1.0 mm, 2.0 mm, 3.0 mm and 4.3 mm tooth crack conditions (crack on the ring-side of a planet gear). When the gearbox is healthy, the RMS of the vibration signal generated by each tooth of a planet gear locates in the range of 38 m/s^2 and 40 m/s^2 as shown in Fig. 5.8. When the gearbox has a cracked tooth 9, the RMS of all other teeth also falls in the range of 38 m/s^2 and 40 m/s^2. The RMS of tooth 9 is about 43 m/s^2 for 1.0 mm tooth crack, 47 m/s^2 for 2.0 mm tooth crack, 56 m/s^2 for 3.0 mm tooth crack, and 76 m/s^2 for 4.3 mm tooth crack. When the crack length is 2.0 mm, 3.0 mm or 4.3 mm, the tooth crack can be detected obviously. When the crack length is only 1.0 mm, the tooth crack can also be detected even though the RMS difference between tooth 9 and other teeth is small. The RMS difference between tooth 9 and other teeth indicates that there is a tooth fault in tooth 9.

Overall, the windowing and mapping strategy can effectively decompose the simulated vibration signal into the tooth level. Comparing the RMS of the tooth signals of a planet gear, a single tooth fault can be successfully detected.

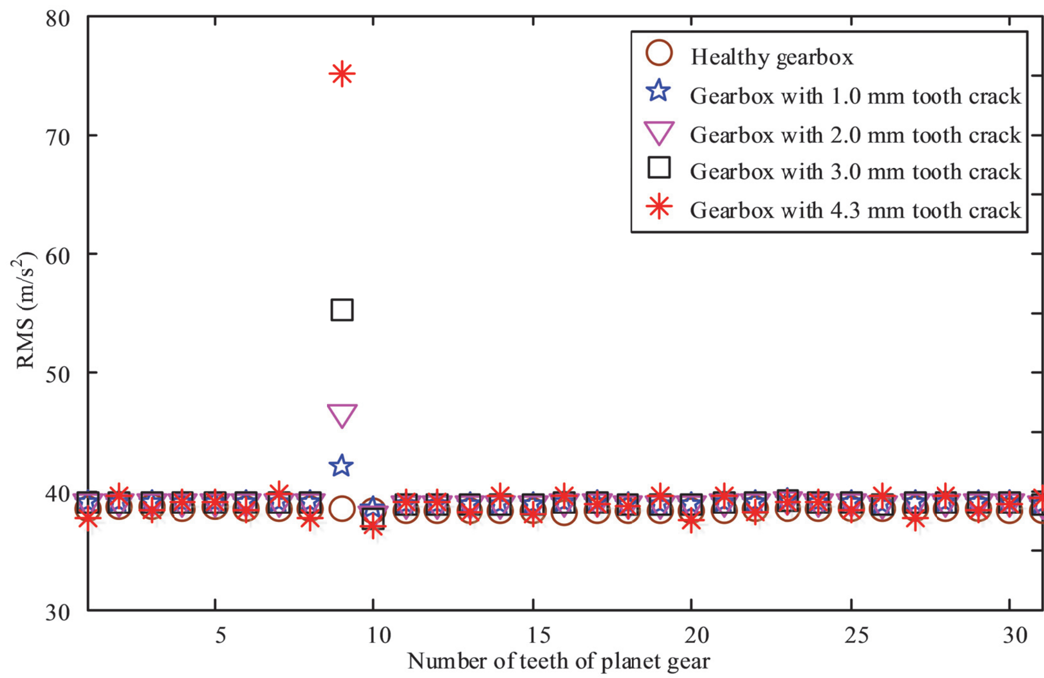

Fig. 5.8: Energy of simulated vibration signal generated by each tooth of a planet gear

5.4.2 Experimental tests

In this section, the proposed windowing and mapping strategy is applied to the experimental signals to further validate its effectives. The experimental data was collected from a planetary gearbox test rig as shown in Fig. 4.14 of Chapter 4. This test rig contains one bevel gearbox, two stages of planetary gearboxes and two stages of speed-up gearboxes. This planetary gear set is used in Chapter 4 for vibration signal analysis. The parameters of the bevel gearbox and the planetary gearboxes are listed in Table 4.4 of Chapter 4. In this chapter, the vibration signals collected from the 2nd stage of planetary gearbox are analyzed. An accelerometer was installed vertically on the housing of the 2nd stage of planetary gearbox to collect the vibration signals. The vibration signals were collected when the 2nd stage of planetary gearbox was in healthy and faulty conditions. In the healthy condition, all the gears are perfect. In the faulty condition, a 4.3 mm tooth crack as shown in Fig. 5.9 was manually made in a planet gear using Electro Discharge Machining. The rotation speed of the drive motor was set to be 1200 RPM and correspondingly the rotation speed of the carrier shaft of the 2nd stage planetary gearbox was 8.87 RPM which is the same as the rotation speed of the carrier shaft of the simulated planetary gearbox. The signal sampling frequency was 5, 000 Hz in all the tests. The detailed experimental procedures and data collection were documented in the technique report [5.31].

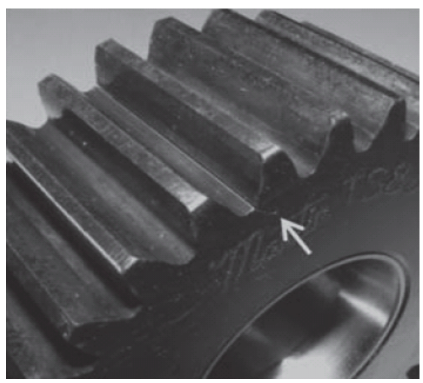

Fig. 5.9: 4.3 mm manually made tooth crack in a planet gear

As shown in Fig. 5.10, one encoder was installed to measure the carrier shaft speed variance. In total 2048 pulses will be generated in one revolution of the encoder. The carrier shaft is the output shaft of the 2nd stage planetary gearbox. By counting the number of pulses generated by the encoder in a given time period, the rotation speed of the encoder can by calculated. The measured average speed of the encoder is 13.61 RPM and the speed variance is 7.6×10^{-7} RPM as shown in Fig. 5.11. Consequently, the speed variance of the carrier shaft is very small as the carrier shaft and the encoder externally mesh. As the speed variance of the carrier shaft is very small, I consider the rotation speed of the carrier shaft to be constant at 8.87 RPM in this study.

The collected experimental vibration signals are presented in Fig. 5.12. Noise level of the experimental signals was estimated using the soft-thresholding method reported in [5.31]. To be specific, it is approximated using the median absolute deviation of the detail coefficients of the 1-level wavelet decomposition (refer to [5.31] for details). The noise level was estimated using five experimental data samples with more than 1.5×10^6 data points in each sample. The obtained noise level was about 4 dB. When there is a tooth fault in a planet gear, the signal amplitude increases slightly. However, there is no obvious fault symptom visually noticeable due to the complexity of the gearbox test rig.

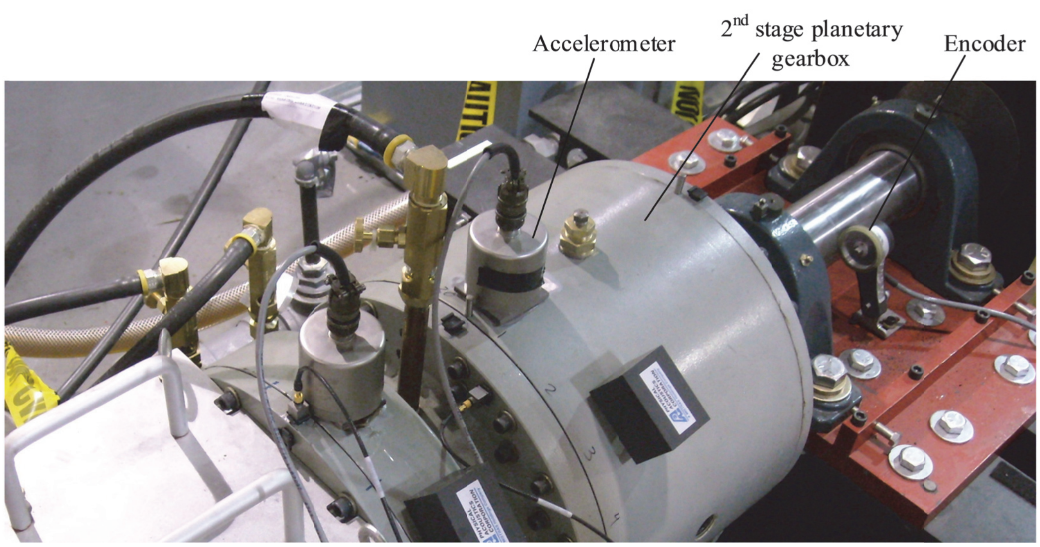

Fig. 5.10: Accelerometer and encoder

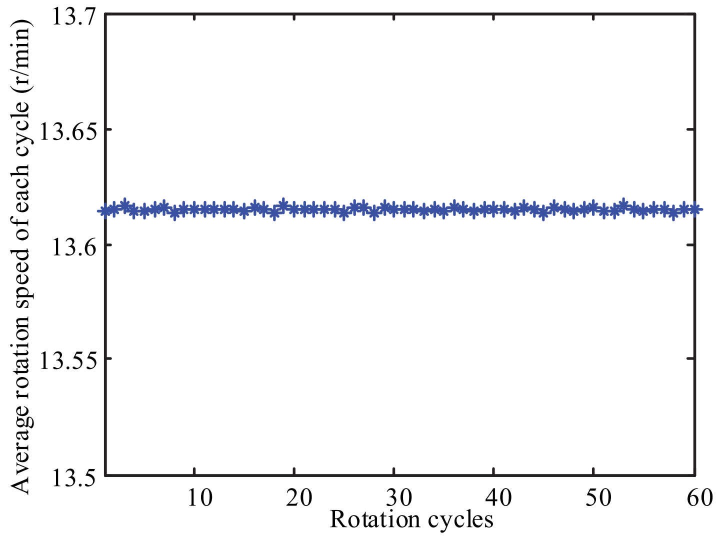

Fig. 5.11: Rotation speed of the encoder

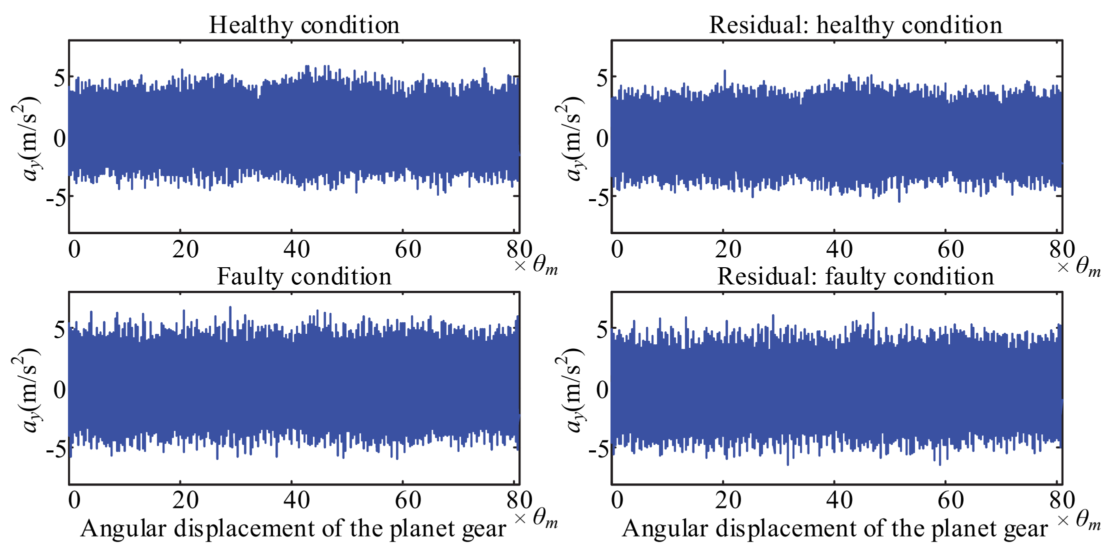

Fig. 5.12: Experimental vibration signals

The collected vibration signal not only contains the vibration information from the 2nd stage planetary gearbox but also contains the vibration information from other components. To reduce the interference from other components, residual signals are generated before applying the proposed windowing and mapping strategy by removing drive motor rotation frequency, bevel gear mesh frequency and harmonics, 1st stage planetary gearbox sun gear rotation frequency and harmonics, 1st stage planetary gearbox planet gear rotation frequency and harmonics, 1st stage planetary gearbox mesh frequency and harmonics; in addition, a low pass filter (up to 800 Hz) is applied to remove the high frequency noise. The vibration of the speed-up gearboxes is not concerned as a chain coupling is applied between the 2nd stage planetary gearbox and the 1st stage speed-up gearbox. The chain coupling is believed to be able to avoid the interference from the speed-up gearboxes. The frequencies to be removed are listed in Table 5.1 and the generated residual signals are shown in Fig. 5.12. In the time domain, the residual signals and the raw vibration signals still do not have big visual differences.

Table 5.1: Frequencies to be removed

Drive motor rotation frequency	Bevel gear mesh frequency	1st stage planetary gearbox		
		Sun gear rotation frequency	Planet gear rotation frequency	Gear mesh frequency
20Hz	360Hz	5Hz	1.9Hz	118.2Hz

Fig. 5.13 shows the decomposed tooth signals from the residual vibration signal of the 2nd stage planetary gearbox without and with a tooth crack in a planet gear using the proposed windowing and mapping strategy. Comparing between these two signals, we cannot visually identify the clear fault symptoms corresponding to the tooth fault. Due to the complexity of the gearbox test rig, the fault symptoms are very week and they are submerged in the vibration signals.

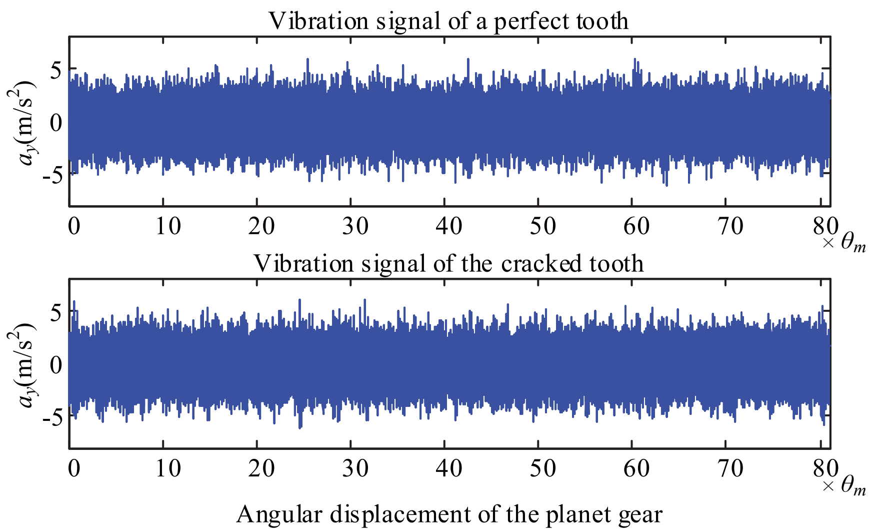

Fig. 5.13: Decomposed tooth signals of an experimental planetary gearbox

However, when we look at the RMS of the tooth signals, some differences appear. Fig. 5.14 presents the energy of the vibration signal generated by each tooth. Let's focus on Fig. 5.14 (b) firstly. When the gearbox is in faulty condition with a cracked tooth in a planet gear, the energy generated by 30 teeth scattered in the range of 16.0 m/s^2 and 16.3 m/s^2. But there is one more tooth (outlier) with the energy of about 16.5 m/s^2 which is much higher than the upper bound (16.3 m/s^2) of the energy generated by other teeth. This outlier corresponds to the cracked tooth. By contrast, when the gearbox is in healthy condition, the energy generated by the planet teeth scattered in the range of 13.2 m/s^2 and 13.6 m/s^2. There is no outlier presented in Fig. 5.14 (a). Therefore, comparing the signal energies generated by all the teeth can effectively identify the cracked tooth.

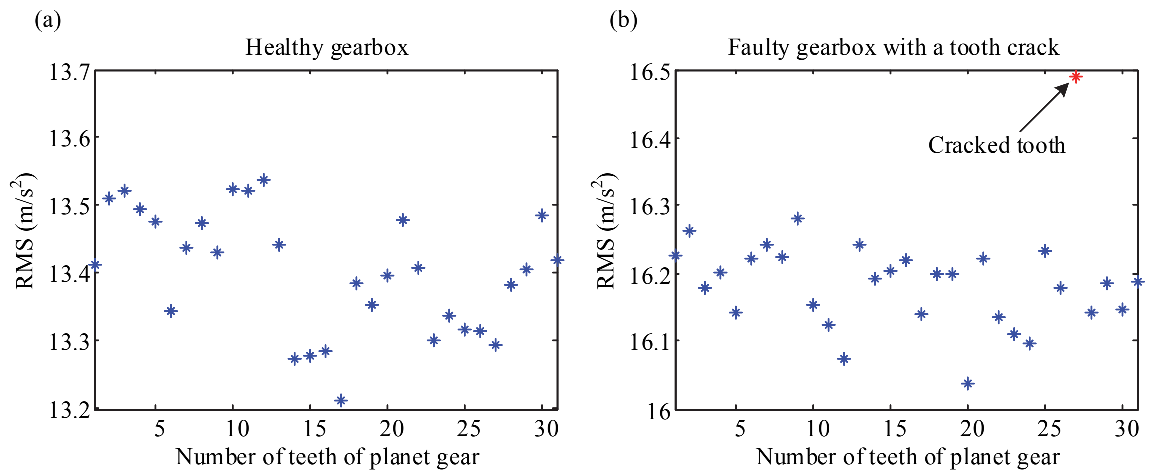

Fig. 5.14: Energy of experimental vibration signal generated by each tooth of a planet gear

In addition, one advantage of this method is that only one vibration signal segment (length of Z_p revolutions of the planet gear) when the gearbox is in faulty condition is adequate to finally find the single cracked tooth as the signals of all healthy teeth can act as the reference signal themselves. It is unnecessary to have the vibration signal of a perfect gearbox to identify the cracked tooth. This advantage can save much effort in the industry as we do not need to collect the vibration signals of a perfect gearbox.

Another phenomenon from the experimental data is that a healthy tooth of a faulty planet gear generates more energy than a healthy tooth of a healthy planet gear. The mechanism of this energy increase is unknown presently. According to the result of the simulated vibration signal presented in Fig. 5.8, the tooth energy of a healthy tooth has no difference between a healthy gearbox and a faulty gearbox. Further investigation is required to clarify the tooth energy increase of a healthy tooth in degraded health conditions of a planetary gearbox.

In this study, the ability to detect incipient defect is not tested on experimental signals. Right now, I only have the experimental data of the gearbox in healthy condition and in the 4.3 mm tooth crack condition. The experimental data was collected in 2011 as documented in Ref. [5.32]. In the future, I will design new experiments and then test the ability of the proposed method to detect incipient defect of much smaller size on experimental signals.

5.5 Conclusions

The purpose of this study is to decompose the vibration signal of a planetary gearbox into the tooth level, and then amplify the fault symptoms generated by a faulty tooth. First, a windowing and mapping strategy is proposed to generate the tooth signals of a planet gear. Then, a numerical optimization algorithm is developed to find the optimal windowing positions for the scenario that a single tooth crack is present in a planet gear. The proposed method is tested on both simulated and experimental vibration signals, and can detect a single tooth fault in a planet gear. The results show that the RMS generated by the cracked tooth of a planet gear is much higher than that generated by the perfect teeth both for the simulated and experimental signals. The RMS difference of the tooth signals can tell the tooth health of the planet gear of interest. A big advantage of the proposed method is that a reference signal when the gearbox in the healthy condition is not required in the fault detection. If the vibration signals of a planetary gearbox are not stationary, the effectiveness of the proposed method is expected to further improve when angular synchronous averaging further removes noise. However, this will not be covered in this thesis.

References

[5.1] X. Liang, M. J. Zuo, and L. Liu, "A Windowing and Mapping Strategy for Gear Tooth Fault Detection of a Planetary Gearbox," *Mech. Syst. Signal Pr.*, Submitted: 06-Jun-2015.

[5.2] X. Liang and M. J. Zuo, "Investigating Vibration Properties of a Planetary Gear Set with a Cracked Tooth in a Planet Gear," in *Proceedings of the 2014 Annual Conference of the Prognostics and Health Management Society*, Fort Worth, Texas, 2014, pp. 1–8.

[5.3] X. Liang, M. J. Zuo, and M. R. Hoseini, "Vibration Signal Modeling of a Planetary Gear Set for Tooth Crack Detection," *Eng. Fail. Anal.*, vol. 48, pp. 185–200, Feb. 2015.

[5.4] F. Chaari, T. Fakhfakh, and M. Haddar, "Dynamic Analysis of a Planetary Gear Failure Caused by Tooth Pitting and Cracking," *J. Fail. Anal. Prev.*, vol. 6, no. 2, pp. 73–78, Apr. 2006.

[5.5] Z. Chen and Y. Shao, "Dynamic Features of a Planetary Gear System with Tooth Crack under Different Sizes and Inclination Angles," *J. Vib. Acoust.*, vol. 135, no. 3, pp. 1–12, Mar. 2013.

[5.6] F. Chaari, T. Fakhfakh, R. Hbaieb, J. Louati, and M. Haddar, "Influence of Manufacturing Errors on the Dynamic Behavior of Planetary Gears," *Int. J. Adv. Manuf. Technol.*, vol. 27, no. 7–8, pp. 738–746, Jan. 2006.

[5.7] Z. Cheng, N. Hu, and X. Zhang, "Crack Level Estimation Approach for Planetary Gearbox Based on Simulation Signal and GRA," *J. Sound Vib.*, vol. 331, no. 26, pp. 5853–5863, Dec. 2012.

[5.8] M. Inalpolat and A. Kahraman, "A Theoretical and Experimental Investigation of Modulation Sidebands of Planetary Gear Sets," *J. Sound Vib.*, vol. 323, no. 3–5, pp. 677–696, Jun. 2009.

[5.9] M. Inalpolat and A. Kahraman, “A Dynamic Model to Predict Modulation Sidebands of a Planetary Gear Set Having Manufacturing Errors,” *J. Sound Vib.*, vol. 329, no. 4, pp. 371–393, Feb. 2010.

[5.10] Z. Feng and M. J. Zuo, “Vibration Signal Models for Fault Diagnosis of Planetary Gearboxes,” *J. Sound Vib.*, vol. 331, no. 22, pp. 4919–4939, Oct. 2012.

[5.11] P. D. Samuel and D. J. Pines, “A Review of Vibration-based Techniques for Helicopter Transmission Diagnostics,” *J. Sound Vib.*, vol. 282, no. 1–2, pp. 475–508, Apr. 2005.

[5.12] C. G. Cooley and R. G. Parker, “A Review of Planetary and Epicyclic Gear Dynamics and Vibrations Research,” *Appl. Mech. Rev.*, vol. 66, no. 4, pp. 1–15, Jun. 2014.

[5.13] Y. Lei, J. Lin, M. J. Zuo, and Z. He, “Condition Monitoring and Fault Diagnosis of Planetary Gearboxes: A review,” *Measurement*, vol. 48, pp. 292–305, Feb. 2014.

[5.14] S. Braun, “The Synchronous (Time Domain) Average Revisited,” *Mech. Syst. Signal Process.*, vol. 25, no. 4, pp. 1087–1102, May 2011.

[5.15] P. D. McFadden, “A Technique for Calculating the Time Domain Averages of the Vibration of the Individual Planet Gears and the Sun Gear in an Epicyclic Gearbox,” *J. Sound Vib.*, vol. 144, no. 1, pp. 163–172, Jan. 1991.

[5.16] G. D’Elia, E. Mucchi, and G. Dalpiaz, “On the Time Synchronous Average in Planetary Gearboxes,” in *the International Conference: Surveillance 7,* Institute of Technology of Chartres, France, 2013, pp. 1–11.

[5.17] D. G. Lewicki, K. E. LaBerge, R. T. Ehinger, and J. Fetty, “Planetary Gearbox Fault Detection Using Vibration Separation Techniques,” National Aeronautics and Space Administration, Glenn Research Center, Technical Report NASA/TM—2011-217127, 2011.

[5.18] J. M. Ha, J. Park, B. D. Youn, and Y. H. Jung, “Fault Diagnostics of Planet Gears in Wind Turbine Using Auto-correlation-based Time Synchronous Averaging

(ATSA)," in *the Second European Conference of the Prognostics and Health Management Society 2014*, Nantes, France, July 8 - 10, pp. 1–8.

[5.19] F. Combet and L. Gelman, "An Automated Methodology for Performing Time Synchronous Averaging of a Gearbox Signal without Speed Sensor," *Mech. Syst. Signal Process.*, vol. 21, no. 6, pp. 2590–2606, Aug. 2007.

[5.20] P. D. McFadden, "Window Functions for the Calculation of the Time Domain Averages of the Vibration of the Individual Planet Gears and Sun Gear in an Epicyclic Gearbox," *J. Vib. Acoust.*, vol. 116, no. 2, pp. 179–187, Apr. 1994.

[5.21] B. D. Forrester, "Method for the Separation of Epicyclic Planet Gear Vibration Signatures," Patent: US6298725B1, Oct-2001.

[5.22] P. D. Samuel, J. K. Conroy, and D. J. Pines, "Planetary Transmission Diagnostics," NASA Technical Report, NASA technical report NASA/CR—2004-213068, 2004.

[5.23] X. Liang, M. J. Zuo, and M. Pandey, "Analytically Evaluating the Influence of Crack on the Mesh Stiffness of a Planetary Gear Set," *Mech. Mach. Theory*, vol. 76, pp. 20–38, Jun. 2014.

[5.24] A. Belsak and J. Flasker, "Detecting Cracks in the Tooth Root of Gears," *Eng. Fail. Anal.*, vol. 14, no. 8, pp. 1466–1475, Dec. 2007.

[5.25] D. C. H. Yang and J. Y. Lin, "Hertzian Damping, Tooth Friction and Bending Elasticity in Gear Impact Dynamics," *J. Mech. Des.*, vol. 109, no. 2, pp. 189–196, Jun. 1987.

[5.26] X. Liang, M. J. Zuo, and T. H. Patel, "Evaluating the Time-varying Mesh Stiffness of a Planetary Gear Set Using the Potential Energy Method," *Proc. Inst. Mech. Eng. Part C J. Mech. Eng. Sci.*, vol. 228, no. 3, pp. 535–547, Feb. 2014.

[5.27] K. R. Fyfe and E. D. S. Munck, "Analysis of Computed Order Tracking," *Mech. Syst. Signal Process.*, vol. 11, no. 2, pp. 187–205, Mar. 1997.

[5.28] S. Wu, M. J. Zuo, and A. Parey, “Simulation of Spur Gear Dynamics and Estimation of Fault Growth,” *J. Sound Vib.*, vol. 317, no. 3–5, pp. 608–624, Nov. 2008.

[5.29] Y. Lei, D. Kong, J. Lin, and M. J. Zuo, “Fault Detection of Planetary Gearboxes Using New Diagnostic Parameters,” *Meas. Sci. Technol.*, vol. 23, no. 5, p. 055605, May 2012.

[5.30] X. Zhao, M. J. Zuo, Z. Liu, and M. R. Hoseini, “Diagnosis of artificially created surface damage levels of planet gear teeth using ordinal ranking,” *Measurement*, vol. 46, no. 1, pp. 132–144, Jan. 2013.

[5.31] D. L. Donoho, “De-noising by soft-thresholding,” *IEEE Trans. Inf. Theory*, vol. 41, no. 3, pp. 613–627, May 1995.

[5.32] M. Pandey, T. Patel, X. Liang, T. Tian, and M. Zuo, “Descriptions of Pitting Experiments, Run-to-failure Experiments, Various Load and Speed Experiments, and Crack Experiments Carried Out on the Planetary Gearbox Test Rig,” Reliability Research Lab, Mechanical Department, University of Alberta, Technical Report, 2011.

Chapter 6: Summary and Future Work

This chapter summarizes the contributions on dynamics based vibration signal modeling for fault detection of planetary gearboxes and describes some problems that remain to be addressed.

6.1 Summary of contributions

Vibration analysis has been widely used in the condition monitoring of a planetary gearbox system. The understanding of vibration properties of a planetary gearbox in healthy and faulty conditions helps the development of effective tools in the fault detection a planetary gearbox. This study aims to simulate and investigate the vibration properties of a planetary gearbox for the detection of gear tooth crack fault. The contribution of this thesis is summarized in four categories as described in the next four sections.

6.1.1 Evaluating time-varying mesh stiffness of a planetary gear set using potential energy method

Time-varying mesh stiffness is one of the main excitations of vibration of a gear transmission system. An efficient and effective way to evaluate the time-varying mesh stiffness is essential for comprehensively understanding the dynamic properties of a planetary gear set. In this thesis, potential energy method is used to derive equations of an internal gear pair. Hertzian stiffness, bending stiffness, shear stiffness and axial compressive stiffness are analytically derived for an internal gear pair without any assumption of the gear tooth involute curve. Considering a sun-planet gear pair as a fixed-shaft external gear pair, and a ring-planet gear pair as a fixed-shaft internal gear pair, and combining the mesh phases of gear pairs, the mesh stiffness of a planetary gear set is obtained. The proposed method is illustrated to calculate the mesh stiffness of a planetary gear set in three structures: fixed carrier, fixed ring gear and fixed sun gear.

6.1.2 Analytically evaluating the influence of crack on the mesh stiffness of a planetary gear set

The time-varying gear mesh stiffness shape will change if a tooth fault appears and consequently the vibration properties of the gear system will change. In this thesis, potential energy method analytically evaluates the time-varying mesh stiffness of a planetary gear set when gear tooth crack occurs. A modified cantilever beam model is proposed for an external gear tooth and the equations of bending stiffness, shear stiffness and axial compressive stiffness are derived for an external gear tooth. The stiffness results show that it is important to model the gear tooth starting from the root circle rather than the base circle. A crack propagation model is developed for an external gear and the equations of gear mesh stiffness are derived for different crack levels. The mesh stiffness reduction is quantified when a crack appears in the sun gear, a planet gear (sun gear side) or a planet gear (ring gear side).

6.1.3 Vibration signal modeling of a planetary gear set for tooth crack detection

Even though many fault detection methods have been developed to analyze the vibration signals of planetary gearboxes, the vibration properties of a planetary gear set is still not well investigated. In this thesis, a dynamics based vibration signal modeling method is proposed to simulate and investigate the resultant vibration signals of a planetary gearbox in healthy and cracked tooth conditions. A lumped-parameter model is developed to simulate the vibration signals of each gear, including the sun gear, planet gears and ring gear. A modified Hamming function is proposed to reflect the effect of the transmission path. Incorporating multiple vibration sources and the effect of transmission path, the resultant vibration signals of a planetary gear set at the sensor location are simulated. The results show obvious fault symptom in the time domain vibration signals of an individual gear, like the sun gear. However, the fault symptoms attenuate in the resultant vibration signal. Obvious amplitude modulation appears in the resultant vibration signal due to the rotation of the carrier. In the frequency domain, a large number of sidebands appear when there is a crack in the sun gear tooth. These sidebands are investigated and located, which can help detect the crack fault. The vibration properties found by the proposed signal modeling method are confirmed by comparing with those of the experimental signals.

6.1.4 A windowing and mapping strategy for gear tooth fault detection of a planetary gearbox

Based on the understanding of vibration properties of a planetary gear set in healthy and cracked tooth conditions, this thesis develops a method to decompose the vibration signal of a planetary gearbox into the tooth level of a planet gear to amplify the fault symptom.

A windowing and mapping strategy is proposed to generate the tooth signals of a planet gear. A numerical optimization algorithm is developed to find the optimal windowing positions for the scenario that a single tooth crack is present in a planet gear. The results show that the RMS generated by the cracked tooth of a planet gear is much higher than that generated by perfect teeth for both simulated and experimental signals. The RMS difference of the tooth signals tells the tooth health of a planet gear. A big advantage of the proposed method is that a reference signal when the gearbox in the healthy condition is not required in the fault detection. I have tested the proposed method on both simulated and experimental vibration signals, and demonstrated it to be able to detect a single tooth fault in a planet gear.

6.2 Future work

Although the structure of this thesis is defined in the sense that important challenges and limitations of current models in dynamics based vibration signal modeling for fault detection of planetary gearboxes are covered, there are still some problems that need to be further addressed. Based on the scope of this dissertation, the following three perspectives are suggested for future consideration.

6.2.1 Vibration property investigation of a planetary gear set with tooth pitting

In this thesis, the vibration signals of a planetary gear set with a single tooth crack are simulated and investigated. The tooth pitting fault is not covered in this study. However, tooth pitting is a very common failure mode of gearboxes in industrial application. As pitting progresses, it may spread to neighboring and mating teeth. The vibration properties of a planetary gearbox with distributed pitting on multiple teeth have not been investigated. To obtain the vibration signals, the time-varying mesh stiffness of a planetary gear set with distributed pitting on multiple teeth will need to be evaluated first. Then, the signal modeling method proposed in Chapter 4 of this thesis can be used to simulate and investigate the resultant vibration signals.

6.2.2 Validation of the transmission path effect model

In this thesis, a modified Hamming function is proposed to represent the effect of transmission path. This model can represent the varying distance between a planet gear and the vibration sensor. However, I did not provide a validation on the transmission path effect model. Further validation is required in future work.

6.2.3 Time-varying load or random load effect on vibration signals

In this thesis, the applied load on a planetary gearbox is constant. However, in industrial applications, the load is usually time-varying or random. This will cause the vibration signals to be non-stationary. The vibration properties of a planetary gearbox will be much more complicated under time-varying or random load condition than constant load condition. It is necessary to investigate them to develop effective fault detection methods in industrial application.

6.2.4 Development of advanced fault detection techniques based on understanding of vibration properties

Based on the understanding of vibration properties of a planetary gear set, a signal decomposition method is proposed in this thesis to detect a single tooth crack in a planet gear. However, the fault location may be in the sun gear, the ring gear or a planet gear. The proposed method needs to be modified for the fault detection of sun gear tooth crack or ring gear tooth crack. It is best to develop an intelligent fault detection method which can determine the fault severity and fault location simultaneously.

6.2.5 Vibration signal modeling using a combined element/contact mechanics model

Parker et al. [6.1] proposed a combined element/contact mechanics model to investigate the non-linear dynamic response of a spur gear pair. Later, this model was extended to investigate the dynamic response of a planetary gear system [6.2]. This finite element/contact mechanics approach did not require a highly refined mesh at the contacting tooth surfaces. In addition, the time-varying mesh stiffness and mesh contact forces were evaluated internally at each time step. The model reported in [6.2] was used to study the quasi-static loads [6.3] and the root stresses [6.4] in planetary gears, and the effect of manufacturing errors [6.5] and wear [6.6] on planetary gear dynamics. I think this is a very good model and can be extended to simulate the vibration signals of a planetary gear set with tooth crack in the future.

6.2.6 Profile and lead modifications effect on gear mesh stiffness

In [6.7], it is stated that "Modern gearboxes are characterized by high torque load demands, low running noise and compact design. In order to fulfill these demands, profile and lead modifications are being applied more often than in the past." Therefore, it is important to consider profile and lead modifications in gear mesh stiffness evaluation. However, in this thesis, I only derived mesh stiffness equations for a gear pair without profile or lead modifications as my first step. The profile and lead modifications will be considered in future work.

References

[6.1] R. G. Parker, S. M. Vijayakar, and T. Imajo, "Non-Linear Dynamic Response of a Spur Gear Pair: Modelling and Experimental Comparisons," *J. Sound Vib.*, vol. 237, no. 3, pp. 435–455, Oct. 2000.

[6.2] R. G. Parker, V. Agashe, and S. M. Vijayakar, "Dynamic Response of a Planetary Gear System Using a Finite Element/Contact Mechanics Model," *J. Mech. Des.*, vol. 122, no. 3, pp. 304–310, May 1999.

[6.3] H. Ligata, A. Kahraman, and A. Singh, "An Experimental Study of the Influence of Manufacturing Errors on the Planetary Gear Stresses and Planet Load Sharing," *J. Mech. Des.*, vol. 130, no. 4, pp. 041701–041701, Mar. 2008.

[6.4] P. E. Prueter, R. G. Parker, and F. Cunliffe, "A Study of Gear Root Strains in a Multi-stage Planetary Wind Turbine Gear Train Using a Three Dimensional Finite Element/contact Mechanics Model and Experiments," in *ASME International Design Engineering Technical Conferences and Computers and Information in Engineering Conference*, 2011, pp. 621–633.

[6.5] G.-J. Cheon and R. G. Parker, “Influence of Manufacturing Errors on the Dynamic Characteristics of Planetary Gear Systems,” *KSME Int. J.*, vol. 18, no. 4, pp. 606–621, Apr. 2004.

[6.6] C. Yuksel and A. Kahraman, “Dynamic Tooth Loads of Planetary Gear Sets Having Tooth Profile Wear,” *Mech. Mach. Theory*, vol. 39, no. 7, pp. 695–715, Jul. 2004.

[6.7] A. Türich, “Producing Profile and Lead Modifications in Threaded Wheel and Profile Grinding,” *Gear Technol.*, vol. 27, no. 1, pp. 54–62, 2010.

Bibliography

A. Al-shyyab and A. Kahraman, “A Non-linear Dynamic Model for Planetary Gear Sets,” *Proc. Inst. Mech. Eng. Part K J. Multi-Body Dyn.*, vol. 221, no. 4, pp. 567–576, Jan. 2007.

A. Belsak and J. Flasker, “Detecting Cracks in the Tooth Root of Gears,” *Eng. Fail. Anal.*, vol. 14, no. 8, pp. 1466–1475, Dec. 2007.

A. Fernandez del Rincon, F. Viadero, M. Iglesias, P. García, A. de-Juan, and R. Sancibrian, “A Model for the Study of Meshing Stiffness in Spur Gear Transmissions,” *Mech. Mach. Theory*, vol. 61, pp. 30–58, Mar. 2013.

A. I. H. Committee, *Friction, Lubrication, and Wear Technology*. ASM International Handbook, 1992.

A. K.S. Jardine, D. Lin, and D. Banjevic, “A Review on Machinery Diagnostics and Prognostics Implementing Condition-based Maintenance,” *Mech. Syst. Signal Process.*, vol. 20, no. 7, pp. 1483–1510, Oct. 2006.

A. Kahraman, “Load Sharing Characteristics of Planetary Transmissions,” *Mech. Mach. Theory*, vol. 29, no. 8, pp. 1151–1165, Nov. 1994.

A. Kapelevich and Y. Shekhtman, “Tooth Fillet Profile Optimization for Gears with Symmetric and Asymmetric Teeth,” *Gear Technol.*, pp. 73–79, 2009.

A. Pintz, R. Kasuba, J. L. Frater, and R. August, “Dynamic Effects of Internal Spur Gear Drives,” National Aeronautics and Space Administration, Scientific and Technical Information Branch, NASA Technical Report No. 3692, 1983.

A. Türich, “Producing Profile and Lead Modifications in Threaded Wheel and Profile Grinding,” *Gear Technol.*, vol. 27, no. 1, pp. 54–62, 2010.

B. D. Forrester, “Method for the Separation of Epicyclic Planet Gear Vibration Signatures,” Patent: US6298725B1, Oct-2001.

B. Xu, Y. Huang, X. Liu, and X. Sun, *Elasticity and Application*. Beijing: China Machine Press, 1983.

B. Zhang, T. Khawaja, R. Patrick, G. Vachtsevanos, M. Orchard, and A. Saxena, “A Novel Blind Deconvolution De-noising Scheme in Failure Prognosis,” *Trans. Inst. Meas. Control*, vol. 32, no. 1, pp. 3–30, Feb. 2010.

C. G. Cooley and R. G. Parker, “A Review of Planetary and Epicyclic Gear Dynamics and Vibrations Research,” *Appl. Mech. Rev.*, vol. 66, no. 4, pp. 1–15, Jun. 2014.

C. G. Cooley and R. G. Parker, “Unusual Gyroscopic System Eigenvalue Behavior in High-Speed Planetary Gears,” *J. Sound Vib.*, vol. 332, no. 7, pp. 1820–1828, Apr. 2013.

C. Song, C. Zhu, and L. Liu, “Mesh Characteristics for Marine Beveloid Gears with Crossed Axes,” *J. Xian Tiaotong Univ.*, vol. 46, pp. 64–69, 2012.

C. Yuksel and A. Kahraman, “Dynamic Tooth Loads of Planetary Gear Sets Having Tooth Profile Wear,” *Mech. Mach. Theory*, vol. 39, no. 7, pp. 695–715, Jul. 2004.

C.-J. Bahk and R. G. Parker, “Analytical Investigation of Tooth Profile Modification Effects on Planetary Gear Dynamics,” *Mech. Mach. Theory*, vol. 70, pp. 298–319, Dec. 2013.

D. C. H. Yang and J. Y. Lin, “Hertzian Damping, Tooth Friction and Bending Elasticity in Gear Impact Dynamics,” *J. Mech. Des.*, vol. 109, no. 2, pp. 189–196, Jun. 1987.

D. C. H. Yang and Z. S. Sun, “A Rotary Model for Spur Gear Dynamics,” *J. Mech. Transm. Autom. Des.*, vol. 107, no. 4, pp. 529–535, Dec. 1985.

D. G. Lewicki, “Gear Crack Propagation Path Studies-Guidelines for Ultra-Safe Design,” *J. Am. Helicopter Soc.*, vol. 47, no. 1, pp. 64–72, 2002.

D. G. Lewicki, K. E. LaBerge, R. T. Ehinger, and J. Fetty, “Planetary Gearbox Fault Detection Using Vibration Separation Techniques,” National Aeronautics and Space Administration, Glenn Research Center, Technical Report NASA/TM—2011-217127, 2011.

D. J. Inman, *Engineering Vibration*. Prentice Hall, 2001.

D. L. Donoho, “De-noising by soft-thresholding,” *IEEE Trans. Inf. Theory*, vol. 41, no. 3, pp. 613–627, May 1995.

D. M. Blunt and J. A. Keller, “Detection of a Fatigue Crack in a UH-60A Planet Gear Carrier Using Vibration Analysis,” *Mech. Syst. Signal Process.*, vol. 20, no. 8, pp. 2095–2111, Nov. 2006.

D. M. Blunt and J. A. Keller, “Detection of a Fatigue Crack in a UH-60A Planet Gear Carrier Using Vibration Analysis,” *Mech. Syst. Signal Process.*, vol. 20, no. 8, pp. 2095–2111, Nov. 2006.

E. Carrera, G. Giunta, and M. Petrolo, *Beam Structures: Classical and Advanced Theories*. John Wiley & Sons, 2011.

F. Chaari, T. Fakhfakh, and M. Haddar, “Analytical Modelling of Spur Gear Tooth Crack and Influence on Gearmesh Stiffness,” *Eur. J. Mech. - ASolids*, vol. 28, no. 3, pp. 461–468, May 2009.

F. Chaari, T. Fakhfakh, and M. Haddar, “Dynamic Analysis of a Planetary Gear Failure Caused by Tooth Pitting and Cracking,” *J. Fail. Anal. Prev.*, vol. 6, no. 2, pp. 73–78, Apr. 2006.

F. Chaari, T. Fakhfakh, R. Hbaieb, J. Louati, and M. Haddar, “Influence of Manufacturing Errors on the Dynamic Behavior of Planetary Gears,” *Int. J. Adv. Manuf. Technol.*, vol. 27, no. 7–8, pp. 738–746, Jan. 2006.

F. Chaari, W. Baccar, M. S. Abbes, and M. Haddar, “Effect of Spalling or Tooth Breakage on Gearmesh Stiffness and Dynamic Response of a One-stage Spur Gear Transmission,” *Eur. J. Mech. - ASolids*, vol. 27, no. 4, pp. 691–705, Jul. 2008.

F. Combet and L. Gelman, “An Automated Methodology for Performing Time Synchronous Averaging of a Gearbox Signal without Speed Sensor,” *Mech. Syst. Signal Process.*, vol. 21, no. 6, pp. 2590–2606, Aug. 2007.

F. L. Litvin and A. Fuentes, *Gear Geometry and Applied Theory*, 2 edition. New York: Cambridge University Press, 2004.

G. D’Elia, E. Mucchi, and G. Dalpiaz, “On the Time Synchronous Average in Planetary Gearboxes,” presented in the International Conference: *Surveillance 7, Institute of Technology of Chartres*, France, 2013, pp. 1–11.

G.-J. Cheon and R. G. Parker, “Influence of Manufacturing Errors on the Dynamic Characteristics of Planetary Gear Systems,” *KSME Int. J.*, vol. 18, no. 4, pp. 606–621, Apr. 2004.

H. Ligata, A. Kahraman, and A. Singh, “An Experimental Study of the Influence of Manufacturing Errors on the Planetary Gear Stresses and Planet Load Sharing,” *J. Mech. Des.*, vol. 130, no. 4, pp. 041701–041701, Mar. 2008.

H. Ma, J. Zeng, R. Feng, X. Pang, Q. Wang, and B. Wen, “Review on Dynamics of Cracked Gear Systems,” *Eng. Fail. Anal.*, vol. 55, pp. 224–245, Sep. 2015.

I. Howard, S. Jia, J. Wang, “The dynamic modeling of a spur gear in mesh including friction and a crack,” *Mech. Syst. Signal Process.*, vol. 15, pp. 831-853, 2001.

J. Antoni, “Blind Separation of Vibration Components: Principles and Demonstrations,” *Mech. Syst. Signal Process.*, vol. 19, no. 6, pp. 1166–1180, Nov. 2005.

J. Kramberger, M. Šraml, S. Glodež, J. Flašker, and I. Potrč, "Computational Model for the Analysis of Bending Fatigue in Gears," *Comput. Struct.*, vol. 82, no. 23–26, pp. 2261–2269, Sep. 2004.

J. Lin and R. G. Parker, "Analytical Characterization of the Unique Properties of Planetary Gear Free Vibration," *J. Vib. Acoust.*, vol. 121, no. 3, pp. 316–321, Jul. 1999.

J. Lin and R. G. Parker, "Mesh Stiffness Variation Instabilities in Two-Stage Gear Systems," *J. Vib. Acoust.*, vol. 124, no. 1, pp. 68–76, Sep. 2001.

J. Liu, W. Wang, and F. Golnaraghi, "An Extended Wavelet Spectrum for Bearing Fault Diagnostics," *IEEE Trans. Instrum. Meas.*, vol. 57, no. 12, pp. 2801–2812, Dec. 2008.

J. M. Ha, J. Park, B. D. Youn, and Y. H. Jung, "Fault Diagnostics of Planet Gears in Wind Turbine Using Auto-correlation-based Time Synchronous Averaging (ATSA)," presented at the *Second European Conference of the Prognostics and Health Management Society 2014*, Nantes, France, July 8 - 10, pp. 1–8.

J. Meagher, X. Wu, D. Kong, and C. H. Lee, "A Comparison of Gear Mesh Stiffness Modeling Strategies," in *Structural Dynamics*, Volume 3, T. Proulx, Ed. Springer New York, 2011, pp. 255–263.

J. Qu, "Support-Vector-Machine-Based Diagnostics and Prognostics for Rotating Systems," PhD Thesis, University of Alberta, 2011.

J. Wang and I. Howard, "The Torsional Stiffness of Involute Spur Gears," *Proc. Inst. Mech. Eng. Part C J. Mech. Eng. Sci.*, vol. 218, no. 1, pp. 131–142, Jan. 2004.

K. R. Fyfe and E. D. S. Munck, "Analysis of Computed Order Tracking," *Mech. Syst. Signal Process.*, vol. 11, no. 2, pp. 187–205, Mar. 1997.

L. Gelman, R. Zimroz, J. Birkel, H. Leigh-Firbank, D. Simms, B. Waterland, and G. Whitehurst, "Adaptive Vibration Condition Monitoring Technology for Local Tooth Damage in Gearboxes," *Insight - Non-Destr. Test. Cond. Monit.*, vol. 47, no. 8, pp. 461–464, Aug. 2005.

L. Walha, T. Fakhfakh, and M. Haddar, "Nonlinear Dynamics of a Two-stage Gear System with Mesh Stiffness Fluctuation, Bearing Flexibility and Backlash," *Mech. Mach. Theory*, vol. 44, no. 5, pp. 1058–1069, May 2009.

M. Inalpolat and A. Kahraman, "A Dynamic Model to Predict Modulation Sidebands of a Planetary Gear Set Having Manufacturing Errors," *J. Sound Vib.*, vol. 329, no. 4, pp. 371–393, Feb. 2010.

M. Inalpolat and A. Kahraman, "A Theoretical and Experimental Investigation of Modulation Sidebands of Planetary Gear Sets," *J. Sound Vib.*, vol. 323, no. 3–5, pp. 677–696, Jun. 2009.

M. Pandey, T. Patel, X. Liang, T. Tian, and M. Zuo, "Descriptions of Pitting Experiments, Run-to-failure Experiments, Various Load and Speed Experiments, and Crack Experiments Carried Out on the Planetary Gearbox Test Rig," Reliability Research Lab, Mechanical Department, University of Alberta, Technical Report, 2011.

M. R. Hoseini and M. J. Zuo, "Literature Review for Creating and Quantifying Faults in Planetary Gearboxes," Reliability Research Lab, Mechanical Department, University of Alberta, Technical Report, May 2009.

P. Association, "North Sea Helicopter Crash Report Says Gearbox Failed after Maintenance Error," *The Guardian*, 24-Nov-2011.

P. D. McFadden, "A Technique for Calculating the Time Domain Averages of the Vibration of the Individual Planet Gears and the Sun Gear in an Epicyclic Gearbox," *J. Sound Vib.*, vol. 144, no. 1, pp. 163–172, Jan. 1991.

P. D. McFadden, "Window Functions for the Calculation of the Time Domain Averages of the Vibration of the Individual Planet Gears and Sun Gear in an Epicyclic Gearbox," *J. Vib. Acoust.*, vol. 116, no. 2, pp. 179–187, Apr. 1994.

P. D. Samuel and D. J. Pines, "A Review of Vibration-based Techniques for Helicopter Transmission Diagnostics," *J. Sound Vib.*, vol. 282, no. 1–2, pp. 475–508, Apr. 2005.

P. D. Samuel, J. K. Conroy, and D. J. Pines, "Planetary Transmission Diagnostics," NASA Technical Report, NASA technical report NASA/CR—2004-213068,

P. D. Samuel, J. K. Conroy, and D. J. Pines, "Planetary Transmission Diagnostics," NASA Technical Report, NASA technical report NASA/CR—2004-213068, 2004.

P. E. Prueter, R. G. Parker, and F. Cunliffe, "A Study of Gear Root Strains in a Multi-stage Planetary Wind Turbine Gear Train Using a Three Dimensional Finite Element/contact Mechanics Model and Experiments," in *ASME International Design Engineering Technical Conferences and Computers and Information in Engineering Conference*, 2011, pp. 621–633.

P. R. Veillette, "Engine, Transmission Failures Lead Causes of Accidents in U.S. Helicopter Logging Operations," *Helicopter Safety*, vol. 26, no. 3, pp. 1–12, 2000.

R. August, R. Kasuba, J. L. Frater, and A. Pintz, "Dynamics of Planetary Gear Trains," National Aeronautics and Space Administration, Scientific and Technical Information Branch, NASA Technical Report No. 3793, 1984.

R. C. Hibbeler, *Engineering Mechanics: Dynamics*. Pearson/Prentice Hall, 2004.

R. G. Parker and J. Lin, "Mesh Phasing Relationships in Planetary and Epicyclic Gears," *J. Mech. Des.*, vol. 126, no. 2, pp. 365–370, May 2004.

R. G. Parker, S. M. Vijayakar, and T. Imajo, "Non-Linear Dynamic Response of a Spur Gear Pair: Modelling and Experimental Comparisons," *J. Sound Vib.*, vol. 237, no. 3, pp. 435–455, Oct. 2000.

R. G. Parker, V. Agashe, and S. M. Vijayakar, "Dynamic Response of a Planetary Gear System Using a Finite Element/Contact Mechanics Model," *J. Mech. Des.*, vol. 122, no. 3, pp. 304–310, May 1999.

R. Kasuba and J. W. Evans, "An Extended Model for Determining Dynamic Loads in Spur Gearing," *J. Mech. Des.*, vol. 103, no. 2, pp. 398–409, Apr. 1981.

R. Tuo, C. J. Wu, and D. Yu, "Surrogate Modeling of Computer Experiments with Different Mesh Densities," *Technometrics*, vol. 56, no. 3, pp. 372–380, 2014.

S. Braun, "The Synchronous (Time Domain) Average Revisited," *Mech. Syst. Signal Process.*, vol. 25, no. 4, pp. 1087–1102, May 2011.

S. Jia and I. Howard, "Comparison of Localised Spalling and Crack Damage from Dynamic Modelling of Spur Gear Vibrations," *Mech. Syst. Signal Process.*, vol. 20, no. 2, pp. 332–349, Feb. 2006.

S. M. Vijayakar, "Calyx Users Manual," 2005, http://ansol.us.

S. Vorkoetter, "Demystifying Gearing and Gearboxes," *Sailplane & Electric Modeler Magazine*, 01-Mar-2000.

S. Wu, M. J. Zuo, and A. Parey, "Simulation of Spur Gear Dynamics and Estimation of Fault Growth," *J. Sound Vib.*, vol. 317, no. 3–5, pp. 608–624, Nov. 2008.

T. Barszcz and R. B. Randall, "Application of Spectral Kurtosis for Detection of a Tooth Crack in the Planetary Gear of a Wind Turbine," *Mech. Syst. Signal Process.*, vol. 23, no. 4, pp. 1352–1365, May 2009.

T. Eritenel and R. G. Parker, "An Investigation of Tooth Mesh Nonlinearity and Partial Contact Loss in Gear Pairs Using a Lumped-parameter Model," *Mech. Mach. Theory*, vol. 56, pp. 28–51, Oct. 2012.

T. Eritenel and R. G. Parker, "Nonlinear Vibration of Gears With Tooth Surface Modifications," *J. Vib. Acoust.*, vol. 135, no. 5, pp. 051005–051005, Jun. 2013.

V. K. Ambarisha and R. G. Parker, "Nonlinear Dynamics of Planetary Gears Using Analytical and Finite Element Models," *J. Sound Vib.*, vol. 302, no. 3, pp. 577–595, May 2007.

W. Kim, J. Y. Lee, and J. Chung, "Dynamic Analysis for a Planetary Gear with Time-varying Pressure Angles and Contact Ratios," *J. Sound Vib.*, vol. 331, no. 4, pp. 883–901, Feb. 2012.

X. Gu and P. Velex, "A Dynamic Model to Study the Influence of Planet Position Errors in Planetary Gears," *J. Sound Vib.*, vol. 331, no. 20, pp. 4554–4574, Sep. 2012.

X. Liang and M. J. Zuo, "Dynamic Simulation of a Planetary Gear Set and Estimation of Fault Growth on the Sun Gear," in Proceedings of *International Conference on Quality, Reliability, Risk, Maintenance, and Safety Engineering (QR2MSE)*, 2013, pp. 1667–1672.

X. Liang and M. J. Zuo, "Investigating Vibration Properties of a Planetary Gear Set with a Cracked Tooth in a Planet Gear," in Proceedings of *Annual Conference of the Prognostics and Health Management Society*, Fort Worth, Texas, 2014, pp. 1–8.

X. Liang, M. J. Zuo, and L. Liu, "A Windowing and Mapping Strategy for Gear Tooth Fault Detection of a Planetary Gearbox," *Mech. Syst. Signal Process.*, Revised: 16-Jan-2016.

X. Liang, M. J. Zuo, and M. Pandey, "Analytically Evaluating the Influence of Crack on the Mesh Stiffness of a Planetary Gear Set," *Mech. Mach. Theory*, vol. 76, pp. 20–38, Jun. 2014.

X. Liang, M. J. Zuo, and M. R. Hoseini, "Understanding Vibration Properties of a Planetary Gear Set for Fault Detection," in *Proceedings of IEEE Conference on Prognostics and Health Management (PHM)*, 2014, pp. 1–6.

X. Liang, M. J. Zuo, and M. R. Hoseini, "Vibration Signal Modeling of a Planetary Gear Set for Tooth Crack Detection," *Eng. Fail. Anal.*, vol. 48, pp. 185–200, Feb. 2015.

X. Liang, M. J. Zuo, and T. H. Patel, "Evaluating the Time-varying Mesh Stiffness of a Planetary Gear Set Using the Potential Energy Method," *Proc. Inst. Mech. Eng. Part C J. Mech. Eng. Sci.*, vol. 228, no. 3, pp. 535–547, Feb. 2014.

X. Liang, M. J. Zuo, and Y. Guo, "Evaluating the Time-Varying Mesh Stiffness of a Planetary Gear Set Using the Potential Energy Method," in *Proceedings of the 7th World Congress on Engineering Asset Management (WCEAM 2012)*, Springer International Publishing, 2015, pp. 365–374.

X. Tian, "Dynamic Simulation for System Response of Gearbox Including Localized Gear Faults," Master Thesis, University of Alberta, Canada, 2004.

X. Tian, M. J. Zuo, and K. R. Fyfe, “Analysis of the Vibration Response of a Gearbox with Gear Tooth Faults,” in *2004 ASME International Mechanical Engineering Congress and Exposition*, Anaheim, California USA, 2004, pp. 785–793.

X. Zhao, M. J. Zuo, Z. Liu, and M. R. Hoseini, “Diagnosis of artificially created surface damage levels of planet gear teeth using ordinal ranking,” *Measurement*, vol. 46, no. 1, pp. 132–144, Jan. 2013.

X. Zhou, Y. Shao, Y. Lei, and M. Zuo, “Time-varying Meshing Stiffness Calculation and Vibration Analysis for a 16DOF Dynamic Model with Linear Crack Growth in a Pinion,” *J. Vib. Acoust.*, vol. 134, no. 1, p. 011011, 2012.

Y. Lei, D. Kong, J. Lin, and M. J. Zuo, “Fault Detection of Planetary Gearboxes Using New Diagnostic Parameters,” *Meas. Sci. Technol.*, vol. 23, no. 5, p. 055605, May 2012.

Y. Lei, J. Lin, M. J. Zuo, and Z. He, “Condition Monitoring and Fault Diagnosis of Planetary Gearboxes: A review,” *Measurement*, vol. 48, pp. 292–305, Feb. 2014.

Y. Pandya and A. Parey, “Failure Path Based Modified Gear Mesh Stiffness for Spur Gear Pair with Tooth Root Crack,” *Eng. Fail. Anal.*, vol. 27, pp. 286–296, Jan. 2013.

Y. Shao and Z. Chen, “Dynamic Features of Planetary Gear Set with Tooth Plastic Inclination Deformation Due to Tooth Root Crack,” *Nonlinear Dyn.*, vol. 74, no. 4, pp. 1253–1266, Dec. 2013.

Z. Chen and Y. Shao, “Dynamic Features of a Planetary Gear System with Tooth Crack under Different Sizes and Inclination Angles,” *J. Vib. Acoust.*, vol. 135, no. 3, pp. 1–12, Mar. 2013.

Z. Chen and Y. Shao, “Dynamic Simulation of Planetary Gear with Tooth Root Crack in Ring Gear,” *Eng. Fail. Anal.*, vol. 31, pp. 8–18, Jul. 2013.

Z. Chen and Y. Shao, “Dynamic Simulation of Spur Gear with Tooth Root Crack Propagating along Tooth Width and Crack Depth,” *Eng. Fail. Anal.*, vol. 18, no. 8, pp. 2149–2164, Dec. 2011.

Z. Chen and Y. Shao, “Mesh Stiffness Calculation of a Spur Gear Pair with Tooth Profile Modification and Tooth Root Crack,” *Mech. Mach. Theory*, vol. 62, pp. 63–74, Apr. 2013.

Z. Cheng, N. Hu, and X. Zhang, “Crack Level Estimation Approach for Planetary Gearbox Based on Simulation Signal and GRA,” *J. Sound Vib.*, vol. 331, no. 26, pp. 5853–5863, Dec. 2012.

Z. Cheng, N. Hu, F. Gu, and G. Qin, "Pitting Damage Levels Estimation for Planetary Gear Sets based on Model Simulation and Grey Relational Analysis," *Trans. Can. Soc. Mech. Eng.*, vol. 35, no. 3, pp. 403–417, 2011.

Z. Feng and M. J. Zuo, "Fault diagnosis of planetary gearboxes via torsional vibration signal analysis," *Mech. Syst. Signal Process.*, vol. 36, no. 2, pp. 401–421, Apr. 2013.

Z. Feng and M. J. Zuo, "Vibration Signal Models for Fault Diagnosis of Planetary Gearboxes," *J. Sound Vib.*, vol. 331, no. 22, pp. 4919–4939, Oct. 2012.

Z. Tian, M. J. Zuo, and S. Wu, "Crack Propagation Assessment for Spur Gears Using Model-based Analysis and Simulation," *J. Intell. Manuf.*, vol. 23, no. 2, pp. 239–253, Apr. 2012.

"Gear," Wikipedia, the free encyclopedia. 13-May-2015.